Distributed optical fiber sensors for thermal reaction and fouling monitoring in a continuous tubular emulsion polymerization reactor

Ortsaufgelöste faseroptische Sensoren zur thermischen Reaktions- und Belagsüberwachung in einem kontinuierlichen rohrförmigen Emulsionspolymerisationsreaktor

Dissertation

with the aim of achieving the doctoral degree *doctor rerum naturalium* (Dr. rer. nat) at the Faculty of Mathematics, Informatics and Natural Sciences

Department of Chemistry University of Hamburg

submitted by

Maria Klippert

Hamburg, 2025

Germany

The experimental part of this thesis was carried out under the supervision of Dr. Werner Pauer from October 2020 to August 2024 at the Institute of Technical and Macromolecular Chemistry, University of Hamburg.

urn:nbn:de:gbv:18-ediss-132704

The following evaluators recommend the admission of the dissertation:

1. Evaluator: Dr. Werner Pauer

2. Evaluator: Prof. Dr. Gerrit A. Luinstra

The Date of the disputation: 24.10.2025

Members of examination committee:

1. Prof. Dr. Lisa Vondung

2. Priv. Doz. Dr. Christoph Wutz

3. Dr. Werner Pauer

Acknowledgements

Der Weg zur und durch die Doktorarbeit wurde mir von vielen Menschen ermöglicht und versüßt, bei denen ich mich ausdrücklich bedanken möchte.

Besonderer Dank geht an Prof. Dr. Hans-Ulrich Moritz, Prof. Dr. Gerrit Luinstra und Dr. Werner Pauer dafür, meine fachliche Ausbildung in die Richtung gebracht zu haben, in der ich für die gesamte Dauer meiner Bachelor-, Master- und Doktorarbeit zufrieden verweilen konnte. Letzterem möchte ich dafür danken mich während all dieser Schritte, aber vor Allem in dem letzten Großen, akademisch betreut und gefördert zu haben.

Dr. Werner Pauer und Prof. Dr. Gerrit Luinstra möchte ich außerdem dafür danken, die Rolle der Erst- und Zweitgutachter übernommen zu haben. Prof. Dr. Lisa Vondung und Dr. Christoph Wutz danke ich für die Übernahme des Vorsitzes und des stellvertretenden Vorsitzes der Prüfungskommission.

Es ist ebenso Dank allen Mitgliedern des KoPPonA 2.0 Projektes auszusprechen, ohne die es meine Dissertation in diesem Rahmen nicht geben würde.

Meinen ehemaligen Praktikanten Jingyi Hu, Moritz Hilgers und Angelique Meyer möchte ich für ihre neuen Perspektiven und ihre Hilfe danken.

Den Mitarbeitern im Fachbereich danke ich, insbesondere Susanne Grieser, Stefan Bleck, Michael Gröger, Holger Stockhusen und den Mitarbeitern der Werkstatt unter Leitung von Ansgar Weidner.

Für die Wärmeleitfähigkeitsmessung von PLA danke ich Johannes Gmeiner. Jonas Krautter danke ich für die Freundschaft und der Hilfe bei der Programmierung der 8FiberScan Software, ohne die die Datenlage dieser Arbeit deutlich schlechter aussähe. Vielen Dank an Devon Martin für das Korrekturlesen und die grundlege textliche Überarbeitung meiner ersten Publikation.

Natürlich bedanke ich mich auch ausdrücklich bei meinen Studiumsgenossen Mareike, Laura, Julian, Guiliano, Zainab und Eike, sowie den ehemaligen und aktuellen Kollegen aus den Arbeitskreisen Moritz/Pauer und Luinstra. Dabei möchte ich Svetlana, Wladislaw, Dominique, Jingyi, Kai, Marlen, Philip, Sören, Marcel, Jens und Moritz namentlich danken. Meinen uniferneren Freunden sei auch kräftig gedankt.

Zu guter Letzt bedanke ich mich bei meinem Partner Tom Friedman für den Beistand und die Motivation, nicht nur durch dieses riesige Projekt, sondern auch durch alle Lebenslagen.

List of publications

Research articles

1. M. Klippert, W. Pauer, Distributed optical fiber sensors for real-time tracking of fouling buildup for tubular continuous polymerization reactors, Chemical Engineering Research and Design 211, p. 168–178 (2024). doi: https://doi.org/10.1016/j.cherd.2024.10.007. Impact Factor (IF) at time of publication: 3.95.

2. M. Klippert, W. Pauer, Determination of the clogging time for continuous emulsion copolymerization in a tubular reactor using distributed optical fiber sensors, Chemical Engineering Research and Design 215, p. 465–475 (2024). doi: https://doi.org/10.1016/j.cherd.2025.02.012. IF at time of publication: 4.34.

3. M. Klippert, W. Pauer, Spatially resolved reaction calorimetry and fouling monitoring in a continuous tubular emulsion polymerization reactor, Industrial & Engineering Chemistry Research: Special Issue "Celebrating the legacy of Prof. José M. Asua: Emulsion Polymerization and Polymer Reaction Engineering" (2025). IF at time of publication: 4.01.

Presentations and posters

1. M. Klippert, S. Rust, W. Pauer, Fibre Optic Sensors for Spatially Distributed Temperature Sensing in Reactors, presentation at the 10th PhD–Student Workshop on Polymer Reaction Engineering (WPPRE), San Sebastian, Spain (2022).

2. M. Klippert, S. Rust, W. Pauer, Fibre Optic Sensors for Spatially Distributed Temperature Sensing in Reactors, presentation at the ACHEMA Congress 2022, Frankfurt am Main, Germany (2022).

3. M. Klippert, W. Pauer, Thermal Fouling Detection using Distributed Optical Fiber Sensors, presentation at the 11th PhD–Student Workshop on Polymer Reaction Engineering (WPPRE), Potsdam, Germany (2023).

4. M. Klippert, W. Pauer, Thermal Fouling Detection using Distributed Optical Fiber Sensors, presentation at the ProcessNet–AA Reaktionstechnik sicherheitstechnisch schwieriger Prozesse (AA–RTSSP) 2023, Darmstadt, Germany (2023).

5. M. Klippert, W. Pauer, Reaktionskalorimetrie in Rohrreaktoren mit ortsaufgelösten faseroptischen Sensoren, presentation at the ProcessNet–AA Reaktionstechnik sicherheitstechnisch schwieriger Prozesse (AA–RTSSP) 2025, Frankfurt am Main, Germany (2025).

Inhaltsverzeichnis

1. Zusammenfassung

Rayleigh Optical Frequency Domain Reflectometry (OFDR) DOFS ermöglichen ortsaufgelöste Temperaturmessungen im Subzentimeterbereich und sind daher besonders interessant für Anwendungen, bei denen Hot- oder Coldspots (bspw. Hitzestau) und thermische Gradienten berücksichtigt werden müssen. Die Implementierung von DOFS in einem kontinuierlichen Rohrreaktor im Labormaßstab (3 m Länge, 6 mm innerer Reaktordurchmesser) wird im vorliegenden Text gezeigt, und die Überwachung von Hotspots wird für die mathematische Modellierung von Belagsablagerungen im Reaktor während der Reaktion verwendet. Die kalorimetrische Messung einer exothermen Reaktion wurde aus den DOFS-Daten über eine Wärmestrommessung ermöglicht. Das Prinzip beruhte auf der Platzierung der DOFS in unterschiedlichen Abständen zum Reaktorinnenraum. Der Wärmeverlust durch die Reaktorwand kann auf diese Weise berechnet werden.

DOFS sind optische Glasfasern, und ihre Handhabung unterscheidet sich daher erheblich von der herkömmlicher Temperatursonden. DOFS, die auf Rayleigh- und Brillouin-Streuung basieren, messen systematisch Dehnungs- und Temperaturänderungen. Je nach Anwendung kann es daher von Interesse sein, DOFS zur Messung der Dehnung robust an ein zu prüfendes Objekt zu binden oder die physische Anhaftung an Objekte zu vermeiden, um eine Temperaturmessung zu ermöglichen. Dehnungsmessungen mit DOFS werden im Bereich der Bauwerksüberwachung routinemäßig durchgeführt, und es finden sich DOFS eingebettet in Eisenbahnschienen, in den Wänden von hohen Gebäuden oder in Brücken. Für diese Anwendungen werden die DOFS mit Beton oder Stahl verbunden, z. B. durch die Verwendung von Polymerharzkleber. Das DOFS-Signal unterscheidet nicht zwischen Dehnung und Temperatur. Um eine präzise Temperaturmessung zu ermöglichen, muss daher eine Dehnung der Faser vermieden oder kompensiert werden.

Die Kalibrierung eines räumlich verteilten Sensors ist ebenfalls nicht trivial, insbesondere wenn der Sensor über Abschnitte mit unterschiedlichen physikalischen Bedingungen (Feuchtigkeit, Dehnung, Biegungen und Verdrehungen) eingesetzt wird. Es wurde experimentell gezeigt, dass dies dazu führt, dass die Online-Kalibrierung von DOFS während der Reaktionsüberwachung mit den verwendeten Methoden der Faserintegration nicht realisierbar ist. Die zuverlässigste Kalibrierung wurde erreicht, wenn die DOFS in den endgültigen Reaktoraufbau integriert wurden und der Reaktor selbst auf verschiedene bekannte Temperaturen als Grundlage für die Kalibrierung aufgeheizt wurde. Später zeigte sich auch, dass innerhalb dieses Reaktoraufbaus eine individuelle Kalibrierung für verschiedene Reaktorabschnitte sinnvoll ist. Dies ist

wahrscheinlich darauf zurückzuführen, dass die Biegungen zwischen den Abschnitten die Dehnung, die die DOFS lokal erfahren, verändern.

Die Reaktoren wurden aus Polylactid (PLA) 3D-gedruckt und die Kanäle für die DOFS wurden bereits im CAD-Programm integriert. Als beste Beschichtung für die Robustheit der DOFS erwies sich Polyimid, und als flexibelste Art der Faserterminierung wurde die Verwendung von indexangepassten Lösungen aus Wasser und Glycerin ermittelt. Mit Hilfe eines Spleißgeräts konnten mit Polyimid beschichtete Fasern mit faseroptischen Steckern verbunden werden. Auf diese Weise konnten DOFS vor Ort hergestellt werden, was eine große Kostenreduzierung bedeutete und die Flexibilität bei der Integration der Fasern in Reaktorkonfigurationen erhöhte. Im Inneren der DOFS-Kanälen in den 3D-gedruckten Reaktorteilen aus PLA wurde eine Wärmeleitpaste eingetragen, um die wärmeisolierende Wirkung von Luft zu vermeiden. Dies diente der Vereinfachung von Berechnungen für die Überwachung von Wärmeverlusten durch die Reaktorwand. Im Hinblick auf die langfristige Stabilität der Fasern wurde festgestellt, dass die Verwendung eines nicht hygroskopischen Gels als Kanalfüllstoff von Vorteil sein könnte.

Der prototypische Charakter des Reaktor-DOFS-Aufbaus führte dazu, dass die DOFS der Feuchtigkeit der Umgebung und mechanischen Störungen ausgesetzt waren. Dies führte zu einem Signaldrift und erforderte häufige Kalibrierung der Sensoren. Es werden Methoden erörtert, um dies in Zukunft zu vermeiden, sowie Möglichkeiten zur Integration von DOFS in Aufbauten, die für Hotspot-Messungen oder Strömungskalorimetrie optimiert sind. Diese Vorschläge werden im Abschnitt Diskussion dieser Dissertation erwähnt und illustriert.

Das reaktionstechnische Problem, das mit der DOFS-Technologie untersucht werden sollte, war die Emulsionscopolymerisation von Vinylacetat und Vinylneodecanoat. Die Reaktion wurde bei einem Monomergehalt von 24 Gew.-% unter Verwendung eines Redox-Initiatorsystems durchgeführt, das aus tert-Butylhydroperoxid, Ascorbinsäure und Ammoniumeisen(III)-sulfat bestand. Als Emulgator und Stabilisator wurde Polyvinylalkohol verwendet (Mowiol 4-88®). Diese Reaktion wurde unter anderen von der Forschungsgruppe von Dr. Pauer der Universität Hamburg, der Gruppe von Dr. Ing. W. Augustin der Universität Braunschweig und der Gruppe um Prof. Dr. Asua vom Polymat im Baskenland untersucht. Sie wurde als Modellreaktion für eine belagsintensive Emulsionspolymerisationsreaktion und als Herausforderung für die Prozessintensivierung durch kontinuierliche Synthese verwendet. Informationen über die Belagsbildung dieser Reaktion sind bekannt und konnten als Bezugspunkte für die auf den DOFS-Daten basierenden Erkenntnisse verwendet werden.

Durch die exotherme Polymerisationsreaktion bildete sich in dem mit DOFS ausgestatteten Rohrreaktor ein überwachbarer Hotspot. Der Hotspot wanderte während der Reaktion stromabwärts, während der gravimetrisch gemessene Monomerumsatz am Auslass abnahm. Dies war darauf zurückzuführen, dass die Ablagerungen im Laufe der Zeit mehr Volumen im Reaktor einnahmen und die Reaktion stromabwärts drängten. Es wurde ein mathematisches Modell entwickelt, um den Volumenverlust innerhalb des Reaktors geometrisch über die Zeit und entlang der Reaktorachse zu beschreiben. Dieses Basismodell wurde auf verschiedene Arten der räumlichen Ablagerung angewandt (stärkere Ablagerung zum Ende oder zur Vorderseite des Reaktors hin, gleichmäßige Ablagerung entlang der Reaktorachse, unterschiedliche Gradienten der Belagsdicke vom Einlass zum Auslass). Der relevante freie Radius (z. B. der Auslassradius für die Ablagerung von Fouling mit einer linearen Zunahme entlang der Reaktorachse ab einer Dicke von 0 am Einlass) wurde als Funktion der Reaktionszeit definiert.

Die DOFS-Daten der Polymerisationsreaktion wurden als Heatmap mit der Reaktionszeit und der Reaktorlänge als x- und y-Achsen und der Temperatur als z-Achse (Farbe) dargestellt. Die z-Achse wurde verwendet, um den Hotspot zu definieren und ihn zu einem beliebigen Zeitpunkt entlang der y-Achse zu lokalisieren. Dieses x-y-Diagramm der Hotspot-Position in Zeit und Raum wurde zur Parametrisierung der Modellfunktionen verwendet. Die Modelle, die die Bewegung des Hotspots am besten beschrieben, betrachteten die Belagsablagerung als gleichmäßig über die gesamte Reaktorlänge und die Ablagerungsrate als linear oder kubisch (eine stark gestreckte kubische Funktion, die der linearen Rate im betrachteten Intervall sehr nahekam). Sowohl die lineare als auch die kubische Ablagerungsrate konnten in der Literatur wiedergefunden werden. Die Modelle mit den besten Übereinstimmungen waren auch in der Lage, die Zeit zu berechnen, zu der der Reaktor verstopfen würde, wenn nur 30 Minuten an Daten vorlagen. Die Verstopfungszeiten wurden in einem Bereich von 0.89 bis 1.28 berechnet, wobei 1 eine perfekte Übereinstimmung mit den experimentellen Daten darstellt, wenn nur die ersten 12 % (ca. 30 min) der Reaktionszeit mit den Modellen betrachtet werden (100 % sind vom Start bis zur Verstopfung).

Die Kanäle für die DOFS wurden in drei verschiedenen Abständen entlang der radialen Achse des Reaktors innerhalb der Reaktorwand positioniert. Dies geschah, um das radiale Temperaturprofil entlang des Reaktors zu messen und den Wärmestrom durch die Wand zu berechnen. Erhitztes Wasser wurde mit einer konstanten Durchflussrate durch den Reaktor geleitet. Der Rektor wurde nur durch natürliche Konvektion der Umgebungsluft bei

Raumtemperatur gekühlt. Die resultierende Abkühlungsrate wurde als Basis für die Kalibrierung der DOFS verwendet, da die Wärmemenge, die das Wasser entlang der Reaktorachse verliert, direkt aus dem Temperaturunterschied, der Wärmekapazität der Wassers und der Flussrate berechnet werden kann. Die Experimente mit erhitztem Wasser wurden genutzt, um die Wärmeübergangskoeffizienten α an der inneren und äußeren Reaktorwand über die Ähnlichkeitstheorie und die Korrelation zwischen der Nußelt-Zahl *Nu* und α zu bestimmen. Mit sechs im Reaktorkanal befindlichen Thermoelementen konnte der axiale Wärmeübergang durch den Reaktor berechnet werden. Wärmeverluste von 2 bis 9 W konnten in diesem Aufbau mit einer Genauigkeit von 0,39 W gemessen werden.

Die gleichen Messungen und Berechnungen wurden für die Copolymerisation von Vinylacetat und Vinylneodecanoat im Rohrreaktor durchgeführt. Die Reaktion ist autotherm und der Reaktor ist isoperibolisch, daher wird die gesamte erzeugte Wärme als Reaktionswärme angenommen. Anhand des vorherigen Kalibrierungs- und Berechnungsprozesses wurde die freigesetzte Wärme ermittelt und durch die theoretisch freigesetzte Wärme bei vollständiger Umwandlung geteilt, um den thermischen Umsatz zu ermitteln. Der thermische Umsatz wurde mit dem gravimetrischen Umsatz, der auf Proben, die am Auslass entnommen und sofort in einer Mikrowellenwaage vermessen wurden, basierte. Die beiden Reaktionszeit-Umsatzkurven wurden verglichen und zeigten in bestimmten Zeiträumen eine gute Übereinstimmung.

Daraus wurde abgeleitet, dass die geringe räumliche Auflösung der sich im Strom befindlichen Temperatur dazu führte, dass die axial transportierte Wärme unterschätzt wurde, wenn das Temperaturmaximum nicht mit einem Thermoelement zusammentraf. Da dies während der meisten Zeit der Fall war, zeigte sich die Auswirkung deutlich in einer Unterschätzung des thermischen Umsatzes. Während Zeiten der örtlichen Übereinstimmung des Temperaturmaximums mit einem Thermoelement betrug die berechnete thermische Umwandlung 79 % ± 3 %, während die gravimetrische Umwandlung 78 % ± 2 % betrug. Dies zeigt, dass die Methode gut funktioniert, wenn die Hotspot-Temperatur korrekt gemessen wird. Die Integration eines DOFS im Fluss würde das Problem der geringen räumlichen Auflösung im Reaktorinneren beseitigen, doch dies ist ein technisches Problem, das weiter untersucht werden muss. Dieses Thema wird auch im Abschnitt Diskussion der Dissertation erörtert, in dem Probleme und Lösungen dargestellt werden.

2. Summary

Distributed Optical Fiber Sensors (DOFS) are currently not part of the traditional chemical engineering toolkit. Rayleigh Optical Frequency Domain Reflectometry (OFDR) DOFS allow spatially resolved temperature measurement on a sub-centimeter scale and are therefore particularly interesting for applications during which hot- or cold spots and thermal gradients need to be considered. The implementation of DOFS in a laboratory-scale continuous tubular reactor setup (3 m length, 6 mm inner reactor diameter) is shown in the present text and hotspot monitoring is used for mathematical modelling of fouling deposition in the reactor during reaction. Calorimetric data of an exothermal reaction is calculated from DOFS data via heat flow measurement based on the placement of DOFS at different distances to the inner reactor space. The heat loss through the reactor wall can be calculated in this manner.

DOFS are optical fibers, and their handling is therefore considerably different from traditional temperature probes. Rayleigh and Brillouin scattering-based DOFS simultaneously read strain and temperature changes. Depending on the application, it may therefore be of interest to robustly bind a DOFS to an object under test to measure strain or avoid physical adherence to any objects to enable temperature measurement. Strain measurements using DOFS are carried out in the field of structural health monitoring routinely and DOFS can be found embedded in train tracks, the walls of skyscrapers or in bridges. For these applications the DOFS are bound to concrete or steel e.g. by use of polymeric resin glue. The DOFS signal does not inherently distinguish between strain and temperature. Therefore, to allow for precise temperature measurement, strain on the fiber must be avoided or compensated for.

The calibration of a spatially distributed sensor is also not a trivial issue especially if said sensor is used over sections of different physical environment (moisture, strain, bends and twists). It was experimentally shown that this causes online calibration of a DOFS during reaction monitoring to be non-feasible with the employed methods of fiber integration. The most reliable calibration was achieved with the DOFS integrated in the final reactor setup and the reactor itself being heated to different known temperatures as basis for calibration. Later, it was also shown that within this reactor setup individual calibration for different reactor sections made sense. This was likely due to bends in between the sections changing the strain the DOFS experienced locally.

Reactors were 3D printed using polylactide (PLA) and channels for the DOFS were integrated in the CAD program. The best coating for DOFS ruggedization was found to be polyimide and

the most flexible way of fiber termination was determined to be the use of index-matched solutions of water and glycerol. With the use of a splicer, bare polyimide coated fiber could be coupled with fiber optical connectors. In this way, DOFS were created in-house at a large cost saving and increased flexibility in fiber integration into reactor setups. Inside the DOFS channels in the PLA 3D-printed reactor parts a thermal paste was applied to avoid the thermal insulating effect of air. This was done to simplify calculations and enable the monitoring of heat loss through the reactor wall. Considering long term fiber stability, it was deduced that use of a non-hygroscopic gel as a channel-filler may be beneficial.

The prototypical nature of the reactor-DOFS setup led to DOFS being subject to moisture from the environment and mechanical disturbance. This caused signal drift and required frequent calibration of the sensors. Methods to prevent this in the future and ways of DOFS integration into setups optimized for hotspot measurement or flow calorimetry are discussed. These suggestions are mentioned and illustrated in the *Discussion* section of this dissertation.

The reaction engineering problem that was chosen to be elucidated with DOFS technology was the emulsion copolymerization of vinyl acetate and vinyl neodecanoate. The reaction was carried out at a 24 w% monomer content using a redox initiator system consisting of tert-butyl hydroperoxide, ascorbic acid and ammonium iron(III) sulfate. As emulsifier and stabilizer polyvinyl alcohol was used (Mowiol 4-88®). This reaction has been studied by the research group of Dr. Pauer and the University of Hamburg, the group of Dr. Ing. W. Augustin at the Technical University of Braunschweig and by the group surrounding Prof. Dr. Asua from the Polymat in Basque country. It has been used as a model reaction for a fouling-heavy emulsion polymerization reaction and as a challenging choice for process intensification by synthesis in a continuous manner. Therefore, fouling information about this reaction is known and has been used as reference points for the findings based on the DOFS data.

The exothermal polymerization reaction caused a monitorable hotspot to form in the tubular reactor equipped with DOFS. The hotspot wandered downstream during the reaction while the gravimetrically measured monomer conversion at the outlet decreased. This was caused by the fouling deposition taking up more volume inside the reactor over time and pushing the reaction downstream. A mathematical model was devised to describe the volume loss inside the reactor geometrically over time along the reactor axis. This basic model was applied to different modes of spatial fouling deposition (more deposition towards the end or front of the reactor, even deposition along the reactor axis, different gradients of fouling deposition from inlet to outlet).

The relevant free radius (e.g. outlet radius for fouling depositing with a linear increase along the reactor axis from a thickness of 0 at the inlet) was defined as a function of the reaction time.

The DOFS data from the polymerization reaction was visualized as a heatmap with the reaction time and the reactor length as the x and y axes and the temperature as the z axis (color). The z axis was used to define the hotspot and locate it at any time along the y axis. This x-y plot of the hotspot position in time and space was used to parameterize the model functions. The models which best described the motion of the hotspot considered the fouling as an even deposition along the entire reactor length and the fouling rate as linear or cuboid (a stretched cuboid that was very close to the linear rate in the observed section). The linear and cuboid fouling rates could both be corroborated by literature findings. The models with the best fits were also able to calculate the time at which the reactor would clog when given only 30 min of data. The clogging times were calculated within a range of 0.89−1.28 with 1 being a perfect fit with experimental data from data describing only the first 12 % of reaction time (100% being from start to clogging).

The channels for the DOFS were positioned at three different distances along the radial axis of the reactor inside the reactor wall. This was done to measure the radial temperature profile along the reactor and calculate the heat flow through the wall. Heated water was conveyed through the reactor at a constant flow rate and the cooling caused by heat transport from the reactor channel to the environment at room temperature via natural convective cooling was monitored using DOFS. These measurements were used to calibrate the DOFS and the heat loss calculation, as the temperature difference between inlet and outlet corresponded directly to the feed rate and heat capacity of water. The experiments with heated water were used to estimate the heat transfer coefficients α at the inner and outer reactor wall via similarity theory and the correlation between the Nußelt number Nu and α. With six instream thermocouples, the axial heat transfer through the reactor could be calculated. Heat losses from 2 to 9 W could be measured with an accuracy of 0.39 W in this setup.

The same measurements and calculations were carried out for the copolymerization of vinyl acetate and vinyl neodecanoate in the tubular reactor. The reaction is autothermal and the reactor is isoperibolic, therefore all created heat is assumed to be reaction heat. With the previous calibration and calculation path, the released heat was calculated and divided by the theoretically released heat at full conversion to give the thermal conversion. The thermal conversion was compared to the gravimetrical conversion based on samples collected at the outlet and immediately processed in a microwave scale to determine solid content. The two

reaction time-conversion curves were compared and showed good agreement during certain timeframes. It was deduced that the low spatial resolution of the instream temperature caused the axially transported heat to be underestimated when the temperature maximum did not align with a thermocouple. As this was the case during the majority of the time, its impact was seen clearly in the thermal conversion by an underestimation. During time of alignment with a thermocouple the calculated thermal conversion was 79 % ± 3 % while the gravimetrical conversion was 78 % ± 2 %. This exemplifies that the method works well if the hotspot temperature is correctly measured. The integration of a DOFS instream would eliminate the low spatial resolution problem, but it is an engineering problem that needs further studying. This topic is also explored in the *Discussion* section of the dissertation where problems and solutions are illustrated.

3. Introduction

3.1. Emulsion polymerization

Heterophase polymerization is a process resulting in a polymer dispersion. Dispersion, suspension, emulsion, micro-emulsion and inverse emulsion systems are part of the heterophase polymerization modes. They can be distinguished using their continuous phase, monomer solubility, initiator type and resulting particle diameter. There is no hard rule for sorting polymerizations into these categories.[1] Commonly and in the scope of the presented work, emulsion polymerization is defined as a polymerization reaction in an aqueous continuous phase with dispersed monomer which possesses a low water-solubility. An amphiphilic stabilizer (e.g. surfactant, polymeric) is used together with a mode of agitation to disperse the organic in the continuous phase. The radical initiator is typically miscible with the continuous phase. Monomer droplets form during dispersion and upon reaction active particles are created. By the end of the reaction polymer particles are suspended in the aqueous phase. The resulting product is called polymer latex. Resulting particles have a diameter of 5 nm to 10 µm.[1,2] Due to the aqueous continuous phase, the reaction temperature range is 0 to 100 °C.

Polymer dispersions are used in water-based coatings, inks, adhesives and additives. They are used in the paper, leather, automotive and construction material (concrete, asphalt, adhesives) industry.[3] Advantages of emulsion polymerization are the direct production of polymer dispersions, the improved thermal safety of the reaction (lowered viscosity and large heat capacity of the aqueous continuous phase) and the high molecular weight of products.[3,4] The water-based polymerization has the benefit of being low in volatile organic compounds (VOCs) in comparison to solvent-based polymerization, therefore addressing environmental concerns.[5]

The product and reaction characteristics can be influenced by a plethora of factors, such as choice of stabilizer, monomers, additives, initiator, (order of) mixing, temperature, respective concentrations of components, oxygen presence and the chosen reactor. The changes in reaction and kinetics are reflected in the number and type of particles, initiator activity, distribution of active species between phases, monomer conversion and rate of termination.[1,2,6] The link between reactor variables and the final product properties can be defined as the polymer microstructure, including e.g. copolymer composition, particle morphology, crosslinking and branching, molecular weight distribution (MWD) and particle size distribution (PSD). Models with these factors are being created to explain and optimize product properties.[5] The number

of variables and heterogeneity of the polymerization system complicates mechanistic and kinetic descriptions and modelling substantially. Industrially, emulsion polymerization has been serviceable and is being continuously improved since before 1945.[7] However, the understanding of the mechanism and kinetics of emulsion polymerization is still being defined, and new ideas are introduced to the present day.[1,7,8]

To gain a deeper understanding of the mechanisms and kinetics of emulsion polymerization and therefore enable process optimization and intensification, different methods of (online) analysis have been suggested in literature. An overview of literature concerning e.g. spectroscopic, light scattering, chromatographic, spectrometric online analysis can be found in chapter 4.4 'Process Engineering' in *Heterophase Polymerization* (2021, Hernandez and Tauer).[1] Due to the complexity of the system, meta-models/soft sensors and predictive models are a subject of further study concerning process variables and optimization. An example of an inferred measurement (soft sensor) is the calculation of particle size using an inline turbidity sensor.[9,10] The use of computational model-based process description has been the basis for the development of nonlinear model predictive control, which has been successfully demonstrated in a pilot plant-scale semi-batch reactor.[11]

3.2. Emulsion polymerization of vinyl acetate

Vinyl acetate is a fairly water-soluble monomer ($20\ \mathrm{g \cdot L^{-1}}$) and PVAc can be hydrolyzed to create polyvinyl alcohol (PVA), which is how products such as Mowiol 4-88 are created (the 88 refers to the mol-percent of hydrolyzation from PVAc).[12] To increase hydrophobicity VAc is often copolymerized with lass water-soluble monomers. Another function of the copolymerization is the decreasing of the glass transition temperature T_g of PVAc (pure PVAc has an approximate T_g of 30 °C). As the resulting dispersions are often used for coatings, it is preferrable to lower the glass transition temperature of the polymer to improve film formation.[6,13] The homo- and copolymers of vinyl acetate and comonomers such as butyl acrylate, long chain vinyl esters or ethylene account for 32 % of global emulsion polymerization products.[14]

Germany and Italy are the leading producers of VAc-based polymers in aqueous dispersions with 58 and 19 % of the annual production quantity in the EU.[15] In 2023 the EU share of this PVAc product sector accounts for approximately 17 % of the global VAc-based product market.[15,16]

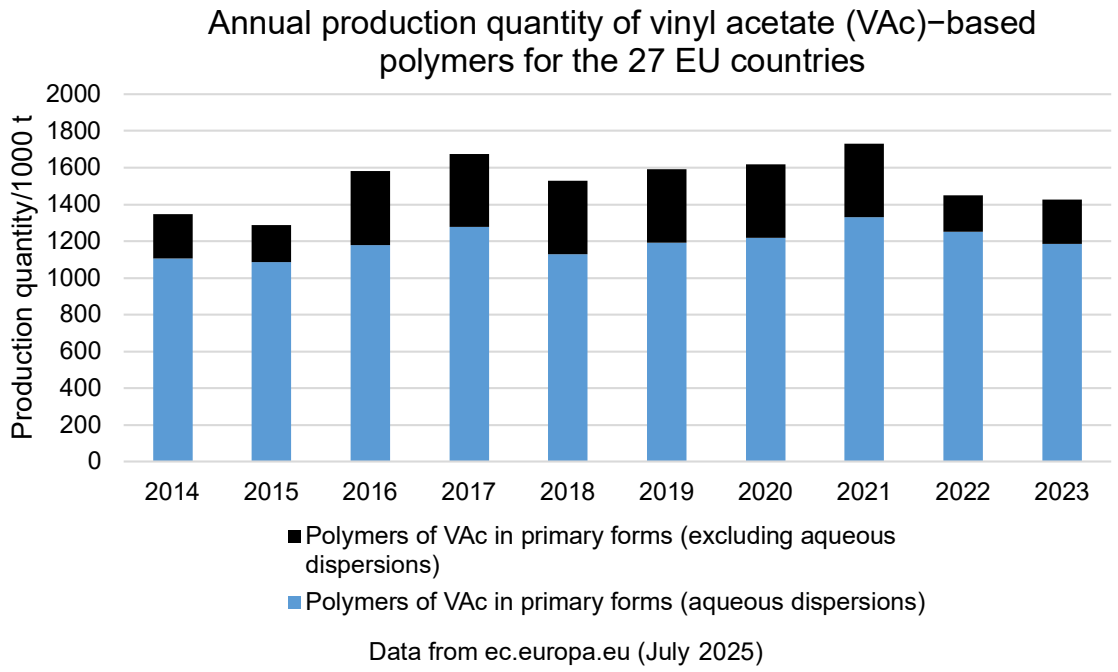

Figure 1: Annual production quantities of vinyl acetate (VAc)-based polymers for the countries of the European Union (EU) as of 2020 (27 countries).[16,17]

Emulsion and mini-emulsion copolymerization of VAc and vinyl neodecanoate (VV10) (VeoVa10® or Versa10®) has been carried out using ionic and nonionic surfactants, such as sodium lauryl (ether) sulfate, PVA and hydroxymethyl/ethyl cellulose.[13,18] Common methods of reaction initiation are the use of thermal peroxide initiators, such as potassium persulfate, or initiator and redox component systems, such as potassium persulfate with sodium metabisulfate, or tert-butyl hydroperoxide with ascorbic acid. A room temperature initiator system using tert-butyl hydroperoxide, ascorbic acid and ammonium iron(III) sulfate has been examined in detail in literature.[19,13,20] It has been shown that the emulsion characteristics in PVA-stabilized polymerizations are impacted by particle coagulation and degree of grafting of polymer and PVA.[13,21,22] For indoor applications the VAc:VV10 weight ratio is often 9:1 to 8:2. Outdoor applications call for a higher protection from hydrolysis, therefore ratios of 8:2 to 7:3 are employed. Industry-like solid contents for VAc-VV10-copolymer dispersions are 40-60 w%[13,23] The high dependence of product characteristics on the properties of PVA stabilizer and the formation of precipitate and fouling on reactor surfaces are challenges that are mentioned since the inception of VAc emulsion polymerization.[19] Nowadays, there are PVA products with narrow property ranges, ensuring reproducibility of reactions. The formation of coagulate and fouling are problems which are still being studied in literature.[16,13,24]

3.3. Continuous polymerization reactors

At present, emulsion polymerization is most commonly carried out in semi batch processes.[25] While the operation of batch reactors is straight forward, flexible and well-studied, there are some disadvantages. For reactions requiring pre-heating, getting the entire reactor up to temperature during every reaction start period is more energy consuming than keeping a reactor at a constant elevated temperature. Many batch reactors are stirred tanks, which have a low surface to volume ratio, increasing the energy needed for temperature control. This latter point is of special interest for polymerization reactions, as they are exothermal. The reaction enthalpy of vinyl acetate is $\Delta H_R = 88.8\ \mathrm{kJ \cdot mol^{-1}}$. In continuous reactors new and intensified modes of mixing, heat transfer and monitoring are possible.[4,6]

The goals of process intensification in chemical reaction engineering are improved sustainability and safety of reactions as well as maximizing profitability. Methods to achieve this involve the integration of several devices and functionalities into one apparatus, online optimization and monitoring, minimization of reaction volumes and improved throughput, static mixing and heat transfer technology, the shortening of diffusion paths and the use of novel synthesis routes (electrochemistry, microwave etc.). Continuous reaction engineering is a large part of process intensification.[4,26] Continuous reactors enable passive mixing, and tubular reactors have a large surface to volume ratio, allowing for improved heat transfer. Continuous analysis methods such as chromatography can be used inline and separation and further processes can be used in series to the continuous reactor in an automated manner.[26]

The transfer of a process from batch to a continuous reactor can cause reaction kinetics and selectivity to change.[27] Reaction calorimetry is an important tool to study such effects and their impact on the safety of the process. To this end, continuous calorimeters are needed, however, not many exist on the market. For continuous reactors which are not continuous stirred-tank reactors (CSTRs), spatially resolved measurements are needed.[28] Continuous calorimeters using a series of thermo- or Seebeck elements can be found in literature, as well as the implementation of Infra-Red (IR) thermography.[29,29-34]

With regards to emulsion polymerization, the use of series of CSTRs, tubular (bent or coiled) and loop reactors have been reported.[35-40] The copolymerization of VAc and VV10 has been carried out in a loop reactor and similar oscillating behavior with regard to the particle size and conversion as observed in CSTR operation has been reported.[40] In a two CSTR cascade a

controlled product with dampened oscillation has been achieved by Agirre and Asua, and a mathematical model for the intensified process is provided.[39]

The improved heat transfer properties of continuous reactors due to the high surface to volume ratio are a fundamental advantage over batch and semi-batch reactors. However, for reactions with precipitation and the formation of a fouling layer, additional surface can be a disadvantage. In process intensification many favorable technologies such as high surface to volume ratio, short diffusion paths and static mixers are also prone to fouling.[4,6]

3.4. Fouling during emulsion polymerization

Fouling is the unwanted deposition of solid material on a surface or the change of said surface in a disadvantageous way. A way to describe fouling by nature of its creation process is the distinction into five categories: crystallization fouling, particulate fouling, reaction fouling, corrosion fouling and biofouling.[41] If a process is prone to fouling from multiple of these categories at once, it is composite fouling.[24] The reactive mixture of an emulsion polymerization can lead to reaction fouling and particulate fouling, therefore it is a composite system. Chemical reaction fouling has been defined by Watkinson in 1997 as the subsequent synthesis of a fouling precursor, followed by formation of soluble and then insoluble fouling precursors, followed by the formation of foulant.[42] Particulate fouling in colloidal systems is dependent on particle sedimentation or diffusion to surfaces. These processes are influenced by the coagulation of the particles.[41,43,44] Surface deposition of particles in colloidal systems can be described with van-der-Waals and electrostatic forces using DLVO theory.[45]

In the context of emulsion polymerization fouling, there is often a focus on coagulation and stability of the dispersion.[18,24] Across multiple studies many factors influencing fouling during emulsion polymerization fouling have been identified: Initiator (degree of initiation, rate), emulsifier (concentration, characteristics), temperature (heat exchange characteristics and heated/cooled surfaces), pH and ionic strength of the aqueous media, stirrer speed, viscosity and solid content.[6,24,46-51] In regard to the influence of stirrer speed, viscosity and collision frequency of particles, shear-induced coagulation appears to be an overarching factor.[52-54] During experiments with active polymer reaction mixture and dead polymer dispersion, it was shown that polymer and polymerization fouling (the particulate and reaction fouling in this system) appear simultaneously, but at different rates during different times in the reaction.[24]

Based on findings in literature it can be summarized that for the emulsion copolymerization of VAc and VV10 using PVA as stabilizing agent fouling is increased by raised (wall) temperature,

higher solid content, higher initiator content, higher emulsifier content and higher ratio of monomers (VAc:VV10).[6,24]

Methods for fouling prevention are the use of additives, surface preparation and coating and technological methods such as the use of specialized reactor geometries.[6,51,55-62] In emulsion polymerization the use of polydimethylsiloxane, wax and titanium dioxide as surface treatments and electropolished surfaces have been studied for fouling reduction.[6,51] Effective fouling prevention and removal is based on understanding of the fouling process. In comparison to emulsion polymerization fouling, fouling formation on membranes and crude oil pipelines has been discussed to a high degree in literature. For example, it has been determined that in wastewater treatment membrane fouling can be traced back to the use of cationic polymer sludge treatment chemicals. Time dependence and fouling removal options for this and other membrane fouling problems have been explored, and irreversible and reversible fouling could be distinguished and modelled mathematically.[63,64] For crude oil fouling, the definition of descriptive and predictive models has been carried out using threshold fouling, and deterministic models. The threshold model works for systems where fouling does not occur if certain conditions are not met. A fouling activation energy is usually defined in this type of model, however the use for the term activation energy in this context is not comparable to the activation energy of a chemical reaction.[65] Deterministic models are based on empirical data and conditions and the deposition of fouling, forgoing the threshold fouling's activation energy. Fouling is correlated to multiple conditions, such as surface roughness, flow pressure drop, mass transfer, surface temperature and surface shear stress.[66-68]

Fouling monitoring and analysis can be subdivided into online and offline techniques. Offline, the fouling deposit can be analyzed regarding its microstructure (e.g. gel content, crosslinking), composition (e.g. SEC, NMR) and physical mass and appearance.[69] Online methods require a way to directly or indirectly measure fouling during reaction. This has been achieved with an ultrasound method, electrochemical impedance spectroscopy and a quartz microbalance in the context of emulsion polymerization.[70-73] These methods have proven to be useful for the early stages of fouling, while the film thickness is still small. Weighing the entire reactor after reaction is less precise than these methods but is applicable for all stages of fouling.[69,74] A method measuring the increase in thermal resistance of the reactor walls caused by the fouling deposit has been used to study different factors influencing the intensity of fouling for the emulsion copolymerization of VAc and VV10.[24,75]

3.5. Distributed Optical Fiber Sensors

Fiber Optical Sensors (FOS) have been used for many decades for a plethora of applications. They can be divided into extrinsic and intrinsic sensors. Extrinsic sensors are such where the fiber optic cable is used as a device to transfer an optical signal from e.g. the detector to an electronic measuring device. These sensors are traditional and can be found in many applications with optical signals in labs all over the world. The probe is at the end of the fiber optic cable and the cable is used in transmission. Intrinsic sensors use the fiber cable itself as the probe and transmission simultaneously.

The intrinsic FOS can be sorted into the categories Distributed Optical Fiber Sensors (DOFS) and non-distributed FOS (point sensors). The latter uses a few altered sections along a fiber optic cable as a series of point sensors (gratings). This sensor type includes Fiber-Bragg-Gratings (FBGs) and fiber optic Fabry-Perot interferometry (FFPI). FOS can be made of optical glass or polymer, which is another distinction commonly made in the field of FOS.

DOFS are FOS in which the entire fiber cable length is used as the sensor. Using Optical Time Domain Reflectometry or Optical Frequency Domain Reflectometry, DOFS provide a spatially distributed measurement. The scattering mechanisms inside the fibers which are used in DOFS technology are Brillouin, Raman and Rayleigh scattering. Distinction between single mode, multimode, polarization-sensitive or -compensated DOFS can also be made. The criteria by which DOFS are compared are measurand resolution, range, spatial resolution (number of sensing points per range) and measurement time. The different combinations of backscatter mechanism, mode of reflectometry and other specifications give rise to a variety of different types of DOFS with varying (measurand and spatial) resolution, measuring range and measurement time. The amount of different FOS types, initial cost of technology, as well as the application and sensing mechanism differing considerably from traditional sensors, are part of why this sensing technique is not more widespread and understood. However, within certain fields a variety of DOFS have become important sensing techniques within the last decades, due to their characteristics and range. Amongst such applications are the monitoring of boreholes and oilwells, high voltage transmission cables, some fire detection applications, structural health monitoring (SHM) and biomedical applications such as intra-aortic catheters. The beneficial characteristics of DOFS sensors are spatially resolved data acquisition, the small form-factor and therefore thermal mass of the sensor itself, the tolerance to a large temperature range (cryogenic to over 1000 °C) and immunity from electromagnetic interference due to the optical character of the data.[72,76-79]

The DOFS technology used in the presented work is Rayleigh-backscatter-based OFDR measurement using telecommunications-grade fiber optic sensors. The following explanation of sensing setup, mechanism and method characteristics are intrinsic to this method.

Figure 2 shows the setup for Rayleigh backscatter sensing in a distributed manner and is based on the work of D. K. Gifford et al. (2007).[80] In this setup, a tunable laser source (TLS) is used to send swept wavelength pulses of laser light into the optic fibers. This is the basis for OFDR measurement. In OTDR, the spatial resolution is created by sending out laser pulses at a known frequency and interpreting the backscattered signal's temporal delay from travelling through the glass medium. In OFDR, the swept-wavelength incident signal enables the inference of spatial information from the mixing of the backscattered light with the light from the reference interferometer. In OTDR a shorter pulse enables a higher spatial resolution (smaller gage length), but at the cost of worsening signal-to-noise ratio (SNR). Rayleigh OTDR can interrogate long distances (kilometers) with a spatial resolution in the meter range, and Rayleigh OFDR can interrogate small distances (meters) with a sub-millimeter spatial resolution.[76,77]

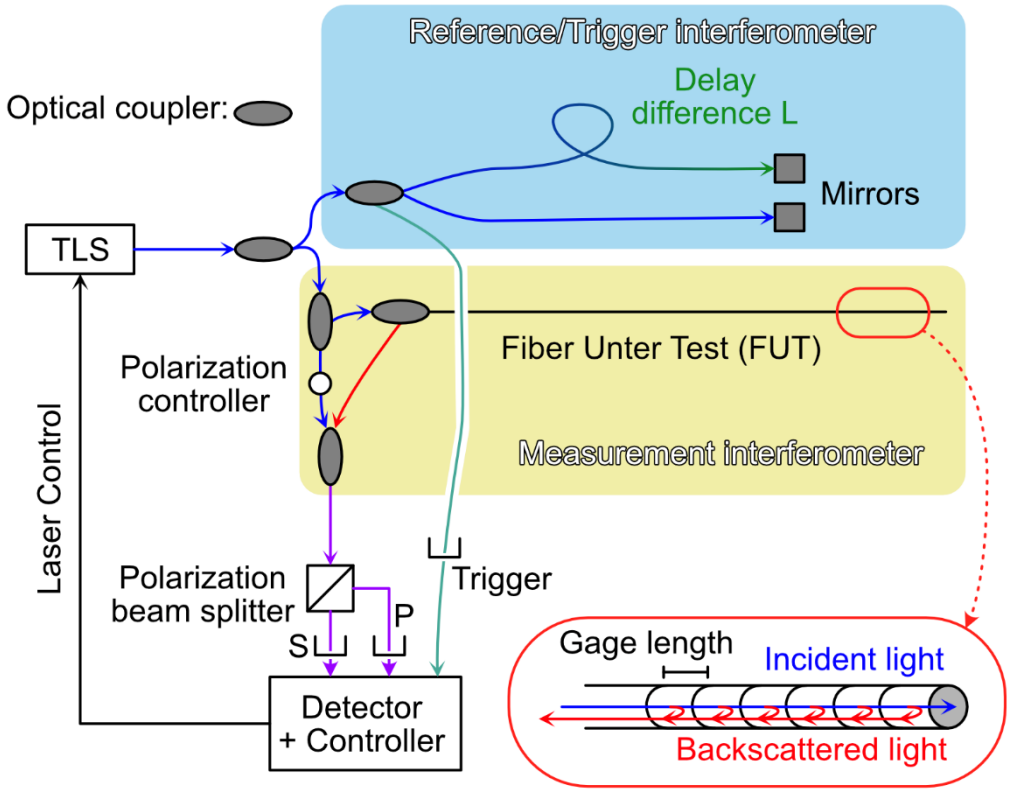

Figure 2: Schematic explaining the interferometric setup to measure Rayleigh backscatter for distributed sensing applications, using a TLS (tunable laser source).

The backscattering inside the cores of optical fibers is caused by any local changes in refractive index (RI). Therefore, every physical fiber has a different backscatter signature, and it can be inferred that fibers with more defects and impurities can enable better SNR by causing more backscatter.[76] Rayleigh-based DOFS measurement is based on the elastic process of Rayleigh scattering. Due to Brillouin and Raman scattering being inelastic processes, a higher probing energy is needed, and the SNR is typically lower than that of Rayleigh measurements.[77]

Figure 3 shows how the scatter centers (impurities/inhomogeneities) are physically distributed in a fiber core, and how the change in their relative positions to each other via fiber stretching alters a DOFS measurement signal. The pictured measurement is merely a graphical aid and not a real measurement.

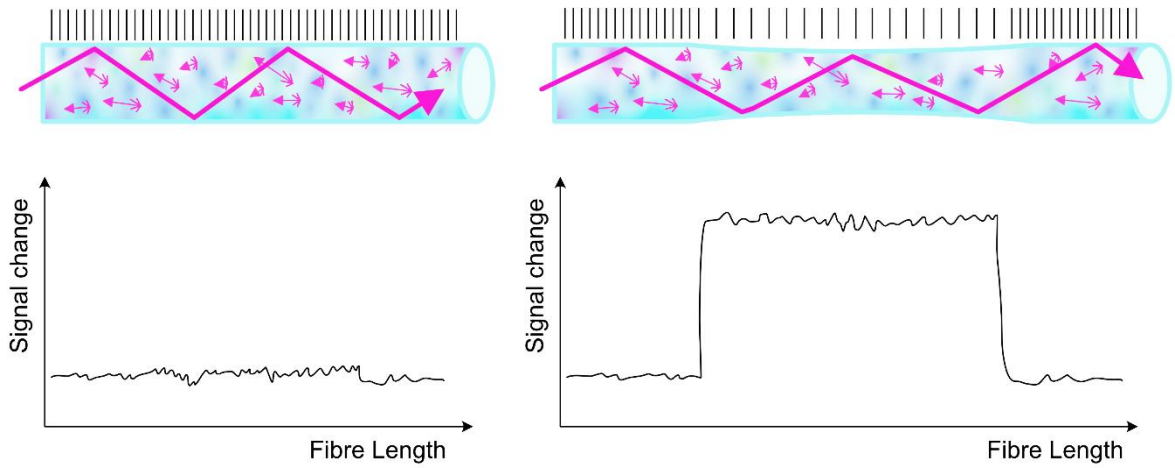

Figure 3: Visual explanation of how an external force can impact the physical arrangement of backscatter centers in a fiber core and therefore create signal that can be measured in a spatially distributed manner along the fiber length.

Based on the mechanism of signal generation it can be understood how the two main measurands of DOFS impact the fiber. Strain, being the introduction of physical deformation to a fiber in compression or tension, is pictured in Figure 3. Temperature causes material to expand or contract and therefore secondary strain is introduced in the fiber core and signal is generated. Raman is a non-elastic thermal scattering process and is therefore only influenced by temperature changes and not by strain. Brillouin and Rayleigh scattering are both influenced by strain and temperature. This can be an advantage, if monitoring for any event is the goal. If the goal is to measure strain exclusively, the DOFS not only needs to be robustly bonded to the object under test, but temperature compensation needs to be performed.[81-83]

In the present work, Rayleigh OFDR DOFS were used for temperature measurement. In the context of these sensors, temperature can only be measured in a relative manner. The physical conformation of the fiber optic sensor cable is very important in minimizing strain from disturbing the temperature measurement (avoidance of tight bends and avoiding bonding to any surfaces to enable free slipping of the fiber).[84,85]

The implementation of FOS in chemical engineering applications can be illustrated via the publications and patents which exist in literature. The most common type of publication in this category is about point FOS.[86] Work has been done on the creation of distributed chemical sensors, which use the monitoring of temperature and strain as a basis for chemical sensors, for example by using special chemo-responsive fiber coatings.[87] DOFS have been used in reactors for hotspot tracking in a fixed bed reactor and there are multiple patents regarding the implementation of various DOFS in reactor components for temperature monitoring or flow measurement.[88-91] Raman-based DOFS have been used in the detection and prevention of corrosion under insulation (CUI) by the company Fluves and their systems can for example be found in the pipelines of the BASF plant in Antwerpen.[92]

For the integration of DOFS in a chemical reactor at laboratory scale, fiber degradation needs to be considered. Silica glass can absorb small molecules, which alter optical properties over time. This has been reported in optical fibers in contact with hydrogen.[93] Mechanical and chemical degradation of optical fibers with and without protective coatings has been studied by Corning Incorporated extensively, and their research is published in white papers.[94,95] A common polymeric coating for fiber protection in FOS is polyimide (PI). PI is relatively hygroscopic, and this causes the coating to exert stain onto the fiber, as well as enable the penetration of moisture into the glass, especially via microcracks.[94,96,97] The two most common types of primary fiber optic cable coatings are PI and polyacrylic resins (PA). Both materials can absorb organic molecules and swell upon contact with solvent. Furthermore, it has been shown that acetone degrades not only coatings substantially, but also the glass fiber itself.[98]

4. Motivation

The spatially distributed nature of DOFS measurement is attractive for use in continuous chemical setups. DOFS are thin, lightweight and have a small thermal mass. Depending on the installation, they have the potential to be used in flow reactors and even microreactors, especially OFDR Rayleigh DOFS with their high spatial resolution. Multiple thermal sensors can be replaced with a single DOFS, which has the potential to simplify setups. In a typical chemical reactor setup, there are often multiple sources of electromagnetic interference present, e.g. magnetic stirring and electro-magnetic valves. Sensors based on thermoelectric effects can be adversely affected. This is not a problem for optical sensors such as DOFS.

Continuous calorimetry's need for spatially resolved temperature and heat measurement has been met with series of thermocouples or Seebeck elements, as stated in literature.[27-34] There is potential in the exchange of a series of point sensors for spatially distributed DOFS, especially if the spatial resolution is increased during the exchange. The DOFS interrogator system available during the creation of the present work is stated to have a spatial resolution of 0.26 cm, which is higher than any series of sensor-based calorimetry systems in literature. Furthermore, the small thermal mass and diameter of a DOFS is thought to enable the parallel use of multiple DOFS inside a reactor wall. With DOFS at different distances to the inside of the reactor, the radial temperature distribution in the reactor wall can be monitored and used for heat calculations.

Polymerization fouling decreases the heat transfer capabilities of a reactor wall significantly, and therefore it is possible to monitor fouling via measurement of the thermal resistance of the surface. This has been shown in the work of Hohlen and Klinkert in the setting of emulsion polymerization.[24,75] The radial temperature distribution in a reactor wall can reflect the increase in thermal resistance inside the reactor, and therefore it is hypothesized, that this can be realized with DOFS.

Spatially distributed temperature sensing enables hotspot monitoring in a chemical reactor.[88] Fouling decreases the available reaction volume in the reactor and therefore shortens residence time.[73] This leads to a downstream propagation of a reaction hotspot for an exothermal reaction. Therefore, it may be possible to make judgements on the state of the fouling and the volume lost to the foulant by monitoring hotspot position.

To enable achievement of any of these goals, research on using DOFS in a laboratory-scale continuous reactor is needed. For this, 3D-printing techniques can be used to manufacture

reactor geometries with channels for DOFS. Optimization of DOFS coating choice, sensor integration method and physical arrangement of the fiber, as well as protection from solvents and other chemicals will be studied. Due to the high cost of dedicated DOFS and the inevitable breaking of multiple sensors in a non-optimized laboratory setting, the in-house manufacture of DOFS out of commercially available and cheap telecommunications fibers will be carried out.

5. Unpublished work

5.1. Different reactor geometries and sensor implementation

All reactors were created using an Ultimaker 2+ with a 0.4 mm brass nozzle and black died or natural PLA as filament. For the reactors the infill was set to 100 %. The channels for the DOFS and the majority of the reactor channel have been printed in horizontal orientation, as this has given best results with minimal warping.

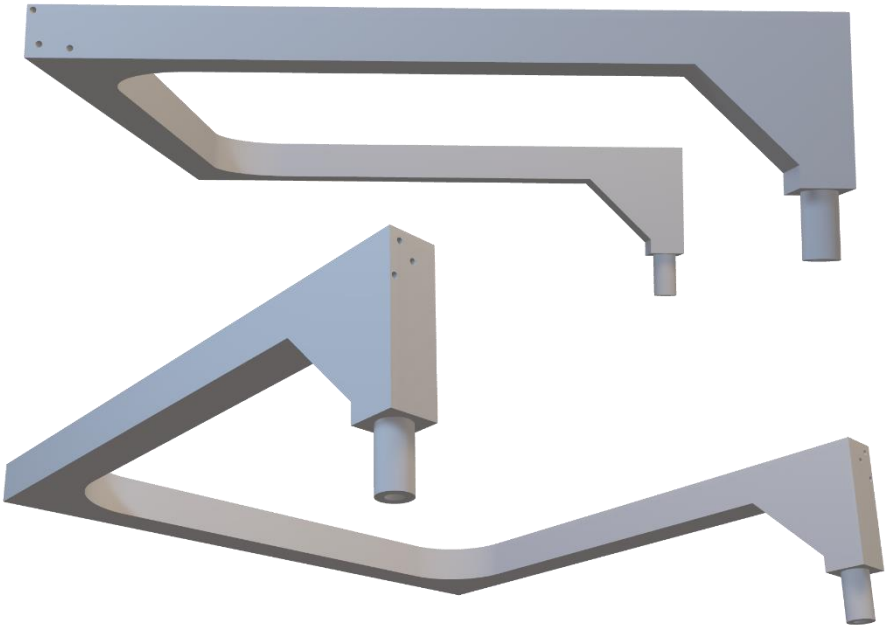

Figure 4: The basic bracket reactor shape (**reactor variant 1 = RV 1**) inherited from previous work with two different placements of DOFS channels, the first 3D render with the channels parallel to the back section of the reactor and the latter 3D render with the channels in parallel to the reaction channel along all straight sections and the two major bends.

The first iterations of reactor geometries have been directly based on previous work by S. Rust.[6] The basic reactor shape with the two 90° bends and the in- and outlet being vertical to

the plane of the reactor, and the inner channel being 6 mm in diameter and the four walls of the square cross section being 12 mm were all directly inherited from previous works. This reactor shape is shown in Figure 4. Two versions of DOFS channel placement are shown. The upper version has three channels for the DOFS along the back section of the reactor. The lower version has two DOFS channels running in parallel to the inner reaction channel along all straight sections and the two major bends, and two more holes allowing access into the reaction stream.

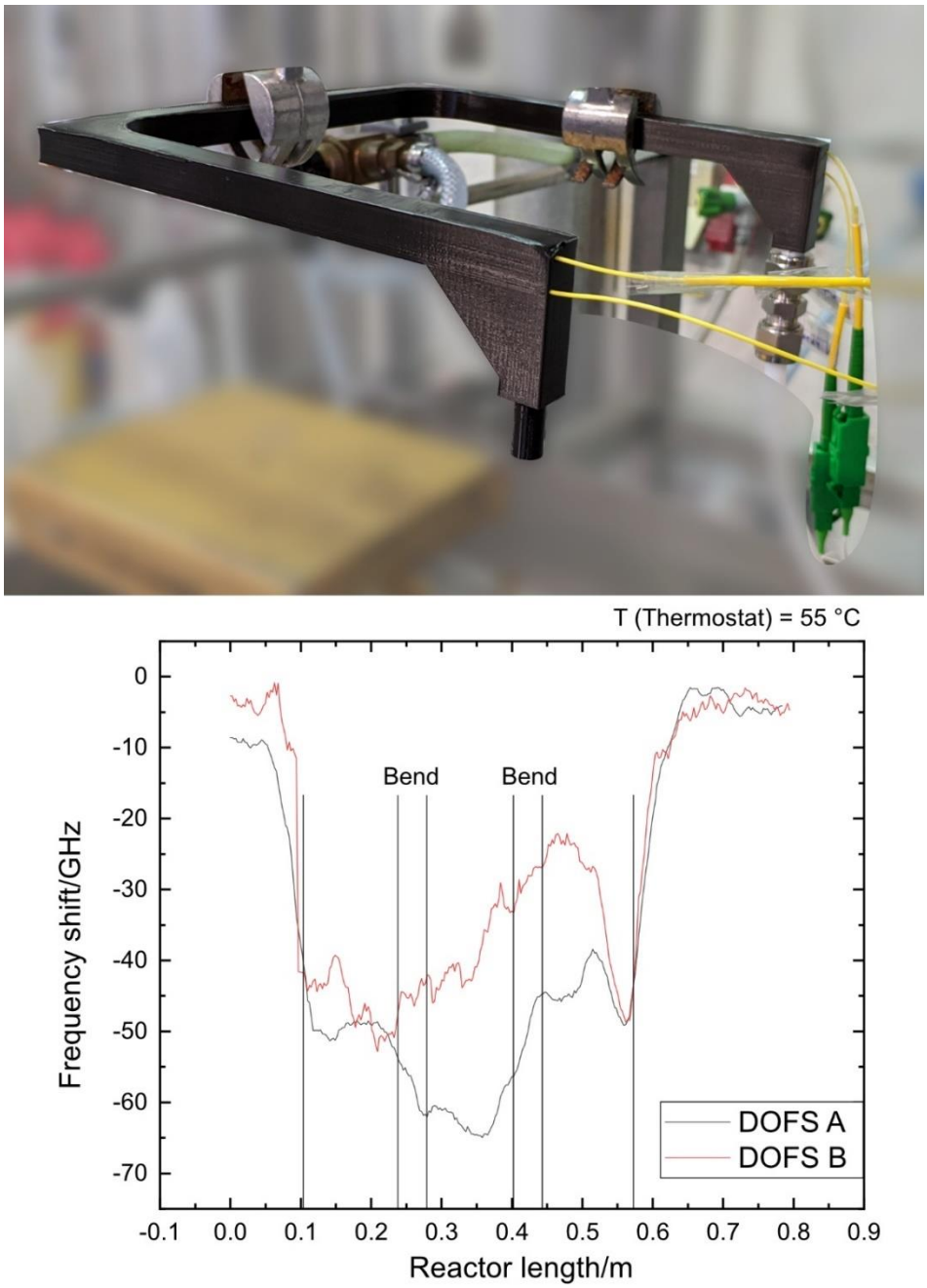

Figure 5: Photograph of the second reactor shown in Figure 4 with DOFS (protected with the first and second acrylic coatings) equipped, and DOFS data measured in this reactor using hot water and natural convective cooling.

In Figure 5 data from DOFS measurements in the bracket reactor is shown. In this instance, the reactor was fed with heated water while the reactor was exposed to natural convection at room temperature. It is expected that the temperature of the water falls along the reactor length. In the frequency shift data, that means the negative shift becomes smaller. This expected trend is seen for DOFS B, though the spatially distributed data is full of artefacts introduced by internal stress from the bends and the protective fiber coating. DOFS A displays artefacts so large that the general downwards trend of the temperature along the reactor path cannot be discerned. It was decided that the DOFS cannot follow the reaction channel along tight bends due to the degradation of the data.

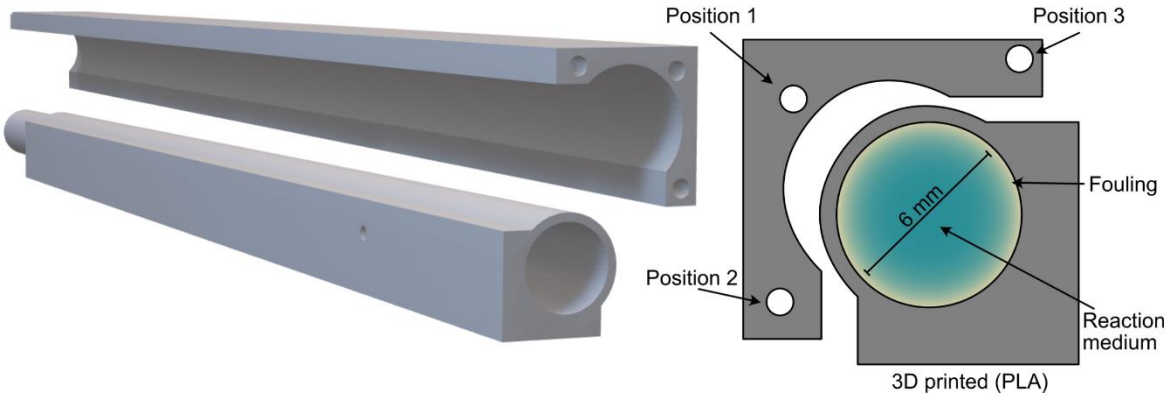

Figure 6: Detachable and stackable reactor portion and clip with three DOFS channels (**reactor variant 2 = RV 2**).

The reactor design was changed to keep the 6 mm inner diameter and the 12 mm outside edge measurement, but without bends. The reactor body was split into two parts which when combined create the same cross-sectional geometry as the reactor before. One part contained the reaction channel and beginnings and ends that plugged into each other to be able to modulate the reactor length despite the limitations of the 3D printer bed size. Holes with a 1.5 mm diameter were created accessing the reactor's inside to enable in stream thermocouple installation. The DOFS were threaded through the channel bracket after the channels had been filled with a dilute thermal paste mixture made of 50 w% aluminium powder (5 µm particle size) and 50 % glycerol. The two halves of the reactor were then slotted into each other with more of the thermal paste on the meeting surfaces, creating one reactor section. In Figure 7 a setup with three such reactor sections in series is shown, with three inserted thermocouples (denoted as sensors 1 to 3). The reactor sections and the thermocouples are all fixed in place with a small amount of silicone (hardware store) and cured for 24 hours. For stabilization the reactor is fitted in parallel to a steel rod, making contact with 3D printed spacers (each 3 cm

wide) at the two joints and ends. In between the spacers there is nothing but air touching the reactor surface, allowing for natural convection. This is shown in Figure 9 for another reactor variant, but with the same spacer and rod setup.

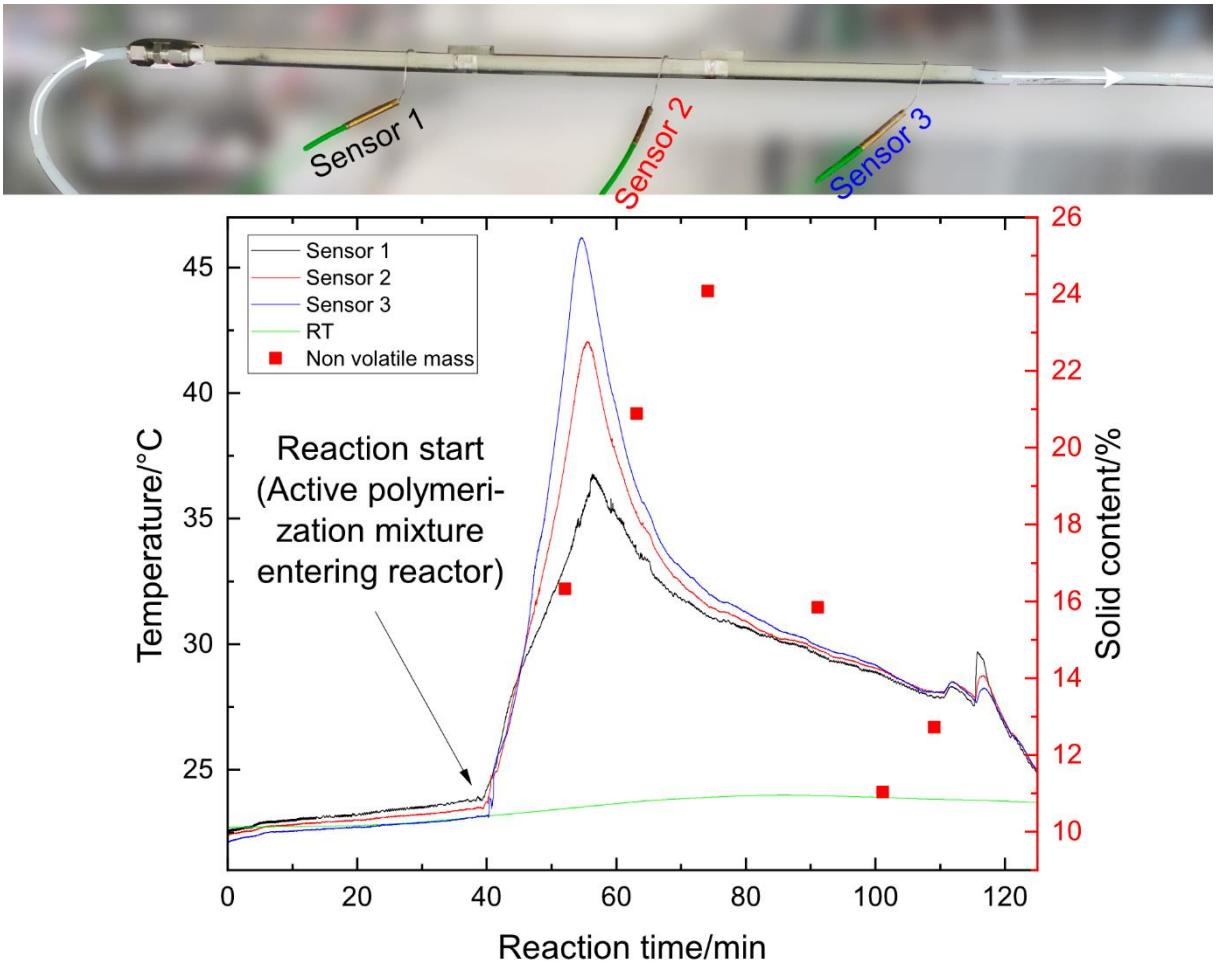

Figure 7: Photograph of three reactor sections from Figure 6 stacked into a 45 cm long reactor, equipped with DOFS and three thermocouples in stream, and thermocouple data from a measurement during polyreaction in this setup.

In the graph depicted in Figure 7 the exothermic copolymerization causes the temperature in the reactor channel to rise once the reaction begins. Sensor 3 registers the highest temperature, signifying that the temperature maximum and therefore point of highest monomer conversion is downstream from the reactor. The outlet tubing is 70 cm long, which explains the high solid content measured via microwave gravimetry (24 w% is a conversion approaching 100 %), as the mixture has had more time to react by the time it reaches the point of sample collection. After the rise in temperature a steep drop follows, soon mirrored by the drop in solid content. This is a direct effect of the fouling layer building rapidly in the reactor (inner reactor surface

is 3D printed PLA), because the volume constriction caused by the fouling is pushing the reaction downstream as inner velocity increases due to unchanged flowrate ($8\ \mathrm{g} \cdot \mathrm{min}^{-1}$).

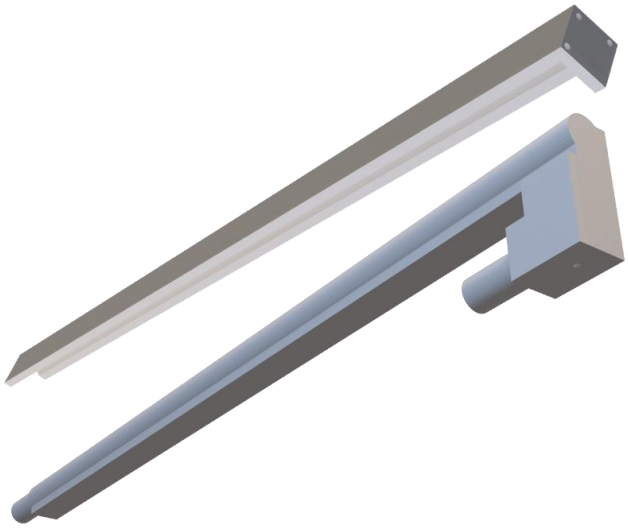

Figure 8: Vertical reactor with detachable reactor and DOFS portions slotting together to create the cross section with an inner diameter of 6 mm and outer edge measurement of 12 mm (**reactor variant 3 = RV 3**).

A vertical variant of the reactor was created but not explored further due to the indication that the reactor needs to be longer to be able to picture the moving of the temperature maximum caused by the monomer conversion during fouling buildup (under the assumption that flow rate, recipe and cross-sectional geometry remains the same).

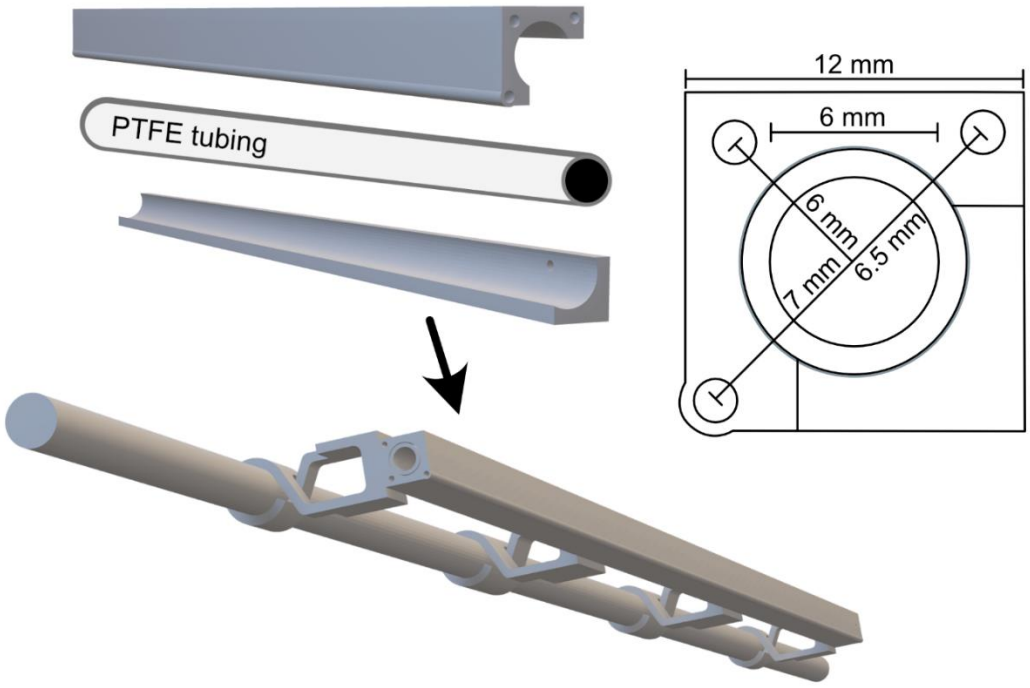

Figure 9: Last iteration of the reactor with PTFE tubing (inner diameter 6 mm, outer diameter 8 mm) and a 3D printed shell consisting of two parts (one for three DOFS channels with an inner diameter of 1.5 mm and one to hold the tubing against the other part, with guide holes for in stream thermocouples) which all together form the established cross section with an outer edge measurement of 12 mm (**reactor variant 4 = RV 4**).

Figure 10: Photograph of RV 4, where three assembled reactor sections are in one level, and there are three total levels between which the PTFE tubing is bent.

Figures 9 and 10 show the last iteration of the reactor. To depict the conversion and temperature maximum of the reaction, the reactor was lengthened by creating a three-tiered reactor. Only the straight portions are equipped with DOFS. In Figure 10 the crosses denote access points for the thermocouples. It was decided to use a PTFE tube as the inner reactor portion in order to slow the intense fouling to allow the sensor setup, whose temporal resolution is limited by the DOFS and accompanying software (usually ca. 1.5 min for one measurement cycle of all three DOFS), to record the temperature change due to fouling formation during reaction. RV 4 is the reactor variant used for the two latter publications “Determination of the clogging time for continuous emulsion copolymerization in a tubular reactor using distributed optical fiber sensors” (2025) and “Spatially resolved reaction calorimetry and fouling monitoring in a continuous tubular emulsion polymerization reactor” (2025).

5.2. Reverse fouling simulation experiments

To test whether a fouling layer could be thermally detected through the reactor wall at the positions of the DOFS, RV 2 was used in the context of a reverse fouling simulation. For this, mustard was fed through the reactor channel with a syringe, the entire setup was vigorously manually shaken and tapped (after being decoupled from the DOFS containing portion of the setup, as they are very brittle) to eliminate air bubbles. Finally, the mustard was pressed out of the reactor with a steady stream of nitrogen. The mustard layer was allowed to cure for 48 h, during which the nitrogen stream was used multiple times a day to replace the air inside the reactor. The reactor was assembled by slotting the prepared artificially fouled reactor into the part containing the DOFS. Warm water was conveyed through the reactor. In Figure 11 the temperature measurements during the experiments are shown. To simplify the spatially resolved data, the DOFS-measured temperature data along the reactor length was averaged and plotted over the experiment time. The reactor warms up from room temperature upon experiment start. The DOFS closer to the inner reactor wall shows a temperature of 35 °C averaged over the reactor length and the further DOFS shows a temperature of 32 °C at a flow rate of 15 $g \cdot min^{-1}$. The color and opacity of the reactor output did not indicate that the mustard layer was washing off, therefore the flowrate was doubled. During an interval of 35 min, both sensors show a temperature rise of 0.5 K, most likely due to changes in the mustard layer (swelling and therefore increased thermal conductivity, gradual removal). The flowrate was then doubled again to create a more turbulent flow, causing the temperature measurement to fluctuate before evening out. The temperature plateaus afterwards, indicating that no more of the fouling layer is being removed.

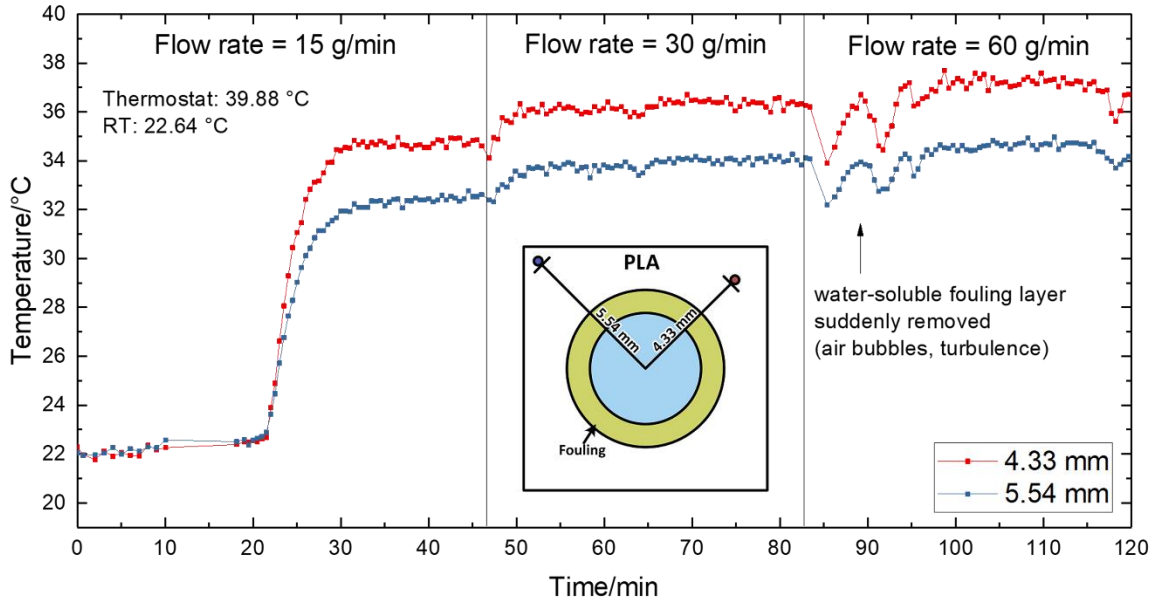

Figure 11: Graph depicting the spatially resolved DOFS measurements of the two sensors at 4.33 mm and 5.54 mm from the center of the reactor, averaged over the reactor length, during the conveying of warm water through the reactor RV 2 with a dried mustard layer on the inside.

It was concluded that due to the mustard being removed very slowly and potentially non-uniformly in the absence of turbulence, that this course of experiments was not to be followed further. The experiment showed that the temperature difference between two parallel DOFS in the reactor wall is sufficiently resolved under these conditions and that the presence of the fouled surface impacts the measurement in a noticeable way. The expected flow rate dependency of the measured temperature inside the DOFS channels could be visualized, as well as turbulence with fouling removal in the reactor. This scenario is similar to that during reaction of an air bubble or a piece of fouling breaking off and dislodging the layer as it travels downstream.

5.3. Steel half shell reactor

The Fluitec ContiPlant LAB ® half-shell reactor was modified to allow for insertion of DOFS or other sensors in between the reaction channel and the channels for the temperature medium. The steel reactor is intensely temperature controlled and it was unclear whether it would be possible to measure the reaction heat and any changes due to fouling buildup in a thermal manner. The position of the added sensor channels was therefore chosen to be between the reaction channel and the channels for the temperature medium.

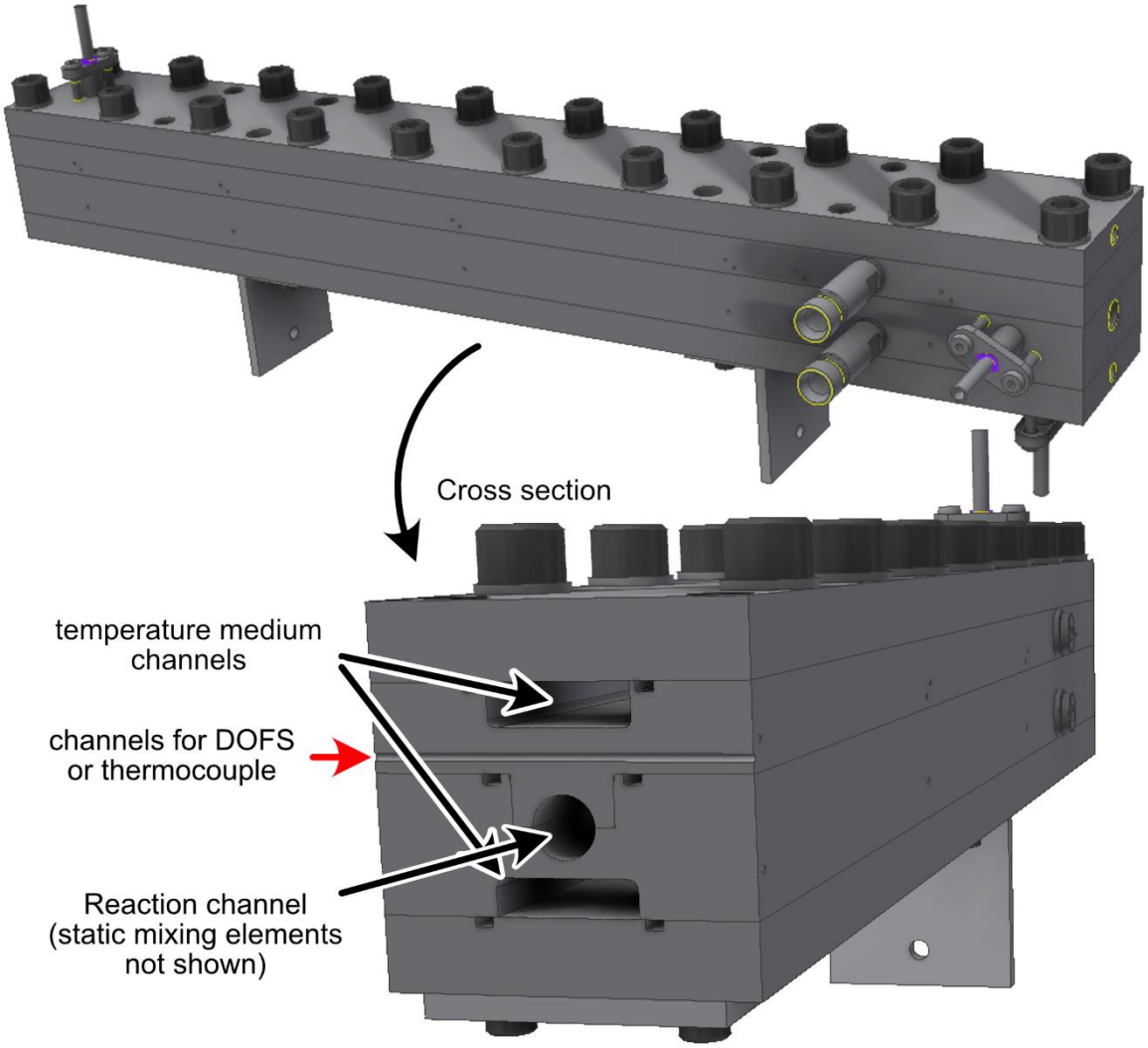

Figure 12: 3D renders of the Fluitec ContiPlant LAB ® reactor and a cross-sectional view showing the reaction channel, the channels for the temperature medium and the added channels for the temperature sensors (rectangular small channels to the right and left of the major channels are for the gasket).

In this configuration copolymerization experiments were carried out. Multiple measurements with both DOFS weaved through the sensor channels and thermoelements positioned in the middle of the channels were collected. In Figure 13 two graphs are shown, one showing the thermocouple measurement during a reaction for four thermocouples placed along the reactor. It can be seen that the reactor mantle was heated to 34 °C (sensor 1) and that the reaction releases heat downstream from this sensor. The temperature maximum is closest to sensor 3 and therefore inside the reactor and not behind it. This indicates that the main conversion is happening inside the reactor under these circumstances. The measured temperatures fall after their maximum, which can again be explained by the fouling buildup. The substantial and fast

fouling on the reactor wall and on the CSE-X static sixing elements in the heated reactor lead to quick clogging (120 min after reaction start). In the lower portion of Figure 12 a singular channel equipped with a DOFS is shown. The way the heat spreads from the central temperature medium channels towards the edges during the heating process is pictured. The reaction is shown to cause a temperature rise and a following gradual decline as the fouling progresses.

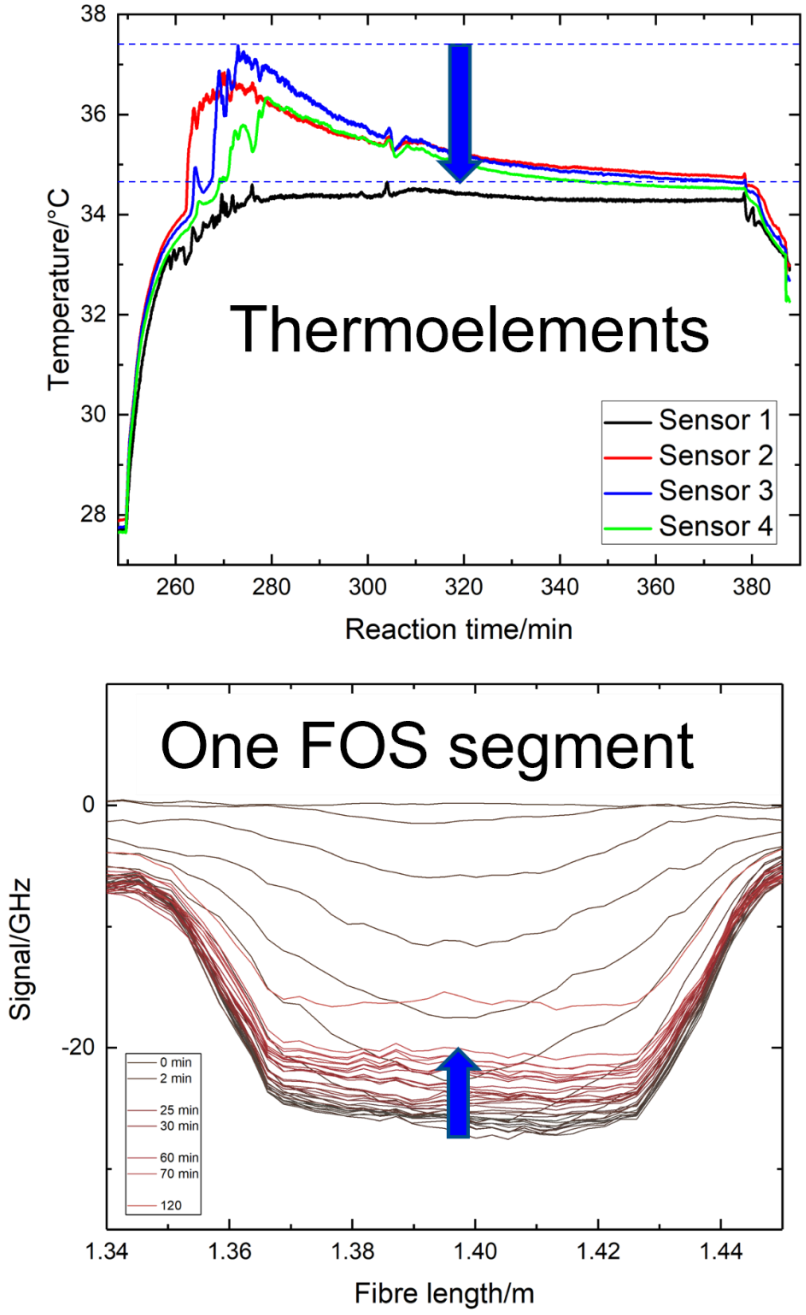

Figure 13: Temperature changes caused by the copolymerization reaction in the Fluitec ContiPlant LAB ® reactor, as measured by thermocouples and a DOFS.

6. Cumulative part of the dissertation

The three publications which have been created during this dissertation work are summarized and then shown in their entirety in this chapter. Through the three works the progression from DOFS integration into a reactor to their use in two different cases is shown. The first case is hotspot monitoring and mathematical modelling to describe the fouling process based on the DOFS data. The second and final use case is a proof of concept for reaction calorimetry in a continuous tubular reactor using DOFS.

6.1. Distributed optical fiber sensors for real-time tracking of fouling buildup for tubular continuous polymerization reactors

Maria Klippert, Werner Pauer

Synopsis:

The first step to achieve DOFS monitoring in a continuous tubular reactor was carried out in this publication. The integration of fiber optic cable into the wall of a flow reactor was achieved by manufacture of the reactor via 3D printing (100 % infill, poly lactide PLA). DOFS channels with a diameter of 1.5 mm were added parallelly to the reaction channel in the CAD reactor model in three of the four corners of the square cross section of the reactor.

At this point in the research process, the copolymerization of VAc and VV10 had been chosen to be the studied reaction. The redox initiation system was chosen to be able to carry the reaction out at room temperature. That way, the only heat measured in the reactor would be caused by the exothermal reaction itself. The heat would dissipate through the reactor wall and be cooled externally by free convection. Therefore, it was hypothesized that measuring the temperature in the reactor wall at different radial distances would make it possible to measure the heat flow through the wall. Because of this, the DOFS channels were located in different corners of the reactor, so that the heat flow (from the middle to the DOFS) could be assumed to be influenced only by the reaction, the internal heat transfer and the PLA wall. To eliminate the insulating influence of air in the DOFS channels, the channels were filled with thermal paste (50 w% aluminium particles in glycerol) and the DOFS were inserted afterwards.

Experiments with varying fiber optic cables were carried out to facilitate the choice of an optimal base for DOFS. Due to the inherent brittleness of glass fibers, all studied fibers were protected to varying degrees. The multi-layered coating with an air gap which is common for fiber optic patch cables was eliminated as an option. Naked fiber was also eliminated due to

handling issues. Therefore, fibers with acrylic (PA) or polyimide (PI) coating were considered for further research and DOFS created with them were calibrated (coating diameter ca. 250 µm). For calibration, two methods were studied. It was assumed that a calibration setup parallel to the reactor would be preferrable than an integrated method in the DOFS length inserted in the reactor. Because of this, another section of those same DOFS were submerged in a thermostat and calibrated online, as opposed to inline. It could be shown that such a setup was possible for PI coated fibers, but between the reactor and the calibration sections for PA coated fibers a calibration factor difference of 20 % was observed.

Furthermore, for ease of DOFS installation fibers with no termination were used and then terminated in place. The fiber termination is paramount to the DOFS monitoring process, because a bad termination would function as a mirror and send much light back towards the detector, so that the much weaker Rayleigh backscattered light would not be detectable. Coreless termination fiber was used, but it has the disadvantage that it needs to be spliced to the existing fiber. Due to the need to minimize strain for temperature measurement and limited cable lengths used (up to 5 m only), the optical and mechanical faults introduced by the splicing and during the splicing process (because it must be carried out in place inside the reactor setup) were sometimes interfering with the DOFS measurement. Because of this termination using an index-matched glycerol-water mixture was carried out and the optimal RI range and how to mix the dry glycerol and water to achieve it were noted.

In the publication, the requirements for DOFS in the application of temperature monitoring in emulsion polymerization and possible thermal detection of a present fouling layer on the inside of the reactor wall, were outlined. The required temperature resolution was determined to be 0.8 K for a hypothetical emulsion polymerization case based on reactions and thermal fouling measurements in literature. After calibration of the PA and PI-clad DOFS a temperature resolution of 0.1 K was realized for the reactor section (ca. 20 cm).

In the paper, it is deduced that the chosen method to integrate DOFS into a chemical reactor's wall is feasible and that PI and PA-clad fibers with a diameter of ca. 250 µm with an inline calibration (or PI only with an online calibration) can be used to progress to heat flow measurements during polymerization. The method for fiber integration and termination was discussed in detail and an assessment of the expected stability of DOFS in a macromolecular laboratory setup was made.

Chemical Engineering Research and Design 211 (2024) 168–178

Contents lists available at ScienceDirect

Chemical Engineering Research and Design

journal homepage: www.elsevier.com/locate/cherd

Distributed optical fiber sensors for real-time tracking of fouling buildup for tubular continuous polymerization reactors

Maria Klippert, Werner Pauer *

Institute for Technical and Macromolecular Chemistry, University of Hamburg, Bundesstraße 45, Hamburg 20146, Germany

ARTICLE INFO

Keywords:
Distributed temperature sensing
Continuous emulsion polymerization
Fouling monitoring

ABSTRACT

Early online fouling detection is expected to be a real step forward in the operation of continuous tubular reactors. As an online technology, the Rayleigh backscatter based **D**istributed **O**ptical **F**iber **S**ensor (DOFS) technology was evaluated with respect to temperature measurement resolution, reproducibility and the best online calibration method. Different coatings and terminations were characterized for emulsion polymerization reactors. Commercially available sensors with acrylate primary coatings, dual acrylate coatings, and polyimide coatings were all compared with each other. It is shown that the presence of a secondary coating significantly alters sensor behaviour. Sensors with only a primary coating showed a temperature resolution of 0.1 °C. Online calibration for temperature readout was carried out and validation tested on segments of fiber integrated in a 3D-printed reactor channel (diameter 1.5 mm). Acrylate coated sensors showed a deviation of 20 % for the calibration coefficients when inside the reactor channel compared to the online calibration, leading to errors in temperature measurement. Polyimide coated sensors showed a deviation of just 0.6 % in this validation test, demonstrating good capabilities for online calibration with accurate temperature measurements. The possibility of spatial and temporal monitoring of fouling buildup through a heat exchanging wall equipped with DOFS was evaluated.

1. Fiber optic sensors in chemical reactors

Fiber Optical Sensors (FOS) can be used as point sensors at the end of the fiber, using backscattered light in order to infer various characteristics of the matter past the end of the fiber. For example, this mechanism is used in turbidity measurements, refractive index measurements and particle size distribution measurements (Li et al., 2012; Rust and Pauer, 2022). Furthermore, FOS can be used as intrinsic sensors by measuring the backscattered light within the fiber itself to generate a measurement that detects and quantifies outside forces. For this, backscattered light from inside the fiber itself is detected. These sensor interrogation systems exist for Rayleigh, Raman and Brillouin backscattered light. Information about Rayleigh backscatter FOS can, for example, be found in (Froggatt et al., 2006) and (Galal et al., 2021). More about Raman-based temperature sensing can be found in (Lopez-Higuera et al., 2016), and studies concerning Brillouin-based FOS can be found in (Bolognini et al., 2019). These techniques have been researched for decades and a lot of topics are covered in literature. FOS have been adapted to measure refractive index, acoustic signals, chemical compositions, pH, and many other variables (Li et al., 2012; Hartog, 2018; Bao and Chen, 2012). They are thin, light-weight, and do not suffer from electromagnetic interference. Therefore, they can be used as minimally invasive probes in reactors for online measurements under industrial operating conditions (Li et al., 2012). Fiber Bragg gratings (FBGs) are manufactured reflectors within the core of an optical fiber, generating a particularly strong backscattered light signal. Distributed Optical Fiber Sensors (DOFS) do not contain any of these gratings. The intrinsic fluctuations of the refractive index within their cores provides the source of backscattered light for measurement. This can be used to infer information along the entire fiber length, in short distance intervals. This creates a spatially distributed measurement. Physical changes to the fiber modulate the signal, so that temperature and strain can be measured intrinsically using FOS technology. Further measurements can be inferred given the right modifications to create, for example, spatially distributed chemical sensors (Lu et al., 2019). Several reviews on FOS and their many applications and technical details have been published in, for example, (Bao and Chen, 2012) and (Liu et al., 2018). Foundational information about fiber optical

* Corresponding author.
E-mail address: werner.pauer@uni-hamburg.de (W. Pauer).

https://doi.org/10.1016/j.cherd.2024.10.007
Received 3 June 2024; Received in revised form 26 September 2024; Accepted 5 October 2024
Available online 9 October 2024

communication systems can be found in books, such as (Agrawal, 2010) and (Venghaus and Grote, 2017). The foundations of DOFS measurement and technology are covered in (Hartog, 2018).

In conclusion, FOS technology has been integrated into the engineering tool kit. These sensors are particularly useful in infrastructure monitoring applications, due to their ability to generate spatially distributed measurements. These sensors can be used to locate faults and monitor changes in large structures (Fernandez et al., 2023; Li et al., 2012; Wang et al., 2021; Zhong and Broere, 2023; Goltz, 2011). Shape changes due to mechanical forces on a component can be measured using FOS (Xu and Khodaei, 2020). For these applications the intrinsic strain sensing capabilities of DOFS are used. Both strain and temperature sensing have been used in groundwater and pipeline monitoring (Offerhaus, 2021; Ooi, 2002).

In chemical reaction engineering temperature is of more importance than strain sensing in order to control and monitor reactions, storage containers and chemical plant infrastructure (Fluves, 2024; Nestler et al., 2021). The requirements to measure temperature in a spatially distributed manner are different from the monitoring of strain.

In experimental laboratory work, frequent changes and adjustments in setup are to be expected and therefore must be considered in the integration of DOFS. Mechanical movement and exposure to chemicals which may interact with the fiber and its coating can alter the signal. This primarily affects the strain experienced by the fiber, which in turn reflects in the temperature measurement when Rayleigh backscatter based DOFS are used, because strain and temperature are measured at the same time within the same signal.

Various reports exist in literature related to the use of FOS technology for monitoring chemical reactions. Most of these papers feature point sensors at the end of the fiber (Li et al., 2012; Rust and Pauer, 2022). Distributed temperature measurements have been carried out, particularly ones using FBG-sensors, in reactors covering temperatures of up to 400 °C. Of special interest is hotspot detection, power plant safety and kinetic study of reactions (Nestler et al., 2021; Liu et al., 2022; Zhang et al., 2014).

The range of temperatures during a reaction and thermal run-away is highly dependent on the components used in the reaction, and on the reactor itself. For example: a thermal run-away for a gas-phase reaction with heterogeneous catalyst, such as an oxidation, nitration or dehydration process, may result in hotspots above 700 °C; whereas an emulsion polymerization carried out in water can only reach a maximum temperature of 100 °C, as long as water is still present (Egner et al., 2014; Lovell and Schork, 2020). In order to gain kinetic and calorimetric information from measuring temperature during the reaction, the applied sensors have to provide the right amount of temperature resolution, and high accuracy and reproducibility. In the case of FOS technology, this is not only dictated by the make of the functional optical sensor and interrogator system, but also by the coating used to protect the fiber, fiber termination, and mode of sensor integration. In emulsion polymerization, the temperature window of interest is rather narrow (0–100 ℃), and so the sensor must provide suitable characteristics. The goal of this paper is to evaluate whether this is possible using Rayleigh backscatter based DOFS with common telecommunication fibers and their coatings. Frequently changing laboratory setups may require replacements of DOFS, due to their fragility. Because of this, emphasis is placed on the use of commercially available telecommunications fibers as DOFS. Spools of fiber with various coats and optical properties can be purchased and turned into FOS as well, cutting costs in comparison to purchasing specialized FOS.

In the literature, telecommunication fibers have been successfully used for distributed measurements, even in high temperature environments (up to 1100 °C) (Chen et al., 2022). Existing networks of fiber optic cables have been used for traffic monitoring and marine research (Huang et al., 2022; Storvik et al., 2022). Due to the fact that optical data transmission is much less susceptible to electromagnetic interference, FOS are being used in high temperature and high energy environments, such as nuclear reactor testing facilities (McCary et al., 2018; Girard et al., 2013). In Fig. 1 the field of fiber optic technology is represented and some major sub-sections are shown. To effectively use DOFS, many of these topics need to be focused on at the same time.

2. Fiber optic sensor structure, coating and termination effects

A typical single mode telecommunication cable is comprised of a silica glass fiber core and a glass cladding of a lower refractive index. This allows for total reflection and the light to travel through the entirety of the fiber with small losses. For mechanical purposes, a coating is applied to the glass fiber during production. Often, a dual-coating approach is used. Both coatings are typically based on UV-cured polyurethane-acrylate resins, and the primary coating is commonly soft and elastic, while the secondary coating provides additional thickness and stiffness (Glaesemann, 2017; Kouzmina and Davis, 2021). For use in transmission, these fibers are put into a loose polymer sleeve, which is commonly made from materials such as Polyvinylchloride (PVC) or Low Smoke Zero Halogen (LSZH). The length of the outer sleeve is slightly shorter than the fiber inside. This allows for installation of cables under some tension without risk of the optical fiber snapping easily (Glaesemann, 2017).

In comparison to a telecommunications cable, a DOFS, as shown in Fig. 2, is less protected from the environment, because it is meant to interact with it. To cut down on response time the optical fibers used in DOFS are normally coated by a single layer, except on the connector side. The connector's own weight might cause the fiber to be compromised if the adjacent fiber section is not further coated for stability (Jacobs, 2004). Two commonly available types of coatings for DOFS are acrylate and polyimide coatings.

Common acrylate coatings are used in a temperature range from −40 °C to 85 °C, whereas polyimide coatings can withstand much higher temperatures, up to 300 °C. Because of this, polyimide coatings are more often applied in FOS. It has been shown that dual acrylate coated fibers can withstand up to 150 °C when a hydrogen scavenging gel is used (Stolov et al., 2022).

While the polymer coating is indispensable for mechanical stability, it may alter the signal of the FOS. Therefore, the behaviours of various coatings and fiber integration methods into the experimental set up have to be examined. The change in signal caused by the coating may be used productively, as has been demonstrated for FOS at cryogenic temperatures (Lu et al., 2017). In laboratory and plant settings, FOS may come into contact with solvents, solvent-rich atmospheres or gasses. Solvents,

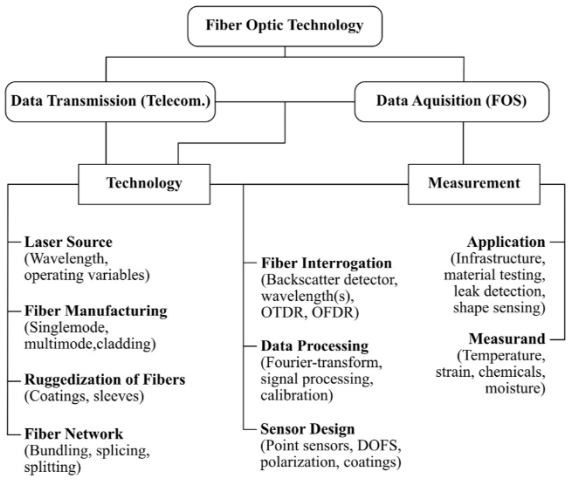

Fig. 1. Schematic overview of the field of fiber optic technology.

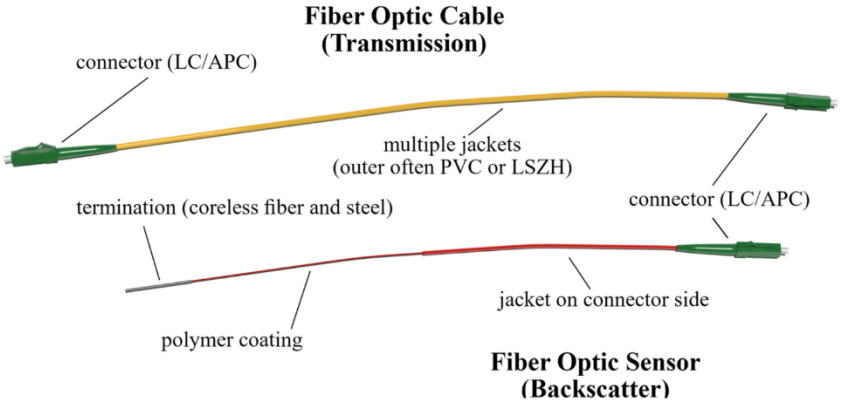

Fig. 2. Structure of a fiber optic cable or ethernet cable and a FOS in comparison with each other.

moisture, and gasses can diffuse through the coatings and degrade the fiber inside. Small gas atoms such as hydrogen or helium can diffuse into the glass itself and change its properties (Jacobs, 2004; Palmer et al., 2017). Moisture and other Lewis acids are able to degrade silica glass chemically. Some flaws exist on the surface of glass fibers and migration of degrading compounds into these cracks will corrode the fiber further (Glaesemann, 2017). Organic, non-polar solvents are less likely to react with the silica, but they may cause the coating to swell and alter the signal of the fiber. Strength degradation caused by the movement of the coating against the glass surface has been reported and studied (Glaesemann, 2017; Kurkjian et al., 1993). Moisture can cause this phenomenon in polyimide coatings due to its polarity (Lin et al., 2014). Changes in volume of the coating in relation to the silica fiber can be caused by these mechanisms, as well as temperature, due to different thermal expansion coefficients. Strain and micro-bending is introduced during these processes, the latter of which may result in signal loss (Kouzmina and Davis, 2021).

Rayleigh backscatter DOFS measure temperature and strain indiscriminately from each other. This complicates the measurement of just one of these forces. For a strain measurement, the coating of the fiber must adhere tightly to the measured object and not slip. Less elastic coatings are often chosen in order to account for the strain transferred from the object to the glass fiber. For temperature measurements, the glass fiber should not be under any strain, unless the strain changes reliably in response to the temperature of the object being measured. In that case, calibrations can be made to account for the strain. Adhering the sensor with glue is therefore not permissible and the coating's temperature response has to be factored in for highly time-sensitive measurements (Palmer et al., 2017; Huang et al., 2016; Jones et al., 2022).

The backscattered light from a DOFS is very weak in relation to the incident light, therefore the strong light must be led out of the fiber end and not back to the sensor, so as not to overpower the measurement signal. Fiber terminations are often made from coreless fiber, which has a similar refractive index to of the fiber core. This allows the light to leave the fiber. The point of connection between two fused together fiber sections, such as for the termination, is called a splice. Anytime fibers are connected by fusing (splicing), optical and mechanical faults are introduced. To protect against the mechanical weakness at the splice, they are commonly encased, for example with a metal sleeve, as shown in Fig. 2. The optical quality of a splice or any connection can be tested with an optical time domain reflectometer (OTDR) measurement. In this spatially resolved backscatter measurement, reflections are identified as a peak with subsequent amplitude change (step transition). The relative change in amplitude of the step transition can be used to calculate the optical return loss (ORL) and judge the quality of a connection (Glaesemann, 2017; Davis, 2023).

3. Requirements for fiber optic temperature sensing in emulsion polymerization reactors

Polymerizations are highly exothermic reactions with the reaction enthalpies for common monomers ranging from −35 to −101 kJ/mol (−295 to −3620 kJ/kg) (BG RCI, 2015). The benefits of emulsion polymerizations include improved safety and thermoregulation, due to the fluid medium regulating and conducting the heat, as well as lowering the viscosity of the mixture (Lovell and Schork, 2020). The temperature rise under isoperibolic conditions for the mono- and co- emulsion polymerization of vinyl acetate with 20 w% monomer using redox initiators is 10–20 °C (Schroeter, 2018; Hohlen et al., 2019; Copelli et al., 2011). For the monitoring of such a reaction, thermocouples are commonly employed. A class 1 type K thermocouple can be used in the range from −40–1000 °C with a permissible deviation of ± 1.5 °C. For a class 2 type K thermocouple these values are −40–1200 °C and ± 2.5 °C, respectively (DIN EN 60584-1:2014-07, 2014). For kinetic and thermodynamic studies, better performing sensors are commonly used, such as pt100, which come in the classes AA to C with temperature ranges of −50–250 °C and −196–600 °C, as well as a permissible deviations of ± 0.1 and ± 0.6 °C, respectively (DIN EN 60751:2009-05, 2009). According to the manufacturer, temperature measurements in the range of −40–200 °C with a resolution of <0.1 °C and a repeatability of ± 0.01 % can be achieved using the (Luna Inc, 2017, ODiSI-B). These values are highly dependent on the equipped sensor and its make, as well as the way it is integrated into the measurement setup. This publication aims to characterize DOFS made inexpensively from commercially available telecommunication glass fibers with varying terminations using the ODiSI-B. The cost of the fiber optic tools needed to create sensors, such as the splicer, fiber cleaner and strippers, can be covered by less than 1000 USD. Patch cables, coreless termination, acrylate, and polyimide coated silica fibers range in cost per meter from 1 to 16 USD. In comparison, a fiber optic sensor can have a base price of 300 USD, with additional 30 USD per meter length. For applications with a high probability of sensor breakage, building sensors is therefore the more frugal option. In this publication, the self-made sensors are to be compared to traditional temperature sensors. The goal of the comparison is to evaluate whether distributed temperature measurement can be utilized successfully for the monitoring of emulsion polymerizations, or even for kinetic and thermodynamic studies.

The spatially resolved nature of DOFS measurement is particularly attractive for continuous flow calorimetry. The state of modern chemical synthesis is leaning more towards process intensification and improved reaction safety by employing continuous flow reactors of various

dimensions. The transfer of a reaction from a stirred tank to a flow reactor is not straight forward and therefore flow calorimetry is of importance (Frede et al., 2022; Maier et al., 2020; Moser et al., 2021).

Due to the small scale of milli-reactors in particular, sensors with a larger volume, such as pt100, become hard to use. Thermoelements can be manufactured to be small, but DOFS require even less space and are less thermally conductive due to the lack of metal in their build. A distributed thermal measurement allows for real-time hotspot monitoring as well, which is particularly important for process safety (Maier et al., 2020).

Polymers are typically poor thermal conductors and the thermal conductivity of non-specialized, common polymer bulk materials range from 0.1 to 0.7 W/(mK) (Huang et al., 2018; Saechtling, 1983). Layers of polymer that form on the insides of the reactor during synthesis or on the inside walls of storage containers and pipes are called fouling. They decrease the rate of heat exchange drastically as they thicken, due to their insulating properties. This can lead to rising temperatures inside a reactor, or, for an endothermic process, large portions of unreacted monomer in the product. Fouling monitoring and inhibition are therefore important aspects of polymerization reactor plant engineering. For the copolymerization of vinyl acetate with a redox initiator, and the conveying of a similar polymer dispersion product through a continuous loop system, average fouling layer thicknesses have been reported to range from 23 to 120 µm (Hohlen et al., 2019).

In order to estimate the temperature difference caused by a fouling layer, the following situation is assumed as an example: The RC1e calorimeter by Mettler Toledo equipped with a 500 mL steel reactor has an estimated inner heat transfer surface area A of 280 m^2. According to Schroeter (2018), an emulsion copolymerization of vinyl acetate and vinyl neodecanoate (9:1 ratio) with a monomer weight percentage of 20 w% reaches a maximum reaction heat flux of 70 W at a temperature difference of the bulk mixture and cooling mantle of an estimated 16 K (Schroeter, 2018). Therefore, the thermal conductance at that point in the reaction is 4.4 W/K, as it is the quotient of power and temperature difference. The reverse is the thermal resistance R, which is 0.23 K/W in this example. Hohlen et al. (2019) ran a reactor for 2 h at a monomer weight ratio of 38 w% to build up 50 µm of fouling deposit (Hohlen et al., 2019). To roughly estimate the thermal resistance R_f added by a fouling layer of 50 µm thickness x_f, ignoring the volume constriction caused by the buildup and assuming the thermal conductivity of the fouling layer to be the same as the polymer (with thermal conductivity λ = 0.22 W/mK), the following equation is used:

$$R_f = \frac{x_f}{A \bullet \lambda} \quad (1)$$

The resulting thermal resistance caused by fouling is 0.01 K/W. Adding the two resistance values together and using 70 W as the power again, the resulting temperature difference is 16.8 K. Therefore, the measurable temperature difference caused by the hypothetical fouling is 0.8 K. This can be used as a reference to gauge the needed temperature resolution to detect and measure fouling formation thermally with traditional temperature sensors and DOFS.

4. Materials and devices

Three different types of fiber optic cables were used. The first was a single mode patch cable with a G.657.A1 glass fiber containing a 9 µm silicon glass core and a 125 µm cladding layer. This patch cable was protected with a soft primary acrylate coat (diameter 250 µm), a more rigid and tightly buffered secondary acrylate coat (diameter 900 µm), followed by a loosely fitting outer sleeve (outer diameter 2.8 mm, inner approximately 2 mm) made from LSZH (Low Smoke Zero Halogen material) and filled with aramid yarn as the strength member. The second type of patch cable used was a loose tube cable. The silica fiber and outer components were the same as the first cable, with a primary acrylate coat (diameter 250 µm), and the secondary acrylate coat (outer diameter 900 µm) not tightly buffered to the primary. Unaltered cables possessed two LC/APC 8° connectors. The temperature range for the cables provided by the supplier (Fiber24 GmbH) is −20–80 °C. The third cable was a DOFS sold by Luna Inc. under the name HDS03LC220P. The fiber was coated with a polyimide primary coat (diameter 155 µm) and possessed a stainless-steel protected termination (diameter 286 µm). The sensor was rated for a temperature window of −40–220 °C.

The removal and scoring of jacket and coating layers of the acrylate coated fibers was carried out using fiber cable strippers. Before cutting and before splicing the fibers, the exposed glass ends were cleaned with dust-free wipes and isopropyl alcohol. The fiber ends were cleaved using the High Precision Fiber Optic Cleaver FS-08C. Fiber alteration is done using splicing, where two bare ends of fiber are fused together using an electric arc. The splicer used for this purpose is the Mini FTTx Fusion Splicer DVP-740. All fiber optical connections were made using appropriate adapters and cleaning tools.

A coreless fiber (diameter 125 µm, FG125LA glass rod, acrylate coating) from Thorlabs was used for fiber termination. Additionally, the impact of the termination refractive index was explored by using glycerol solutions with varying refractive indices. They were put into 2 mL crimp-top vials with a needle port. The vials were additionally wrapped in black tape. Glycerol-water solutions were prepared in steps of 0.0010 refractive index. The refractive indices were confirmed to be within the range by use of a manual refractometer. The actual refractive indices of the ten solutions were 1.4690, 1.4685, 1.4670, 1.4665, 1.4660, 1.4645, 1.4640, 1.4625, 1.4620 and 1.4605. In the following, the intended indices were used in the 0.0010 steps instead of the measured indices.

For temperature control, the thermostat Julabo SE 6 was used with water as a medium.

The ODiSI-B (spatial gauge of 0.26 cm and 10 m sensing range, emitted wavelength 1510–1570 nm) by Luna Technologies was used as the sensor interrogator. The optic switch (FOS08 by Luna Technologies) was used to interrogate multiple sensors in the setup without manually switching. The sensors were connected to the fiber optic switch using a patch cable and LC/APC connectors. Sensors created by various methods will be compared in the following text to determine their characteristics.

5. Experimental section

5.1. Coating removal

In order to judge the impact of the fiber coatings on the temperature measurement, the acrylate coated cables were stripped to varying degrees. To remove the loose outer jacket coating and the strength member, one connector was cut off the patch cable and the LSZH sleeve and aramid yarn was cut on the opposing end.

On tightly buffered acrylate patch cables the primary and secondary coat can only be removed together, leaving the unprotected silica fiber behind. This was achieved by scoring the fiber every centimeter orthogonally and soaking in acetone. It must be noted that this might cause degradation of the fiber strength due to the mechanical abrasion caused by the swelling of the plastic and subsequent movement of potentially present hard particles inside it (Kurkjian et al., 1993). After swelling, the two coats could be removed manually. Naked fibers were tried as sensors, but their fragility made them unfeasible contenders. The tight buffered acrylate cables were therefore used with the first two coats, primary and secondary, attached to the fiber. Such cables were merely stripped from the outer-most layer and the strength member and then terminated.

Loose tube acrylate coated patch cables were stripped of the outermost layer, the strength member, and the secondary coating, by scoring the coatings to be removed with a fiber stripper tool while leaving the primary acrylate coat intact.

In general, specialized strippers for polyimide coated fibers do exist, but in this case the polyimide coated cable was used as purchased. If the need for repair or splicing arises, the coating may be burned off. For

these operations, it is important to avoid contact with the cable or fibers, and to avoid bending or twisting them, otherwise their mechanical integrity may be compromised.

5.2. Termination

An adequate fiber termination is needed for good signal quality. An unaltered cable may work as a FOS directly upon connecting it to the interrogator, because the connection on the opposite end can function as a termination. Alternatively, splicing can be used to fix broken terminations in commercially available FOS, turn bulk fiber into sensors by terminating and connectorizing, or adapt telecommunication cables into FOS.

A 5 cm piece of coreless fiber was cleaved and spliced onto the sensor to create the termination. For a removeable protection that does not introduce strain into the setup, the spliced ends were enveloped in a loose aluminium foil sleeve and the sleeve adhered to the setup and out of the way. It was found that direct adhesion between the sleeve and the termination may result noisy and unsteady measurements.

A more modular method of terminating FOS is the use of index matching gels. This has been used as a foundation for a simple terminating approach using glycerol and water to adjust the refractive index. The refractive index of the coreless fiber is 1.444 at a wavelength of 1550 nm, as stated by the manufacturer (Thorlabs). The refractive index of silica, as well as some other materials, lowers with increasing wavelength. The refractive index of silica glass under visible light is 1.46 to 1.47. In order to determine the influence of the refractive index of the terminating material a range of refractive indices from 1.4600 to 1.4690 were covered using glycerol and water mixtures.

5.3. Sensor implementation

To effectively implement a sensor, considerations must be made about the type of sensor, the goal of measurement, the setup geometry, and the material across which the measurements will be taken. For spatially resolved real-time measurements of chemical reactions, it is most fitting to integrate the sensors into the reactor stream. However, protection from chemicals and their vapours must be considered. Often, metal capillaries are used for this purpose. In order to measure the fouling formation and temperature along the path of a continuous reactor simultaneously, the FOS were integrated into the walls of the reactor. That way, the flow regime inside the reactor was undisturbed. The used reactor was designed using Computer Assisted Design (CAD) Software and then 3D-printed using the Ultimaker 2e+ 3D printer. This manufacturing approach allowed for easy integration of channels for the FOS at predetermined positions inside the wall. A square cross section was chosen for the reactor, in order for the FOS to be positioned in the corners at varying distances from the center, with the intention of monitoring for sedimentation and phenomena. The inner reactor diameter was 6 mm, and the edge length of the square cross section was 12 mm. The channels were printed with a circular cross section of a diameter of 1.5 mm. The printer used was capable of printing sensor channels at 0.5 and 1 mm diameters, however, misprints became more frequent in these smaller sizes. Therefore, the 1.5 mm diameter was chosen for the channels in order to avoid introducing strain from potentially uneven channel walls. The total reactor length was 18 cm.

Thermal paste was applied inside the 3D printed channels before the sensors were installed, in order to minimize the insulating effect of unwanted air. This paste was comprised of 50 w% aluminium particles (diameter 5 μm) and 50 w% glycerol. This glycerol heavy recipe was chosen to facilitate insertion into the small channels; however, it should be noted that glycerol is hydroscopic and a Lewis acid, and can therefore degrade the optical fiber.

Before a FOS is used to measure temperature or strain, the sensor configuration may be tested using OTDR. The Optical Return Loss (ORL) can be calculated, and the quality of the connection can be judged. The ORL is defined as the decadic logarithm of the quotient of incident power and reflected power at a connection, times the factor ten. A bad connection reflects an excess of light, causing a low ORL value. Empirically, the equation shown in Eq. 2 describes the ORL as measured via OTDR. In the equation, A is the height of the reflection peak in dB, and B is the Rayleigh backscatter coefficient in dB, which can be found in literature for specific kinds of fibers. The SMF-28 and SMF-28e+ fibers have a value of $B = 82$ at 1550 nm, as stated by I. Davis at Corning (Davis, 2023). The variable D is the pulse width in ns.

In an example calculation, the OTDR measurement of a functioning DOFS with a primary acrylate coat and a LC/APC 8° connector is used. The height of the FOS connection point was at 120 dB (± 0.5 dB), and the base attenuation of the sensor was at 97 dB (± 0.5 dB). This results in a difference A of 23 dB between peak and baseline. Using the formula given in Eq. 2, the ORL can be calculated, and connection quality can be evaluated numerically.

$$\mathrm{ORL} = \quad B - 10 \cdot \log_{10}\left(\left(10^{\frac{A}{5}} - 1\right) \bullet D\right) \tag{2}$$

Assuming a pulse width D of 100 ns, the ORL is 16, and assuming a pulse width of 1000 ns the ORL is 6. These values are well below the upper acceptable ORL value defined by Corning (60); therefore, the connection can be assumed to be valid (Davis, 2023).

5.4. Calibration and validity testing thereof

To test the temperature dependence of the signal and (re-)calibrate the sensors, an online calibration was used. The FOS were threaded through a 30 cm loose sleeve submerged in a thermostat. The temperature of the thermo-regulated vessel of the thermostat and the reactor were tracked using calibrated K-type thermocouples and a pt 100 resistance thermometer. The temperature of the reactor was measured underneath the thermal insulation, made of a 2 cm thick foam sheet. The transferability of the calibration created in the thermo-regulated vessel to the fiber section inside the reactor was tested for validity in this setup, which is shown in Fig. 3.

Four fiber cables were used for temperature measurement behaviour tests for implementation in chemical reactors. One cable was the polyimide coated DOFS by Luna Inc., and the other cables were adapted specimens from the acrylate coated fiber types. The tight buffered fiber was used with primary and secondary acrylate coating in place. The loose tube fiber was used both with primary and secondary acrylate coating in place, as well as with only the primary coating.

DOFS do not measure strain or temperature directly. Instead, the values are determined by the effect of these variables on the Rayleigh backscatter. The frequency shift is calculated by cross-correlation of the spectrum of the sensor being tested versus a previously recorded key or fingerprint spectrum. This frequency shift is correlated to the interacting outside forces. The polynomial conversion of the signal shift ν in GHz provided by the interrogator and temperature T in °C is shown in Eq. (3).

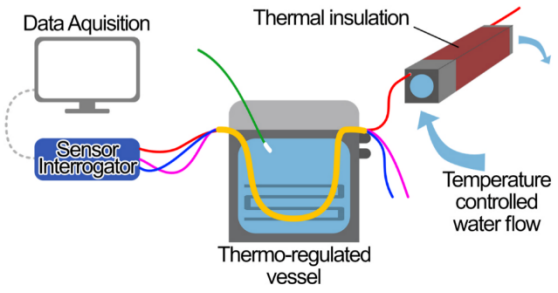

Fig. 3. Calibration of a DOFS using a section in a thermo-regulated vessel with minimal mechanical strain and using a section in a temperature-controlled channel with more strain.

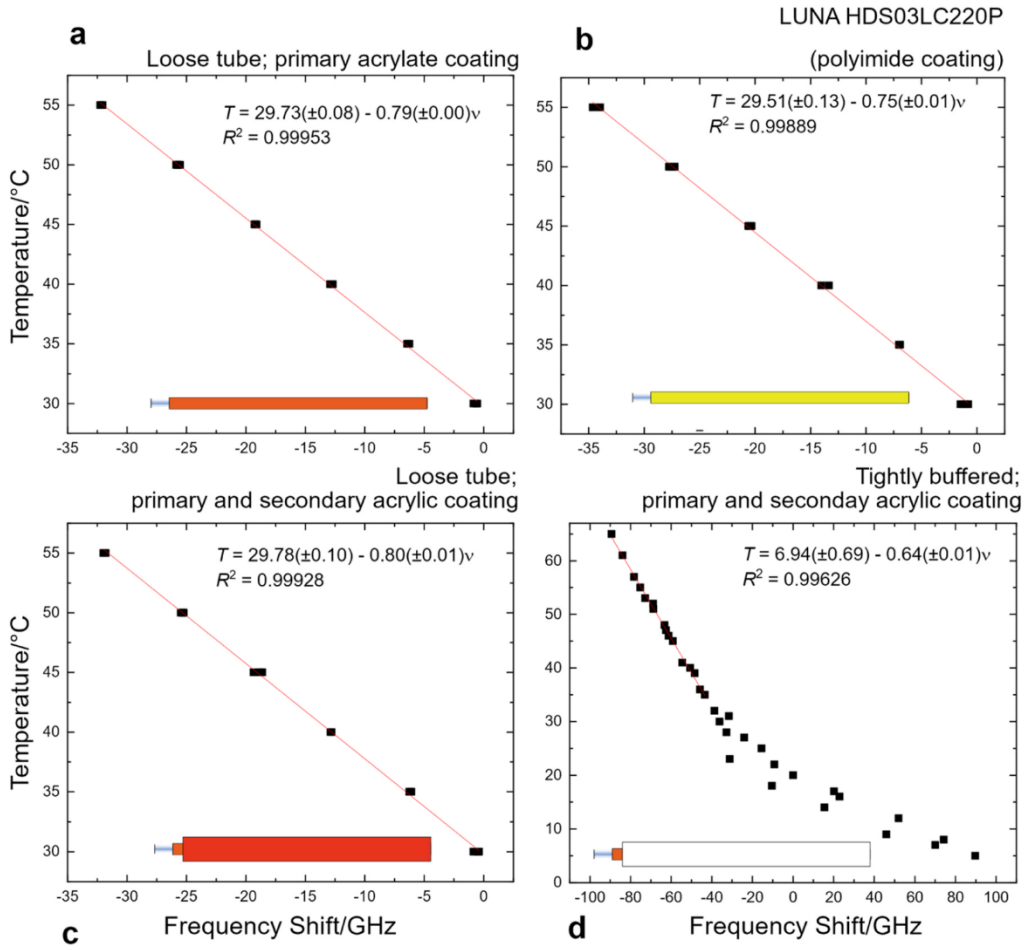

Fig. 4. Correlation between frequency shift and temperature of four DOFS; a loose tube telecommunication cable stripped to its acrylate primary coating (4.a), the commercially available DOFS LUNA HDS03LC220P (4.b) with a polyimide coating, and a loose tube and a tightly buffered acrylate coated cable, stripped to their secondary layers each (4.c and 4.d).

The variable A_0 represents the fiber temperature at the point of initial measurement. This value will serve as the reference point for all following signal shifts and should be the same temperature as the room in an equalized temperature setup. If the correlation between the measured signal shift ν and the real temperature T is linear, the power of ν is 1 and the slope of the line is A_1. If the correlation is non-linear, higher power terms j can be added, with their own coefficients A_j. The default maximum power set in the software for the ODiSI-B is four.

$$T = \quad A_0 + \nu^1 \bullet A_1 + \ldots + \nu^j \bullet A_j \tag{3}$$

5.5. Sensor readout and data evaluation

A software to facilitate the convenient reading of up to eight FOS at the same time has been created. It is designed to handle sensor reading, averaging of subsequent scans (temporal averaging), saving the data, and cleanup of errors. The user interface allows for the quick set up of a measurement, and parameter choice. For a tare measurement the software scans each sensor 540 times. A normal scan takes 14 s per meter of sensor with all signal processing, and each sensor is scanned 120 times.

For the experiments conducted with water, a known upper and lower limit for valid temperature readings was used. Due to the stochastic nature of the Rayleigh backscatter Optical Frequency Domain Reflectometry (OFDR) the spatially resolved frequency shift, resulting from the cross correlation providing the basis for the temperature and strain signal, is often fluctuating. Large errors occur frequently in signal measurement points (Zhang et al., 2019). To cut down on such artifacts, the following data cleanup was automated.

1 °C translates to around −0.7 GHz in spectral shift in such measurements, and therefore, given an emulsion polymerization reaction, reasonable cutoff points are spectral shifts correlating to −5 and +105 °C. The starting temperature before each experiment was room temperature (around 20 °C), which would then equal the base frequency shift of 0 GHz. At the stated upper and lower cutoff points, the frequency shifts equal +18 GHz and −60 GHz respectively. Data points out of this range were set to the value of the previous point on the fiber path. These changes are clearly visible, due to the high unlikelihood of exactly repeating measurements in two adjacent points. The same was done to measurement points reading a non-numerical value or points displaying a sudden frequency shift of over 30 GHz (corresponding to 21 °C across 0.26 mm) compared to the point prior.

Values from the previous automated measurement for a sensor were copied to the next measurement and only replaced with actual new data if the sensor was identified automatically and read without problem. Therefore, exact repeating measurement values show that the sensor

was not identified. This was integrated into the program because sensors were sometimes not identified if they were subject to undue strain or in a bad position, causing big changes in the backscattered spectrum. These sensors were kept active in the measurement because they were sometimes re-identified when temperature or strain improved.

6. Results and discussion

6.1. Assessment of measurement quality across sensors with varying coating and termination

All temperature measurement and calibration experiments were carried out as shown in Fig. 3. The sensors were arranged in a slightly bent configuration in the thermo-regulated vessel and were bent leading up to the reactor portion and behind it. Any fixed bends introducing tension can distort the measurement considerably. Previously, measurements in a bracket shaped reactor with 1.5 mm channels following two 90° bends (bending radius ca. 2.5 cm) were carried out, but this setup was found to be unviable due to the distortion. This should be considered when designing micro- and lab-on-a-chip-style reactors. On such a small scale it is advisable to either increase the bend length (and therefore radius) and straighten out the fiber path about 10 cm (for the presented setup using FOS and the ODiSI-B for Rayleigh backscatter OFDR) before the measurement region, or to use a different sensor per measured linear region.

All sensors except the tightly buffered telecommunication cables with primary and secondary acrylate coatings (4.d) can be sufficiently described using a linear correlation (Eq. 3). The sensor shown in 4. d shows a linear signal response above a temperature of roughly 35 °C. This may be in correlation to polymer softening and thermal expansion.

The range of the coefficient of thermal expansion (CTE) for technical glasses is 3 – 12 ppm/K. For polyimide and polyacrylate polymethylmethacrylate it is 36 – 60 ppm/K and 70 – 77 ppm/K, respectively (Thermal Properties of Plastic Materials, 2024; Technical glasses Physical and Technical Properties, 2024). Due to the large differences between CTEs, the expansion of the polymer coatings can exert strain on the glass surface if they are adhered tightly. This may cause non-linear signal shift in relation to temperature. Due to the comparatively large volume of the secondary protective coating on the fiber optic cable, the force transferred to the glass from its thermal expansion appears to be enough to cause such an effect.

DOFS with acrylate primary coatings and polyimide coatings were used in validation of calibration experiments. Due to the underlying mechanism of temperature measurement, DOFS are relative sensors. Therefore, calibration with other temperature probes is necessary to measure absolute temperature. The factor of conversion A_1 (°C/GHz) is dependent on the environment surrounding the fiber. As has previously been stated, fiber coating can modulate the measured signal, and it may also swell or contract due to factors such as moisture. The bending and torsion introduced when integrating a fiber sensor into a capillary or channel may also change the local strain of the fiber, affecting the temperature response. To validate these hypotheses and estimate the temperature error introduced by online calibration at another part of the system, two types of DOFS were tested using the setup shown in Fig. 3.

The temperature values shown in Fig. 5 are derived from averaging the temperature measured across the section of fiber inside the thermostat (35 cm) and the fiber section inside the reactor channels (12 cm). In the thermostat portion, the standard deviation of the average signal in these DOFS segments is 0.77 GHz for DOFS with primary acrylate coating and 0.67 GHz for DOFS with primary polyimide coating. The equivalent values across the reactor section are 0.66 GHz for DOFS with primary acrylate coating and 0.58 GHz for DOFS with primary polyimide coating. The value of A_0 was determined directly inside the thermostat (black line) or the reactor region underneath the thermal insulation (green line) and used for T calculation from the measured signal shifts. Using the A_1 values estimated via the calibration in the thermostat shows good agreement between the T measurement using the pt100 resistance thermometer in the thermostat and the DOFS. However, using the same A_1 values to calculate the temperature in the reactor region from the measured signal shift shows good agreement for the polyimide coated fiber only. For this sensor, A_1 values derived from the thermostat region and the reactor region differ only by 0.6 %. The acrylate coated fiber yields overestimated temperatures above A_0 (28 – 29 °C in reactor portion) and underestimated temperatures below A_0. Therefore, the factor A_1 is incorrect, and yields errors of multiple °C, worsening over a larger temperature range. A calibration across the reactor segment shows that the A_1 values derived from this calibration are smaller here than the ones from the thermostat region by 20 % for the DOFS with the acrylate coat.

Fig. 6 shows a temperature step from 40 to 30 °C during the calibration experiments, to show the temperature inaccuracies and emphasize some typical behaviors of the DOFS. The temperature was

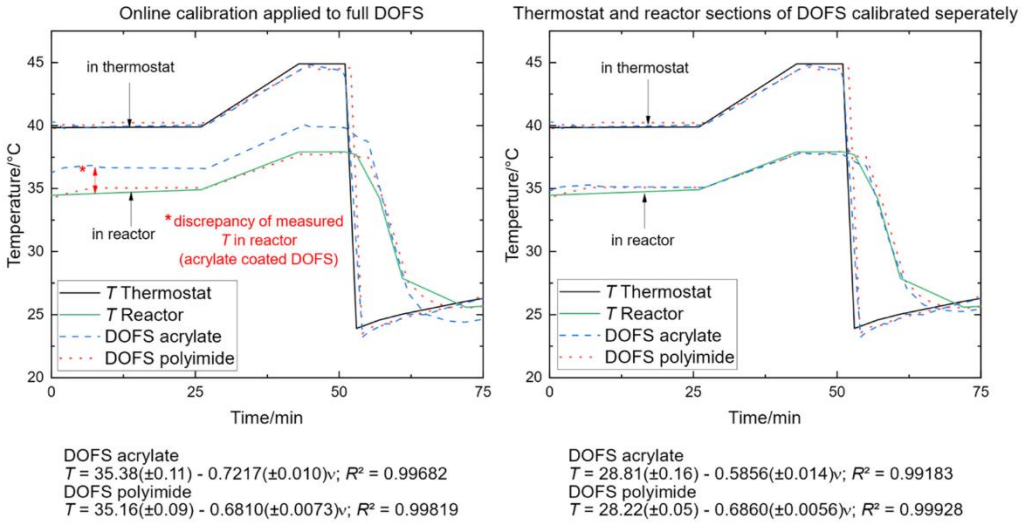

Fig. 5. Temperature measurement of DOFS with acrylate primary coatings and polyimide coatings, as calculated using online calibration (in a thermostat) and separate calibration for the DOFS segment in the reactor channels.

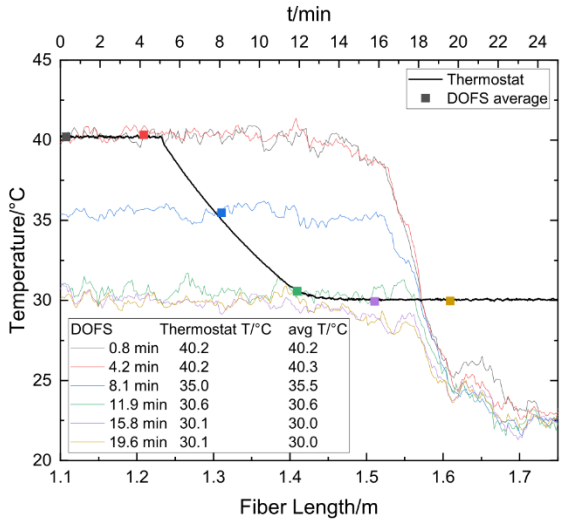

Fig. 6. Spatially resolved T measurement with calibrated DOFS inside thermostat during temperature step from 40 to 30 °C.

recorded in the thermostat and the specially resolved fiber measurement shown is from this same portion. The area of transition from inside the thermostat to the outside environment is shown at the end of the length to illustrate the distortions common for measurements in bends. This needs to be taken into consideration when averaging across segments.

Due to the loose sleeves the fibers were threaded through in the thermostat, there is a considerable delay in temperature response. The sleeves were made from PVC with a thickness of roughly 0.5 mm and an outer diameter of 2.8 mm, and there was air inside them. The measurement software takes 120 readings in sequence, before averaging them, applying post-processing, and saving the data. This delay and the insulating influence of the sleeve explains a temperature difference of 0.5 °C during a steep change in temperature, showing a delay of 20 s in this case. Because the calibration and the shown averages are derived from the same readings and averaged across the same 35 mm (1.1 m to 1.45 m fiber length), good accuracy is expected. Fig. 6 shows that a temperature difference of 0.1 °C can be resolved with accurate calibration and averaging. The high level of noise (± 0.5 °C) is to be considered.

Connector and termination quality can be characterized using OTDR measurements. The attenuation-fiber length plots show the attenuation along the sensor fiber and the following drop off to the noise floor, preceded by the end reflection peak. A linear drop off along the entire plot is expected for long fiber lengths, but this effect is hardly noticeable here because the sensing range is small (10 m in total). Therefore, the attenuation level along the sensor and the noise floor are assumed to be horizontal, and the average for them is estimated given this assumption. In Fig. 7 two such profiles are shown, as taken from the key configuration software by Luna Inc. The manual of the configuration software instructs the user to aim for a difference of 10 dB between the sensor baseline and the noise floor (Luna Inc, 2017, User's Guide). This can be achieved by connecting the sensor cleanly and terminating accordingly. An improper termination can cause a low difference of baseline to noise floor and warping, as shown in the second half of Fig. 7. A slight warping on the side of the noise floor does not cause a significant negative impact on the measurements, but a warping that extends to the left of the end reflection, as shown in Fig. 7, can cause a significant rise in the probability of errors, high mean deviation, or a lack of measurement due to the sensor not being identified by the software.

The temperature responses of two DOFS were measured, dependent on varying termination, which were created with varying glycerol-water solutions. In Fig. 8 the signal shift responses of a DOFS with a primary acrylate coating (red) and a DOFS with tightly buffered primary and secondary acrylate coatings (purple) are shown. Error bars indicate mean deviation. During the second step-cycle, terminations were used that were significantly incompatible with the DOFS, and the sensor identification failed upwards of 35 °C. The significant drift introduced by the secondary coating on the second DOFS is also apparent in this figure. Upon increased strain in the coating with significantly different CTE than the silica glass, the signal seems to shift to larger values and upon relaxation with time, the signal shift becomes smaller. At higher temperatures and after repeated cycles, this behaviour appears less pronounced, possibly due to loosening of internal strain in the polymer material or lessening adhesion between the glass fiber and coating. Upon cooling down, some strain or adhesion appears to return, as can be seen in the last step on the last cycle.

From these measurements, the mean deviation of signal shift along the central 30 cm of the fiber inside the thermo-regulated vessel is plotted against the refractive index used for termination. The same is done for the difference between the attenuation baseline of the sensor and the noise floor. The resulting plots are shown in Fig. 9. An approximate correlation can be seen between the applied refractive index, the baseline to noise floor difference, and the deviation which is representative of noise. It appears that the best refractive index range for terminating the present telecommunication fibers used as DOFS is 1.4630 – 1.4640.

In practice, glycerol-water mixtures are not applicable for long term termination of DOFS, because of the degrading effect these chemicals may have on the glass and the slow change of the refractive index expected from the hygroscopic character of glycerol.

6.2. *Suitability of DOFS for temperature measurement during continuous emulsion polymerization*

Local calibration using acrylate coated sensors, or online calibration

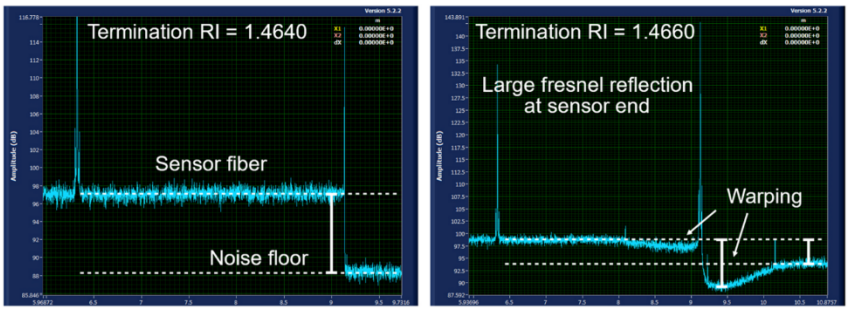

Fig. 7. Attenuation-fiber length profiles for the same fiber with two different glycerol-water solutions as termination.

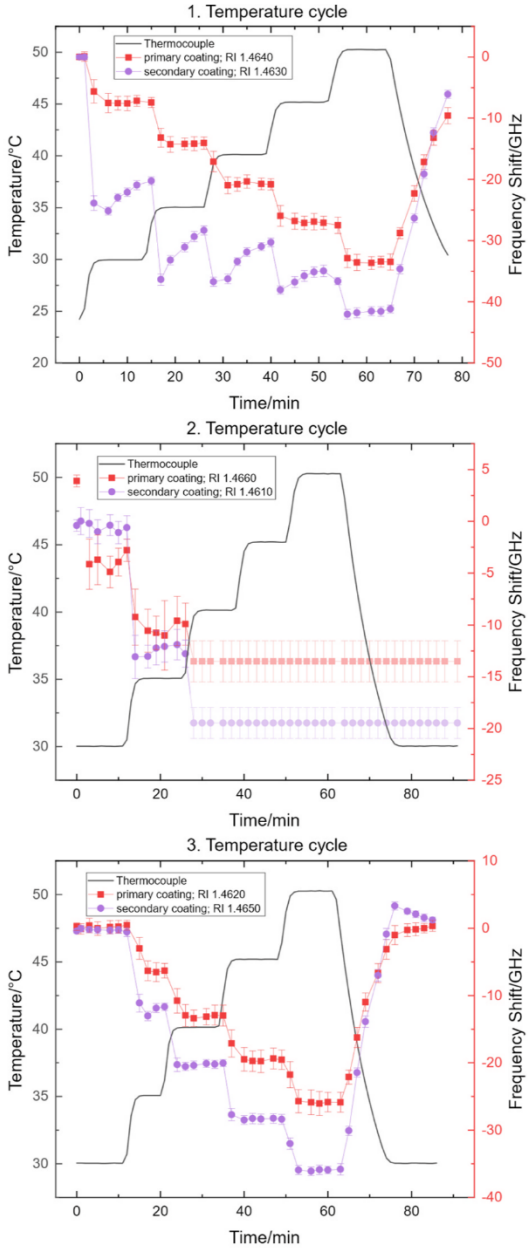

Fig. 8. Three consecutive temperature step cycles taken with two DOFS, one with a primary acrylate coating (red) and one with tightly buffered primary and secondary acrylate coatings (purple) as well as with varying glycerol-water solutions as termination.

using polyimide coated sensors, allows for a temperature measurement accuracy of 0.1 °C. In the context of continuous emulsion polymerization, and in particular fouling monitoring, the generous spatial averaging (30 cm) used to achieve the resolution of 0.1 °C, is not desirable. In small laboratory or meso- and micro-reactor scale, the entire length of the interrogated reactor portion may be smaller than 30 cm. The ODiSI-B allows for sensor readout with a 2.6 mm resolution. Without spatial averaging the considerable noise level of ± 0.5 °C is limiting the resolution and sensitivity. Temporal averaging is already being carried out to achieve this result, as explained in the experimental section.

Due to the increased thermal exchange properties of a flow reactor over a bulk setup, exothermic reactions and any reactions needing intense temperature control may be considered for transfer into a continuous flow process. To monitor reaction progress and safety, a temperature resolution of 0.5 °C can be considered as sufficient for fouling monitoring in tubular continuous polymerization reactors.

Temperature changes of multiple degrees, over multiple minutes, can be tracked reliably with the DOFS. Therefore, hot and coldspot detection can be carried out. This may be of use for fouling detection, as increased fouling layer thickness on the inside channel lowers the temperature measured in the reactor wall. If fouling is formed as the reaction progresses in the flow reactor, most of the fouling can be expected at the end of the channel. As mentioned previously, a polymer fouling layer formed over 2 h of reaction time accumulating a thickness of 50 μm may cause a temperature loss of 0.8 K in the reactor wall. Given no spatial averaging, such a change would be identifiable in the length-temperature plot of a calibrated DOFS measuring wall temperature. It can be extrapolated that this technology is useful in monitoring for clogging, and maintenance scheduling, as well as process safety monitoring in tubular continuous polymerization reactors

7. Summary

Different variations of fiber coating and termination were examined for suitability as spatially resolved temperature sensors for chemical reactors. It could be determined that, given suitable calibration and setup, temperature differences of 0.1 °C can be resolved. The standard deviation across the averaged segments is 0.5 °C, illustrating the noise level of a DOFS measurement with only temporal averaging applied (120 consecutive scans, under 14 s). Such a resolution may be sufficient for some kinetic and calorimetric measurements and is sufficient for general temperature control. This has been evaluated for a temperature range of 0 – 70 °C, the range for emulsion polymerization. Online calibration was carried out in order to calibrate the sensors in one segment while a reaction can be carried out using another. It could be shown that for polyimide coated DOFS such an approach may be sufficient, but acrylate coated fibers require in-segment calibration. The physical difference between the surroundings of the online calibration segment and the segment inside the reactor caused a change in the conversion factor A_1 of 20 %. It is possible, that periodic calibration segments along a reactor length where the DOFS and a thermometer are both present in the same location would solve this problem. In between these segments the factor A_1 can, for example, be changed linearly to approximate the strain gradient. Such segments would need to be positioned after bends and similar changes in physical environment. Using such an approach a good temperature accuracy could be achieved across larger lengths and complicated fiber paths. Measurement segments should be as straight as possible to minimize strain.

Given such an in-segment calibration, the main difference between polyimide and acrylate coatings are the thermal expansion and chemical and physical stability. The larger CTE difference for acrylate and silica in comparison to polyimide and silica explains why the factor A_1 of the acrylate coated fibers is consistently larger in absolute value. Polyimide is known to take up moisture, which can impact the measurement. The polymer coatings can swell upon contact with solvent and solvent vapours. Long term stability of silica fibers can be impacted negatively by moisture, as well. These factors can affect distributed temperature measurements but could also be counter-acted by periodic re-calibration in segments. DOFS with a secondary coating are considerably stronger than fibers with only a primary coating. However, the secondary coating causes temperature measurement delay, non-linear signal shift to temperature relation and drifting signal shift responses during periods of constant temperature. Whether a secondary coating clad fiber is suitable as a sensor depends on the needed accuracy and the individual fiber, as

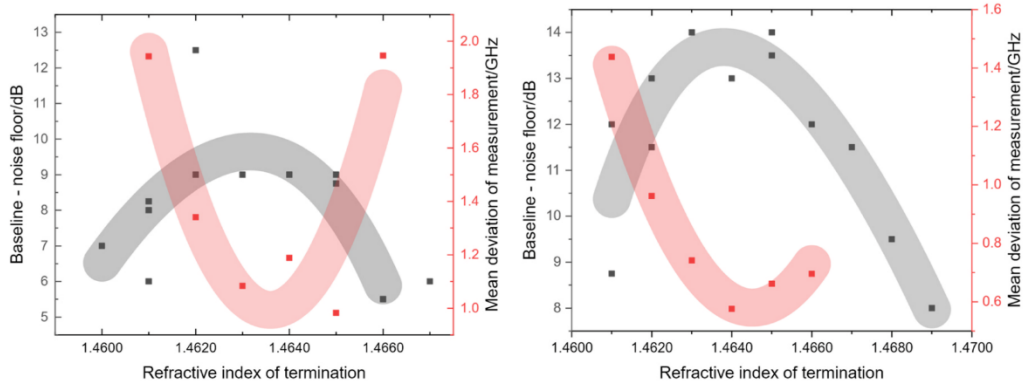

Fig. 9. Two diagrams for the two different DOFS displaying the base to noise floor distance in dB, as measured from the attenuation-fiber length profiles, and the mean deviation across the DOFS section under test in the thermos-regulated vessel plotted against the refractive indices of the glycerol-water solutions used for fiber termination.

coating adhesion and other properties cause different fibers to behave differently.

The refractive index of the fiber termination has been varied to see its effect on measurement quality and an optimum around 1.4630–1.4640 has been illustrated. The refractive index of the coreless glass fiber used specifically for termination is 1.4644 at 1550 nm and therefore close to this approximate range. Glycerol-water mixtures with adjusted refractive index can be used as temporary termination.

It can be concluded that Rayleigh-based DOFS may offer sufficient resolution to measure fouling formation spatially and thermally during emulsion polymerization. They can be used to monitor temperature during emulsion polymerization and locate and quantify hotspots caused by reaction heat. With DOFS real-time changes in the system, such as flow changes, could be identified in real chemical reactor systems.

Funding information

This work has been funded by the German Federal Ministry for Economic Affairs and Climate Action, Germany as part of the ENPRO Initiative (KoPPonA 2.0, FKZ: 03EN2004M).

Author contributions

W.P. has initiated and supervised the presented research and M.K. has carried it out, written the article and prepared the images. Both authors have edited the manuscript.

CRediT authorship contribution statement

Werner Pauer: Writing – review & editing, Supervision, Project administration, Funding acquisition, Conceptualization. **Maria Klippert:** Writing – original draft, Visualization, Validation, Software, Methodology, Investigation, Formal analysis, Data curation, Conceptualization.

Declaration of Competing Interest

The authors declare that they have no known competing financial interests or personal relationships that could have appeared to influence the work reported in this paper.

Acknowledgements

The authors would like to thank the ENPRO initiative, particularly the members of the KoPPonA 2.0 project (ger. *Kontinuierliche Prozesse für Polymerspezialitäten mit Hilfe neuer Apparatekonzepte*, Continuous processes for polymerization with the help of new technological concepts), Jonas Krautter, and Devon Martin.

Data availability

The data that support the findings of this study are available from the corresponding author upon reasonable request.

References

Agrawal, G.P., 2010. Fiber-optic communication systems. Fiber-Optic Communication Systems. Wiley.
Bao, X., Chen, L., 2012. Recent progress in distributed fiber optic sensors. Sensors 12 (7), 8601–8639. https://doi.org/10.3390/s120708601.
BG RCI, 2015. Merkblatt R 008 Polyreaktionen und polymerisationsfähige Systeme, Ausgabe 05/2015.
Bolognini, G., et al., 2019. Optical fiber sensing cables for Brillouin-based distributed measurements. Sensors 19, 5172. https://doi.org/10.3390/s19235172.
Chen, C., Chen, L., Bao, X., 2022. Distributed temperature profile in hydrogen flame measured by telecom fiber and its durability under flame by OFDR. Opt. Express 30 (11), 19390. https://doi.org/10.1364/OE.455640.
Copelli, S., Derudi, M., sempere, J., Serra, E., Lunghi, A., Pasturenzi, C., Rota, R., 2011. Emulsion polymerization of vinyl acetate: safe optimization of a hazardous complex process. J. Hazard. Mater. 192, 8–17. https://doi.org/10.1016/j.jhazmat.2011.04.066.
Davis, I., 2023. Corning Incorporated, White Paper 1281: Explanation of Reflection Features in OTDR Measurement Traces.
DIN EN 60584-1:2014-07, Beuth Verlag GmbH, 10772 Berlin (2014).
DIN EN 60751:2009-05, Beuth Verlag GmbH, 10772 Berlin (2009).
Egner, F., Bank, R., Bauer, A., Verbeek, D., Lainer, M., 2014. U.S. National Stage Application US10173190B2, Fibre-optic temperature measurement in a catalyst. material.
Fernandez, I., Berrocal, C.G., Almfeldt, S., Rempling, R., 2023. Monitoring of new and existing stainless-steel reinforced concrete structures by clad distributed optical fibre sensing. Struct. Health Monit. 22 (1), 257–275. https://doi.org/10.1177/14759217221081149.
Fluves, 2024. Fiber optic sensing: A game-changer for industry 4.0 monitoring.
Frede, T.A., Maier, M.C., Kockmann, N., Gruber-Woelfler, H., 2022. Advances in continuous flow calorimetry. Org. Process Res. Dev. 26, 267–277. https://doi.org/10.1021/acs.oprd.1c00437.
Froggatt, M., et al., 2006. Distributed strain and temperature discrimination in unaltered polarization maintaining fiber. Opt. Fiber Sens. doi: 10.1364/OFS.2006.ThC5.
Galal, M., et al., 2021. On the measurement accuracy of coherent Rayleigh-based distributed sensors. Opt. Express 29 (26), 42538–42552. https://doi.org/10.1364/OE.442790.
Girard, S., Marcandella, C., et al., 2013. Radiation effects on silica-based optical fibers: recent advances and future challenges. IEEE Trans. Nucl. Sci. 60 (3), 2015–2036. https://doi.org/10.1109/TNS.2012.2235464.
Glaesemann, G.S., 2017. Corning Incorporated, White Paper 8002: Optical Fiber Mechanical Reliability Review of Research at Corning's Optical Fiber Strength Laboratory.
Goltz, M., 2011. A contribution to Monitoring of Embankment Dams by means of Distributed Fiber Optic Measurements, Dissertation at Leopold-Franzens-University Innsbruck.

Hartog, A.H., 2018. An introduction to distributed optical fiber sensors. An introduction to distributed optical fiber sensors. Taylor & Francis Group.
Hohlen, A., Augustin, W., Scholl, S., 2019. Quantification of polymer fouling on heat transfer surfaces during synthesis, 1900035-1900045 Macromol. React. Eng. 14. https://doi.org/10.1002/mren.201900035.
Huang, Y.K., et al., 2022. Distributed fiber sensor network using telecom cables as sensing media: technology advancements and applications. J. Opt. Commun. Netw. 14 (1), A61–A68. https://doi.org/10.1364/JOCN.439175.
Huang, L., Dyer, R.S., Lago, R.J., Stolov, A.A., Li, J., 2016. Mechanical properties of polyimide coated optical fibers at elevated temperatures. Proc. SPIE 9702. https://doi.org/10.1117/12.2210957.
Huang, C., Qian, X., Yang, R., 2018. Thermal conductivity of polymers and polymer nanocomposites. Mater. Sci. Eng. R. 132, 1–22. https://doi.org/10.1016/j.mser.2018.06.002.
Jacobs, J.M., 2004. Corning Incorporated, White Paper 9007: The Impact of Hydrogen on Optical Fibers.
Jones, J.T., Sweeney, D.C., Birri, A., Petrie, C.M., Blue, T.E., 2022. Calibration of distributed temperature sensors using commercially available SMF-28 optical fiber from 22° C to 1000° C. IEEE Sens. J. 22 (5), 4144–4151. https://doi.org/10.1109/JSEN.2022.3146185.
Kouzmina, I., Davis, I., 2021. Corning Incorporated, White Paper 3703: Corning ® CPC® Protective Coating – An Overview.
Kurkjian, C.R., Simpkins, P.G., Inniss, D., 1993. Strength, degradation and coatings of Silica Lightguides. J. Am. Ceram. Soc. 76 (5), 1106–1112.
Li, X., Yang, C., Yang, S., Li, G., 2012. Fiber-optical sensors: basics and applications in multiphase reactors. Sensors 12 (9), 12519–12544. https://doi.org/10.3390/s120912519.
Lin, Y., Gong, Y., Wu, Y., Wu, H., 2014. Polyimide-coated fiber bragg grating for relative humidity sensing. Photon. Sens. 5, 60–66. https://doi.org/10.1007/s13320-014-0218-8.
Liu, T., et al., 2018. Distributed optical fiber sensors based on optical frequency domain reflectometry: a review. Sensors 18, 1072. https://doi.org/10.3390/s18041072.
Liu, Y., Si, X., Wu, L., Mo, C., Zhuang, Y., 2022. European Patent Application EP000003945297A1, Reactor Temperature Measurement System, Reactor and Method for preparing a Fiber Bragg Grating.
Lopez-Higuera, J.M., et al., 2016. High-temperature distributed sensor based on Raman and multimode standard telecom fiber. Opt. NOMA. https://doi.org/10.1364/IPRSN.2016.JTu4A.21.
Lovell, P.A., Schork, F.J., 2020. Fundamentals of emulsion polymerization. Biomac 21, 4396–4441. https://doi.org/10.1021/acs.biomac.0c00769.
Lu, X., Soto, M.A., Thévenaz, L., 2017. Impact of the fiber coating on the temperature response of distributed optical fiber sensors at cryogenic ranges. J. Light. Technol. 36 (4), 961–967. https://doi.org/10.1109/JLT.2017.2757843.
Lu, X., Thomas, P.J., Hellevang, J.O., 2019. A review of methods for fibre-optic distributed chemical sensing. Sensors 19 (13), 2876. https://doi.org/10.3390/s19132876.
Luna Inc., 2017. ODiSI-B Data Sheet.
Luna Inc., 2017. User's Guide ODiSI-B Sensor Config. Version 5.2.2.
Maier, M.C., Leitner, M., Kappe, C.O., Gruberr-Woelfler, H., 2020. A modular 3D printed isothermal heat flow calorimeter for reaction calorimetry in continuous flow. React. Chem. Eng. 5, 1410–1420. https://doi.org/10.1039/d0re00122h.
McCary, K.M., Wilson, B.A., Birri, A., Blue, T.E., 2018. Response of distributed fiber optic temperature sensors to high-temperature step transients. IEEE Sens. J. 18 (21), 8755–8761. https://doi.org/10.1109/JSEN.2018.2868429.
Moser, M., Georg, A.G., Steinemann, F.L., Rütti, D.P., Meier, D.M., 2021. Continuous milli-scale reaction calorimeter for direct scale-up of slow chemistry. J. Flow Chem. 11, 691–699. https://doi.org/10.1007/s41981-021-00204-y.
Nestler, F., Müller, V.P., Ouda, M., Hadrich, M.J., Schaadt, A., Bajohr, S., Kolb, T., 2021. A novel approach for kinetic measurements in exothermic fixed bed reactors: advancements in non-isothermal bed conditions demonstrated for methanol synthesis. React. Chem. Eng. 6, 1092–1107. https://doi.org/10.1039/D1RE00071C.
Offerhaus, H.L., et al., 2021. Comparison of three types of fiber optic sensors for temperature monitoring in a groundwater flow simulator. Sens. Actuators A: Phys. 331, 112682. https://doi.org/10.1016/j.sna.2021.112682.
Ooi, S., et al., 2002. A review of distributed fiber–optic sensing in the oil and gas industry. *Jounral*. Light. Technol. 40 (5). https://doi.org/10.1109/JLT.2021.3135653.
Palmer, R.K., McCary, K.M., Blue, T.E., 2017. An analytical model for the time constants of optical fiber temperature sensing. IEEE Sens. J. 17, 5492–5502. https://doi.org/10.1109/JSEN.2017.2722982.
Rust, S., Pauer, W., 2022. Determination of inline-particle sizes by turbidity measurement in high solid content emulsion polymerisations. J. Polym. Res. 29, 307. https://doi.org/10.1007/s10965-022-03141-z.
Saechtling, H., 1983. Kunststoff Taschenbuch, 23. edition. Hanser, München, Wien. ISBN: 3-446-14611-3.
B. Schroeter, Kinetik von Redoxinitiatoren für die Emulsionspolymerisation, Dissertation at University of Hamburg, 2018.
Stolov, A.A., Li, J., Hokansson, A.S., Hines, M.J., 2022. Effects of hydrogen scavenging cable gel on the strength and attenuation of optical fibers. J. Light. Technol. 40 (18), 6264–6271. https://doi.org/10.1109/JLT.2022.3190817.
Storvik, F., et al., 2022. Sensing whales, storms, ships and earthquakes using an Arctic fibre optic cable. Sci. Rep. 12 (1), 19226. https://doi.org/10.1038/s41598-022-23606-x.
Technical glasses Physical and Technical Properties, Schott, Archived Brochure, last accessed 29.02.2024.
Thermal Properties of Plastic Materials, Professional Plastics Inc., last accessed 29.02.2024.
Venghaus, H., Grote, N., 2017. Fiber optic communication. Fiber Optic Communication. Springer International Publishing.
Wang, S., Staeter, E., Lasn, K., 2021. Comparison of DOFS attatchement methods for time-dependant strain sensing. Sensors 21, 6879. https://doi.org/10.3390/s21206879.
Xu, C., Khodaei, Z.S., 2020. Shape sensing with Rayleigh backscattering fibre optic sensor. Sensors 20, 4040. https://doi.org/10.3390/s20144040.
Zhang, L., Costa, L.D., Yang, Z., Soto, M.A., Gonzalet-Herráez, M., 2019. L. Thévenaz, Analysis and reduction of large errors in rayleigh-based distributed sensor. J. Light. Technol. 37 (18), 4710–4719. https://doi.org/10.1109/JLT.2019.2917746.
Zhang, Y., Song, L., Kaiser, G., Hergenrother, M.L., Stober, B.K., Kalamaras, P.H., Umansky, B.S., 2014. U.S. National Stage Application US9746434B2, Method and system for determining flow distribution through a component.
Zhong, X., Broere, W., 2023. Design of a distributed optical fiber sensor system for measuring immersed tunnel joint deformations. Tunn. Undergr. Space Technol. 131, 104770. https://doi.org/10.1016/j.tust.2022.104770.

6.2. Determination of the clogging time for continuous emulsion copolymerization in a tubular reactor using distributed optical fiber sensors

Maria Klippert, Werner Pauer

Synopsis:

With the established methodology for DOFS monitoring in a tubular reactor, the copolymerization reaction of VAc and VV10 was carried out. It was determined by gravimetrical conversion monitoring and the online DOFS measurement that the reaction needed a certain reactor length to reach the point of maximum conversion rate (the hotspot T_{max}). In order to follow the hotspot, the reactor setup was changed prior to the recording of the data presented in the publication. The reactor length was increased from 70 cm total (only 20 cm covered with DOFS due to the size limitation of the 3D printer) to 350 cm total (150 cm monitored with DOFS in three horizontal sections). To further decelerate the fouling for better temporal hotspot monitoring, the reaction was not carried out in a channel made of 3D printed PLA, but instead in a polytetrafluoroethylene (PTFE) tube with the same internal diameter. To keep the same cross-sectional geometry and enable the integration of three DOFS at different radial distances the tubing was inserted in a 3D printed PLA bracket system to complete the previously established radial reactor geometry. The reaction execution was changed, too. A pre-emulsion of monomer, water and PVA (Mowiol® 4-88) was created and stirred continuously during dosing for the copolymerization reaction. In the previous execution the monomer was mixed with the PVA solution and the redox components in a 10 mL CSTR directly before initiation and entrance into the reactor (four streams instead of 3). The pre-emulsifying was incorporated to ensure good homogenization of the reaction mixture. The reactor shape (three horizontal sections and two bends, plus curved inlet and outlet sections) was chosen for spatial fit and for reaction mixture agitation to prevent creaming.

The changes enabled the reactor hotspot to be detected and monitored in the reactor sections equipped with thermocouples and DOFS. It was observed that the shape the hotspot's path traced in the reactor length-reaction time plot was similar between reactions. This confirmed repeatability of the reaction and comparable course of fouling deposition during reaction between experiments. The hotspot was pushed downstream and out of the reactor each reaction. This is expected due to the volume loss to the foulant. It was hypothesized that it is possible to create mathematical models to describe the reactor volume decrease and use the DOFS data to parameterize the equations.

Mathematical models were established to geometrically describe the shape change of the free inner volume of the reactor, one variant considering the entire reactor volume and one considering only the volume leading up to T_{max}' current position. The models were constructed using different fouling rates (linear, falling, asymptotic, rising) and different resulting shapes of inner volume (even tube, cone segment, parabolic radius decrease). It was known that the fouling deposited more towards the end of the reactor than the inlet, but all options were explored. Furthermore, it was already known from literature that the fouling rate during this particular reaction appears to be linear (mass-time deposition).

The mathematical models were fitted to the length-time hotspot plots from the DOFS measurements. The models best describing the fouling were the ones with linear or cubic fouling rates. The foulant volume could be calculated with the models directly and the results were compared with literature. When plotted over reaction time, the foulant volume of the linear and cubic rates were overlapping a lot (very stretched cubic function within observed interval, could be described as quasi-linear). A linear correlation has been found by Rust et al. (2024), and a cubic correlation has been found by Klinkert et al. (2024). [24,73] Furthermore, the foulant mass-reaction time data published by Rust et al. for the reaction at 20 °C shows high similarity to the foulant mass calculated by the models. This lends credence to the models' validity.

Additionally, the DOFS data was cut to describe only the first 30 min of reaction time after reaction start and the models were used on this cut data. The calculated time for the reactor clogging from this data was within a range of 0.89–1.28 (1 expressing perfect agreement with the measured data for the clogging time). The 30 min beginning interval is 12 % of the entire reaction time from beginning to clogging.

Chemical Engineering Research and Design 215 (2025) 465–475

Contents lists available at ScienceDirect

Chemical Engineering Research and Design

journal homepage: www.elsevier.com/locate/cherd

Determination of the clogging time for continuous emulsion copolymerization in a tubular reactor using distributed optical fiber sensors

Maria Klippert, Werner Pauer *

Institute for Technical and Macromolecular Chemistry, University of Hamburg, Bundesstraße 45, Hamburg 20146, Germany

ARTICLE INFO

Keywords:
DOFS
Polymerization fouling
Continuous reaction
Emulsion polymerization
Fouling prediction

ABSTRACT

A non-intrusive method for fouling monitoring using DOFS (Distributed Optical Fiber Sensors) in tubular reactors is presented. The hot spot, caused by the exothermal emulsion polymerization reaction of vinyl acetate and vinyl neodecanoate, was used as a marker to track the fouling progression during the reaction. Due to fouling, the reactor volume was constricted, causing the hot spot to migrate further downstream. This migration was spatially and temporally resolved as a hot spot position-time plot and used describe the time of clogging using mathematical models. From these models, it could be deduced, that the fouling influencing the hot spot is best described by an even constriction of the entire tubular reactor. The mathematical model was able to determine the time of clogging with an accuracy of 0.89–1.28 (with 1 being in perfect agreement with the measured clogging time), starting from 30 min of reaction time. This time is equivalent to 12 % of the entire time of reaction from start to clogging.

1. Introduction

Emulsion polymerization is the practice of synthesizing a polymer as a latex, small particles dispersed in a continuous phase. In most cases, the continuous phase is water, and the dispersed phase is the lipophilic monomer. A surfactant is usually used to stabilize the emulsion and control the number and size of the monomer particles. An initiator, often water soluble, is added to initiate the reaction. The reaction begins in the water phase, and the reactive oligomer together with monomer forms an active latex particle. The monomer and surfactant migrate from the monomer droplets to the latex particles, until the monomer is used up (Chern, 2006; Schroeter, 2018).

In reality, the processes behind emulsion polymerization are complicated and manifold, but the simplified view helps establish a three-phase model, which is empirically confirmed in literature. Fig. 1 shows the three phases in terms of released reaction heat. Phase I is the nucleation phase, phase II is the growth phase and phase III is the phase where residual monomer is consumed (Schroeter, 2018; Klinkert et al., 2024).

Emulsion polymerization is used to fabricate products used in applications such as adhesives, coatings and additives for building materials. Due to polymerizations being exothermic reactions, temperature control is very important during synthesis. Continuous reactor systems, such as tubular reactors, are therefore an attractive option for process intensification, due to their increased heat-exchange abilities. The main problem in the adaptation of emulsion polymerizations into such processes is the tendency of these systems to create a fouling layer. The thermally insulating fouling layer decreases heat removal capabilities and parts of the fouled material being reintroduced into the product stream decrease product quality (Urrutia and Asua, 2021). The study of fouling can be partitioned into formation, monitoring, mitigation and removal. Due to the inherent production of solid product in the polymerization process, the fouling formation is directly linked to the main reaction. The inherent instability of a dispersed system, having a large surface area across many particles, is itself cause for fouling formation. Generally, it is accepted to describe fouling formation in the vein of coagulation and particle destabilization, undesired formation of long or crosslinked polymer, and as a mechanism of soluble fouling precursor formation with subsequent wall-adhesion of insoluble material (Klinkert et al., 2024; Urrutia and Asua, 2021; Welzel and Nieken, 2024). Fouling monitoring has been explored in a variety of ways, such as with gravimetric, thermal resistance, ultrasound and pressure drop measurement methods. The change of residence time distribution is also a way to monitor fouling (Welzel and Nieken, 2024; Osenberg et al., 2022; Bernstein, 2017; Rust et al., 2024; Deshannavar and Marappagounder, 2021; Böttcher et al., 2016). Additives to stabilize the particles during

* Corresponding author.
E-mail address: werner.pauer@uni-hamburg.de (W. Pauer).

https://doi.org/10.1016/j.cherd.2025.02.012
Received 6 December 2024; Received in revised form 6 February 2025; Accepted 10 February 2025
Available online 11 February 2025

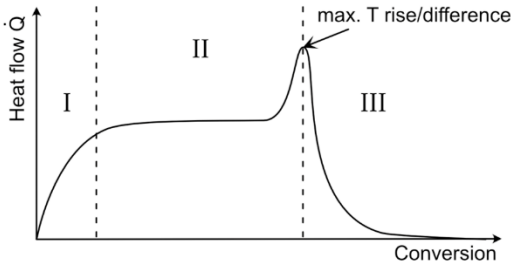

Fig. 1. The three-phase model of emulsion polymerization in terms of reaction heat with significant gel effect.

reaction and therefore mitigate fouling, as well as wall coatings to discourage foulant adhesion have been reported (Arhancet, 1998; Tong, 2015; Grundmeier et al., 2022; Movsesian et al., 2020). Removal of fouling has been, for example, achieved by using flushing with solvent and ultrasonic cavitation effect (Dorton and Gardener, 2012; Fang et al., 2020).

In literature, modeling in the context of emulsion polymerization is mostly concerned with reaction kinetics and prediction of product properties (D'hooge et al., 2016). Modeling of fouling processes can be primarily found in relation to membrane fouling and crude oil pipelines, as well as large polymerization processes such as the LDPE (Low Density Polyethylene) synthesis (Murat et al., 2022; Hannon et al., 2005; Fries, 2019). LDPE is synthesized from a gaseous monomer at high temperatures and pressures in tubular reactors. The process is very different from emulsion polymerization, therefore, the present publication is breaching a novel subject in literature. With a method to monitor and quantify fouling, predictive models can be built. Such models can help with

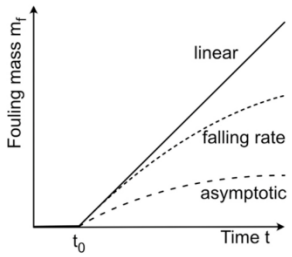

Fig. 3. Fouling rates as distinguished by Epstein in 1983 (Epstein, 1983).

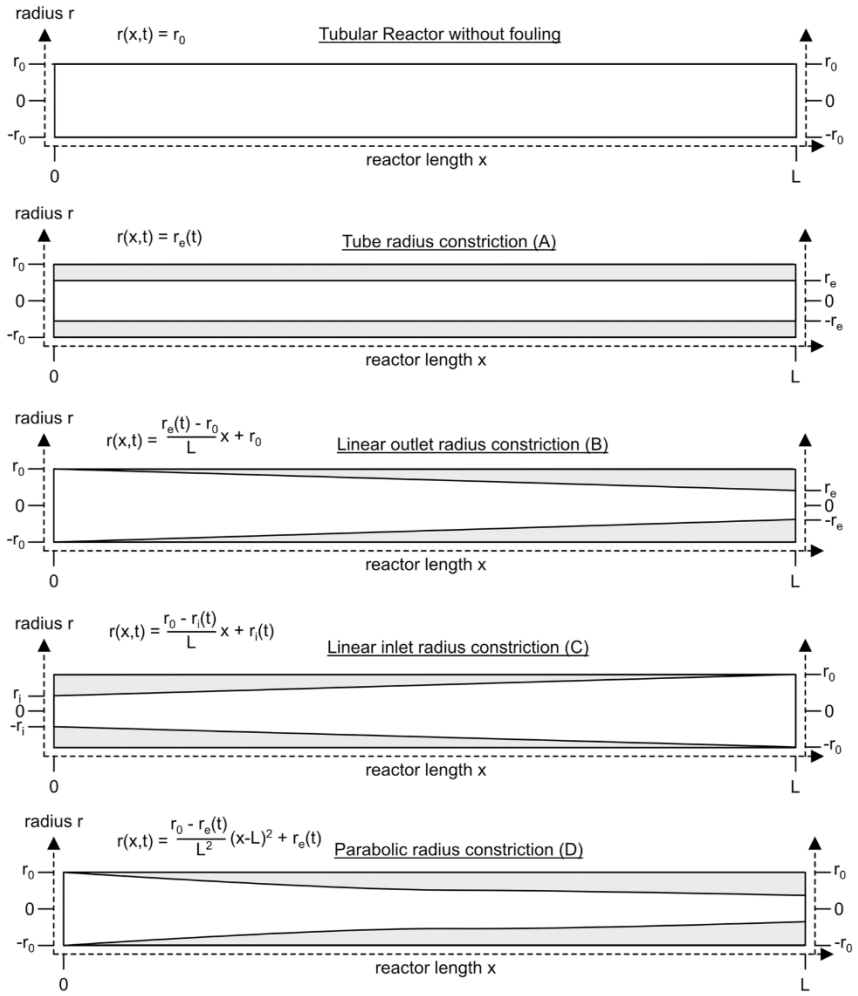

Fig. 2. Functions describing the inner radius of the tubular reactor along its length.

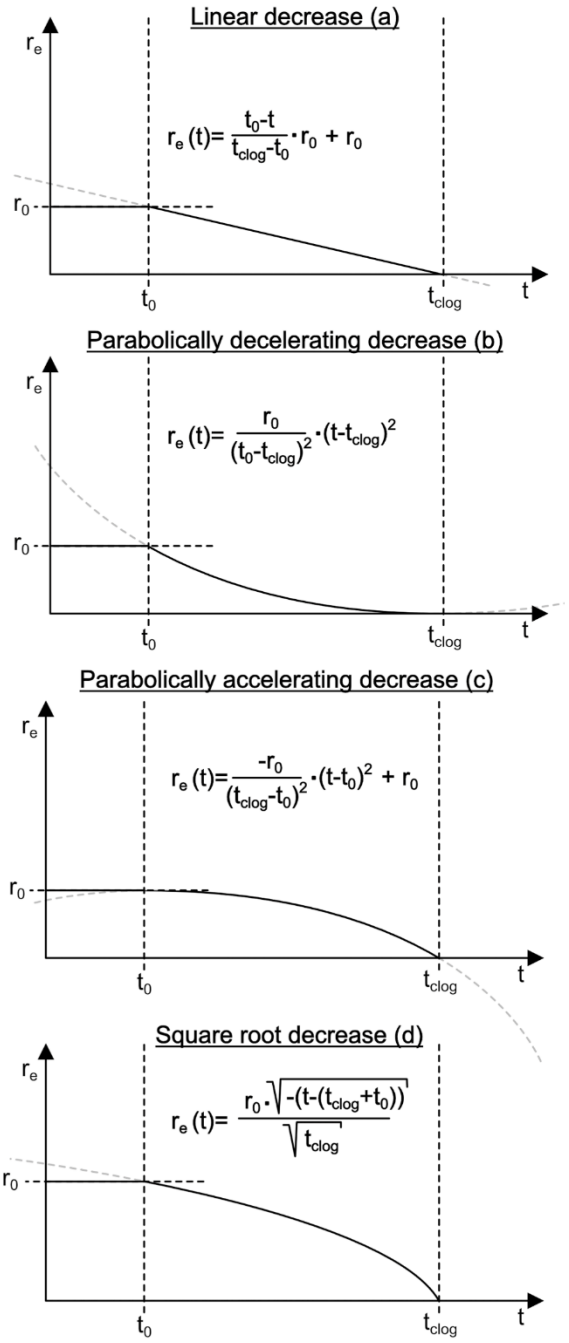

Fig. 4. Change of the end tube radius r_e, during reaction time, with t_0, being the time of the first detectable change in x_{max}, due to fouling, until a full obstruction occurs at t_{clog}.

further fouling reduction. There are two general types of models, deterministic and threshold fouling models (ur Rehman et al., 2023). Threshold fouling models are often used for crude oil fouling and predict fouling, which starts at a certain threshold variable (Deshannavar and Marappagounder, 2021). This method is not applicable for the emulsion polymerization reaction discussed in the presented work, because fouling always occurs and no variables that prevent fouling entirely have been identified (Welzel and Nieken, 2024). Deterministic models focus on identifying the causes and mechanisms of fouling empirically, and predict the fouling formation based on empirical and measured interdependencies (ur Rehman et al., 2023; Rammerstorfer, 2020). In 1997 Watkinson and Wilson wrote about fouling in organic fluids, identifying the general process order: synthesis/presence of fouling reactants, followed by formation of soluble fouling precursors, followed by the formation of foulant (Watkinson and Wilson, 1997). It was stated that in order to take steps towards fouling mitigation, the reactants needed to be identified. The kinetics of precursor and foulant formation needed to be understood and furthermore, the question of whether the foulant formed in the bulk phase, in the thermal layer, or on the observed surface needed to be answered. This concept was expanded on, introducing various modes of fouling formation and addition or subtraction to the surface, in order to create a more thorough understanding of the kinetics concerning fouling (ur Rehman et al., 2023; Rammerstorfer, 2020; Ardsomang et al., 2013). If the fouling process was controlled by the chemical reaction forming the foulant, the fouling rate would increase with rising temperatures and decrease with rising flow velocity, due to decreased residence time. If the fouling process was controlled by the deposition of the foulant on the surface, the fouling rate would rise with the surface temperature. If desorption of foulant from the fouling layer was controlling the rate, the fouling would decrease with increased wall temperature. In the case, that the transport to the wall were the rate controlling step, the fouling rate would rise with the temperature (Rammerstorfer, 2020). From these observations, educated guesses can be made about the main pathway of fouling formation for a given reaction.

The examined copolymerization of vinyl acetate and vinyl neodecanoate has been previously carried out and fouling measurement data is present in literature (Osenberg et al., 2022; Rust et al., 2024; Rust and Pauer, 2023; Hohlen et al., 2019; Jacob et al., 2022). In the case of a steel reactor with static mixing elements, it was reported that the total fouling mass was increased due to higher temperature and increasing concentrations of initiator, monomer, and emulsifier respectively (Rust and Pauer, 2023). The spatial distribution of the fouling mass was reported to be high at the outlet initially, but even along the entire length by the end of the reaction, this is applicable for a cool and hot outer surface (Rust et al., 2024). Different findings show a continuously increasing fouling mass across the entire reactor, with fouling present at the inlet as well, if the channel surface is cooled (Hohlen et al., 2019). The latter reaction was performed in a cyclic system where the reaction mixture is passed through the measurement channel and then reintroduced to a CSTR (Continuously Stirred Tank Reactor), from which the mixture is continuously fed back into the channel. The former in a tubular reactor without any loop reactor characteristics. It has been shown that a non-reactive latex product suspension being pumped through the measurement section, as well as a reactive mixture, tend to foul at the beginning of the measurement channel on a heated surface, as opposed to the end (outlet) (Hohlen et al., 2019).

In these studies, the formed fouling mass was also examined over the reaction time. One study found that the total fouling mass increases linearly over time (Rust et al., 2024). Another study (with the described looping set up) found that the total fouling mass inside the channel increases with the time to the power of three (Klinkert et al., 2024).

DOFS are fiber optics based sensors, which can measure variables in a spatially distributed manner along the glass fiber length. For such a measurement, a light emitter, an optical fiber, and a detector is needed. The light is emitted from a strongly coherent laser, and then enters the optical fiber. Density fluctuations and impurities within the otherwise homogenous glass material cause backscattering of some of the light. Methods to use Rayleigh, Brillouin and Raman scattering exist. The scattered light which has propagated back towards the beginning of the fiber is then detected (Zheng et al., 2021). For OFDR (Optical Frequency Domain Reflectometry), a swept wavelength laser source is used, and the

c

$$r_e(t) = \left(-\frac{r_0}{(t_{clog} - t_0)^2} \cdot (t - t_0)^2 + r_0 \right)$$

A

$$x_{HS}(x,t) = \frac{\dot{m} \cdot L \cdot t_0}{\rho \cdot \int_0^L \pi (r_e)^2 dx}$$

Ac

$$x_{HS}(x,t) = \frac{\dot{m} \cdot L \cdot t_0}{\rho \cdot \int_0^L \pi \left(r_0 - \frac{r_0}{(t_{clog} - t_0)^2} \cdot (t - t_0)^2 + r_0 \right)^2 dx}$$

Scheme 1. Explanation of how the final equation for $x_{HS}(x,t)$ is constructed using formula A and formula c, the latter explicitly expressing the time-dependence.

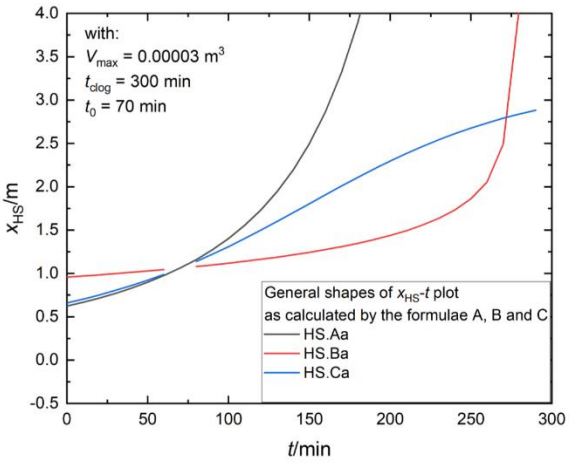

Fig. 5. Example plots for how a hot spot would move inside a constricting tubular reactor volume, using the equations from Table 5 (supporting information).

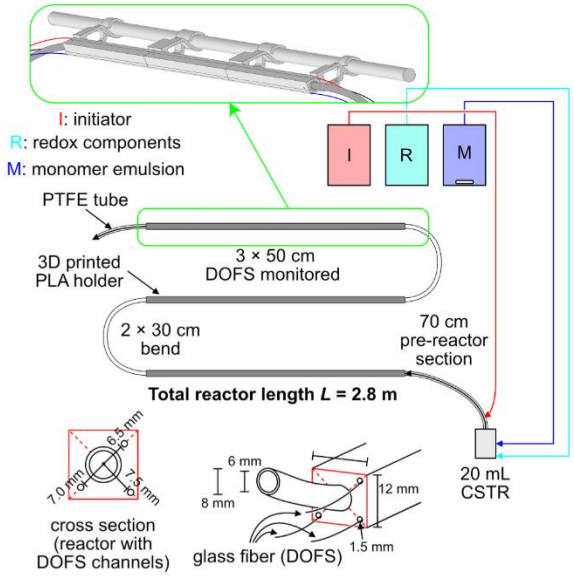

Fig. 6. Schematic of the experimental set up and reactor geometry.

Table 1
Overview over the feed streams for the emulsion polymerization with flow rates.

	Flow rate/ $\frac{g}{min}$	Components	Component flow rate/ $\frac{g}{min}$
Stream 1	5.6	vinyl acetate	1.729
		vinyl neodecanoate	0.192
		polyvinyl alcohol	0.134
		demineralized water	3.545
Stream 2	0.5	(L)-Ascorbic acid	0.038
		Ammonium-iron(III)sulfate-dodecahydrate	0.003
		demineralized water	1.890
Stream 3	1.9	tert-Butylhydroperoxide	0.019
		demineralized water	0.490

interference of the backscattered light with the incident light is used to create a spatial distribution of the signal (Zheng et al., 2021; Hartog, 2017). Any force that interacts with the fiber in a way to alter the backscattered light can be detected via the signal and located via the spatially distributed nature of the signal. For Rayleigh backscatter sensors, common measurands are strain and temperature, but dynamic forces such as vibration can also be measured. Fiber optics based sensors (FOS) are immune to electromagnetic interference and some corrosive substances metal is highly impacted by (Zheng et al., 2021; Hartog, 2017). Furthermore, they can be used to measure cryogenic temperatures and up to high temperatures of 1100 °C (Chen et al., 2022; Lu et al., 2017; Jones et al., 2022). Because of these attractive attributes, the technology has been broadly adapted in fields such as infrastructure integrity (Hartog, 2017; Bao and Chen, 2012), ground water measurement (Offerhaus et al., 2021), shape sensing (Xu and Khodaei, 2020), chemical sensing (Lu et al., 2019) and as thermometers in a few existing chemical reactors (Liu et al., 2022; Zhang et al., 2014; Egner et al., 2014). In the present publication the copolymerization of vinyl acetate and vinyl neodecanoate was carried out with DOFS (Distributed Optical Fiber Sensors) implemented along the reactor length in order to track the hot spot created by the unheated exothermal reaction. A redox-initiator system active at room temperature was used to confirm that the measured heat is chiefly created by the reaction. The location of the hot spot, correlating to the peak in Fig. 1, was tracked temporally and spatially using the DOFS. From the time-space plots, information about the fouling can be gained, using this non-invasive technique. The information pertains to the speed of the fouling formation via the volumetric loss in the reactor. The temporal location shift of the hot spot leads to deductions about whether the reaction is fouling primarily at the front, the back, or evenly along the entire reactor surface. Furthermore, the empirical time of clogging can be calculated from the data gained with the DOFS measurement.

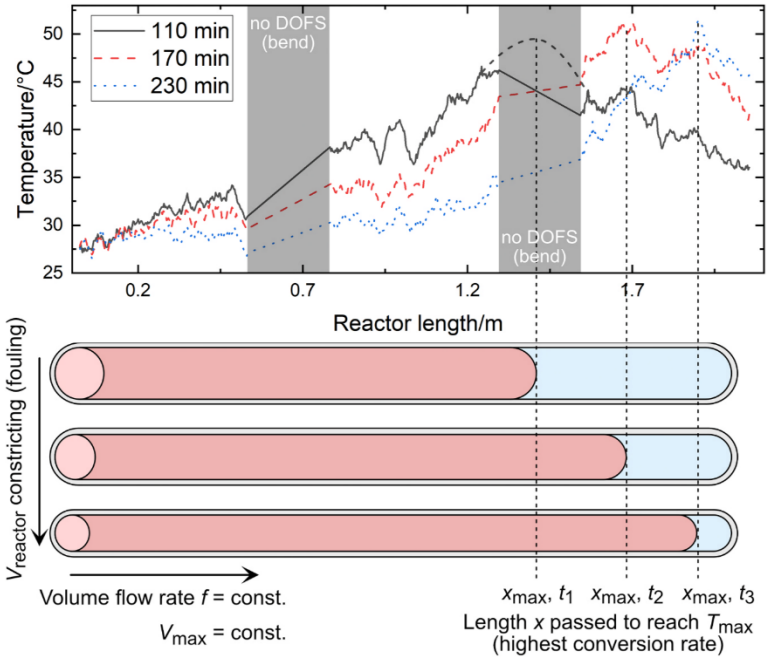

Fig. 7. Measured DOFS data, showing the downstream movement of the hot spot, and an illustration of how the volume loss due to fouling is assumed to relate to the movement.

2. Mathematical models for fouling monitoring using DOFS

Accumulating fouling mass constricts the available reactor volume V during reaction, which causes the hot spot (T_{max}) from the exothermal reaction to migrate downstream. This migration can be recorded using the DOFS. Assuming constant reaction kinetics through the entire duration of the reaction, then the time which a fractional volume of reaction mixture needs in order to reach its maximum temperature is also constant. In reality, this is not the case, as the reaction progress, heating of the surrounding reactor and heat conduction along its length all factor in to change the speed of reaction along reaction path. How far along reactor length x_{HS} (HS = Hot Spot) this fractional volume travels depends on the volume flow rate and the available cross sectional area A. Non-uniform fouling along the reactor axis x will lead to A changing along the axis. Given a circular geometry, this change can be shown by varying the radius of the free tubular volume with the function $A = \pi(r(x,t))^2$.

The fouling accumulates over time, and therefore, A is also a function of time. This is expressed by defining $r(x,t)$ with the help of a nominative radius. In the case of outlet-fouling, this is the end radius r_e, and in the case of inlet fouling this is the inlet radius r_i. Four different geometries, shown in Fig. 2, were explored. The initial radius of the tubular reactor $r_0 = 3mm$ is modified along the reactor axis using the nominal radius, the reactor length $L = 2.8m$ and the form of function. The nominal radius is defined as a function of time. In Fig. 4 the temporal functions $r_{e\ or\ i}(t)$ are shown.

The four functions $r(x,t)$ in Fig. 2 encompass tube radius constriction, linear outlet radius constriction, linear inlet radius constriction and parabolic outlet radius constriction. The functions are abbreviated with A, B, C and D respectively.

Epstein distinguished three types of fouling via the rate at which fouling mass accumulates: linear, falling rate and asymptotic (Epstein, 1983), which are shown in Fig. 3. As fouling increases and the effective cross-sectional area of flow shrinks, the flow velocity and shear rate increases. If the fouling material removal and slowing of deposition due to this is significant, then a falling fouling rate will be observed. If the deposition and removal approach an equilibrium, an asymptotic fouling rate establishes (Welzel and Nieken, 2024).

The fouling mass m_f can be expressed with the fouling volume V_f using the density of the fouling precipitate. The volume $V_f = L \bullet A(x,t) = L \bullet \pi \bullet r(x,t)^2$ is a parabolic function of the radius $r(x,t)$. For a linear increase of V_f with time, $r(x,t)$ would have to follow a square root function. A falling fouling rate could be expressed as a parabola, and therefore a linear change of $r(x,t)$ would be used in that case. The cases shown by Epstein are idealized, and therefore $r(x,t)$ was explored with more than a square root and a linear relationship with the time. In Fig. 4, models for the decrease in end radius are defined. The linear, the parabolically decelerating, the parabolically accelerating decrease, and the square root decrease, are respectively abbreviated as a, b, c and d.

2.1. General volumetric approach

In Eq. 1 the calculation of x_{HS}, the position of the hot spot (HS) along the reactor length, in dependence of the volume flow $\dot{V}$ and the cross-sectional area A, is shown.

$$x_{HS}(x,t) = \frac{\dot{V} \bullet t_0}{A(x,t)} \tag{1}$$

Because A changes along the reactor axis with fouling present, it can be expressed as $\frac{V}{L}$ with V being the reactor volume and L the reactor length. The volume flow can be expressed as the mass flow $\dot{m}$ (in the presented experiments $\dot{m} = 0.008\ \frac{kg}{min}$), using the density of the reaction mixture ρ (calculated for the presented system $\rho = 9840\ \frac{kg}{m^3}$), resulting in Eq. 2.

$$x_{HS}(x,t) = \frac{\dot{m} \bullet L \bullet t_0}{\rho \bullet V(x,t)} \tag{2}$$

The reactor volume can be calculated from the functions shown in Fig. 2 and with them as base the functions for rotational solids

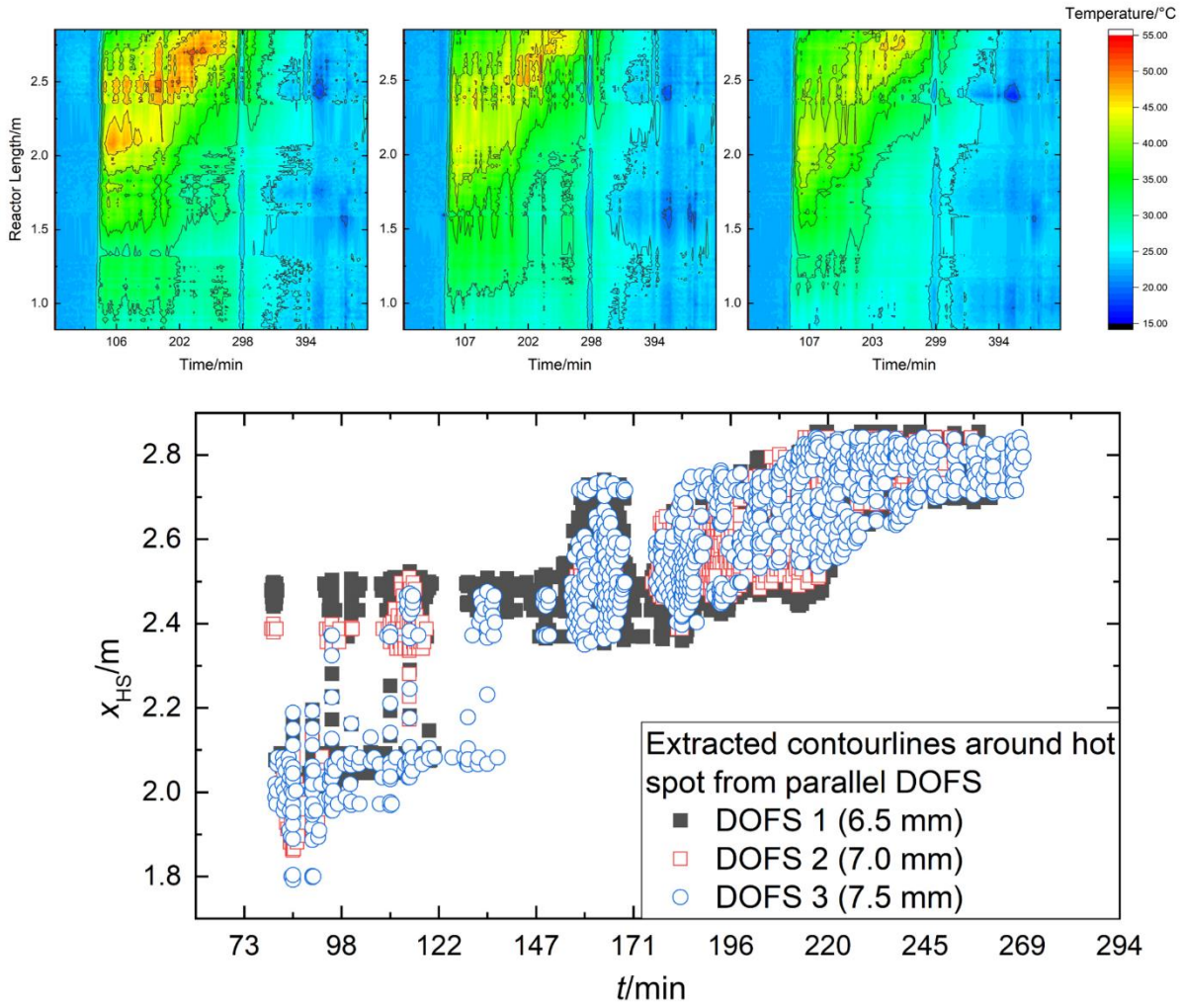

Fig. 8. Contour plot heatmaps of the parallel measurements of DOFS during a reaction and extracted contour data, showing good spatial-temporal agreement between the three DOFS.

describing the unfouled reactor volume, Eq. 3 is formulated. The rotational solid along the reactor axis with the start and end conditions 0 and L, is written as the integral in the equation.

$$x_{HS}(x,t) = \frac{\dot{m} \bullet L \bullet t_0}{\rho \bullet \int_0^L \pi(r(x,t))^2 dx} \quad (3)$$

In order to express the time-dependence of V, the functions shown in Fig. 4 can be used to substitute r_e or r_i in the functions from Fig. 2. This approach considers the entire reactor volume, and not just the volume leading up to the hot spot T_{max}. Therefore, if a clog presents itself downstream from the hot spot, the model will be able to calculate it. In Table 1 in the supporting information an overview over the combinations of formulas is given. General volumetric approach is abbreviated using GV in the following to distinguish it from the hot spot tracking approach.

The construction of the GV.Ac model is shown in the following scheme. The GV approach is used, which considers the entire volume of the reactor, therefore GV is mentioned in the model's name. The reactor volume is assumed to be constricting along its entire axis evenly, following formula A. The end radius, which is defined as the overall tube radius in formula A, is constricting over the course of the reaction time is a manner following the parabolic formula shown as formula c. These considerations are summarized in the moniker GV.Ac.

After the formulae are inserted in this way, and integration has been carried out, the equations were rearranged to describe x_{HS}, and the constants were summarized in the variables D, E, a, b, c, d, e and f. These variables are defined underneath the formulae in the following tables and are not to be confused with any existing mathematical and physical variables. Scheme 1

After validation, the tool integralrechner.de, created by David Scherfgen, was used to derive stem functions (Scherfgen, 2025). An overview of all final functions can be found in Table 1 in the supporting information.

2.2. Hot spot tracking approach

The volume past the hot spot's position does technically not influence the distance x_{HS} directly, unless there is a clog downstream. Given the assumption that a clog will not form downstream, the following mathematical modeling approach can be used. It should be able to

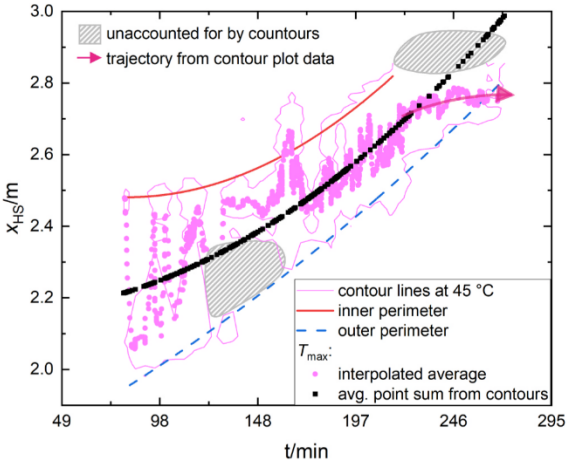

Fig. 9. Extraction of the hot spot position data from the DOFS data, using the contour lines from the heatmaps.

Table 2
HS-Fit parameters and coefficient of determination for the three runs' parabolically extrapolated data.

		Run 1	Run 2	Run 3
HS.Ac	D/m^3	$2.02\cdot10^{-5}$	$1.36\cdot10^{-5}$	$1.91\cdot10^{-5}$
	$a/\frac{m}{min^2}$	$-1.21\cdot10^{-8}$	$-1.50\cdot10^{-8}$	$-1.11\cdot10^{-8}$
	R^2	0.97205	0.94896	0.96422
HS.Ad	D/m	2.88	1.88	2.69
	a/min	619	426	577
	R^2	0.99734	0.99215	0.99952
HS.Ba	D/m^2	$2.13\cdot10^{-5}$	$5.75\cdot10^{-5}$	$2.02\cdot10^{-5}$
	$a/\frac{m}{min}$	$-5.14\cdot10^{-6}$	$-8.88\cdot10^{-7}$	$-5.42\cdot10^{-6}$
	b/m	$-1.37\cdot10^{-4}$	$2.07\cdot10^{-4}$	$-1.83\cdot10^{-4}$
	c/m	$1.37\cdot10^{-4}$	$-1.28\cdot10^{-3}$	$1.83\cdot10^{-4}$
	R^2	0.99851	0.99686	0.98729

describe the movement of the hot spot more precisely than the general volumetric approach but may struggle accurately calculating t_{clog}.

$$V_{max} = \pi \bullet \int_0^{x_{max}} (r(x))^2 dx \quad (4)$$

In Eq. 4, the reactor volume from inlet to x_{HS}, V_{max}, is calculated from the base functions shown in Fig. 2, using x_{HS} as the upper integration limit. $x_{HS,0}$ and $V_{max,0}$ denote the position and the volume passed by a fractional volume from inlet to that position, at t_0. After integration and solving for x_{HS}, the resulting equations are shown in Table 5 of the supporting information. Substitutions with variables are carried out, to summarize the formulas and enable analytical fitting using Origin 2012 by OriginLab. The abbreviation HS stands for Hot Spot tracking approach. An overview of all equations resulting from the formula combinations can be found in Table 5 of the supporting information.

The equations from Table 1 and 5 from the supporting information are set up to be valid between t_0 and t_{clog}. The formulae A, B and C define the general shape the $x_{HS}(t)$ plot can take, while the implementation of a, b, c and d modify these shapes to describe the real data better.

Given the knowledge about the general shapes caused by fouling depicted in Fig. 5, with A: the same along the entire length of the reactor, B: primarily building at the end of the reactor or C: primarily building at the front of the reactor, a given reaction can be sorted into one of these three categories.

3. Experimental section

A depiction of the reactor setup, the sensors and the pumps can be seen in Fig. 6. The two monomers vinyl acetate and vinyl neodecanoate (Versa10®) were used as a 9:1 mixture, with a total monomer concentration of 24 w% regarding the total reaction mass. An emulsion was created from the monomers and polyvinyl alcohol (PVA) (Mowiol® 4–88; degree of hydrolysis of 4–88 %; molecular weight ~31 kDa) with a PVA concentration of 7 w% regarding monomer weight. Vinyl acetate, vinyl neodecanoate and PVA were purchased from Wacker Chemie AG, Burghausen. L(+)-ascorbic acid, purchased in analysis grade from Carl Roth, and ammonium-iron(III)-sulfate-dodecahydrate, purchased in analysis grade from Merck, were used to start the reaction, together with the initiator. The initiator was tert-butyl hydroperoxide, purchased as a 70 w% solution in water from Thermo Fisher Scientific. The redox initiator system was used with 1:1:0.3 molar ratio of ascorbic acid to tert-butyl hydroperoxide (t-BHP) to ammonium-iron(III)-sulfate, with 1 w% of tert-butyl hydroperoxide in regard to the monomer. Table 1 shows the flow rates of the reaction mixture's components. All solutions were degassed for a minimum of 3 h with a low stream of nitrogen before reaction. For the monomer emulsion, the demineralized water and the monomers were degassed separately and then combined under nitrogen counterflow, and the PVA was added. This was done to prevent excessive bubble formation. The mixture was stirred (500 rpm) overnight on a hotplate set to 30 °C. The next day, the emulsion had formed. The resulting emulsion can sit for roughly 10 min unstirred, before any visible separation takes place. Reemulsification after separation is much easier than the initial formation of the emulsion, because the PVA is already in solution. During reaction, the emulsion is constantly stirred at 100 rpm. Before and after reaction, the solid content of the monomer emulsion was tested using microwave gravimetry, to confirm that the contents were used uniformly, and no creaming had occurred.

ProMinent gamma-X series diaphragm pumps were used for all flows. Due to the low flowrates, stroke length from 15 % to 20 % were used. The dosing tubes were made from PTFE and had an inner radius of 2 mm. In Fig. 6 these tubes are signified by the colored arrows leading from the vessels to the CSTR. After the T-connection with the initiator line, the radius of the single outgoing tube is 3 mm.

The continuous emulsion polymerization reactor, comprised of a PTFE tube and three DOFS sensors inside a 3D printed PLA holder (100 % infill, 4 mm nozzle, Ultimaker 2 + Extended, printed it a total of 9 parts), is shown in Fig. 5. The three reactant feeds are for the initiator (I), the redox components (R) and the monomer emulsion (M). The feed compositions are shown in Table 1, together with the feed rates. The redox initiator system was chosen to allow polymerization at room temperature (Jacob et al., 2022). Therefore, the measured temperature rise can be traced back purely to the chemical reaction. The reactant emulsion's stability is of great importance, because the considerable reactor length and the low flow rate result in a hydrodynamic residence time of 10 min. The pre-emulsifying of the monomers with PVA and constant magnetic stirring of the feed stock aided in the stabilization. In a 20 mL steel CSTR with two inlets and one elevated outlet, the redox components, having formed the active species Fe^{2+}, are being mixed with the monomer emulsion. The CSTR is stirred magnetically with a 1 cm rod at an rpm of 800. The initiator is added to the feed stream via a junction shortly after the outlet of the CSTR. More on the initiator system, as well as the polymerization reaction, can be found in the work of Jacob, Pauer and Schroeter (Jacob et al., 2022). Before any reaction, the entire system was flushed with nitrogen. All flows were turned on simultaneously at the beginning of the reaction, but the initiator stream was replaced with demineralized water. After the flow was established and the solid content collected at the end of the reactor correlated with the expected value at zero percent conversion, the initiator flow was switched from water to the t-BHP solution.

The entire length passed by the reaction mixture from the CSTR to the outlet encapsulates the pre-reactor section, the three DOFS moni-

Table 3
Calculated time of reactor clogging t_{clog}, and volume used by the reaction from inlet to hot spot before fouling $V_{max,0}$.

	t_{clog}/min $V_{max,0}$/m^3	Run 1	Run 2	Run 3
Empirical	t_{clog}	218	273	244
	$V_{max,0} \cdot 10^{-5}$	5.37	4.78	5.94
GV.Aa	t_{clog}	1030	534	851
GV.Ab	t_{clog}	2140	1176	1917
GV.Ac	t_{clog}	222	138	208
GV.Ad	t_{clog}	451	323	419
GV.Ba	t_{clog}	133	12	83
GV.Bb	t_{clog}	-63536	201	194
GV.Da	t_{clog}	725	366	1039
GV.Db	t_{clog}	201	282	187
GV.Dc	t_{clog}	477	457	517
HS.Ac	t_{clog}	487	448	519
	$V_{max,0} \cdot 10^{-5}$	6.34	4.28	6.00
HS.Ad	t_{clog}	279	161	262
	$V_{max,0} \cdot 10^{-5}$	8.15	5.32	7.61
HS.Ba	t_{clog}	611	3146	587
	$V_{max,0} \cdot 10^{-5}$	6.26	1.68	5.93
Color coding Deviation	< 10 %	< 20 %	< 50 %	< 100 %	< 200 %	< 300 %

tored sections inside 3D printed holders, and two unmonitored bends. This length is $L = 2.8$ m, the total reactor length. The inner radius of the PTFE tube is $r_0 = 3$ mm. The PLA holder provides channels for the tubular reactor and the three simultaneously operating DOFS to be secured and measured. In Fig. 6 a 3D view of the reactor, the DOFS inside the PLA holder, and the steel rod it is all mounted to, is shown.

The three DOFS were assembled in-house from single mode polyimide clad glass fiber (9 µm Ge-doped silica core, 125 µm cladding, 145 µm coating), purchased from ThorLabs, pigtails and index-matched glycerol-water mixtures as termination (Klippert and Pauer, 2024). The ODiSI-B (Optical Distributed Sensor Interrogator) from Luna Tec. was used to interrogate the fibers. In order to measure multiple fibers simultaneously, a custom software was created on the basis of C+ +.

4. Results and discussion

The spatial resolution of the DOFS allowed for hot spot tracking along the reactor length. The three DOFS in the channels parallel to the reactor were averaged. In Fig. 7 the temperature maximum is indeed moving downstream over time. Furthermore, the problem introduced by the two DOFS-free reactor bends is illustrated. An approach to overcome this will be described.

In Fig. 7 it is indicated that the gaps are covered by a line from the last point before, and the first point after it. The hot spot as shown in Fig. 8 is affected by the last gap ($x_{HS} = 2.1$–2.4 m), which is covered with a linear section, and the end of the reactor as cut off points for the data. The data collected by the three parallel DOFS during one reaction is shown below in Fig. 8. Extraction of the contour data for areas of high temperatures (45–52 °C, contour plot and contour extraction via Origin 2012 by OriginLab) yields the data shown underneath the three heatmaps. Because a strong rise in temperature correlates to outlines being closer together, clustering of the data points shows where the hot spot is. The three DOFS each indicate the same position for the hot spot. The exact temperature of it is of less importance to the following mathematical operations, and therefore it is viable to summarize the data from the three DOFS to create a large, single data set.

The impact of the two bends and the reaction leaving the detectable DOFS length is explored in Fig. 9. Shown is the heatmap contour data for one DOFS. The contours at 45 °C are shown (pink), as well as the average position of the hot spot as derived from the summation of all contours from 45 to 52 °C, and a subsequent 10 point sliding average operation (pink dots). The hot spot is located between the outer borders signified by the contours at 45 °C. Due to the borders passing through the bends the hot spot's position, as derived from the pink dots, is overestimated in

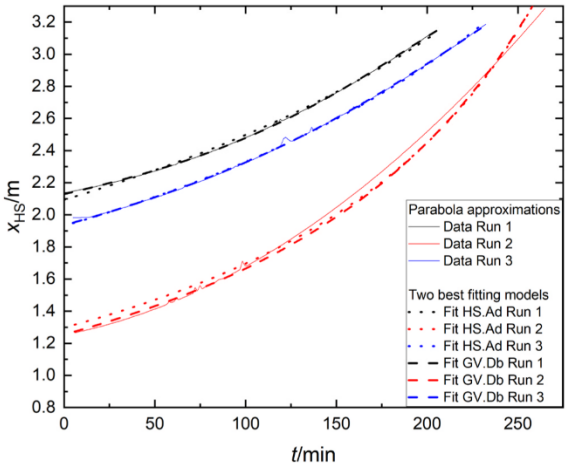

Fig. 10. Shown here are the two models GV.Db and HS.Ad, which best describe the data extrapolated from the parabolas, fit to the inner and outer perimeter of the contour plots, alongside the data they are modeled to.

the downstream direction, when the hind border is not measured (t = 125–160 min). When the reaction is leaving the reactor, the front border is not measured (t = 210 min onwards). Therefore, the hot spot's position is underestimated. This trend in particular is shown with the pink arrow in Fig. 9. In the gray hatched areas measurement points are missing due to the borders entering and leaving the gap region. In order to solve this problem, the inner and outer perimeter of the contour lines (fit for inner perimeter with R^2 = 0.7910, fit for outer perimeter with R^2 = 0.9738) have been used to fit parabolic functions onto them. By interpolating the calculated data from the functions, the middle parabola is created, shown in Fig. 9 with black spots.

It can be seen that the shape of the plot derived from the fits for the inner and outer perimeter of the hot spot region (black squares) is most closely following the curve of formula A, as shown in Fig. 5. This already points to the possibility, that the reactor may be fouling evenly along the length directly influencing the hot spot.

The mathematical models shown in Table 1 and 5 (supporting information) have been fitted to the interpolated parabola shown in the lower part of Fig. 8. Because both sets of data produced similar results, only the results for the parabolas will be discussed in the following.

The starting parameters for the fit were calculated using the empirically estimated data for t_0, t_{clog} and $x_{HS,0}$. A complete overview of the starting parameters can be found in the supplemental materials. All variables were constrained to either negative or positive values, depending on their mathematical definition. In both categories, 0 was included. In the case of the GV models, all, but the GV.Bc equations yielded good to very good coefficients of determination R^2. For the HS models, the three equations with the best R^2 values are shown in Table 2, together with all parameters resulting from the fitting. Three repeat reactions were chosen to perform the fits on.

From the fitted parameters, the values of t_{clog} and $V_{max,0}$ were calculated. Table 3 shows the calculated values from all fits with good R^2. The color coding illustrates the deviation of the calculated values from the empirical ones.

Model GV.Ac, GV.Ad, GV.Db, HS.Ac and HS.Ad display the best agreement with the empirical values, which were measured directly during the experiments. The calculation of t_{clog} with GV.Ac results in underestimation by 22 % (± 20 %), when all runs are averaged. For GV.Ad, t_{clog} is overestimated by 66 % (± 36 %). In GV.Db, t_{clog} is underestimated with a deviation of 11 % (± 9 %). For HS.Ac, t_{clog} is overestimated by 100 % (± 25 %) and $V_{max,0}$ is overestimated by 10 % (± 7 %). Lastly, HS.Ad underestimates t_{clog} by 2 % (± 29 %) and overestimates $V_{max,0}$ by 30 % (± 17 %).

In summary, the best calculation of t_{clog} is possible using the models GV.Db or HS.Ad. The HS model was likely able to calculate t_{clog}, because the hot spot does actually leave the reactor before it clogs. In Fig. 10 the

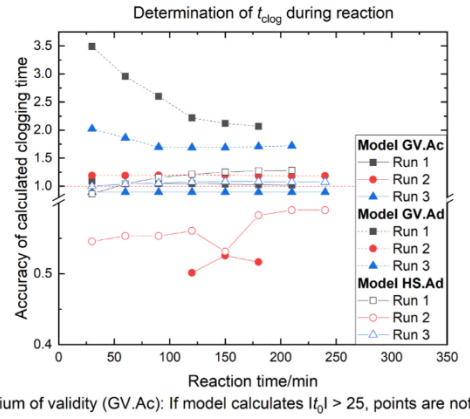

Fig. 12. Determination of t_{clog} using the models GV.Ac, GV.Ad and HS.Ad for the three reaction runs, as calculated as different points in time.

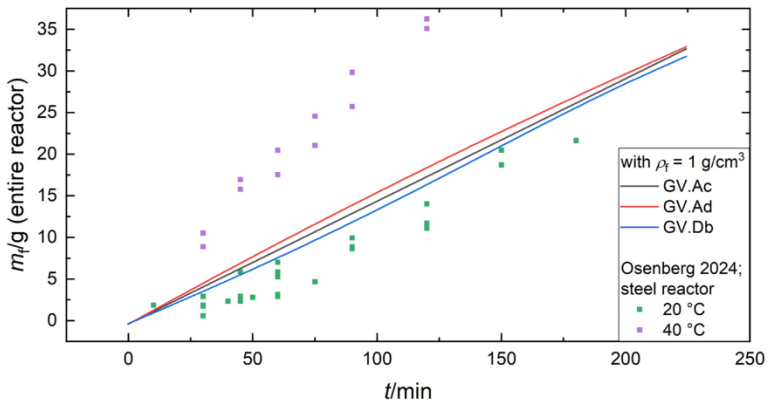

Fig. 11. Estimated mass of fouling m_f as calculated from the mathematical models GV.Ac, GV.Ad and GV.Db, normed to begin at 0 g, as well as literature reference from the same poly reaction carried out in another reactor under different conditions (Osenberg et al., 2022).

fitted models are shown alongside the extracted contour plot data.

Following Eq. 2, the fouling volume V_f is proportional to $\frac{1}{x_{HS}}$. This is underlined in Eq. 5. For the calculation of V_f, only the GV models were used, because only they calculate the entirety of the reactor, and not just until the hot spot.

$$V_f(t) = \frac{\dot{m} \bullet L \bullet t_0}{\rho \bullet x_{HS}(t)} \quad (5)$$

Epstein's fouling models were depicted in Fig. 3. From Fig. 11, it appears that the fouling exhibited by the explored reaction in a tubular reactor follows a linear rate. It was previously stated, how the change of the defining radius $r(x,t)$ dictates the type of fouling rate. A linear fouling rate requires $r(x,t)$ to be a square root function of the time. This is the case for model Ad. For the other two depicted models, $r(x,t)$ is a parabolic function of the time, therefore the fouling rate is a cubic function. Their shape in the examined region of the function is very close to linear. A constant fouling rate regarding the fouling in weight per minute, was found for the exact same reaction in a steel reactor with static mixers by Rust et. al in 2024. They also found that the fouling first forms at the end of the reactor, but by the end of the reaction, the entire reactor is fouled evenly. When examining the mechanism of the fouling process, Rust et al. determined in 2023, that the fouling mass correlated most with temperature and initiator concentration. It may therefore be assumed, that the fouling process is controlled by the radical concentration more, than by the affinity of the fouling material to the reactor wall material. With this assumption, it is possible, that similar trends were seen in a steel and in a PTFE reactor (Rust et al., 2024; Rust and Pauer, 2023). The observations from Rust et al. would fit model HS.Ad exactly. The fouling forming at the very end of the reactor first would not influence the hot spot much, as long as it is still far enough upstream. Klinkert et al. found a cubic dependence of the fouling mass with the reaction time, linking it to polymer and polymerization fouling (Klinkert et al., 2024). The same cubic shape can be seen in Fig. 11 for Model GV. Db, though stretched into a more linear shape. Klinkert et al. performed the same polymerization, but within a loop set up with a CSTR. The fouling was measured specifically in a channel through which material was pumped constantly. It may be that these different conditions allow the cubic character of the fouling rate to be more pronounced. For the presented experiments and the findings of Rust et al., the fouling rate is observed to be linear. In Fig. 11 data from Osenberg et al. is shown as reference, however they carried out the reaction in a steel reactor with temperature control and static mixers. The reported fouling mass is normalized to the mass of the mixing elements, which is sum is 117 g in the unfouled state (Osenberg et al., 2022). To estimate the fouling mass from the fouling volume V_f from the GV models, a density $\rho_f = 1$ g/cm^3 is assumed for the fouling, which is roughly between the density of polyvinylacetate product and the density expected from the reaction dispersion at 20 w% solid content (Hohlen et al., 2019).

The best models were tested for their potential as predictive algorithms, to be ran alongside a reaction and estimate the time at which the reactor will clog. Only models which converged on a certain value are presented in Fig. 12, these were GV.Ac, GV.Ad and HS.Ad. In this context, the difference between the runs 1, 2 and 3 is highlighted. In the x_{HS} plot shown in Fig. 10, the similarities between run 1 and 3 are visible, as are the differences to run 2. Models GV.Ac and HS.Ad determine t_{clog} for the two similar runs within a margin of error (0.89–1.28, 1 being in full agreement with the measured time) from the first 30 min after the start of the reaction. The t_{clog} for run 2, however is, is determined to be half as long as measured (0.50–0.59). Model GV.Ad calculates the t_{clog} for run 2 well and quick, only 30 min after the start of the reaction. The calculated values for the other two runs are two or three times too long (1.68–3.49). Overall, given the shape of the x_{HS} plot, determination of t_{clog} with one of the models GV.Ad or HS.Ad is possible from 30 min after the start of the reaction within a margin of error of 0.89–1.28. GV.Ac is disregarded, because t_{clog} values can be very wrong, if the fitting does not result in a prediction for $t_0 > 25$. This criterion allows for filtering of bad values, but the approach is not as consistent as the other two models. Following this, it is concluded that the models can determine t_{clog} in a predictive manner, but that further tests need to be carried out to improve the models and create a predictive algorithm.

5. Conclusion

Fouling monitoring via hot spot detection using DOFS (Distributed Optical Fiber Sensors) was carried out successfully. Three DOFS were implemented parallel to the reactor axis within a 3D printed holder to enable measurement. The position of the hot spot caused by the exothermal polymerization reaction within a tubular reactor, plotted against the reaction time, was examined mathematically. All runs of the polymerization reaction were not stopped before clogging occurred. Various models based on the physical shape the fouling within the reactor is expected to take, and the rate, at which the radius of the reactor is shrinking, were tested for agreement with the data.

Models describing the fouling as growing evenly along the entire reactor length were the most successful (formula A). Furthermore, an accelerating radius constriction, either in the form of a polynomial or a square root function, described the data best (formulae c and d). The models Ac and Ad described the hot spot-reaction time plot with an average coefficient of determination across all Ac and Ad models of 0.99 ($\pm$ 0.02) and were able to calculate the time of clogging. The best model (HS.Ad) agreed with the measured clogging times with a discrepancy of 2 % ($\pm$ 29 %).

The models were successfully used to determine the time of clogging for three reaction runs in a predictive manner starting as soon as 30 min after the beginning of the reaction (12 % of the reaction time from start to clogging). The calculation was accurate within 0.89–1.28, with 1 expressing perfect agreement with the measured data for the clogging time. Using the presented calculations as a starting point and with further experiments a predictive algorithm could be created to determine the time at which a reactor will clog during a particular run.

Funding

This work has been partially funded by the German Federal Ministry for Economic Affairs and Climate Action, Germany as part of the ENPRO Initiative (KoPPonA 2.0, FKZ: 03EN2004M).

CRediT authorship contribution statement

Klippert Maria: Writing – original draft, Visualization, Validation, Software, Methodology, Investigation, Formal analysis, Data curation, Conceptualization. **Pauer Werner:** Writing – review & editing, Supervision, Resources, Funding acquisition, Conceptualization.

Declaration of Competing Interest

The authors declare no conflict of interest.

Acknowledgments

The authors would like to thank the ENPRO initiative, particularly the members of the KoPPonA 2.0 project (ger. *Kontinuierliche Prozesse für Polymerspezialitäten mit Hilfe neuer Apparatekonzepte*, Continuous processes for polymerization with the help of new technological concepts) and Devon Martin.

Author contributions

W. P. has initiated and supervised the presented research and M. K. has carried it out, written the article and prepared the images. Both

authors have edited the manuscript.

Appendix A. Supporting information

Supplementary data associated with this article can be found in the online version at doi:10.1016/j.cherd.2025.02.012.

Data availability

The data that support the findings of this study are available from the corresponding author upon reasonable request.

References

Ardsomang, T., Hines, W.W., Upadhyaya, B.R., 2013. Heat exchanger fouling and estimation of remaining useful life. In: Proceedings of the Annual Conference of the PHM Society 2012, 5(1), doi: https://doi.org/10.36001/phmconf.2013.v5i1.2773.

Arhancet, G., 1998. Compositions and methods for inhibiting fouling of vinyl monomers. Wo 98/47593 29.

Bao, X., Chen, L., 2012. Recent progress in distributed fiber optic sensors. Sensors 12 (7), 8601–8639. https://doi.org/10.3390/s120708601.

Bernstein, C., 2017. Methoden zur Untersuchung der Belagsbildung in chemischen Reaktoren. Dissertation at University of Hamburg.

Böttcher, A., et al., 2016. Fouling pathways in emulsion polymerization differentiated with a quartz crystal microbalance (QCM) integrated into the reactor wall. Macromol. React. Eng. 16. https://doi.org/10.1002/mren.202100045.

Chen, C., Chen, L., Bao, X., 2022. Distributed temperature profile in hydrogen flame measured by telecom fiber and its durability under flame by OFDR. Opt. Express 30 (11), 19390. https://doi.org/10.1364/OE.455640.

Chern, C.S., 2006. Emulsion polymerization mechanisms and kinetics. Prog. Polym. Science 31 (5). https://doi.org/10.1016/j.progpolymsci.2006.02.001.

Deshannavar, U.B., Marappagounder, R., 2021. Revisiting threshold fouling models for crude oil fouling. Heat. Transf. Eng. 42 (17). https://doi.org/10.1080/01457632.2020.1800276.

D'hooge, D.R., Van Steenberge, P.H.M., Reyniers, M.-F., Marin, G.B., 2016. The strength of multi-scale modeling to unveil the complexity of radical polymerization. Prog. Polym. Sci. 58. https://doi.org/10.1016/j.progpolymsci.2016.04.002.

Dorton, M., Gardener, G., 2012. Process for removing polymeric fouling. p. US20120174948A1.

Egner, F., Bank, R., Bauer, A., Verbeek, D., Lainer, M., 2014. Fiber-optic temperature measurement in a catalyst material, U.S. National stage application US10173190B2.

Epstein, N., 1983. Heat. Transf. Eng. 4 (43), 43–56. https://doi.org/10.1080/01457638108939594.

Fang, R., et al., 2020. Methodology for removing fouling within liquid-filled pipelines based on ultrasonic guided waves cavitation effect. Appl. Acoust. 157. https://doi.org/10.1016/j.apacoust.2019.107018.

Fries, S., 2019. Modelling of fouling mechanisms in the LDPE synthesis, Thesis, Technical University of Darmstadt.

Grundmeier, G., et al., 2022. Thin organic-inorganic anti-fouling hybrid-films for microreactor components. Macromol. React. Eng. 17. https://doi.org/10.1002/mren.202200043.

Hannon, J., et al., 2005. Modeling fouling effects in LDPE tubular polymerization reactors. 1. Fouling thickness determination. Ind. Eng. Chem. Res. 44 (5). https://doi.org/10.1021/ie040157q.

Hartog, A.H., 2017. An Introduction to Distributed Optical Fiber Sensors. Taylor & Francis Group. https://doi.org/10.1201/9781315119014.

Hohlen, A., Augustin, W., Scholl, S., 2019. Quantification of polymer fouling on heat transfer surfaces during synthesis. Macromol. React. Eng. 14 (1), 1900035. https://doi.org/10.1002/mren.201900035.

Jacob, L.I., Pauer, W., Schröter, B., 2022. Influence of redox initiator component ratios on the emulsion copolymerisation of vinyl acetate and neodecanoic acid vinyl ester. RSC Adv. (22). https://doi.org/10.1039/D2RA01811J.

Jones, J.T., Sweeney, D.C., Birri, A., Petrie, C.M., Blue, T.E., 2022. Calibration of distributed temperature sensors using commercially available SMF-28 optical fiber from 22° C to 1000° C. IEEE Sens. J. 22 (5), 4144–4151. https://doi.org/10.1109/JSEN.2022.3146185.

Klinkert, A., Friedrich, Z., Glatt, E., Augustin, W., Scholl, S., 2024. Polymer versus polymerization fouling: basic deposition mechanisms during emulsion polymerization by the example of a vinyl acetate and versa 10 copolymer. Macromol. React. Eng. 18. https://doi.org/10.1002/mren.202300057.

Klippert, M., Pauer, W., 2024. Distributed optical fiber sensors for real-time tracking of fouling buildup for tubular continuous polymerization reactors. Chem. Eng. Res. Des. 211. https://doi.org/10.1016/j.cherd.2024.10.007.

Liu, Y., Si, X., Wu, L., Mo, C., Zhuang, Y., 2022. Reactor temperature measurement system, reactor and method for preparing a fiber bragg grating, European patent application EP000003945297A1.

Lu, X., Soto, M.A., Thévenaz, L., 2017. Impact of the fiber coating on the temperature response of distributed optical fiber sensors at cryogenic ranges. J. Light. Technol. 36 (4), 961–967. https://doi.org/10.1109/JLT.2017.2757843.

Lu, X., Thomas, P.J., Hellevang, J.O., 2019. A review of methods for fibre-optic distributed chemical sensing. Sensors 19 (13), 2876. https://doi.org/10.3390/s19132876.

Movsesian, N., Hirth, S., Speros, J., Gupta, M., 2020. Robust vapor-deposited antifouling fluoropolymer coatings for stainless steel polymerization reactor components. Ind. Eng. Chem. Res. 59 (34). https://doi.org/10.1021/acs.iecr.0c02646.

Murat, M.N., et al., 2022. Nonlinear control of fouling in polyethylene reactors. ACS Omega 7. https://doi.org/10.1021/acsomega.2c03078.

Offerhaus, H.L., et al., 2021. Comparison of three types of fiber optic sensors for temperature monitoring in a groundwater flow simulator. Sens. Actuators A: Phys. 331, 112682. https://doi.org/10.1016/j.sna.2021.112682.

Osenberg, M., et al., 2022. Ultrasound based fouling detection in polymerization processes. Sensors and Measuring Systems; 21th ITG/GMA-Symposium. VDE Verlag GmbH, Berlin, Offenbach.

Rammerstorfer, E., 2020. The kinetics and mechanisms of fouling in crude oil heat transfer. Heat. Transf. Eng. 41 (8). https://doi.org/10.1080/01457632.2018.1564202.

Rust, S., Osenberg, M., Musch, T., Pauer, W., 2024. Ultrasonic and conversion-based inline fouling measurements for continuous emulsion copolymerisation of vinyl acetate in a tubular reactor. Sci. Rep. 14, 4077. https://doi.org/10.1038/s41598-024-54321-4.

Rust, S., Pauer, W., 2023. Formulation and process determined fouling prediction for the continuous emulsion co polymerisation of vinyl acetate. J. Polym. Res. 30, 242. https://doi.org/10.1007/s10965-023-03588-8.

Scherfgen, D., Integralrechner, link: https://www.integralrechner.de (accessed Feb 2025).

Schroeter, B., 2018. Kinetik von Redoxinitiatoren für die Emulsionspolymerisation, Dissertation at. University of Hamburg, pp. 161–166.

Tong, D. Y., 2015. Reducing polymer fouling and agglomeration in acrylate/methacrylate processes. US 2016/0102189 Al.

ur Rehman, O., et al., 2023. Modeling strategies for crude oil-induced fouling in heat exchangers: a review. Processes 11 (4). https://doi.org/10.3390/pr11041036.

Urrutia, J., Asua, J.M., 2021. Reactor fouling in emulsion polymerization. Ind. Eng. Chem. Reserach 60. https://doi.org/10.1021/acs.iecr.1c00097.

Watkinson, A.P., Wilson, D.I., 1997. Chemical reaction fouling: a review. Exp. Therm. Fluid Sci. 14 (4). https://doi.org/10.1016/S0894-1777(96)00138-0.

Welzel, S., Nieken, U., 2024. Fouling during polymerization in different continuous reactor setups. Chem. Ingeneur Tech. 96 (12). https://doi.org/10.1002/cite.202400086.

Xu, C., Khodaei, Z.S., 2020. Shape sensing with Rayleigh backscattering fibre optic sensor. Sensors 20, 4040. https://doi.org/10.3390/s20144040.

Zhang, Y., Song, L., Kaiser, G., Hergenrother, M.L., Stober, B.K., Kalamaras, P.H., Umansky, B.S., 2014. Method and system for determining flow distribution through a component, U.S. National Stage Application US9746434B2.

Zheng, H., et al., 2021. Distributed optical fiber sensor for dynamic measurement. J. Light. Technol. 39 (12). https://doi.org/10.1109/JLT.2020.3039812.

6.3. Spatially resolved reaction calorimetry and fouling monitoring in a continuous tubular emulsion polymerization reactor

Maria Klippert, Werner Pauer

Synopsis:

The previously discussed reaction setup and recipe was used in order to attempt calorimetric calculations using the DOFS data. For DOFS inline calibration and then calibration of the measured heat flow, heated water was conveyed through the reactor at a constant flow rate. Due to no addition of heat in the reactor setup, the sinking temperature of the water throughout the reactor could be linked directly to the heat loss through the wall. The temperature of the water instream was monitored in six places by thermocouples and three DOFS were positioned in the walls. The axially transported heat was calculated from the instream measurements, the constant flow rate and the heat capacity of water. The temperature differences between the DOFS were used to calculate heat loss through the wall. The calculated raw values could be correlated with the heat loss calculated from the instream measurements with a linear function. After this correlation, heat losses (from 2 to 9 W) for water heated to different initial temperatures could be calculated with an accuracy of 0.39 W.

In the first chapter of the cumulative part of this dissertation, it was mentioned that a temperature accuracy of 0.1 °C for a DOFS in a 20 cm long reactor was possible. For the longer reactor with multiple bends exerting strain on the DOFS, this figure had to be corrected towards a value to 0.5 °C. DOFS temperature measurements are always relative. Therefore, accurate calibration is of utmost importance to be able to compare the data from multiple individual DOFS. Due to the spatially resolved nature and high dependence of the calibration coefficients on the surrounding media (introduced strain from the DOFS channel and bends, interaction with the aluminium particles and glycerol in the thermal paste, moisture from the air, solvent vapors etc.) this calibration could not be carried out to a high degree of accuracy. As a result, the temperature differences between the DOFS and calculated heat flow do not result in spatially resolved heat flow data, as the errors are too large in size and number. However, the lengthwise summation of the heat flow data, resulting in the overall heat loss through the wall during reaction progress or calibration process, exhibited systematicity. As the DOFS were all in the same system at the same time, their responses are correlated with the temperature changes in this system. It is therefore not an unlikely coincidence, but a systematic and physical result, that the summation of their signal can be used to monitor the system itself. This is the way in which

the heat losses for the entire reactor length were calculated for the experiments with heated water during calibration, and later during the copolymerization.

The axial temperature profile was monitored using six thermocouples. The spatial resolution instream was much lower than in the walls (42 cm and 0.26 cm respectively). This meant, that the hotspot's maximum was always monitored from within the walls when it was inside the three horizontal reactor parts equipped with DOFS but instream its position and exact maximum temperature could only be picked up by the thermocouples for a maximum of six times during the reaction. During any other times, the maximum temperature of the hotspot was not recorded instream. The calculated axial heat transfer was therefore too low for all times except the ones where hotspot and a thermocouple align.

The calculation of the heat released by the reaction was carried out by summation of axial and radial heat transfer, meaning thermocouple data and DOFS data. By doing this and comparison to the theoretical maximal released heat at 100 % conversion, the calculated thermal conversion reached a maximum value of 79 % ± 3 %, meaning that a heat flow of 35.3 W was measured. The gravimetrical conversion during that reaction time reached 78 % ± 2 %. The two conversions agree well.

Outside the times when the hotspot aligned with a thermocouple and generally towards the end of the reaction, the thermal conversion was below the gravimetrical conversion. This can be explained by the low spatial resolution of the instream temperature measurement and the fact that the outlet of 70 cm past the last monitored reactor section allowed for more conversion. The samples for gravimetrical conversion monitoring were collected at the end of this outlet portion.

Spatially resolved reaction calorimetry and fouling monitoring in a continuous tubular emulsion polymerization reactor

Journal:	*Industrial & Engineering Chemistry Research*
Manuscript ID	ie-2025-025489.R2
Manuscript Type:	Article
Date Submitted by the Author:	n/a
Complete List of Authors:	Klippert, Maria; Universität Hamburg, Chemie Pauer, Werner; Universitat Hamburg, Chemie

Spatially resolved reaction calorimetry and fouling monitoring in a continuous tubular emulsion polymerization reactor

Maria Klippert and Werner Pauer*

Institute for Technical and Macromolecular Chemistry, University of Hamburg, Bundesstraße 45, 20146 Hamburg, Germany

* Correspondence: werner.pauer@uni-hamburg.de

1. Abstract

A modular flow reactor setup for the continuous emulsion copolymerization of vinyl acetate and vinyl-neodecanoate has been fitted with Distributed Optical Fiber Sensors (DOFS) based on Rayleigh backscatter and instream thermocouples. After segment-wise calibration of the DOFS for temperature measurement, they were used as sensors for online thermal analysis in the reactor. Calorimetric analysis and thermal conversion determination was conducted online during the reaction using the DOFS as spatially distributed temperature sensors which span the length of the reactor. Three DOFS in the reactor wall at different diameters enable the quantitative calculation of the thermal energy transferred between the DOFS and therefore determine the heat transport through the reactor wall. In experiments with heated water, the radial heat loss for reference values from 2 to 9 W could be determined with an accuracy of 0.39 W.

The sensor equipped tubular reactor (length 1.95 m) was used for the emulsion copolymerization of vinyl acetate and vinyl-neodecanoate with a redox initiator reactive at room temperature. The quick and intense fouling process of the reaction could be reflected in the thermal measurements. From the immediate shifting of the reaction hotspot (length of highest monomer conversion) downstream, it could be deduced that the chosen reaction does not have an induction period pertaining to fouling. The broadness of the hotspot and the maximum hotspot temperature T_{max} could be monitored during reaction. Due to the fouling constricting available reactor volume at constant feed rate, the hotspot became broader with time and T_{max} dropped. The drop of T_{max} could be tracked especially well with the DOFS in the wall, in comparison to the thermocouples in stream, and is deduced to be a useful parameter for fouling monitoring. The heat released from the reaction was calculated using the thermocouples instream for axially transported heat and the DOFS for radially transported heat. It could be seen clearly, that during the times T_{max} was not aligned with one of the six

thermocouples, the axial heat was estimated as too low. The radial heat measurement had a high spatial resolution of the DOFS (0.26 cm) and always captured T_{max}. During good alignment of T_{max} and one of the six thermocouples, the calculated total reaction heat was 35.3 W, or a 79 % ± 3 % monomer conversion. This correlates well with the gravimetrical conversion measurement, averaging 78 % ± 2 % conversion for that timeframe in the range of 8 to 16 dimensionless residence times.

2. Introduction

Vinyl acetate copolymers are widely used in the formulation of water-based coatings and adhesives. Comonomers are used to improve film formation characteristics and reduce material degradation due to reaction with moisture.[1] The copolymerization with vinyl-neodecanoate can be carried out in emulsion and without the use of a high-pressure reactor, making this comonomer an attractive choice. Emulsion polymerization product can be used as-is for formulating coatings and adhesives, and the presence of water as the continuous phase allows for intense heat removal.[2,3]

For emulsion polymerization the monomers are suspended in a continuous aqueous phase with the help of a stabilizer. In the presented case polyvinylalcohol (PVOH) is used for this purpose. The redox-initiator system enables the creation of radicals at low reaction temperatures.[4,5] In Figure 1, an overview of the reactions and processes underlying the emulsion copolymerization of vinyl acetate with vinyl-neodecanoate is presented.

It has been shown, that PVOH strongly affects the resulting polymer microstructure and that grafting is confirmed to happen,[2] The reaction kinetics are affected by the stabilizer, as transport of radicals and monomer through the outer layer of monomer droplets and growing polymer particles is directly influenced, and reaction with PVOH itself is present. The radical formation from the initiator system occurs in the aqueous phase, therefore the start of the polymerization chain reaction is also likely to happen there. The growing chains become less soluble and polymer particle nucleation occurs. Once the reactive particles are formed, the reaction progresses in the growth phase, where monomer transfers into the growing particles until it is used up. Multiple radicals are likely to recombine and stop the chain reaction, therefore each active particle has a limited number of growing centres. With increasing chain length, the movement of the polymer chains becomes more hindered and with depleting monomer reserves, the reaction slows. Finally, the particles are starved of monomer and the chains terminate.[2,3,6]

The rate of radical creation and polymerization are strongly influenced by temperature.[4,5] The self-heating and accelerating chain reaction must be controlled for safe operation. During and after the reaction the polymer particles can interact with each other. The stabilizing steric forces can be overcome, and coagulation occurs. This can destabilize the suspension and cause precipitation of solid mass.

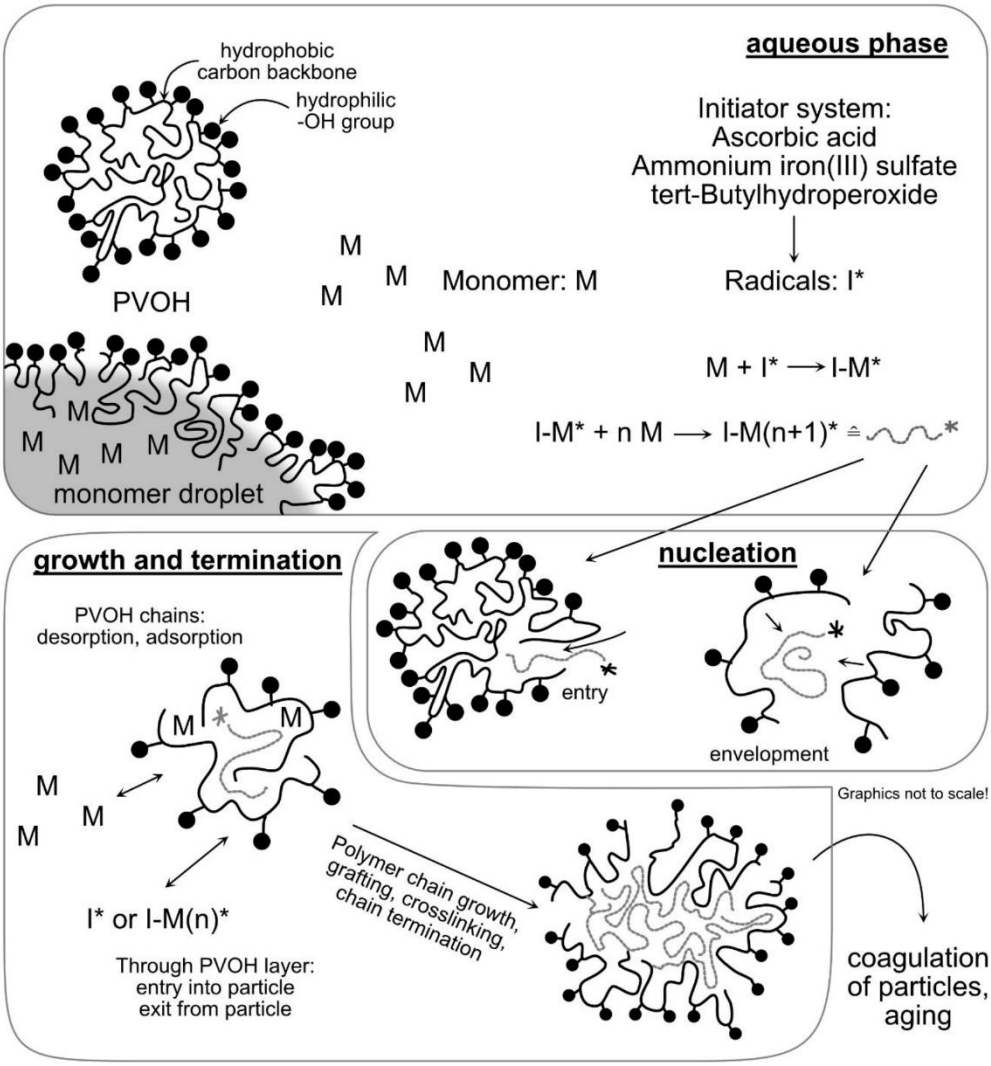

Figure 1: Schematic of the emulsion copolymerization of vinyl acetate and vinyl-neodecanoate with PVOH as the stabilizer and the redox-initiator system.

The large-scale use of emulsion polymerization products and the exothermicity of the reaction lend themselves to continuous production. Process intensification by synthesis of product in a

continuous reactor with built-in monitoring, temperature control and process optimization is an industrial goal. At the moment, emulsion polymerization is most carried out in batch processes due to them being well-researched and the fouling accumulation.[7,8,9]

When a reaction is transferred from batch to continuous reactor, reaction kinetics and selectivity can change. Reaction calorimetry is used to investigate this, as well as safety. Continuous calorimeters are uncommon and only few exist on the market.[10] Such analytical capabilities are important for process safety and optimization, as it has been shown that the measured heat of reaction for non-selective reactions can differ substantially from the values obtained by batch calorimetry.[11]

Continuous reaction calorimeters which can be found on the market or in literature employ either a series of point sensors or a temperature measurement system covering an area, such as Infra-Red (IR) thermography. Thermoelements or Seebeck elements are most commonly used to measure temperature or heat flux respectively.

An early iteration of a continuous (micro)reactor outfitted with a series of thermocouples for calorimetric and kinetic analysis can be found in 2005.[12] Following publications continued using a microreactor and employed Seebeck elements and IR thermography.[10,13,14] The first meso-fluidic continuous reaction calorimeter was published in 2017, using a series of 10 thermocouples along a 51 cm reactor. The data was iteratively processed by using heat balance equations.[15] The reactor set up and computational approach was further developed in the same year.[11] A 3D printed modular continuous reaction calorimeter employing both thermocouples and Seebeck elements was published soon after.[16] Another approach to continuous reactor calorimetry involved placing the entire reactor in a batch calorimeter.[17]

In an ideal continuous tube reactor, the axial position correlates to the reaction progress, or the reaction time in an ideal batch stirred tank reactor. In the latter time resolved temperature measurement can be carried out by implementing a temperature sensor and logging the data. From this, temperature profiles of the main reaction and possible side reactions can be created. The corresponding measurement in a continuous tubular reactor is the spatial temperature profile along the reactor length. This is the reason why a series of point sensors or another kind of spatially distributed measurement along the reactor is often employed to gain the data needed for calorimetric calculations in a continuous setup. Figure 2 illustrates this for an exothermal reaction with passive cooling (room temperature RT). For this mode of operation, the reaction self-heats until a point is reached where the produced heating rate equals the removed heating

rate. Onward, the mixture's temperature decreases. In steady state, this progression can be seen along the x-axis of an ideal tubular reactor.

The copolymerization reaction presented in this publication is a self-heating reaction and the cooling is realized via passive convection. The rate of heat production has been shown to increase at higher temperatures, as the reactions progress faster.[4,5] Due to the passive cooling a faster heat generation results in a higher temperature maximum. In the case of the discussed polymerization, higher temperatures result in higher rates of fouling.[18] It may be the case that the particle suspension is destabilized at higher temperatures and precipitate is formed on the reactor walls. It can be deduced, that more fouling will be formed at and after the region of the hotspot. Due to the volume taken up by the precipitate, the reactor volume shrinks. This is expected to cause the residence time to decrease and therefore push the temperature maximum downstream. With it, the profile of increased reaction rate due to temperature also moves downstream.

This reaction system offers the challenge of dynamicity caused by the fouling accumulation and it is the hypothesized, that it is possible to carry out continuous reaction calorimetry as well as monitor the fouling rate in the reactor at the same time.

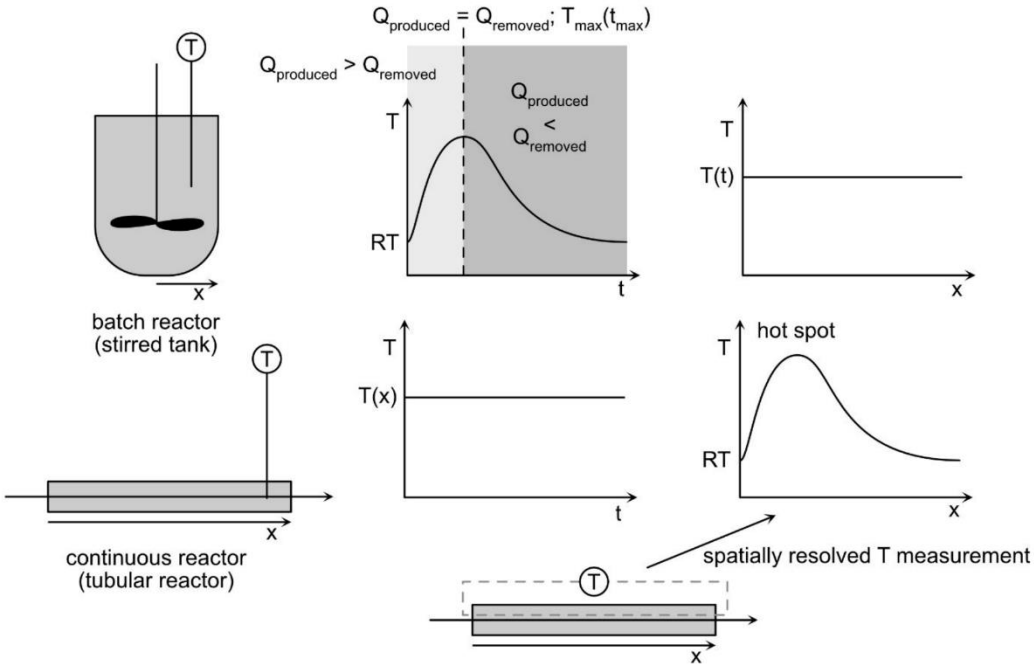

Figure 2: Comparison of the temperature profile of an exothermal, passively cooled reaction measured in an ideal batch reactor and an ideal continuous tubular reactor.

The previously presented continuous reaction calorimeters illustrate various ways spatially resolved heat measurement can be realized. Such sensor arrays or IR thermography can be used to locate and measure hot- or cold spots and further reactor safety and optimization. The drawback of series and arrays of point sensors is that the lengths in between the sensors are unmonitored and depending on the density of measurement points along the reactor spots may be overlooked. IR-thermography measures the outside surface of the reactor only.

Spatially distributed temperature measurement can be carried out with a Distributed Optical Fiber Sensor (DOFS).[19] There are multiple different technologies which can be used in the context of DOFS. The use of optical frequency-domain reflectometry (OFDR) based on Rayleigh backscatter is attractive due to the high spatial resolution and acoustic bandwidth.[20,21] The interferometric measurement employs the fiber as a local oscillator and fiber under test. With the use of a reference measurement of spatially distributed frequency shift signal, derived from the interference of the local oscillator and the incident backscattered light under test, effects influencing the fiber can be quantified. Mechanical strain and temperature changes influence the backscattered light along the fiber and therefore the measured frequency shift.[19] Due to the fact that strain and temperature influence the same signal, they are measured parallelly. In literature, a number of approaches to decouple strain and temperature have been published.[22,23] If no de-coupling mechanism is employed, as is often the case for commercially available OFDR and DOFS for Rayleigh backscatter, temperature measurements are influenced directly not only by thermo-optic effects, but also by the strain created between the silica DOFS and the coating used to protect the brittle sensor.[21] This effect has been used constructively to create chemical sensors where the coating swells with measurand, or enable precision measurement at cryogenic temperatures.[24,25]

The statistical nature of scattered light signal and the low intensity of Rayleigh-backscatter leads to noisy measurements. In 2022 the journal Sensors published a special edition with the title ‘Distributed Optical Fiber Sensors: Applications and Technology’ containing seventeen publications on a variety of sensing mechanisms, including Rayleigh-, Brillouin- and Raman backscatter. Eight of the seventeen texts deal extensively with the calibration and de-noising of DOFS signal. It can therefore the summarized, that DOFS is an ever-evolving field of research. Exact and accurate temperature measurements have been attempted with a variety of calibration approaches and dynamic approaches also considering the change of signal over time. Such a dynamic calibration was for example performed by Y. Ghafoori et. al. (2022), employing model-independent parameter estimation and improving sensing accuracy to a

maximum possible error of ± 0.52 °C.[26] Signal reconstruction at high temperatures and signal optimization was for example performed by D. C. Sweeney et. al. (2021) with graphical optimization and the inchworm algorithm.[27]

DOFS offer benefits besides the spatially distributed sensing, such as resistance against electro-magnetic interference, small physical size and thermal mass. They can be implemented in different ways to traditional sensors such as thermocouples and can be applied in a temperature range from cryogenic temperatures to 1000 °C covering a very large amount of use cases. [21,25,27]

The handling and implementation of DOFS in a measurement setup is not trivial. Strain measurement needs special consideration in regard to the adhesion of the sensor to the object under test.[28] Physical decoupling of strain and temperature can be achieved in part when avoiding strain and adhesion of the sensor to the measurement setup. DOFS are brittle and possess coatings for their protection, which can influence the measurement and must therefore be taken into consideration. Temperature sensors are often coated in polyimide. Such coatings can be hygroscopic and can also swell and contract on contact with solvents and their vapours.[29,30] The sensors rely on total reflexion as common telecommunications fibers do and sharp bends lead to signal loss.

The handling, integration, calibration and data analysis of DOFS is different from other temperature sensors. It is the hope of the authors to illustrate how these sensors can successfully be integrated into a laboratory scale continuous tubular reactor with a length of 3 meters. The sensors are used for calorimetric conversion tracking during a fouling-heavy copolymerization reaction.

DOFS sensors can be used in different applications in chemical reaction engineering, too, and it is the hope of the authors to illustrate their usefulness using this particular example. Additionally, DOFS can be used for any kind of temperature monitoring in an industrial plant and the information can be evaluated in a multitude of ways. For example, online synthesis optimization may profit from real-time spatially resolved temperature monitoring. The presented reaction's DOFS data has been used to create the basis of a potentially predictive model to determine the clogging time of the continuous reactor based on the fouling.[31]

3. Experimental setup and reaction

A modular system was devised to allow for DOFS use in a frequently changing flow reactor setup. It consists of a 3D-printed holder which is installed permanently in the flow hood. Further information about the setup and the 3D printing of the parts can be found in the supplementary materials.

Figure 3 depicts a 3D image of the experimental reactor set up with three steel rods. Between the three horizontal sections the tube is curved, traversing 17 cm in height using 30 cm of tubing. The crosscut in Figure 3 shows the reactor tube, holder and bracket stacked together, along with the three DOFS which were fed through the assembly after the 1.5 mm wide sensor channels were filled with a thermal paste mixture comprised of 50 w% aluminium particles (diameter 5 µm) and 50 w% glycerol. Furthermore, Figure 3 shows six thermal sensors (K-Type thermocouples with 1.5 mm thick feelers, data recorded using a TC-08 datalogger by picoTech). The six point sensors are inserted into the middle of the tube through holes in the holders, brackets and tubing. They are secured in place with silicone.

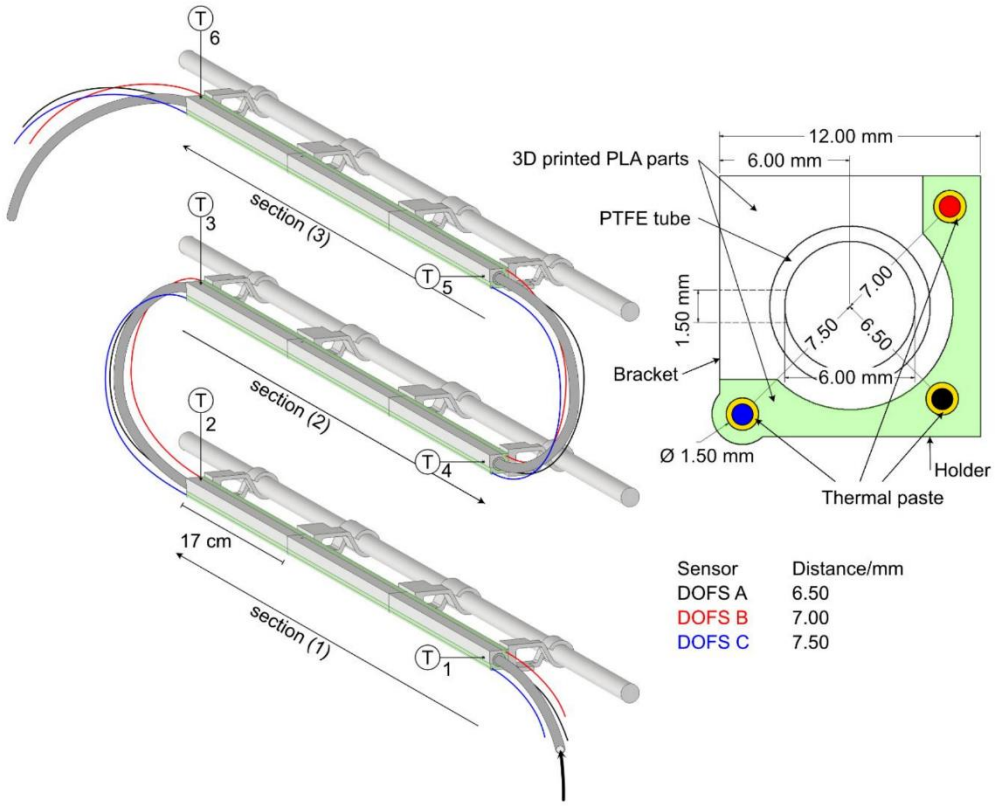

Figure 3: Scheme of the modular reactor system with the permanently installed sensor holder (green) and cross-sectional view of the reactor in the holder and bracket with three DOFS (designated A, B and C) at different distances to the midpoint.

The emulsion copolymerization reaction used two monomers, vinyl acetate and vinyl-neodecanoate (Versa10®), as a 9:1 mixture, with a total monomer concentration of 24 w% regarding the total reaction mass. A pre-emulsion was created from the monomers and polyvinyl alcohol (PVA) (Mowiol® 4-88; degree of hydrolysis of 4-88 %; molecular weight ~31 kDa) with a PVA concentration of 7 w% regarding monomer weight. For initialization, a redox system requiring two further feed streams was used. L(+)-ascorbic acid and ammonium-iron(III)-sulfate were combined in one stream, and tert-butyl hydroperoxide (t-BHP) dissolved in water made up the final stream. Vinyl acetate, vinyl-neodecanoate and PVA were purchased from Wacker Chemie AG, Burghausen. L(+)-ascorbic acid and ammonium-iron(III)-sulfate-dodecahydrate (both in analysis grade) were purchased from Carl Roth and Merck, respectively. The initiator tert-butyl hydroperoxide was purchased as a 70 w% aqueous solution from Thermo Fisher Scientific. The redox initiator system was used with 1:1:0.3 molar ratio of ascorbic acid to tert-butyl hydroperoxide (t-BHP) to ammonium-iron(III)-sulfate, with 1 w% of tert-butyl hydroperoxide regarding the monomer. All chemicals were used as delivered without any further purification.

All solutions were degassed using porous gas diffusers for a minimum of 3 hours with a constant stream of N_2 before reaction (2 to 3 parallel bubble chains). To prevent foam spillage during the degassing of the monomer emulsion, the demineralized water and monomers were degassed separately and then combined under nitrogen counterflow. To dissolve the PVA and form the pre-emulsion, the mixture was stirred using a 6 cm stir bar in a 5 L glass bottle (500 rpm) overnight on a hotplate set to 30 °C. During reaction, the emulsion is constantly stirred with a 6 cm stir bar at 100 rpm at room temperature. To minimize re-oxygenation, the same glass bottle is used throughout all steps, avoiding transfer of the mixture. The solid content of reaction samples, as well as testing for creaming and subsequent non-uniform feeding of the monomer emulsion, was carried out using microwave gravimetry. The reactants were fed into the reactor using ProMinent gamma-X series diaphragm pumps. Due to the low flowrates, stroke lengths from 15-20 % were used. For the pre-emulsion, a flow rate of 5.6 $\frac{\mathrm{g}}{\mathrm{min}}$ was achieved using 120 $\frac{\mathrm{strokes}}{\mathrm{min}}$. The redox components were dosed at a flow rate of 0.5 $\frac{\mathrm{g}}{\mathrm{min}}$ with 36 $\frac{\mathrm{strokes}}{\mathrm{min}}$. The initiator was dosed at a flow rate of 1.9 $\frac{\mathrm{g}}{\mathrm{min}}$ with 45 $\frac{\mathrm{strokes}}{\mathrm{min}}$. For dosing commercial PTFE tubes were

used which had an inner radius of 2 mm. The ascorbic acid solution and the pre-emulsion were combined in a 10 mL CSTR directly before meeting the initiator via a T-junction and then entering the reactor. The described set up is depicted in Figure 4 and an overview of the three feed streams is shown in Table 1.

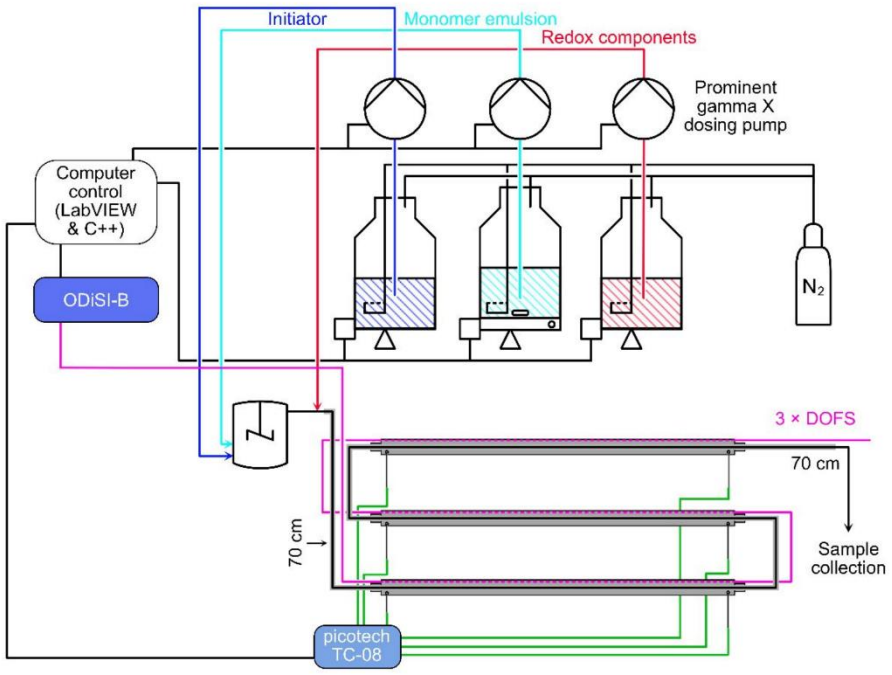

Figure 4: Experimental set up for the copolymerization reaction with six thermocouples (green) and three DOFS (pink), in which the t-BHP (blue) and the monomer emulsion (cyan) are combined in a 10 mL CSTR before meeting with the redox component stream (red) and entering the reactor.

Table 1: Overview over the feed streams for the emulsion polymerization with flow rates.

	Flow rate/$\frac{\mathbf{g}}{\mathbf{min}}$	Components	Component flow rate/$\frac{\mathbf{g}}{\mathbf{min}}$
Monomer emulsion	5.6	vinyl acetate	1.729
		vinyl-neodecanoate	0.192
		polyvinyl alcohol	0.134
		demineralized water	3.545
	0.5	(L)-Ascorbic acid	0.038

	Flow rate/$\frac{\mathbf{g}}{\mathbf{min}}$	Components	Component flow rate/$\frac{\mathbf{g}}{\mathbf{min}}$
Ascorbic acid solution		Ammonium-iron(III)sulfate-dodecahydrate	0.003
		demineralized water	1.890
Initiator solution	1.9	tert-Butylhydroperoxide	0.019
		demineralized water	0.490

In order to calibrate the DOFS and collect calorimetric data in the setup, experiments with heated water were carried out. The reactor was fed at the same flow rate (8 $\frac{\mathbf{g}}{\mathbf{min}}$) as the reaction using demineralized water. The water was heated to different temperatures using a Julabo SE 6 thermostat (temperature range 20 – 70 °C). The cooling temperature along the reactor length and the room temperature were used to determine the reference temperature at the DOFS at every point (spatial resolution 2.6 mm) along their path. This was then used for sensor calibration.

Alternatively, the calibration was also carried out with an additional set of thermocouples and an insulation. The set up is shown in Figure 5. A foam insulation around the three horizontal reactor portions was introduced for this variant and the further set of six thermocouples was positioned parallel to the previous set in between the insulation and the outer bracket and holder wall. This was done to enable the DOFS to experience higher temperatures, expanding the calibration range. Both variants were used and the supplementary material includes an overview over the experiments carried out and which calibration setup was used.

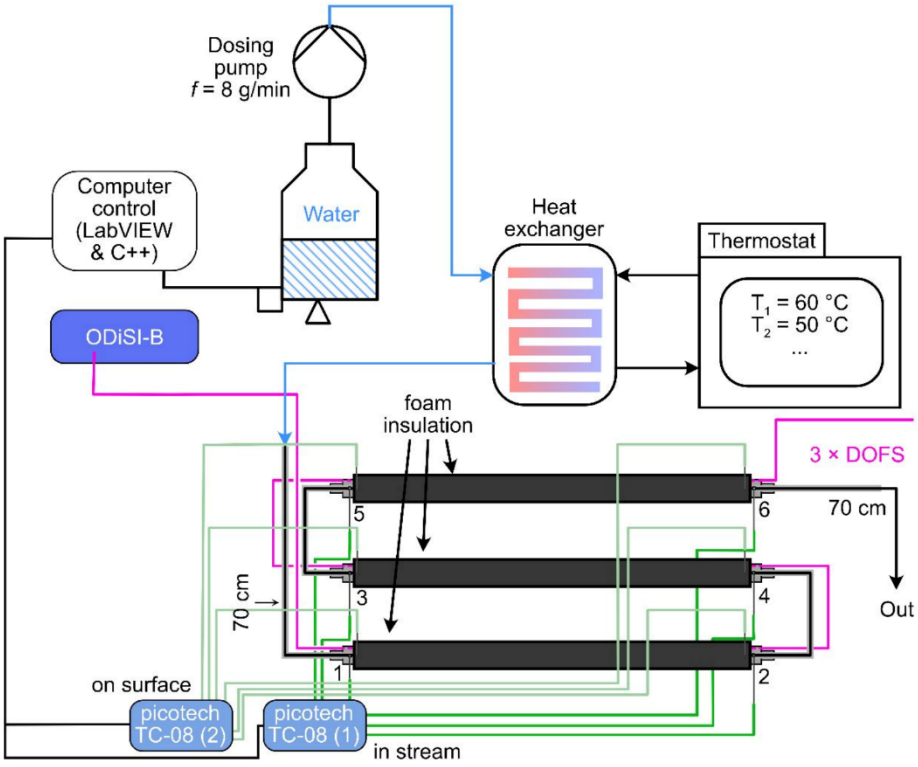

Figure 5: Changed setup for calibration of sensors and calorimetric calibration, where water is temperature-controlled with a heat exchanger before entering the reactor.

4. DOFS calibration and determination of heat released by cooling water

A DOFS measures signal shift ν [GHz] along its length, which needs to be converted into temperature T data for the present application. A polynomic function of up to the power of four is used to convert the signal shift to temperature.[32] Within the examined temperature region (20 – 70 °C), a linear function can be used. In this case, Equation 1 can be used for the conversion. The factor A_1 is the conversion factor and K_1 is the temperature of the fiber at the time of reference (tare) measurement. For example, if the experiment is started when all components are at room temperature (RT), then K_1 = RT in °C The factor A_1 typically is around -0.7 $\frac{°C}{GHz}$.

$$T = \nu \cdot A_1 + K_1 \qquad \text{Equation 1}$$

It has been shown that it is not viable to calibrate only one part of the fiber and extrapolate these parameters to also describe the rest of the length.[33] The conversion factors appear to change

along the fiber, likely due to its changing surroundings (position, strain, moisture). The challenge of calibrating spatially distributed sensors using only point sensors as reference was approached by calculating the conversion factors at all six thermocouple positions. The lengths in between these points were linearly interpolated.

In the attempt to calibrate the sensors with as much exactitude as possible, the following assumptions were made in the case of the un-insulated calibration set up. Inside the tubular reactor, the flow is laminar. The reactor, mantle (holder and bracket), and insulation are treated as a multi-layered tube. The outer fluid is air with natural convection and a homogenous temperature equal to the measured room temperature. From these considerations, an inner thermal coefficient of transport $\alpha_i = 426\,\frac{W}{m^2 \cdot K}$, and an outer coefficient $\alpha_o = 9\,\frac{W}{m^2 \cdot K}$ is calculated, using Equation 2. In this equation Nu is the dimensionless Nußelt number, λ_F the thermal conductivity of the fluid (water or reaction mixture) in $\frac{W}{m \cdot K}$, and the characteristic length L is the length of one horizontal reactor segment (0.45 m). The detailed calculations can be found in the supplemental material.

$$\alpha = \frac{Nu \cdot \lambda_F}{L} \qquad \text{Equation 2}$$

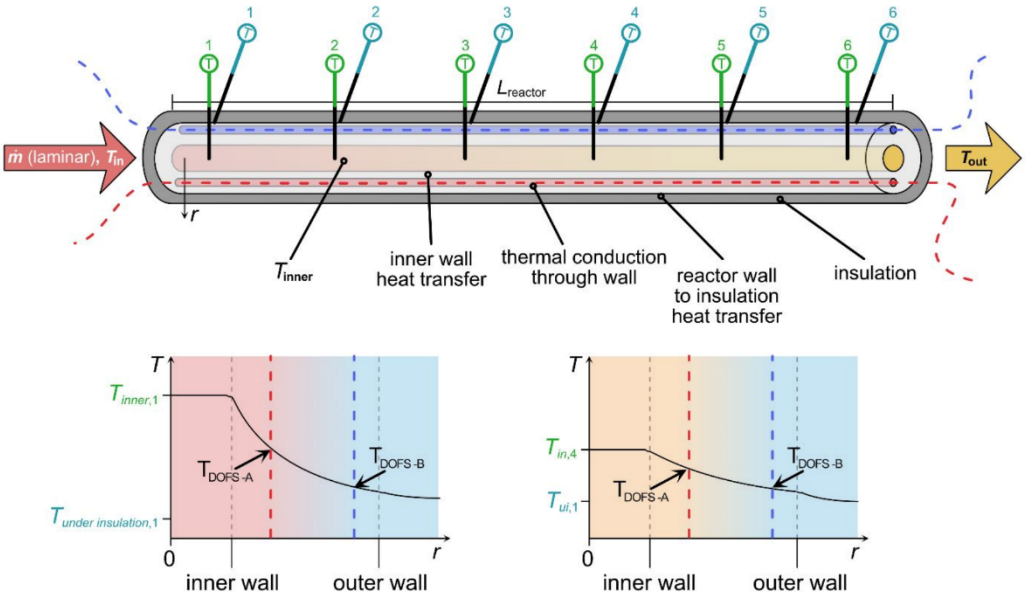

Figure 6: Schematic showing the thermocouple arrangement along the reactor length (shown simplified without any sectioning) with insulation, and influence of the inner temperature decrease on the temperature in the wall at the distance of the individual DOFS.

Using the known inner stream temperature and the heat transfer coefficients, the temperature at the radial distances the three individual DOFS were positioned at could be calculated. This was done for each thermocouple position. Figure 6 illustrated an overview of the calibration process with six pairs of thermocouples along the reactor length. The radial temperature profiles of two such positions are shown and the positions of two exemplary DOFS inside the wall are marked in the graphs. In this way, the calculated DOFS temperatures at each of the six positions for any set of inner and outer temperatures can be determined.

Equation 3.1 defines the radial heat loss $\dot{Q}$ in [W] through the wall of a tube to the outer medium, which is air at RT for the presented experiments. In the equation a tube made from a single wall material with the thermal conductivity coefficient λ is assumed. PTFE is estimated to have a λ of 0.25 $\frac{W}{m \cdot K}$ and PLA to have a λ of 0.19 $\frac{W}{m \cdot K}$.[34,35] Due to the total wall thickness being predominantly made up of PLA, its λ was used for all calculations. The length of tubing over which $\dot{Q}$ is calculated, is L, which is set to the value 0.45 m in this case, as this is the centre length of reactor on each of the three horizontal sections that provides DOFS data undisturbed by the bends. Figure 7 shows a raw DOFS measurement and the effect the bends have. Due to the larger than average signal variance and noise in those regions, they were discarded, and the 0.45 m region was treated as the entire horizontal section. The error introduced by this is corrected via heat measurement calibration later.

$$\dot{Q}_{RT} = \frac{\pi \cdot L \cdot (T_i - T_o)}{\frac{1}{\alpha_i \cdot d_i} + \frac{1}{2 \cdot \lambda} \cdot \ln\left(\frac{d_o}{d_i}\right) + \frac{1}{\alpha_o \cdot d_o}} \qquad \text{Equation 3.1}$$

Knowing the α coefficients and the outside temperature T_o (RT), $\dot{Q}_{RT}$ can be calculated. For the insulated calibration setup (shown in Figure 5), T_o is the outside wall temperature, which is assumed to be the values measured by the second set of thermocouples. In that case, Equation 3.2 is used.

$$\dot{Q}_{ins} = \frac{\pi \cdot L \cdot (T_i - T_o)}{\frac{1}{\alpha_i \cdot d_i} + \frac{1}{2 \cdot \lambda} \cdot \ln\left(\frac{d_o}{d_i}\right)} \qquad \text{Equation 3.2}$$

Finally, Equation 3.2 is solved for T_o and shown in equation 4. It is applied to an outer temperature being inside the reactor wall at the position d_{DOFS}, therefore eliminating the term for the outer heat transport. In this case, T_o is designated T_{DOFS}.

$$T_{DOFS} = T_i - \frac{\dot{Q}_{ins/RT} \cdot \left(\frac{1}{\alpha_i \cdot d_i} + \frac{1}{2 \cdot \lambda} \cdot \ln\left(\frac{d_{DOFS}}{d_i}\right)\right)}{\pi \cdot L} \qquad \text{Equation 4}$$

At all six thermocouple positions, this calculation is done for each calibration measurement. Then, the three horizontal segments are identified as shown in Figure 7. Two centimetres of section length from each of those six positions was averaged to give one value and then correlated with the temperature T_{DOFS} from Equation 4 for all measurements at all different inlet temperatures. These plots (one at each of the six positions) were fitted linearly, which gives the factors A_1 and K_1 directly. Six sets of factors are thusly generated for each of the three DOFS. This underlines that one correlation factor for the entire fiber is unfit, because the variance of the six A_1 values for one DOFS is $\pm 0.1 \frac{°C}{GHz}$ in the non-insulated (RT) setup and $\pm 0.07 \frac{°C}{GHz}$ in the insulated (ins) setup. Further information on the calibration process is available in the supplemental material.

In Figure 7 the presented data has already been averaged over 200 scans (scan rate is 100 Hz) and further improvement to the signal noise by temporal averaging has not been observed. Without spatial averaging (resulting in a spatial resolution of 2.6 mm), the band of noise limits the accuracy of the signal ν to ± 1-2 GHz (approximately 0.5 – 1 °C).

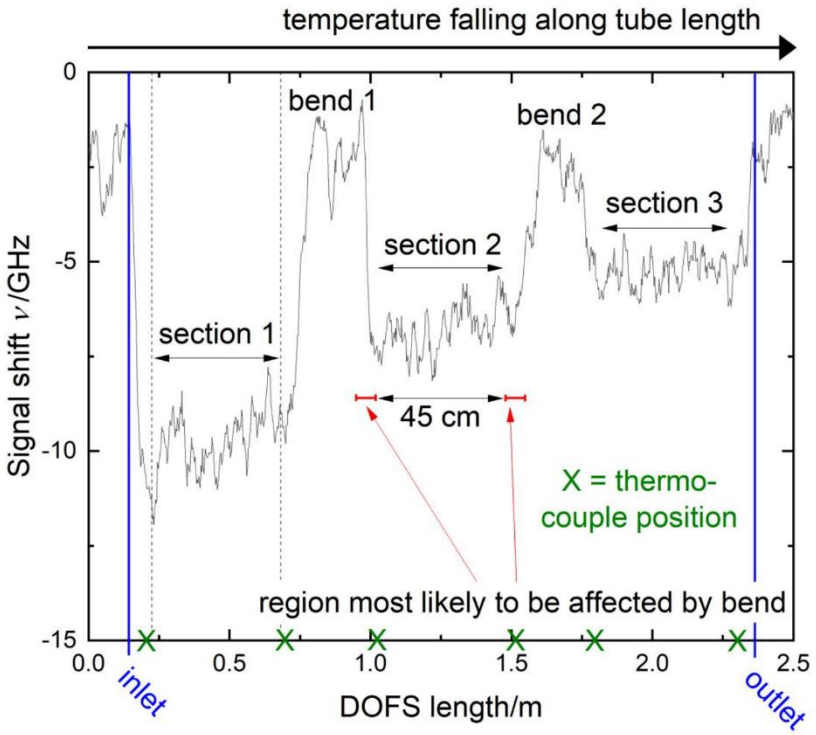

Figure 7: Raw data from a DOFS in the setup shown in Figure 3 with labelled sections, bends and characteristic noise level (the six thermocouple positions are shown with a green X, they are located at each end of the three sections).

Data from one exemplary measurement is discussed in Figures 8 to 10. This calibration made use of an outer insulation. In Figure 8, the spatially distributed temperature data of all three DOFS and the instream thermocouple measurements are shown at one inlet temperature. The overlapping of all three DOFS is caused by the low temperature resolution. The too low temperature at position 1 might be caused by stronger cooling affecting the region due proximity to the edge. A similar effect may be present at position 4. The locations for low temperatures are likely due to dissimilar insulation application or outside influence, because they often cluster on one side of the reactor (positions 1, 4 and 5 being all on one side). These effects change from experiment day to another, especially if the setup was refitted with new tubing and insulation. Despite the inconsistencies, low resolution and noise, it is possible to gain further information from these measurements. The DOFS measurements, as carried out here, do not offer high resolution when attempting to measure distributed temperature, but the signal shifts with temperature change are proportional and individual to each DOFS. The systematicity of this can be used for further data evaluation.

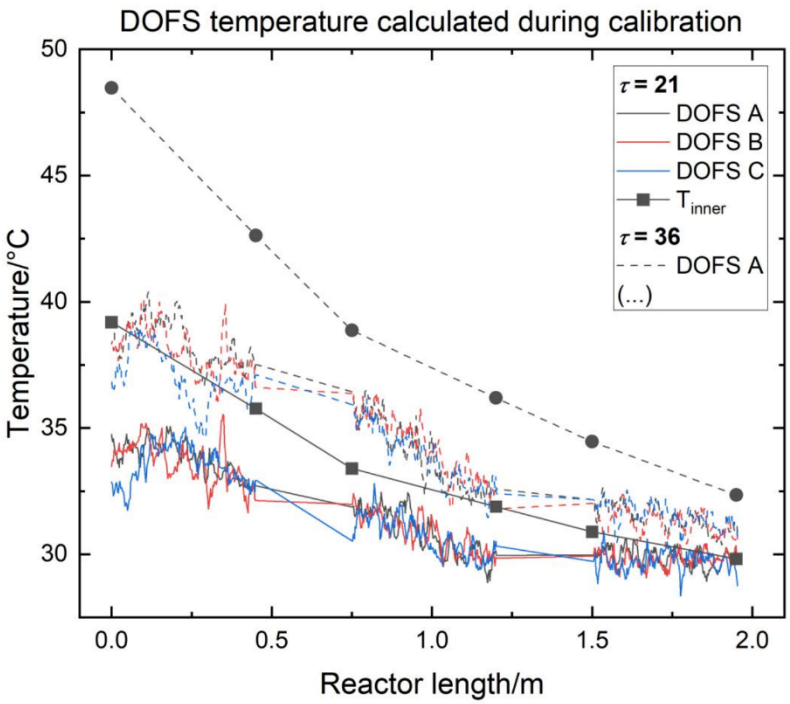

Figure 8: Temperature data measured with all three calibrated DOFS and thermocouples in stream at two different inlet temperatures at different dimensionless times τ in a calibration cycle.

During calibration the only source of heat is the thermostat and the only mode of heat loss in the three DOFS sections is through the reactor walls (radial heat loss) $\dot{Q}_{rad}$. Heat that is not lost through the walls is transported downstream with the liquid (axial heat transport) $\dot{Q}_{ax}$. The lost thermal power between instream thermocouple positions can be calculated using Equation 5, and due to the radial heat loss being the only mode of heat loss, the two must be equal. In the equation position 1 and 6 are used, but the same equation applies for any pair of positions.

$$\dot{Q}_{ax} = (T_{Pos\,1} - T_{Pos\,6}) \cdot c_{p,H_2O} \cdot \dot{m} \qquad \text{Equation 5}$$

The heat capacity of water c_{p,H_2O} is assumed as 4181 $\frac{J}{kg \cdot K}$ and the mass flow is $8\,\frac{g}{min} = 13 \cdot 10^{-5}\,\frac{kg}{s}$. The total thermal power loss between positions 1 and 6 can be calculated and used as reference values to calibrate $\dot{Q}_{ax}$. For this, the *T*-differences between DOFS A and B, A and C and B and C are calculated and used in Equation 6, which derives from Equation 3.1

and 3.2. The characteristic length used in this case was L_{DOFS}, which is the spatial resolution of 2.6 mm.

$$\dot{Q}_{rad\,A-B} = \frac{\pi \cdot L_{DOFS} \cdot (T_{DOFS\,A} - T_{DOFS\,B})}{\frac{1}{2 \cdot \lambda} \cdot \ln\left(\frac{d_{DOFS\,B}}{d_{DOFS\,A}}\right)} \qquad \text{Equation 6}$$

In Figure 9, the spatially resolved heat loss is shown without any signal processing. As previously stated, the spatially distributed temperature measurements were noisy and the resolution was not good enough to resolve the small T differences, therefore, the quality of data depicted in Figure 10 is expected. However, the sum of all data along the reactor length displays a clearer relation to the actual heat lost ($\dot{Q}_{ax}$), because the overall systematicity of the signal shift is included in the overall signal and the good repeatability of measurements allows for relative calculations (repeatability of temperature measurement according to manufacturer is ± 0.01 °C). After a calibration using a linear fit between the lengthwise sum of the DOFS data and the reference data, $\dot{Q}_{rad}$ calculated from the DOFS' temperature differences can be considered an accurate estimate of the actual heat loss.

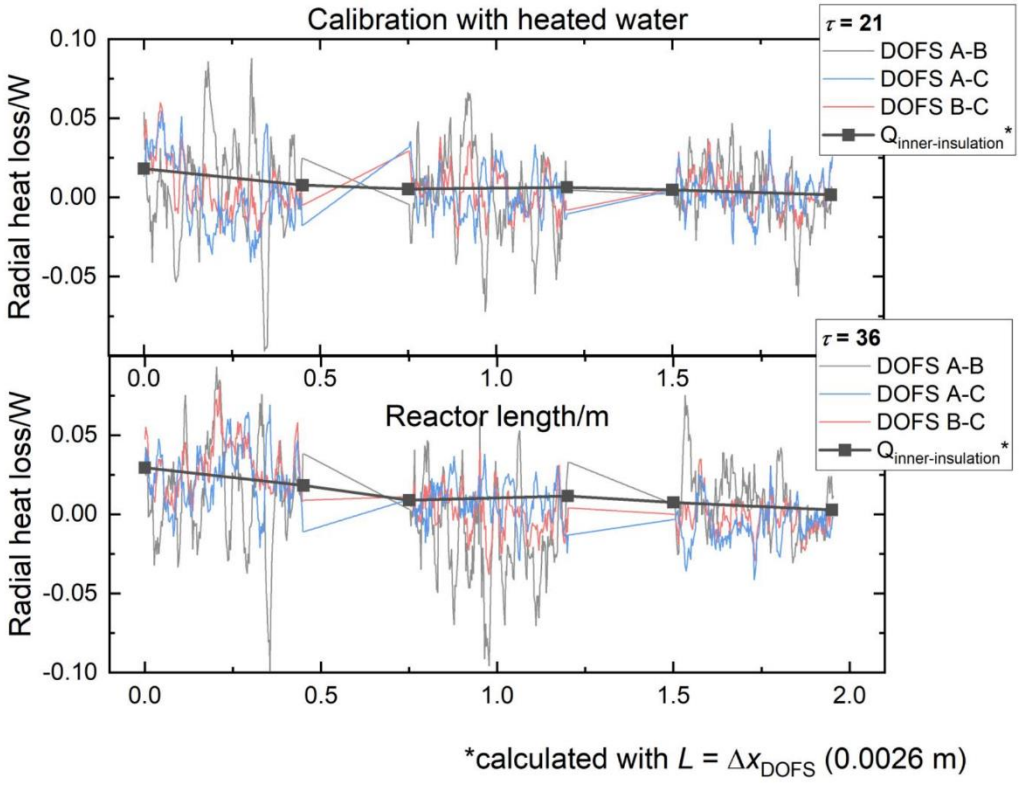

Figure 9: Spatially distributed calculations of the radial heat loss from pairings of DOFS, as well as the T difference between the in stream and outer wall thermocouples (insulated setup), for two different inlet temperatures at different dimensionless times τ in the calibration cycle.

The deviation of the calibrated radial heat loss calculated from the DOFS' temperature differences with $\dot{Q}_{ax}$ is ± 0.43 W for DOFS A and B, ± 0.39 W for DOFS A and C, and ± 0.54 W for DOFS B and C. Because DOFS A and C are at the largest distance from one another, the data from their pairing shows the smallest deviation from the reference $\dot{Q}_{ax}$. The temperature difference between A and B is larger than between B and C, due to A being the hot end of the radial thermal gradient, and therefore the deviation of the pairing A and B is smaller than the one of B and C.

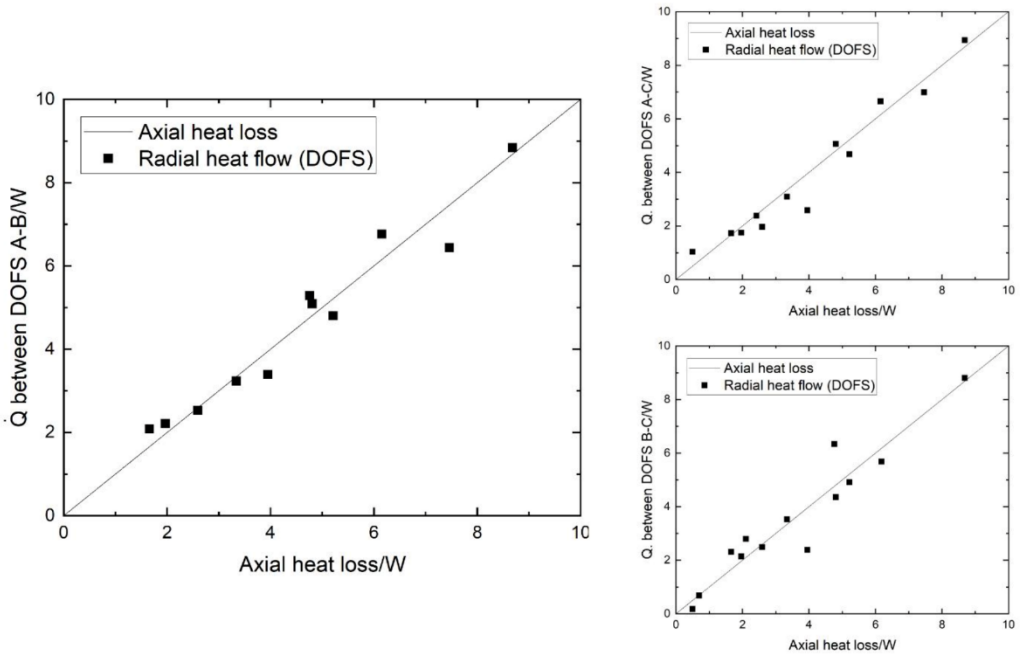

Figure 10: Calculated radial heat loss from the three different DOFS pairings after calibration and their deviation from the reference $\dot{Q}_{ax}$.

5. Determination of reaction heat

After calibration, the spatially distributed temperature profile during the emulsion copolymerization can be recorded and calorimetric information can be gained. A useful view for temporally and spatially distributed data is a contour plot, such as the one shown in Figure 11. It depicts the measurement of one DOFS during a polymerization. The hotspot

caused by the reaction moves downstream over time due to the heavy fouling constricting the reactor volume. The distortions in Figure 11 are caused by the bends, which are replaced by linear interpolation between the last and first measured T−values of a section. In the contour plot, and especially in the following graph, the temperature drop of the maximum T of the hotspot T_{max} can be seen. This is likely caused by the contraction of the volume in the reactor. Due to the virtually shrinking tube diameter the length, in which the majority of the reaction happens, is stretched and pushed downstream. Furthermore, the thermal resistance of the walls increases due to the fouling mass, which should be most apparent in the DOFS measurements and is further discussed in the following text. The downstream movement and temperature change of the hotspot do not have an induction phase but starts from the beginning of the reaction. Therefore, the fouling process of this reaction in this reactor setup also has no induction phase. It has been shown that elevated temperatures lead to greater fouling deposition in this particular system.[18] The section around and downstream of the T_{max} is likely the area of most fouling deposition.

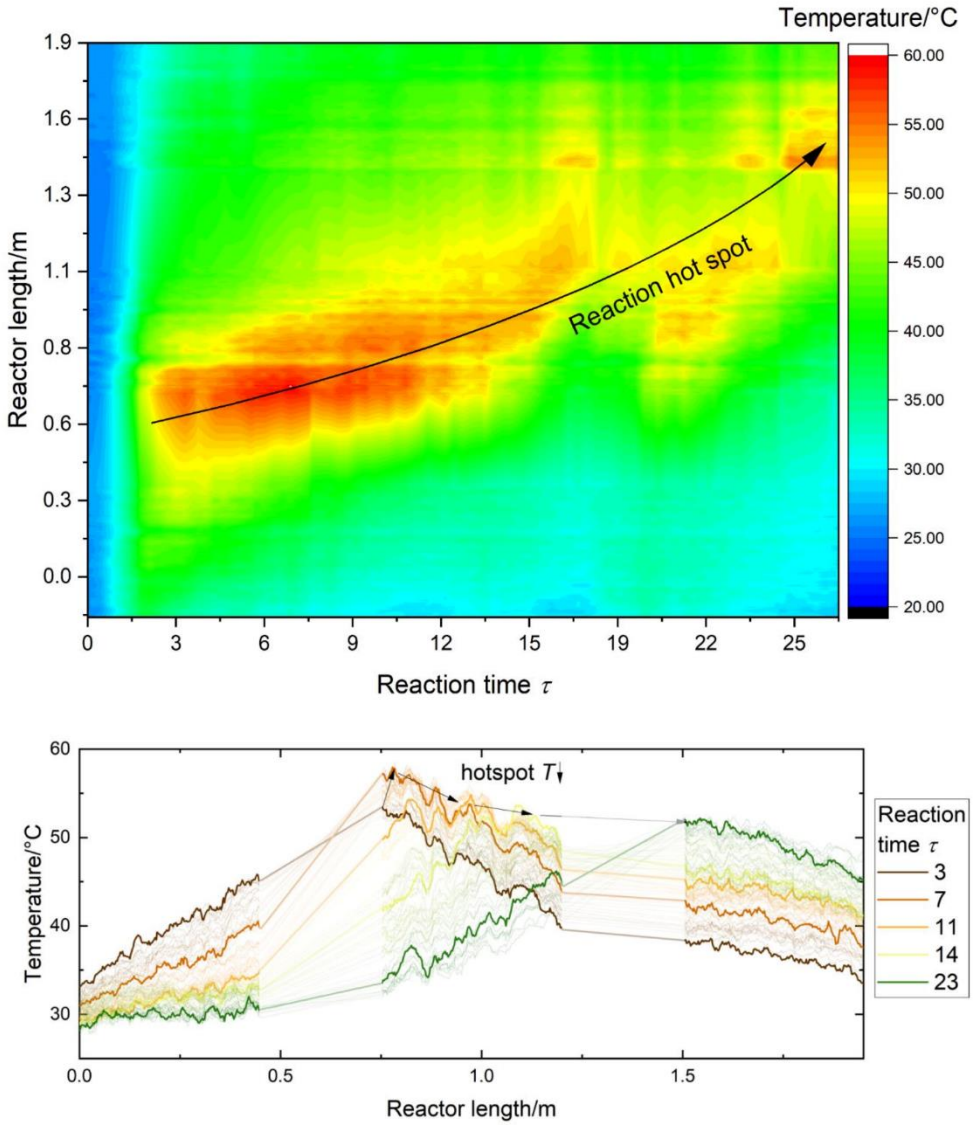

Figure 11: Contour plot showing the reaction hotspot (length of highest conversion) moving through the reactor during the reaction progress and a graph showing the lengthwise DOFS measurement of a sensor, illustrating the drop of the maximum T of the hotspot T_{max}.

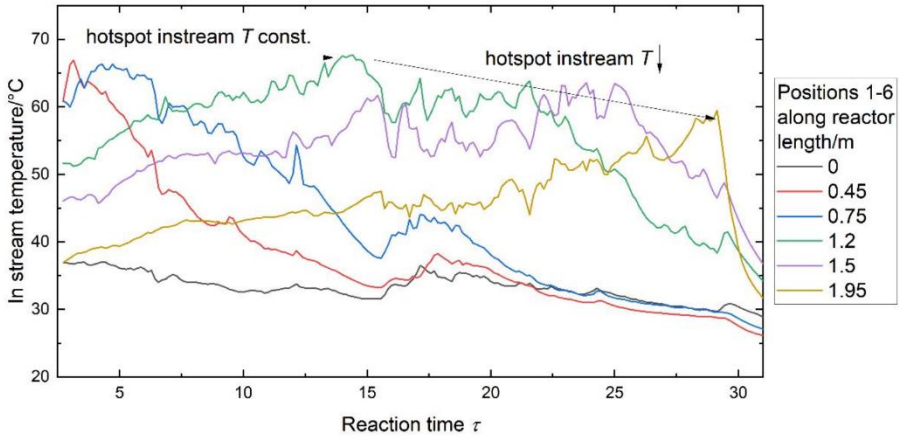

Figure 12: Instream T measurements using the six thermocouples (one at each end of the three sections) during copolymerization showing the movement of the $T_{\max}$ during reaction.

In Figure 12 the instream T measurements are shown. The downstream movement of the hotspot can be seen here, too. Instream, T_{max} at the beginning of the reaction is 66 °C ($\tau = 2$ to 5). At that time, the reactor is still heating up (and the reaction rate is therefore increasing), which can be seen in the DOFS measurements, therefore heat is being absorbed by the reactor mass. This might explain why T_{max} recorded at $\tau = 14$ is 67 °C, when the reactor is at a higher temperature. At $\tau = 25$ the hotspot is at the thermocouple in position 5, at 1.5 m reactor length and T_{max} is 63 °C. The drop in T_{max} is therefore observed in both T measurement methods, but in different ways. T_{max} as measured in the walls drops first quickly, then slowly. In contrast, instream T_{max} drops first slowly, or can even be called constant until $\tau \approx 14$, and then starts to drop slowly. By the time $\tau \approx 14$, T_{max} in the wall has dropped considerably already.

The increased thermal resistance along the inner reactor wall caused by the fouling deposition reduces the overall heat transfer from the inside through the wall. The thermocouples have a considerably smaller surface area than the inside of the reactor along its length. The DOFS measurement spans the reactor length and is therefore likely influenced by the fouling deposit along its length. It can therefore be assumed that due to this smaller area of possible fouling, the effect of the T_{max} drop is different instream, than in the walls. Furthermore, fouling mass has been seen to be removed from the reactor in swaths of material exiting the outlet, and it can be assumed that due to the irregularities in the instream geometry at the thermal couple placements, those areas are more likely have fouling mass be washed off by the reaction stream.

This process may be reflected in the zig-zag pattern of the thermocouple curves in Figure 12.The instream T measurement depicts the broadening and subsequent drop of T_{max}, and the T_{max} drop in the walls is likely also influenced by the fouling layer's thermal resistance. The hotspot broadening is hard to quantify from the present data, as the hotspot is not bordered by baseline (RT) on both sides of the lengthwise measurement. It is too long for the possible sensor length in the current setup and with the used hardware. It is easier to quantify T_{max}, which is only continuously possible with the DOFS. The thermocouples only measure T_{max}, when the two align in position. Additionally, the DOFS are influenced immediately after reaction start, which is when the fouling begins. The thermocouple measurements only show a T_{max} drop after 7 more dimensionless reaction times. Therefore, the DOFS T_{max} is a useful parameter for fouling monitoring for this reaction and might be a useful tool for detection of the beginning of fouling in reactions with an induction period.

The prolonged high $T_{\max}$ value inside the reactor reflects, that the reaction is still progressing to a high degree inside the reactor. The lost volume has only relocated the hotspot, without influencing the completion of the reaction greatly. This hypothesis can be tested by comparison to the conversion rate measured by gravimetry from samples at the end of the reactor and analysis of the polymer. Figure 13 shows these parameters over the reaction time for one exemplary reaction. Both parameters steadily decrease gradually and then show a big drop at the end of the reaction, shortly before the reactor has clogged. This molecular weight distributions of the correlating reaction can be found in the supplementary material.

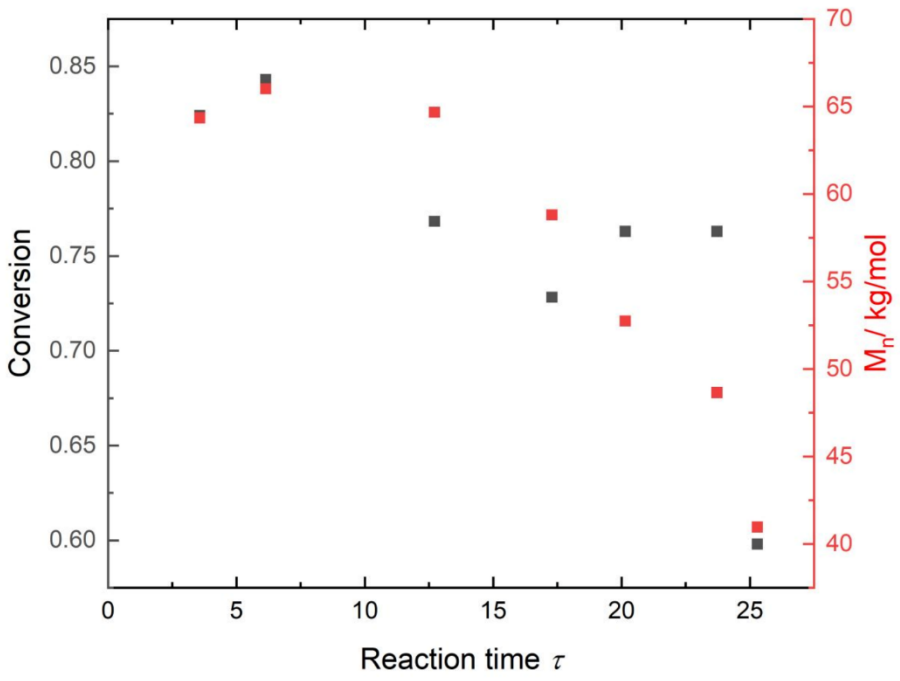

Figure 13: Gravimetrical conversion as measured at the end of the reactor length and molecular weight M_n as measured from the same samples.Work has previously been published on fouling quantification using the position of T_{max} as measured by DOFS. It could be established, that the fouling mass in the entire reactor grows in a linear manner with reaction time.[25] The same linear trend has been observed by Rust et al. with the same copolymerization system in a steel reactor with active T control.[36] The results of the position-based fouling quantification and the reaction in the steel reactor at 20 °C are very comparable.

Using Equation 6, the radial heat loss $\dot{Q}_{rad}$ can be calculated for the reaction. $\dot{Q}_{ax}$ can be calculated as shown in Equation 7, with the heat capacity of the reaction mixture $c_{p,R} = 3706\ \frac{J}{kg \cdot K}$.

$$\dot{Q}_{ax} = \sum_{n=1}^{5} |T_{Pos\,n} - T_{Pos\,n+1}| \cdot c_{p,R} \cdot \dot{m} \qquad \text{Equation 7}$$

$$\dot{Q}_R = \dot{Q}_{rad} + \dot{Q}_{ax} \qquad \text{Equation 8}$$

The reaction is started at room temperature with a redox initiator system and is not actively cooled or heated during reaction. Therefore, the reaction can be considered autothermal (and the reactor isoperibolic) and Equation 8 is used to calculate the total reaction heat. In Figure 14,

the reaction heat $\dot{Q}_R$, $\dot{Q}_{ax}$ and $\dot{Q}_{rad}$ are shown for one reaction. In this image the drawback of using point sensors in such a setup is illustrated. During the time T_{max} is in between the thermocouples, $\dot{Q}_{ax}$ is calculated as too low. This is not an issue with the DOFS, due to their spatially resolved measurement. Between $\tau \approx 9$ to 17, when T_{max} is between thermocouples 3 and 4, $\dot{Q}_{ax}$ displays a prominent dip, which is not visible in the DOFS based $\dot{Q}_{rad}$ curve. When T_{max} is between the thermocouples 5 and 6, there is no pronounced dip, perhaps due to the broadening of the hotspot. In this time, $\dot{Q}_{rad}$ sinks from ~12 W to ~5 W, which corresponds to the observation that the reaction is leaving the reactor, and the measured heat should sink over time. This is not seen in $\dot{Q}_{ax}$, which is likely also an artefact from T_{max} being between thermocouples. Data is always lost if T_{max} is in the bends, as the DOFS are not located there either. An approximated theoretical curve of what $\dot{Q}_R$ might look like without the missing data from T_{max} being between thermocouples is illustrated in Figure 14. Notably, the points at which the $\dot{Q}_R$ curve is most reliable are the ones when T_{max} coincides with a thermocouple. This is the case at $\tau \approx 6$, 18 and 30. The reaction heat $\dot{Q}_R$ detected with the thermal sensor approach as averaged from the data at $\tau \approx 6$, 18 is 41.6 ± 2.6 W. This corresponds to a conversion of 93 %. During multiple experimental repeats, this illustrates the upper bound of measured thermal conversion.

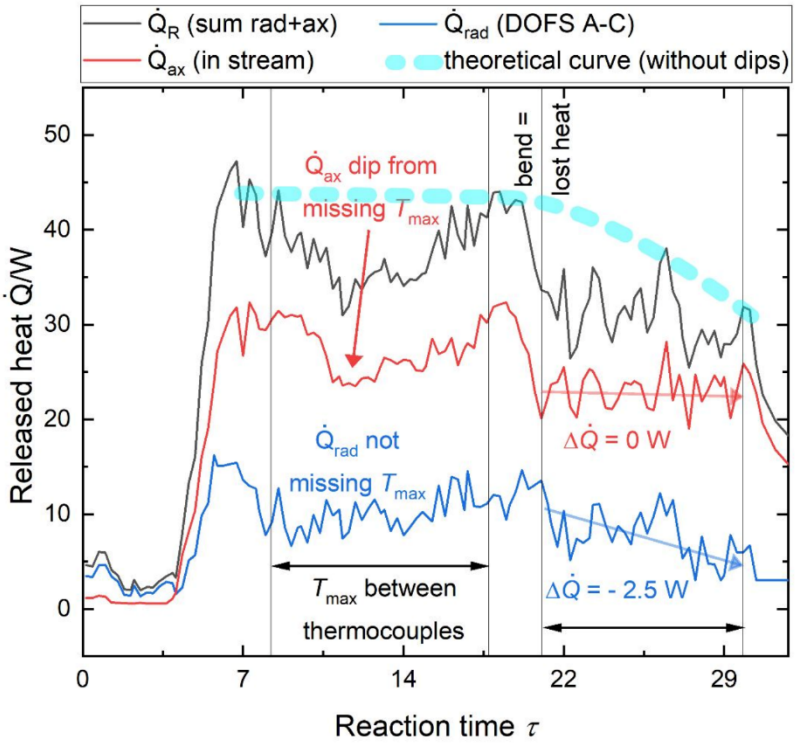

Figure 14: The reaction heat $\dot{Q}_R$, as calculated from $\dot{Q}_{ax}$ and $\dot{Q}_{rad}$ during a reaction and the assumed curve for $\dot{Q}_R$ without the artefacts from lost data between thermocouples (dips).

The maximum solid content given the recipe was 26.2 w%. The theoretical reaction heat released at full conversion is 44.75 W. Given these values, the conversion during reaction time was calculated. These calculations were carried out for a total of three repeat reactions with calibration cycles beforehand. Figure 15 depicts the averaged values of all 3 experiments. The thermal conversion for each of the three experiments could be determined with a standard deviation of 6 - 8 %.

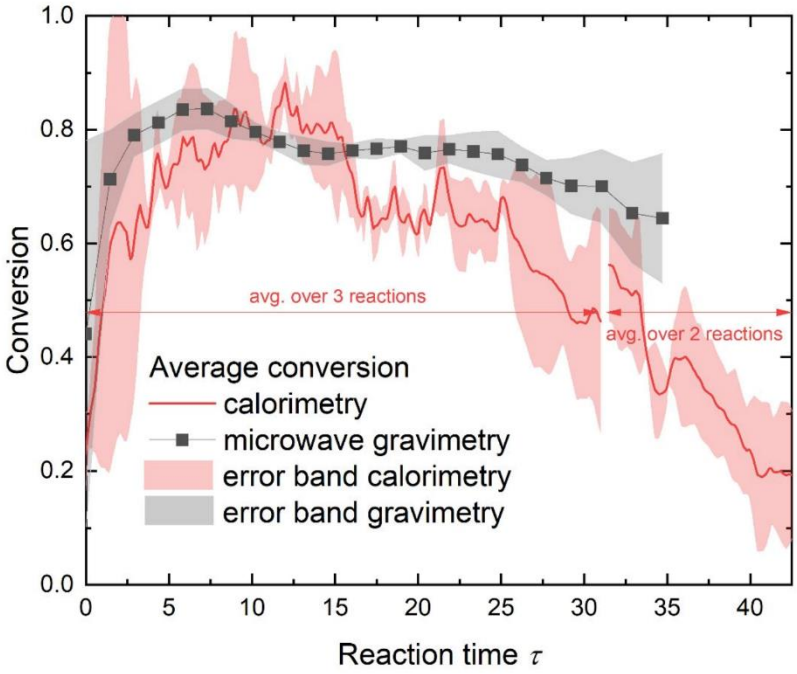

Figure 15: Solid content and thermal conversion based curves for the emulsion copolymerization of vinyl acetate and vinyl-neodecanoate in a tubular reactor, as averaged over three repeat experiments.

The conversion curve based on gravimetry rises faster than the thermal curve to its maximum and then drops slightly over the course of the reaction time. The thermal conversion curve registers a later rise (by ~2 τ). This may be due to the reactor heating up. The two curves coincide from $\tau \approx 8$ to 16, and from 16 onwards, the thermal conversion is significantly lower than the gravimetrical conversion (~12 % difference at 16 τ and ~22 % at 31 τ). The times at which the Δconversion in the graph in Figure 15 first and last equals 0 are approximately the times at which T_{max} is at a thermocouple. This is discussed in more detail pertaining to Figure 14. Therefore, the Δconversion until 16 τ can be attributed at least in part to T_{max} being detected instream by thermocouple. Between $\tau \approx 8$ and 16, Δconversion 5 % on average. In that time frame the average gravimetrical conversion is 78 % and the thermal conversion is 79 %. The following Δconversion shown in the widening discrepancy between the curves can most likely not be explained solely by that reason. An explanation for this is that the reaction has moved to the extra 20 % of reactor length available to the reaction mixture until sample collection. Then, part of the length during which the conversion is highest (hotspot) has left the reactor equipped with the sensors.

6. Summary

The emulsion copolymerization of vinyl acetate and vinyl-neodecanoate using a redox initiation system was carried out in a continuous tubular reactor. The reaction was chosen due it its intense fouling deposition. In order to monitor the fouling in the simplest geometry possible, a process using a constantly stirred pre-emulsion enabled the use of a tube reactor without static mixing elements and with considerable length (3.4 m total, 1.95 m equipped with temperature sensors) because the creaming was successfully reduced for the reaction time.

A modular flow reactor setup was devised that allows for the use of DOFS while still accessing the reactor regularly and exchanging the entirety of the reactor tube without damaging the DOFS. Temperature was measured inside the stream via six thermocouples and in the reactor wall with another set of six. Parallel to the reaction channel, three DOFS were installed at different radial distance to the inner reactor wall. Calibration parameters were determined at the points where the thermocouples were located and linearly interpolated along the DOFS sections in between. Thus, a calibrated temperature measurement inside the reactor wall was possible in a spatially resolved manner with a spatial resolution of 0.26 cm. Despite lacking temperature resolution of the DOFS, heat transfer calculation between the sensors was realized. This sensor system was used to measure the heat released during the emulsion copolymerization of vinyl acetate and vinyl-neodecanoate. Due to the redox initiator system working at room temperature, the reaction was autothermal. Therefore, the reaction heat could be calculated directly from the axially transferred heat inside the stream and the radial heat loss through the wall. It was seen that due to the thermocouples instream being positioned at six points along the 1.95 m long reactor (excluding inlet and outlet, 70 cm each), the axial heat displayed dips when the temperature maximum T_{max} of the reaction hotspot was between two sensors. Due to the high spatial resolution of the DOFS, no dips in conversion were detected in the radial heat loss measurements, underlining the potential usefulness of such sensors for continuous calorimetry. The fouling caused the available reaction volume to lower at a constant feed rate, therefore the reaction hotspot was broadened and pushed downstream. The subsequent lowering of T_{max} (after initial rise due to reaction start within 4 τ) could be measured immediately after the start of the reaction. Based on this, it is deduced that there is no induction time for fouling in this reaction in the current setup. The change of T_{max} for time appears to be a useful parameter for fouling monitoring.

During the times at which T_{max} was aligned with one of the six thermocouples, the estimated axial heat released by the reactor was measured with accuracy. At these points, corresponding to the times $\tau \approx 8$ to 16, the total calculated released heat (axial and radial) was 35.3 W. In terms of monomer conversion this is 79 % ± 3 %. Gravimetrical conversion analysis delivered a conversion of 78 % ± 2 % for this timeframe.

7. Possible improvements for DOFS thermal analysis

The calibration both temperature measurements with DOFS and of the heat measurements have been shown to have an enormous impact on the quality of data, and improvement upon the calibration setup would be beneficial. Without heat measurement calibration the measured heat of cooling for water is off by a factor of up to 5. The temperature window used needs to be increased towards both high and low end (currently 20 to 70 °C, best 0 to 100 °C). For higher temperatures, the reactor needs to be made of a different material, as the 3D printed PLA parts would distort. High temperatures not only at the inlet, but throughout the reactor length would be beneficial, as the reaction hotspot passing through the latter half of the reactor exceeded the calibration temperature window in that section. The temperature resolution of the DOFS can be made less of an obstacle by redesigning the reactor mantle to allow for more material between the DOFS channels. It may for example be beneficial to use a tubular steel reactor with a cooling jacket, the DOFS being positioned in the wall between reaction stream and cooling stream. The instream thermocouple measurement introduced an artificial dip in the heat measurement, which would be circumvented by integrating another DOFS in the reactor stream, however the fouling effect on the integrated sensor would have to be considered. For a stationary and non-fouling reaction, instream T measurements would only be needed for DOFS calibration, and the instream T can be calculated from the DOFS measurement (by solving Equation 4 for T_i).

The bends of the reactor setup cause loss of data, which can be changed by devising a straight reactor, or one with wide enough bends to not disturb the DOFS measurement. It may also be an option to have 90° bends with a small section of lost data where the sensors are put into a loose loop outside this bend to re-enter the 90° shifted reactor portion. Finally, the Rayleigh-based DOFS technology used in this study could be considered outdated and using a more modern sensor interrogator with improved software may increase temperature resolution and therefore enable more accurate calorimetric measurements.

8. Conclusion

It has been shown how heat measurements can be affected if point sensors spread too thinly are used, and how that is not an issue with DOFS (spatial resolution 0.26 cm). Methods for DOFS integration and calibration have been explored and improvement options have been devised.

Using the calibrated sensor system, it was possible to conduct thermal analysis of the emulsion copolymerization of vinyl acetate and vinyl-neodecanoate. The monitoring of the maximum temperature of the reaction hotspot T_{max} in the isoperibolic reactor allowed for the conclusion that the presented reaction and its setup did not have an induction period for the fouling. Furthermore, T_{max} consistently fell during the fouling process. It is therefore an interesting parameter for fouling monitoring. During the reaction time of T_{max} aligning with a thermocouple the axial heat calculation proved to be most reliable. The radial heat calculation using the spatially distributed sensors was reliable throughout the reaction time. It was shown that the polymerization and the subsequent fouling process is reproducible. The thermal monomer conversion calculation from the sum of the axial and radial heat transfer was shown to agree well (thermal conversion 79 % ± 3 % and gravimetrical conversion 78 % ± 2 %) with the gravimetrical conversion measurement (during the times the axial heat calculation is most reliable).

It can be concluded that the need for spatially distributed heat measurements in flow reactor calorimetry can be fulfilled using Distributed Optical Fiber Sensors (DOFS), and fouling monitoring is possible by tracking the reaction hotspot and its peak T_{max}.

Author contributions

W. P. has initiated and supervised the presented research and M. K. has carried it out, written the article and prepared the images. Both authors have edited the manuscript.

Acknowledgements

The authors would like to thank the ENPRO initiative, particularly the members of the KoPPonA 2.0 project (ger. *Kontinuierliche Prozesse für Polymerspezialitäten mit Hilfe neuer Apparatekonzepte*, Continuous processes for polymerization with the help of new technological concepts).

Funding Information

This work has been partially funded by the German Federal Ministry for Economic Affairs and Climate Action, Germany as part of the ENPRO Initiative (KoPPonA 2.0, FKZ: 03EN2004M).

Conflict of Interest

The authors declare no conflict of interest.

Data Availability Statement

The data that support the findings of this study are available at https://doi.org/10.25592/uhhfdm.17646.

Supporting Information

The supplemental material accompanying the present publication provides further information about the experimental setup, the 3D printing technique, an experimental overview, the thermal coefficient of transport calculations, DOFS calibration, DLS and GPC data.

References

[1] Farwaha, R., De Sousa Gomes, L., Vinyl Acetate-Versatic Acid Vinyl Ester Copolymer for Masonry Coatings, white paper by Celanese Emulsions GmbH, 2009 ACSeries Coatings for Concrete, URL: https://www.paint.org/wp-content/uploads/2021/09/Vinyl-Acetate-Versatic-Acid-Masonry-Coatings_Jan-2010.pdf (2009).

[2] Agirre, A., Calvo, I., Weitzel, H.-P-, Hergeth, W.-D., Asua, J. M., Semicontinuous Emulsion Co-polymerization of Vinyl Acetate and VeoVa10, Industrial & Engineering Chemistry Research, 53 (22), DOI: https://doi.org/10.1021/ie4032499 (2013).

[3] Chern, C. S., Emulsion polymerization mechanisms and kinetics, Progress in Polymer Science, 31(5), doi: https://doi.org/10.1016/j.progpolymsci.2006.02.001 (2006).

[4] Schroeter, B., Kinetik von Redoxinitiatoren für die Emulsionspolymerisation, Dissertation, URL: https://ediss.sub.uni-hamburg.de/bitstream/ediss/7920/1/Dissertation.pdf (2018).

[5] Jacob, L. I., Pauer, W., Schröter, B., Influence of redox initiator component ratios on the emulsion copolymerisation of vinyl acetate and neodecanoic acid vinyl ester, RSC Advances, 22, doi: https://doi.org/10.1039/D2RA01811J (2022).

[6] Asua, J. M., Emulsion polymerization: From fundamental mechanisms to process developments, Journal of Polymer Science, 42 (5), DOI: https://doi.org/10.1002/pola.11096 (2004).

[7] Rust, S., Investigations on the formation of fouling in continuously operated polymerisations, Dissertation, URL: https://ediss.sub.uni-hamburg.de/handle/ediss/11054 (2024).

[8] Pauer, W., Reactor Concepts for Continuous Emulsion Polymerization, Advances in Polymer Science, DOI: https://doi.org/10.1007/12_2017_24 (2017).

[9] Keil, F. J., Process intensification, Reviews in Chemical Engineering, 34 (2), DOI: https://doi.org/10.1515/revce-2017-0085 (2017).

[10] Antes, J., Gegenheimer, M., Löbbecke, S., Krause, H., Ortsaufgelöste Reaktionskalorimetrie in mikrostrukturierten Reaktoren, Chemie Ingenieur Technik, 80(9), doi: https://dx.doi.org/10.1002/cite.200750657 (2008).

[11] Moser, M., Georg, A. G., Steinemann, F. L., Rütti, D. P., Meier, D. M., Continuous milli-scale reaction calorimeter for direct scale-up of slow chemistry, Journal of Flow Chemistry, 11, 691-699; doi: https://doi.org/10.1007/s41981-021-00204-y (2021).

[12] Schneider, M. -A., Stoessel, F., Determination of the kinetic parameters of fast exothermal reactions using a novel microreactor-based calorimeter, Chemical Engineering Journal 115 (1-2), 73-83, doi: https://doi.org/10.1016/j.cej.2005.09.019 (2005).

[13] Romano, M., Pradere, C., Toutain, J., Batsale, J. C., Quantitative kinetics and enthalpy measurements of biphasic underflow chemical reactions using infrared thermography, Experimental Thermal and Fluid Science, 67, 14 – 17, doi: https://doi.org/10.1016/j.expthermflusci.2014.11.002 (2015).

[14] Reichmann, F., Millhoff, S., Jirmann, Y., Kockmann, N., Reaction Calorimetry for Exothermic Reactions in Plate-Type Microreactors Using Seebeck Elements, Chem. Eng. Technol., 40 (11), 2144 – 2154, doi: https://doi.org/10.1002/ceat.201700419 (2017).

[15] Mortzfeld, D. et al., Reaction Calorimetry in Continuous Flow Mode: A New Approach for the Thermal Characterization of High Energetic and Fast Reactions, Org. Process Res. Dev., 24, 2004 – 2016, doi: https://dx.doi.org/10.1021/acs.oprd.0c00117 (2020).

[16] Maier, M. C., Leitner, M., Kappe, C. O., Gruber-Woelfler, H., A modular 3D printed isothermal heat flow calorimeter for reaction calorimetry in continuous flow, React. Chem. Eng., 5, 1410-1420; doi: https://doi.org/10.1039/d0re00122h (2020).

[17] Glotz, G., Knoechel, D. J., Podmore, P., Gruber-Woelfler, H., Kappe, C. O., Reaction Calorimetry in Microreactor Environments – Measuring Heat of Reaction by Isothermal Heat Flux Calorimetry, Org. Process Res., 21, 763−770, doi: https://doi.org/10.1021/acs.oprd.7b00092 (2017).

[18] Klinkert, A., Friedrich, Z., Glatt, E., Augustin, W., Scholl, S., Polymer Versus Polymerization Fouling: Basic Deposition Mechanisms During Emulsion Polymerization by the Example of a Vinyl Acetate and Versa 10 Copolymer, Macromolecular Reaction Engineering, 18 (3), DOI: https://doi.org/10.1002/mren.202300057 (2024).

[19] Hartog, A. H., An introduction to distributed optical fiber sensors (Taylor & Francis Group, 2018).

[20] Osenberg, M., Foerster, J., Westerdick, S., Tebruegge, J., v. Grotthuss, E., Musch, T., Ultrasound based Fouling Detection in Polymerization Processes, Sensors and Measuring Systems; 21th ITG/GMA-Symposium, VDE Verlag GmbH, Berlin, Offenbach, ISBN 978-3-8007-5835-7 (2022).

[21] Marcon, L., Chiuchiolo, A., Castaldo, B., Bajas, H., Galtarossa, A., Bajko, M., Palmieri, L., The Characterization of Optical Fibers for Distributed Cryogenic Temperature Monitoring, Sensors, 22 (11), 4009; doi: https://doi.org/10.3390/s22114009 (2022).

[22] Froggatt, M., Soller, B. J., Kreger, S. T., Wolfe, M. W., Distributed Strain and Temperature Discrimination in Unaltered Polarization Maintaining Fiber, Optical Fiber Sensors, OSA Technical Digest (CD), Optica Publishing Group; doi: https://doi.org/10.1364/OFS.2006.ThC5 (2006).

[23] Smith, J., Brown, A., DeMerchant, M., Bao, Y., Simultaneous distributed strain and temperature measurement, Applied Optics, 38, 25, 5372-5377: doi: https://doi.org/10.1364/AO.38.005372 (1999).

[24] Lu, X., Thomas, P. J., Hellevang, J. O., A Review of Methods for Fibre-Optic Distributed Chemical Sensing, Sensors 19(13), 2876; https://doi.org/10.3390/s19132876 (2019).

[25] Lu, X., Soto, M. A., Thévenaz, L. Impact of the fiber coating on the temperature response of distributed optical fiber sensors at cryogenic ranges. *Journal of Lightwave Technology* **36(4),** 961-967; https://doi.org/10.1109/JLT.2017.2757843 (2017).

[26] Ghafoori, Y., Vidmar, A., Kryžanowski, A., A Dynamic Calibration of Optical Fiber DTS Measurements Using PEST and Reference Thermometers, Sensors, 22 (10), 3890; doi: https://doi.org/10.3390/s22103890 (2022).

[27] Sweeney, D. C., Sweeney, D. M., Petrie, C. M., Graphical Optimization of Spectral Shift Reconstruction for Optical Backscatter Reflectometry, Sensors, 21, 6154; doi: https://doi.org/10.3390/s21186154 (2021).

[28] Drake, D. A., Sullivan, R. W., Wilson, J. C., Distributed Strain Sensing from Different Optical Fiber Configurations, Inventions, 16(3), doi: https://doi.org/10.3390/inventions3040067 (2018).

[29] Glaesemann, G. S., Corning Incorporated, Optical Fiber Mechanical Reliability Review of Research at Corning's Optical Fiber Strength Laboratory, WP8002, July 2017.

[30] Kurkjian, C. R., Simpkins, P. G., Inniss D. Strength, degradation and coatings of Silica Lightguides. J. Am. Ceram. Soc. 76(5), 1106-12 (1993).

[31] Klippert, M., Pauer, W., Determination of the clogging time for continuous emulsion copolymerization in a tubular reactor using distributed optical fiber sensors, Chemical Engineering Research and Design, 215, doi: https://doi.org/10.1016/j.cherd.2025.02.012 (2025).

[32] Jones, J. T., Sweeney, D. C., Birri, A., Petrie, C. M., Blue, T. E. Calibration of distributed temperature sensors using commercially available SMF-28 optical fiber from 22° C to 1000° C. IEEE Sensors Journal 22(5), 4144-4151; https://doi.org/10.1109/JSEN.2022.3146185 (2022).

[33] Klippert, M., Pauer, W., Distributed optical fiber sensors for real-time tracking of fouling buildup for tubular continuous polymerization reactors, Chemical Engineering Research and Design, 211, doi: https://doi.org/10.1016/j.cherd.2024.10.007 (2024).

[34] Price, D. M., Jarrat, M., Thermal conductivity of PTFE and PTFE composites, Thermochimica Acta, 392(393), doi: https://doi.org/10.1016/S0040-6031(02)00105-3 (2002).

[35] Elkholy, A., Rouby, M., Kempers, R., Characterization of the anisotropic thermal conductivity of additively manufactured components by fused filament fabrication, Progress in Additive Manufacturing, 4, doi: https://doi.org/10.1007/s40964-019-00098-2 (2019).

[36] Rust, S., Osenberg, M. Musch, T., Pauer, W., Ultrasonic and conversion-based inline fouling measurements for continuous emulsion copolymerization of vinyl acetate in a tubular reactor, Scientific Reports, 14, 4077, doi: https://doi.org/10.1038/s41598-024-54321-4 (2024).

7. Discussion

In the presented dissertation the process of understanding Rayleigh OFDR DOFS and reaction engineering surrounding the continuous copolymerization of VAc and VV10 is recorded, culminating in the application of these DOFS for mathematical fouling modelling and flow reactor calorimetry. The first publication *Distributed Fiber Optic Sensors for real-time tracking of fouling buildup for tubular continuous polymerization reactors* (2024) was focused on the integration of DOFS into a flow reactor and the optimization of DOFS installation, manufacture from telecommunications cables and DOFS calibration. The second publication *Determination of the clogging time for continuous emulsion copolymerization in a tubular reactor using Distributed Optical Fiber Sensors* (2025) explored ways to use the spatial resolution of DOFS temperature measurement for hotspot tracking during a reaction with heavy fouling. Mathematical models describing the spatial and temporal change of the free reactor volume were created and fitted to the DOFS data. The found parameters were able to elucidate the rate at which fouling is deposited inside the reactor and the shape of the free internal reactor volume during reaction progress. From the free volume, the foulant volume could be calculated, and from this estimation of the foulant mass was possible. The resulting fouling rate (deposition mass over time) aligned well with the fouling rate recorded for the same reaction at 20 °C in another reactor.[73] The models were also used on cut data sets in order to try extrapolating from this limited data and predict the time at which the reactor will clog. The predicted clogging times were within a range of 0.89–1.28 (1 expressing perfect agreement with the experimental clogging time). The third publication *Spatially resolved reaction calorimetry and fouling monitoring in a continuous tubular emulsion polymerization reactor* (2025) presented a proof of concept for the use of DOFS for the construction of continuous flow calorimeters. The reaction heat of the copolymerization of VAc and VV10 could be found in thermal calculations with the DOFS and thermocouple data in the setup. The thermal conversion evolution throughout the reaction time was comparable to the gravimetrical conversion and discrepancies could be explained.

The integration of DOFS into the walls of a tubular flow reactor and their calibration needs to be discussed further, as well as the results of the mathematical studies on reactor fouling and the improvement of the continuous flow calorimeter setup.

First and foremost, during the progress of the experiments discussed in this document, a palpable degradation of the DOFS integrated into the reactor setup was noticed. This is caused in part by the mechanical stress the DOFS face from being in a flow hood where experiments

are carried out, and in a setup where the reactor tubing is entirely removed and replaced between each experiment. Due to the prototypical nature of the setup the DOFS were never sufficiently integrated and protected from the environment and disturbances. Another part of the degradation is likely caused by the absorption of glycerol, moisture and solvent vapor into the protective polymer coating of the DOFS and then possibly into the glass itself. In literature the presence of Lewis acids is repeatedly mentioned as a factor in silica fiber degradation. Amongst the highly polar and hygroscopic environment the thermal paste provides, it may be possible that some of the elemental aluminium reacts and forms other aluminium compounds, many of which are notorious Lewis acids. Over the course of half a year of a DOFS being inside a reactor channel with such a paste, the DOFS have become much more likely to break from careful rearrangement than before. This decrease in strength has not been quantified. The data quality from the DOFS has also decreased over time, with more artifacts and higher drift over time. This likely contributed to the reason why the DOFS needed to be re-calibrated for every measurement, even though an undisturbed fiber should not exhibit a strong drift. These fibers, as they were integrated in the discussed way, were subject to substantial parameter drift.

This has further complicated the calorimetric calculations presented in this dissertation, as they have bene carried out in the final setup over the course of many months, with actively degrading DOFS. The glycerol termination solutions are likely to absorb more moisture from the environment, as glycerol is highly hygroscopic. This changes the refractive index and may cause a gradual mismatch of the index of the termination and the glass fiber core. Such a change also results in signal degradation. The effect of a bad RI match between fiber and termination are illustrated in the first publication discussed in this cumulative dissertation.

During experiments in the half shell steel reactor the integrated DOFS was in contact with acetone after each experiment and the data was instantly affected negatively. Within three experiments the data had become unusable and during a majority of the experiments, the DOFS were destroyed during handling. An exoskeleton for the reactor to protect DOFS has been built but not explored further.

Figure 14 shows a suggestion for a reactor setup similar to the last setup used in the work leading up to this publication. A circular cross section is shown, too. This setup would be able to protect the DOFS much more efficiently and with rigid scaffolding material (e.g. steel) the mechanical destruction of the DOFS would be prevented. Elimination of mechanically introduced strain (changes) in the DOFS would also combat the drift experienced in the previous setup and may therefore ensure that calibration frequency could be reduced. The

terminations of the fibers should be put into a dark box but not held in place there firmly to minimize strain. Use of a longer fiber with at least four meters of excess length at the end would make the termination issue less critical, as the reflected light at the end of the fiber would be attenuated on its way back into the measurement section. However, adequate termination is still preferrable to ensure the best SNR.

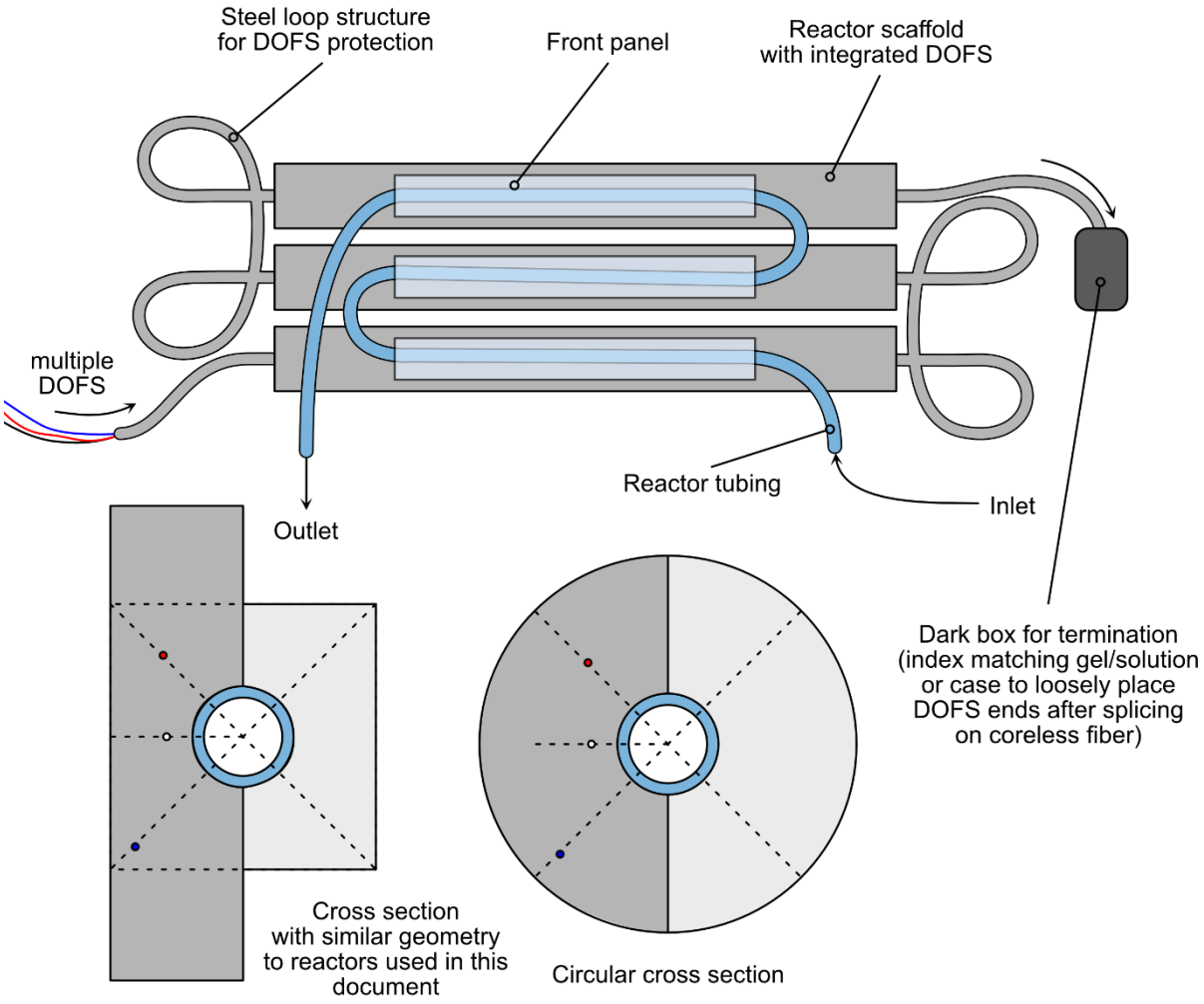

Figure 14: Sketch of a suggested flow reactor setup for DOFS protection with the possibility of exchanging reactor tubing between reactions.

An alternative to the thermal paste as a channel filler may be hydrogen scavenger or non-hygroscopic gel. Such gels have been studied in conjunction with long term stability of fiber optic cables. Their thermal properties would need to be examined.[99,100] It may be useful to investigate pre-loading the DOFS with a constant strain (e.g. using springs) over straight sections of fiber for compensation of the effect of strain changes on the DOFS signal.

The temperature resolution and calibration complications have been recurring topics throughout the presented work. The previously used method for calibration used hot water conveyed into the reactor at raised temperature and cooling off during reactor passage. Therefore, the front of the reactor was always calibrated over a bigger temperature range than the end of the reactor. In the case of the copolymerization reaction the hotspot formed towards the middle of the reactor and moved downstream. That region of the reactor and therefore of the DOFS was never calibrated at a temperature range big enough to cover the high hotspot temperature (over 60 °C). The high temperature also caused the PLA to warp after repeated experiments.

To enable calibration over a bigger temperature range for the entirety of the reactor length, a different method of temperature control is needed. An option may be the use of a half shell reactor model. The half-shell steel reactor presented in the *Unpublished work* section could be used as a model for such a reactor. In the previous reactor-DOFS setup thermocouples were used in six places instream to determine the temperature at their locations. In a half-shell reactor, it would be beneficial to insert two thermocouples in the space for the heat exchange medium, one at the inlet and one at the outlet of the medium. That way the total removed or added heat from the reactor could also be calculated via the temperature difference within the medium (if external heat transfer is accounted for). In order for precise and simple DOFS calibration it would be beneficial to adjust the temperature in stream and in the heat exchange medium to each other, ensuring that all three DOFS at the three different radial distances were at the same temperature. This would allow for skipping of the heat transfer calculations within the reactor wall for the DOFS calibration.

With external temperature control it may be possible to create a stronger temperature gradient in the reactor wall during reactions and therefore raise the temperature difference between the different DOFS. This would improve the resolution and precision of thermal calculations. The heat transfer of the inner shell with DOFS to the heat exchange medium could also be described with less use of assumptions. Previously, the external heat exchange was between the PLA reactor surface and the room temperature air in the laboratory with no temperature, flow and moisture control. Figure 15 shows a suggestion for how such a reactor may be built in a cross-sectional view. The gasket and heat exchanger configuration of the Fluitec steel reactor could be combined with the concept shown in Figure 15.

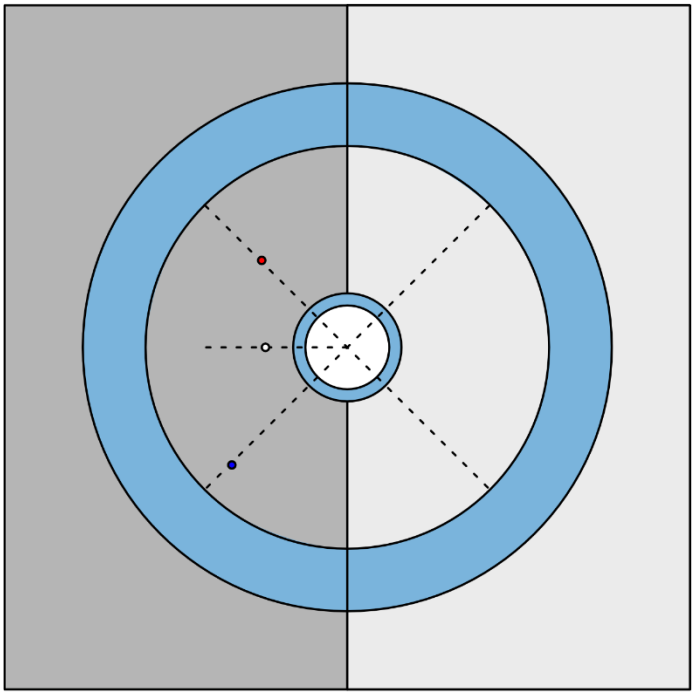

Figure 15: Proposal of a half shell reactor with integrated DOFS.

The spatial resolution of the DOFS could be used to a higher degree if the calibration were improved and the temperature difference between the DOFS was larger. The calculation of spatially distributed heat flow was not possible in the presented setup, because the small temperature differences were impossible to resolve meaningfully given the problems with calibration. With a better setup, improved DOFS integration and protection, as well as better calibration, spatially resolved calorimetric studies could be carried out.

For a reaction or process without fouling, the instream temperature can be calculated from the DOFS data. For other processes, an instream temperature measurement is needed. Previously, thermocouples were used, but the low spatial resolution (over 40 cm) caused the axial heat transfer to be underestimated. An instream integration of a DOFS in a thin steel capillary may be an option to remedy this issue. However, this steel capillary would need to be removed and cleaned after fouling heavy reactions, like the ones carried out in the presented document. This could cause damage. The fouling buildup on an axial instream capillary may also be greater than on the radially inserted thermocouples (lower shear strength, bigger surface area). This may cause the measured temperature inside the capillary to be lower than in the stream. It may be an option to use a capillary with a DOFS, if a fouling prevention coating were applied to its

outside. The issue of instream temperature measurement for fouling heavy processes is one that requires further research. Without it, the axially transported heat released during reaction cannot be measured and the calorimeter would only be able to measure heat loss. The reaction calorimeter model presented in this document cannot function without instream temperature measurement.

The half-shell reactor model is suggested in the framework of calorimetry and hotspot tracking experiments of heavily fouling reactions. In Figure 14 and 15 an exchangeable tube is shown to be the inside of the reactor in order to allow weighing of the tube and its exchange between reactions. Such a tube could also be replaced with any tubing with the same outer diameter. Therefore, coatings could be applied externally and then the pretreated tubing could be inserted for an experiment. The tube could also be cleaned externally and then be reused, if such a process is feasible. In this context the instream temperature measurement becomes a problem again. Previously, the thermocouples were inserted through small ports in the side of the reactor tubing and PLA printed parts and then closed off with silicone. A port system for a DOFS capillary would be an engineering issue worth studying for a reaction flow calorimeter as it is being suggested.

The DOFS data captured to use for hotspot tracking and modelling of fouling behavior for the second publication discussed in this dissertation was not ideal for determining the exact hotspot position. Figure 16 is a visualization of the problem.

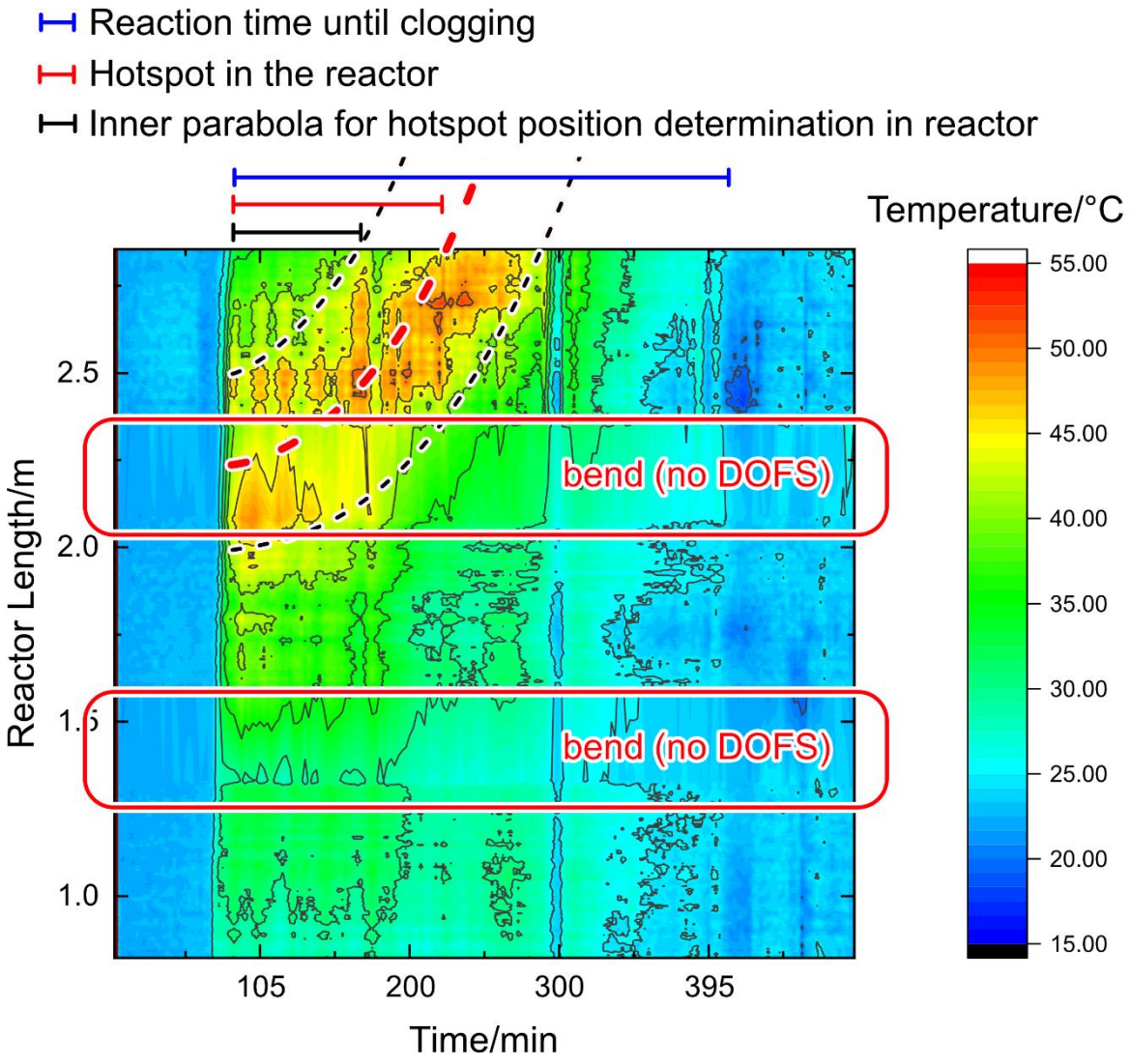

Figure 16: Heatmap used for hotspot tracking with highlighted parabolic curves (black) fitted from contour data at certain temperatures, enclosing the real hotspot position to the left and right, and the estimated hotspot position (red).

The time window in which the inner parabola used to estimate the hotspot position is overlapping the heatmap is relatively small in comparison to the reaction time until clogging (less than 30 %). There is also an overlap of the outer parabola and the area of the bend (hind-end of hotspot as defined by area between the parabolas not in section with DOFS). These two prolonged instances of data defining hotspot positions being lost significantly lower the precision with which the hotspot was located. This would be remedied by a fundamental change in reactor setup. A reactor without any bends would be preferrable in this case, as DOFS cannot be used reliably in bends (this may actually be possible if the bend radius is large and the fiber channels allow for good slip, but it would need further research). Furthermore, if the current reaction setup was used, a lengthening of the inlet tube by ca. 80 cm would move the hotspot

upstream and towards the beginning of the section with DOFS monitoring. This would make it possible to record the movement of the hotspot for a longer time. The broadness of the hotspot is also large in comparison to the reactor length. During the fouling process the hotspot does not only move downstream but also broadens, but this latter process cannot be pictured in this data set. A longer inlet tube and a longer reactor with DOFS monitoring would help with this.

The mathematical functions describing hotspot movement were parameterized using this data. It was necessary to establish realistic starting parameters and, in some cases, narrow the parameter range (for example the fouling volume would have been predicted as negative for some functions without range definitions). Without these pre-definitions many of the models do not yield valid results, however, to the author's knowledge, this is a known problem in modelling and simulating.

Overall, it was shown that DOFS are a valuable addition to chemical engineering and their spatially resolved temperature measurements can be used for a variety of applications. Hotspot tracking and subsequent modelling of the fouling deposition during reaction was successfully carried out, as well as calorimetric calculations using DOFS data. In this chapter the sub-optimality of the setups these experiments were carried out in was discussed in detail and more optimal setups and methods of DOFS integration were suggested and explained.

8. References

[1] H. Hernandez, K. Tauer, Heterophase Polymerization: Basic Concepts and Principles, Jenny Stanford Publishing, 1. Edition, DOI: https://doi.org/10.1201/9781003119296 (2021).

[2] C. S. Chern, Emulsion polymerization mechanisms and kinetics, Progress in Polymer Science, 31(5), p.443-486, DOI: https://doi.org/10.1016/j.progpolymsci.2006.02.001 (2006).

[3] K. Takamura, edited by D. Urban, Polymer Dispersions and Their Industrial Applications, Wiley-VCH Verlag GmbH & Co. KGaA, DOI: https://doi.org/10.1002/3527600582 (2002).

[4] W. Pauer, Reactor Concepts for Continuous Emulsion Polymerization, Advances in Polymer Science, DOI: https://doi.org/10.1007/12_2017_24 (2017).

[5] J. M. Asua, Emulsion polymerization: From fundamental mechanisms to process developments, Journal of Polymer Science, 42 (5), p.1025-1041, DOI: https://doi.org/10.1002/pola.11096 (2004).

[6] S. Rust, Investigations on the formation of fouling in continuously operated polymerisations, Dissertation, URL: https://ediss.sub.uni-hamburg.de/handle/ediss/11054 (2024).

[7] J. Herrera-Ordonez, Controversies on the mechanism and kinetics of emulsion polymerization: An updated critical review, Advances in Colloid and Interface Science, 320, 103005, DOI: https://doi.org/10.1016/j.cis.2023.103005 (2023).

[8] J. M. Asua, Challenges in Polymerization in Dispersed Media, Polymer Reaction Engineering of Dispersed Systems, DOI: https://doi.org/10.1007/12_2017_21 (2017).

[9] S. Rust, W. Pauer, Determination of inline-particle sizes by turbidity measurement in high solid content emulsion polymerization, Journal of Polymer Research, 29, DOI: https://doi.org/10.1007/s10965-022-03141-z (2022).

[10] D. Bloch, P. Bröge, W. Pauer, Inline Turbidity Measurements of Batch Emulsion Polymerization, Macromolecular Reaction Engineering, 11, DOI: https://doi.org/10.1002/mren.201600063 (2017).

[11] Zubov, A., et al., Bringing the on-line control and optimization of semibatch emulsion copolymerization to the pilot plant, Macromolecular Reaction Engineering, 11(4), DOI: https://doi.org/10.1002/mren.201700014 (2017).

[12] Institut für Arbeitsschutz der deutschen gesetzlichen Unfallversicherung GESTIS-Stoffdatenbank, URL: https://gestis.dguv.de/search (accessed 2025).

[13] A. Agirre et al., Semicontinuous Emulsion Co-polymerization of Vinyl Acetate and VeoVa10, Industrial & Engineering Chemistry Research, 53 (22), DOI: https://doi.org/10.1021/ie4032499 (2013).

[14] D. Distler, Wässrige Polymerdispersionen, Wiley-VCH Verlag GmbH, DOI: https://doi.org/10.1002/3527603263 (1998).

[15] Eurostat, Total production, ds-056121, [20165230] Polymers of vinyl acetate, in aqueous dispersion, in primary forms, URL: https://ec.europa.eu/eurostat/databrowser/bookmark/dd8da52b-a4c4-4838-925e-25a11325fa89?lang=en, last update: 15.07.2025.

[16] Research and Markets. Global Vinyl Acetate Market Report 2013-2018 & 2023; 2019.

[17] Eurostat, Total production, ds-056121, [20165250] Polymers of vinyl acetate, in primary forms (excluding in aqueous dispersion), URL: https://ec.europa.eu/eurostat/databrowser/bookmark/eab7ccd3-a345-4b83-9f93-0fcce6a50b4c?lang=en, last update: 15.07.2025.

[18] M. S. El-Aasser, J. W. Vanderhoff, Emulsion Polymerization of Vinyl Acetate, Applied Science Publishers ltd, DOI: https://doi.org/10.1007/978-94-009-8114-0 (1981).

[19] B. Schroeter, Kinetik von Redoxinitiatoren für die Emulsionspolymerisation, Dissertation, URL: https://ediss.sub.uni-hamburg.de/bitstream/ediss/7920/1/Dissertation.pdf (2018).

[20] L. I. Jacob, W. Pauer, B. Schröter, Influence of redox initiator component ratios on the emulsion copolymerisation of vinyl acetate and neodecanoic acid vinyl ester, RSC Advances, 22, doi: https://doi.org/10.1039/D2RA01811J (2022).

[21] B. M. Budhlall, Role of grafting in the emulsion polymerization of vinyl acetate with poly(vinyl alcohol) as an emulsifier. I. Effect of the degree of blockiness on the kinetics and mechanism of grafting, Journal of Polymer Science, 39 (20), DOI: https://doi.org/10.1002/pola.10016 (2001).

[22] S. J. Bohórquez, J. M. Asua, Poly(vinyl alcohol) Grafting in Miniemulsion Polymerization, Macromolecules, 41 (22), DOI: https://doi.org/10.1021/ma801476e (2008).

[23] R. Farwaha, L. De Sousa Gomes, Vinyl Acetate-Versatic Acid Vinyl Ester Copolymer for Masonry Coatings, white paper by Celanese Emulsions GmbH, 2009 ACSeries Coatings for Concrete, URL: https://www.paint.org/wp-content/uploads/2021/09/Vinyl-Acetate-Versatic-Acid-Masonry-Coatings_Jan-2010.pdf (2009).

[24] A. Klinkert et al., Polymer Versus Polymerization Fouling: Basic Deposition Mechanisms During Emulsion Polymerization by the Example of a Vinyl Acetate and Versa 10 Copolymer, Macromolecular Reaction Engineering, 18 (3), DOI: https://doi.org/10.1002/Fmren.202300057 (2024).

[25] A. Durand, S. Engell, Batch to Conti Transfer of Polymer Production Processes, Macromolecular Reaction Engineering, 10 (4), DOI: https://doi.org/10.1002/mren.201600031 (2016).

[26] F. J. Keil, Process intensification, Reviews in Chemical Engineering, 34 (2), DOI: https://doi.org/10.1515/revce-2017-0085 (2017).

[27] M. Moser, et al., Continuous milli-scale reaction calorimeter for direct scale-up of slow chemistry, Journal of Flow Chemistry, 11, 691-699; DOI: https://doi.org/10.1007/s41981-021-00204-y (2021).

[28] J. Antes, et al., Ortsaufgelöste Reaktionskalorimetrie in mikrostrukturierten Reaktoren, Chemie Ingenieur Technik, 80(9), DOI: https://dx.doi.org/10.1002/cite.200750657 (2008).

[29] M. -A. Schneider, F. Stoessel, Determination of the kinetic parameters of fast exothermal reactions using a novel microreactor-based calorimeter, Chemical Engineering Journal 115 (1-2), 73-83, DOI: https://doi.org/10.1016/j.cej.2005.09.019 (2005).

[30] M. Romano, C. Pradere, J. Toutain, J. C. Batsale, Quantitative kinetics and enthalpy measurements of biphasic underflow chemical reactions using infrared thermography, Experimental Thermal and Fluid Science, 67, 14 – 17, DOI: https://doi.org/10.1016/j.expthermflusci.2014.11.002 (2015).

[31] F. Reichmann, S. Millhoff, Y. Jirmann, N. Kockmann, Reaction Calorimetry for Exothermic Reactions in Plate-Type Microreactors Using Seebeck Elements, Chem. Eng. Technol., 40 (11), 2144 – 2154, DOI: https://doi.org/10.1002/ceat.201700419 (2017).

[32] D. Mortzfeld, et al., Reaction Calorimetry in Continuous Flow Mode: A New Approach for the Thermal Characterization of High Energetic and Fast Reactions, Org.

Process Res. Dev., 24, 2004 – 2016, DOI: https://dx.doi.org/10.1021/acs.oprd.0c00117 (2020).

[33] M. C. Maier, M. Leitner, C. O. Kappe, H. Gruber-Woelfler, A modular 3D printed isothermal heat flow calorimeter for reaction calorimetry in continuous flow, React. Chem. Eng., 5, 1410-1420; DOI: https://doi.org/10.1039/d0re00122h (2020).

[34] G. Glotz, D. J. Knoechel, P. Podmore, H. Gruber-Woelfler, C. O. Kappe, Reaction Calorimetry in Microreactor Environments – Measuring Heat of Reaction by Isothermal Heat Flux Calorimetry, Org. Process Res., 21, 763−770, DOI: https://doi.org/10.1021/acs.oprd.7b00092 (2017).

[35] A. Agirre, H.-P. Weitzel, W.-D. Hergeth, J. M. Asua, Process intensification of VAc–VeoVa10 latex production, Chemical Engineering Journal, 266, DOI: https://doi.org/10.1016/j.cej.2014.12.053 (2015).

[36] B. M. Marks, Process of polymerization, Patent US2161481 (1937).

[37] Improvements in or relating to the manufacture of synthetic rubber-like masses, Patent GB517951A (1937).

[38] D. C. Adams, Loop reactor for emulsion polymerization, Patent EP20120160094 (2012).

[39] J. M. Asua, Challenges and Opportunities in Continuous Production of Emulsion Polymers: a Review, Macromolecular Reaction Engineering, 10 (4), DOI: https://doi.org/10.1002/mren.201500032 (2015).

[40] K. R. Geddes, Start-up and Growth Mechanisms in the Loop Continuous Reactor, British Polymer Journal, 21, DOI: https://doi.org/10.1002/pi.4980210513 (1989).

[41] N. Epstein, Thinking about Heat Transfer Fouling: A 5x5 Matrix, Heat Transfer Engineering, 4 (1), DOI: https://doi.org/10.1080/01457638108939594 (1983).

[42] A. P. Watkinson, D. I. Wilson, Chemical reaction fouling: A review, Experimental Thermal and Fluid Science, 14(4), DOI: https://doi.org/10.1016/S0894-1777(96)00138-0 (1997).

[43] T. R. Bott, Fouling of Heat Exchangers, Elsevier Science B.V., DOI: https://doi.org/10.1016/B978-0-444-82186-7.X5000-3 (1995).

[44] H. Müller-Steinhagen, M. R. Malayeri, A. P. Watkinson, Heat Exchanger Fouling: Mitigation and Cleaning Strategies, Heat Transfer Engineering, 32 (3-4), DOI: https://doi.org/10.1080/01457632.2010.503108 (2011).

[45] R. Oliviera, Understanding adhesion: A means for preventing fouling, Experimental Thermal and Fluid Science, 14 (4), DOI: https://doi.org/10.1016/S0894-1777(96)00134-3 (1997).

[46] J. Urrutia, A. Peña, J. M. Asua, Reactor Fouling by Preformed Latexes, Molecular Reaction Engineering, 11 (1), DOI: https://doi.org/10.1002/mren.201600043 (2016).

[47] C. S. Chern, Y. C. Chen, Stability of the polymerizable surfactant stabilized latex particles during semibatch emulsion polymerization, Colloidand Polymer Science, 275 (2), (1997).

[48] M. F. Kemmere, J. Meuldijk, A. A. H. Drinkenburg, A. L. German, Emulsification in batch emulsion polymerization, Journal of Applied Polymer Science, 74 (13), DOI: https://doi.org/10.1002/(SICI)1097-4628(19991220)74:13<3225::AID-APP26>3.0.CO;2-3 (1999).

[49] M Zubitur, J.M Asua, Factors affecting kinetics and coagulum formation during the emulsion copolymerization of styrene/butyl acrylate, Polymer, 42 (14), DOI: https://doi.org/10.1016/S0032-3861(01)00039-8 (2001).

[50] C. Kiparissides, J. F. Macgregor, A. E. Hamielec, Continuous emulsion polymerization of vinyl acetate. Part I: Experimental studies, The Canadian Journal of Chemical Engineering, 58 (1), DOI: https://doi.org/10.1002/cjce.5450580108 (1980).

[51] E. Gelinski, Coagulation, fouling and mixing during VDF emulsion polymerization, Dissertation, URL: https://theses.hal.science/tel-03967165v1 (2023).

[52] H. Bianco, Y. Cohen, M. Narkis, Coagulum formation and elimination in emulsion copolymerization of tribromostyrene with styrene, Polymers for Advanced Technologies, 7 (10), DOI: https://doi.org/10.1002/(SICI)1099-1581(199610)7:10<809::AID-PAT582>3.0.CO;2-0 (1996).

[53] R. C. Elgebrandt et al., Analysis of shear-induced coagulation in an emulsion polymerisation reactor using computational fluid dynamics, Chemical Engineering Science, 60 (7), DOI: https://doi.org/10.1016/j.ces.2004.12.010 (2005).

[54] V. Lowry, M. S. El-Aasser, J. W. Vanderhoff, A. Klein, Mechanical Coagulation in Emulsion Polymerizations, Journal of Applied Polymer Science, 29 (12), DOI: https://doi.org/10.1002/app.1984.070291225 (1984).

[55] M. A. Apecetche, X. Bai, K. J. Cann, Process for reducing polymer build-up in recycle lines and heat exchangers during polymerizations employing butadiene, isoprene, and/or styrene, Parent EP0935614B1 (1996).

[56] D. Y. Tong, Reducing polymer fouling and agglomeration in acrylate/methacrylate processes, Patent US9884951B2 (2015).

[57] S. Rust, W. Pauer, Formulation and process determined fouling prediction for the continuous emulsion co polymerisation of vinyl acetate, Journal of Polymer Research, 30, DOI: https://doi.org/10.1007/s10965-023-03588-8 (2023).

[58] L. Cohen, Polymerization reactors coated with polymer-inhibitor complexes, Patent US4256864A (1979).

[59] L. K. Wempe, B. D. Bauman, Method for reducing wall fouling in vinyl chloride polymerization, Patent US4420591A (1982).

[60] D. M. McFadden, R. S.-H.Wu, The reduction of polymer fouling on reactor surfaces in a continuous process for preparing polymers, Patent EP 1 024 149 A2 (2000).

[61] J. S. Lowell, K. A. Dooley, R. Li, D. K. Aruho, Systems and methods for mitigating polymer fouling, Patent WO2022173784A1 (2022).

[62] A. C. S. M. Carvalho, D. L. Chicoma, C. Sayer, R. Giudici, Development of a Continuous Emulsion Copolymerization Process in a Tubular Reactor, Industrial & Engineering Chemistry Research, 49 (21), DOI: https://doi.org/10.1021/ie100422v (2010).

[63] Y. Ekowati, et al., Synthetic organic polymer fouling in municipal wastewater reuse reverse osmosis, Water Reuse, 4 (3), DOI: https://doi.org/10.2166/wrd.2014.046 (2014).

[64] N. AlSawaftah, W. Abuwatfa, N. Darwish, G. Husseini, A Comprehensive Review on Membrane Fouling: Mathematical Modelling, Prediction, Diagnosis, and Mitigation, Water, 13 (9), DOI: https://doi.org/10.3390/w13091327 (2021).

[65] U. B. Deshannavar, R. Marappagounder, Revisiting Threshold Fouling Models for Crude Oil Fouling, Heat Transfer Engineering, 42(17), DOI: https://doi.org/10.1080/01457632.2020.1800276 (2021).

[66] O. ur Rehman, et. al, Modeling Strategies for Crude Oil-Induced Fouling in Heat Exchangers: A Review, Proesses, 11(4), DOI: https://doi.org/10.3390/pr11041036 (2023).

[67] E. Rammerstorfer, The kinetics and mechanisms of fouling in crude oil heat transfer, Heat Transfer Engineering, 41(8), DOI: https://doi.org/10.1080/01457632.2018.1564202 (2020).

[68] T. Ardsomang, W. W. Hines, B. R. Upadhyaya, Heat Exchanger Fouling and Estimation of Remaining Useful Life, Proceedings of the Annual Conference of the PHM Society 2012, 5(1), DOI: https://doi.org/10.36001/phmconf.2013.v5i1.2773 (2013).

[69] C. Bernstein, Methoden zur Untersuchung der Belagsbildung in chemischen Reaktoren, Dissertation, URL: https://ediss.sub.uni-hamburg.de/handle/ediss/7311 (2017).

[70] M. Osenberg, et al., Ultrasound based Fouling Detection in Polymerization Processes, Sensors and Measuring Systems; 21th ITG/GMA-Symposium, VDE Verlag GmbH, Berlin, Offenbach, ISBN 978-3-8007-5835-7 (2022).

[71] A. Böttcher et al., Fouling Pathways in Emulsion Polymerization Differentiated with a Quartz Crystal Microbalance (QCM) Integrated into the Reactor Wall, Macromolar Reaction Engineering, 16 (2), DOI: https://doi.org/10.1002/mren.202100045 (2022).

[72] V. Neßlinger,S. Rust, J. Atlanov, W. Pauer, G. Grundmeier, Monitoring Polymeric Fouling in a Continuous Reactor by Electrochemical Impedance Spectroscopy. Chemie-Ingenieur-Technik, 93 (3), DOI https://doi.org/10.1002/cite.202300032 (2023).

[73] S. Rust, M. Osenberg, T. Musch, W. Pauer, Ultrasonic and conversion-based inline fouling measurements for continuous emulsion copolymerisation of vinyl acetate in a tubular reactor, Scientific Reports, 14, DOI: https://doi.org/10.1038/s41598-024-54321-4 (2024).

[74] M. Madani, Belagsbildung in chemischen Reaktoren unter Berücksichtigung von Oberflächenaspekten, Dissertation, URL: https://ediss.sub.uni-hamburg.de/handle/ediss/7630 (2017).

[75] A. Hohlen, W. Augustin, S. Scholl, Investigation of Polymer Depositions During the Synthesis in a Heat Exchanger, Chemie Ingenier Technik, 92 (5), DOI: https://doi.org/10.1002/cite.201900130 (2020).

[76] A. H. Hartog, An Introduction to Distributed Optical Fibre Sensors, CRC Press Taylor & Francis Group, DOI: https://doi.org/10.1201/9781315119014 (2017).

[77] L. Palmieri, L. Schenato, M. Santagiustina, A. Galtarossa, Rayleigh-Based Distributed Optical Fiber Sensing, Sensors, 22 (18), DOI: https://doi.org/10.3390/s22186811 (2022).

[78] C. Chen, L. Chen, X. Bao, Distributed temperature profile in hydrogen flame measured by telecom fiber and its durability under flame by OFDR. Optics Express 30(11), DOI: https://doi.org/10.1364/OE.455640 (2022).

[79] X. Lu, M. A. Soto, L. Thévenaz, Impact of the fiber coating on the temperature response of distributed optical fiber sensors at cryogenic ranges. Journal of Lightwave Technology 36(4), DOI: https://doi.org/10.1109/JLT.2017.2757843 (2017).

[80] D. K. Gifford, et al., Swept-wavelength interferometric interrogation of fiber Rayleigh scatter for distributed sensing applications, Proceedings, 6770 (Fiber Optic Sensors and Applications V), DOI: https://doi.org/10.1117/12.734931 (2007).

[81] M. F. Bado, J. R. Casas, A. Barrias, Performance of Rayleigh-Based Distributed Optical Fiber Sensors Bonded to Reinforcing Bars in Bending, Sensors, 18 (9), DOI: https://doi.org/10.3390/s18093125 (2018).

[82] S. Wang, E. Staeter, K. Lasn, Comparison of DOFS Attatchement Methods for Time-Dependant Strain Sensing, Sensors 21, 6879; https://doi.org/10.3390/s21206879 (2021).

[83] I. Fernandez, C. G. Berrocal, S. Almfeldt, R. Rempling, Monitoring of new and existing stainless-steel reinforced concrete structures by clad distributed optical fibre sensing. Structural Health Monitoring 22(1), 257-275; https://doi.org/10.1177/14759217221081149 (2023).

[84] T. Yang, Y. Wang, X. Wang, High-precision calibration for strain and temperature sensitivities of Rayleigh-scattering-based DOFS at cryogenic temperatures, Cryogenics, 124, DOI: https://doi.org/10.1016/j.cryogenics.2022.103481 (2022).

[85] M. Froggatt, et al. Distributed strain and temperature discrimination in unaltered polarization maintaining fiber. Optical Fiber Sensors, DOI: https://doi.org/10.1364/OFS.2006.ThC5 (2006).

[86] X. Li, C. Yang, S. Yang, G. Li, Fiber-Optical Sensors: Basics and Applications in Multiphase Reactors, Sensors 12(9), 12519-12544; https://doi.org/10.3390/s120912519 (2012).

[87] X. Lu, P. J. Thomas, J. O. Hellevang, A Review of Methods for Fibre-Optic Distributed Chemical Sensing, Sensors 19(13), 2876; https://doi.org/10.3390/s19132876 (2019).

[88] F. Nestler, V. P. Müller, M. Ouda, M. J. Hadrich, A. Schaadt, S. Bajohr, T. Kolb, A novel approach for kinetic measurements in exothermic fixed bed reactors: advancements in non-isothermal bed conditions demonstrated for methanol synthesis, Reaction Chemistry & Engineering 6, 1092-1107, https://doi.org/10.1039/D1RE00071C (2021).

[89] Y. Liu, X. Si, L. Wu, C. Mo, Y. Zhuang, European Patent Application EP000003945297A1, Reactor Temperature Measurement System, Reactor and Method for preparing a Fiber Bragg Grating (2022).

[90] Y. Zhang, L. Song, G. Kaiser, M. L. Hergenrother, B. K. Stober, P. H. Kalamaras, B. S. Umansky, U.S. National Stage Application US9746434B2, Method and system for determining flow distribution through a component (2014).

[91] F. Egner, R. Bank, A. Bauer, D. Verbeek, M. Lainer, U.S. National Stage Application US10173190B2, Fibre-optic temperature measurement in a catalyst material (2014).

[92] Fluves, Fiber optic sensing: A game-changer for industry 4.0 monitoring, URL: https://www.fluves.com/ (2024).

[93] J. M. Jacobs, Corning Incorporated, The Impact of Hydrogen on Optical Fibers, WP9007, September 2004.

[94] G. S. Glaesemann, Corning Incorporated, Optical Fiber Mechanical Reliability Review of Research at Corning's Optical Fiber Strength Laboratory, WP8002, July 2017.

[95] I. Kouzmina, I. Davis, Corning Incorporated, Corning ® CPC® Protective Coating – An Overview, WP3703, November 2021.

[96] Li, J., et al. Mechanical properties of polyimide coated optical fibers at elevated temperatures. Proceedings SPIE **9702**; https://doi.org/10.1117/12.2210957 (2016).

[97] Y. Lin, Y. Gong, Y. Wu, H. Wu, Polyimide-Coated Fiber Bragg Grating for Relative Humidity Sensing, Photonic Sensors, 5, 60-66, https://doi.org/10.1007/s13320-014-0218-8 (2014).

[98] Kurkjian, C. R., Simpkins, P. G., Inniss D. Strength, degradation and coatings of Silica Lightguides. J. Am. Ceram. Soc. 76(5), 1106-12 (1993).

[99] Corning Optical Communications, Gel-filled optical fiber cables with one or two buffer tubes for inter and intrabuilding, PG S026, URL: https://www.corning.com/catalog/coc/documents/generic-specifications/PGS026.pdf (2017).

[100] A. A. Stolov, J. Li, A. S. Hokansson, M. J. Hines, Effects of Hydrogen Scavenging Cable Gel on the Strength and Attenuation of Optical Fibers, Journal of Lightwave Technology, 40 (18), DOI: https://doi.org/10.1109/JLT.2022.3190817 (2022).

8. Appendix

8.1 Table of chemicals

Table 8.1: Chemicals used and their classification according to GHS including hazard pictograms, safety and precautionary statements.[12]

Chemical (CAS registry number)	GHS hazard pictogram	H-statements	P-statements
Acetone (67-64-1)		H225, H302, H319, H336, H373	P210, P235, P260, P305+P351+338
Aluminium powder (5 µm) (7429-90-5)		H250, H261	P210, P231+232, P233, P280, P302+335+334, P370+378
Ammonium iron (III) sulfate dodecahydrate (7783-83-7)		H318	P280, P305+351+338, P310
Ascorbic acid (50-81-7)	–	–	–
Glycerol (56-81-5)	–	–	–
Mowiol 4-88 (9002-89-5)	–	–	–
tert-Butyl hydroperoxide (75-91-2)		H226, H242, H302, H311, H330, H314, H317, H341, H411	P210, P220, P280, P301+330+331, P303+361+353, P305+351+338, P310

Chemical (CAS registry number)	GHS hazard pictogram	H-statements	P-statements
Tetrahydrofuran (109-99-9)		H225, H302, H319, H335, H336, H351	P210, P280, P301+312+330, P305+351+338, P370+378, P403+235
Vinyl acetate (108-05-4)		H225, H332, H335, H351, H412	P202, P210, P233, P273, P304+340+312, P308+313
Vinyl neodecanoate (51000-52-3)		H410	P273, P391, P501
Water	–	–	–

8.2 Supporting Information for *Determination of the clogging time for continuous emulsion copolymerization in a tubular reactor using distributed optical fiber sensors*

Supplemental Material

Determination of the clogging time for continuous emulsion copolymerization in a tubular reactor using Distributed Optical Fiber Sensors

Maria Klippert and Werner Pauer*

Institute for Technical and Macromolecular Chemistry, University of Hamburg, Bundesstraße 45, 20146 Hamburg, Germany

* Correspondence: werner.pauer@uni-hamburg.de

Table of Content

1. Geometry of available reactor volume with fouling

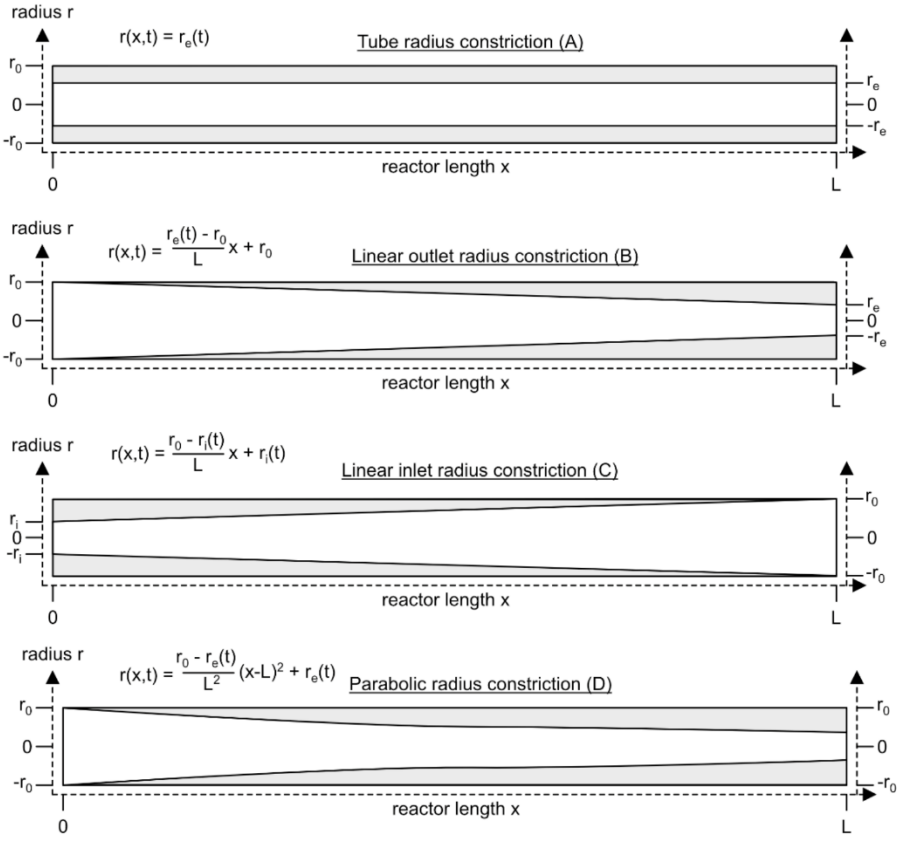

Figure 1: Geometrical assumptions of volumetric decrease due to fouling accumulation along the reactor length.

The equations shown in Figure 1 describe the perimeters of the reactor tube when fouling is constraining its volume. The reactor volume can be then calculated from these equations by using them as basis for a rotational solid, integrated over the length of the reactor (0 to L).

Decrease of r_e with time

Fouling is a dynamic process, and while the equations describe the shape of the free volume in the fouled reactor, the following equations depict the temporal change of the outlet or inlet diameter of the reactor between t_0 and t_{clog}, the start of fouling and the time of clogging. Times smaller than t_0 are not covered by the model.

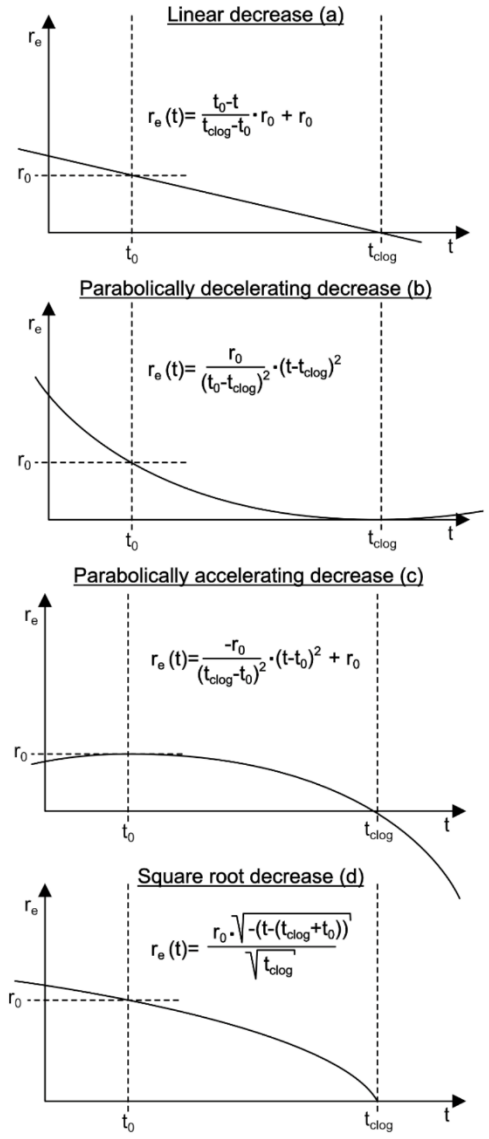

Figure 2: Change of the end tube radius r_e during reaction time, with t_0 being the time of the first detectable change in x_{max} due to fouling, until a full obstruction occurs at t_{clog}.

Linear decrease (a)

$$r_e(t) = -\frac{r_0 t}{t_{clog} - t_0} + r_0\left(1 + \frac{t_0}{t_{clog} - t_0}\right) = \frac{t_0 - t}{t_{clog} - t_0} r_0 + r_0$$

Cubically decelerating decrease (b)

$$r_e(t) = \left(\frac{r_0}{\left(t_0 - t_{clog}\right)^2} \cdot \left(t - t_{clog}\right)^2\right)$$

Cubically accelerating decrease (c)

$$r_e(t) = \left(-\frac{r_0}{\left(t_{clog} - t_0\right)^2} \cdot (t - t_0)^2 + r_0 \right)$$

Square root decrease (d)

$$r_e(t) = r_0 \frac{\sqrt{-\left(t - \left(t_{clog} + t_0\right)\right)}}{\sqrt{t_{clog}}}$$

2. General Volumetric Approach

$$x_{HS}(x,t) = \frac{\dot{m} \cdot L \cdot t_0}{\rho \cdot \int_0^L \pi (r(x,t))^2 dx}$$

Tube radius constriction (cylinder) (A)

$$x_{HS}(x,t) = \frac{\dot{m} \cdot L \cdot t_0}{\rho \cdot \int_0^L \pi (r_e(t))^2 dx}$$

With $D = \frac{\dot{m} \cdot L \cdot t_0}{\rho \cdot \pi}$

$$x_{HS}(t) = \frac{D}{[x\, r_e(t)^2]_0^L} = \frac{D}{L\, r_e(t)^2}$$

Linear outlet radius constriction (frustum) (B)

$$x_{HS}(x,t) = \frac{\dot{m} \cdot L \cdot t_0}{\rho \cdot \int_0^L \pi \left(\frac{r_e(t) - r_0}{L} \cdot x + r_0 \right)^2 dx}$$

With $D = \frac{\dot{m} \cdot L \cdot t_0}{\rho \cdot \pi}$

$$x_{HS}(x,t) = \frac{D}{\int_0^L \left(\frac{r_e(t) - r_0}{L} \cdot x + r_0 \right)^2 dx}$$

$$x_{HS}(t) = \frac{D}{\left[\frac{\left(\frac{r_e(t)-r_0}{L}x + r_0\right)^3}{3\frac{r_e(t)-r_0}{L}}\right]_0^L}$$

$$x_{HS}(t) = \frac{3D}{3Lr_0{}^2 + 3Lr_0(r_e(t)-r_0) + L(r_e(t)-r_0)^2}$$

$$x_{HS}(t) = \frac{3D}{Lr_e(t)^2 + Lr_0r_e(t) + Lr_0{}^2}$$

Linear inlet radius constriction (reverse frustum) (C)

$$x_{HS}(x,t) = \frac{\dot{m}\cdot L\cdot t_0}{\rho\cdot\int_0^L \pi\left(\frac{r_0-r_i}{L}\cdot x + r_i\right)^2 dx}$$

With $D = \frac{\dot{m}\cdot L\cdot t_0}{\rho\cdot\pi}$

$$x_{HS}(t) = \frac{D}{\left[\frac{\left(\frac{r_0-r_i}{L}x + r_i\right)^3}{3\frac{r_0-r_i}{L}}\right]_0^L}$$

Parabolic radius constriction (D)

$$x_{HS}(x,t) = \frac{\dot{m}\cdot L\cdot t_0}{\rho\cdot\int_0^L \pi\left(\frac{r_0-r_e(t)}{L^2}(x-L)^2 + r_e(t)\right)^2 dx}$$

With $D = \frac{\dot{m}\cdot L\cdot t_0}{\rho\cdot\pi}$

$$x_{HS}(t) = \frac{D}{\left[\frac{1}{15}\left(3\left(\frac{r_0-r_e(t)}{L^2}\right)^2(x-L)^5 + 10r_0\frac{r_0-r_e(t)}{L^2}(x-L)^3\right) + r_e(t)^2x\right]_0^L}$$

$$x_{HS}(L,t) = \frac{15D}{3L(r_0-r_e(t))^2 + 10r_e(t)L(r_0-r_e(t)) + 15r_e(t)^2L}$$

$$x_{HS}(L,t) = \frac{15D}{8Lr_e(t)^2 + 4Lr_0r_e(t) + 3Lr_0{}^2}$$

2.1 Time-dependency of the geometrical change given the previous assumptions (General Volumetric approach)

In all formulas variables are used, which exist in order to summarize constants. They are called *D*, *E*, *a*, *b*, *c*, *d*, *e* and *f*. These are not to be confused with other physical and mathematical variables.

Exemplary derivation of GV.Aa:

A

$$x_{HS}(x,t) = \frac{\dot{m} \cdot L \cdot t_0}{\rho \cdot \int_0^L \pi (r_e(t))^2 dx}$$

c

$$r_e(t) = \left(-\frac{r_0}{\left(t_{clog} - t_0\right)^2} \cdot (t - t_0)^2 + r_0 \right)$$

Ac

$$x_{HS}(t) = \frac{\dot{m} \cdot L \cdot t_0}{\rho \cdot \int_0^L \pi \left(r_0 - \frac{r_0}{\left(t_{clog} - t_0\right)^2} \cdot (t - t_0)^2 + r_0 \right)^2 dx}$$

with $D = \frac{\dot{m} \cdot L \cdot t_0}{\rho \pi}$ for all formulas

GV.Aa

$$x_{HS}(x,t) = \frac{D}{\int_0^L \left(\frac{t_0 - t}{t_{clog} - t_0} r_0 + r_0 \right)^2 dx}$$

$$x_{HS}(t) = \frac{D}{\left[\left(\frac{t_0 - t}{t_{clog} - t_0} r_0 + r_0 \right)^2 x \right]_0^L}$$

$$x_{HS}, t) = \frac{D}{L \left(\frac{t_0 - t}{t_{clog} - t_0} r_0 + r_0 \right)^2}$$

For the simplification $a = \frac{r_0}{t_{clog} - t_0}$.

$$x_{HS}(t) = \frac{D}{L(a(t_0 - t) + r_0)^2}$$

GV.Ab

With $a = \frac{r_0}{\left(t_0 - t_{clog}\right)^2}$.

$$x_{HS}(x,t) = \frac{D}{\int_0^L \left(a \cdot \left(t - t_{clog}\right)^2 \cdot x\right)^2 dx}$$

$$x_{HS}(t) = \left[\frac{3D}{a^2\left(t - t_{clog}\right)^4 x^3}\right]_L^0$$

$$x_{HS}(t) = \frac{3D}{a^2\left(t - t_{clog}\right)^4 L^3}$$

To simplify, $E = \frac{3\dot{m} \cdot t_0}{L^2 \rho \pi}$

$$x_{HS}(t) = \frac{E}{a^2\left(t - t_{clog}\right)^4}$$

GV. Ac

with $a = -\frac{r_0}{\left(t_{clog} - t_0\right)^2}$.

$$x_{HS}(x,t) = \frac{D}{\int_0^L \left((a \cdot (t - t_0)^2 + r_0) \cdot x\right)^2 dx}$$

$$x_{HS}(t) = \left[\frac{3D}{(a(t - t_0)^2 + r_0)^2 x^3}\right]_L^0$$

$$x_{HS}(t) = \frac{3D}{(a(t - t_0)^2 + r_0)^2 L^3}$$

With $E = \frac{3\dot{m} \cdot t_0}{L^2 \rho \pi}$

$$x_{HS}(t) = \frac{E}{(a(t - t_0)^2 + r_0)^2}$$

GV. Ad

With $E = \frac{\dot{m} \cdot L}{\rho \cdot \pi}$

$$x_{HS}(t) = \frac{E t_0}{L\left(r_0 \frac{\sqrt{-\left(t - \left(t_{clog} + t_0\right)\right)}}{\sqrt{t_{clog}}}\right)^2}$$

$$x_{HS}(t) = -\frac{Et_{clog}t_0}{Lr_0{}^2}\frac{1}{\left(t-\left(t_{clog}+t_0\right)\right)}$$

With $D = \frac{\dot{m}}{\rho\cdot\pi\cdot r_0{}^2}$

$$x_{HS}(t) = Dt_{clog}t_0\frac{1}{\left(t-\left(t_{clog}+t_0\right)\right)}$$

GV.Ba

$$x_{HS}(x,t) = \frac{D}{\int_0^L\left(\frac{\frac{t_0-t}{t_{clog}-t_0}r_0+r_0-r_0}{L}\cdot x+r_0\right)^2 dx}$$

With $a = \frac{r_0}{(t_{clog}-t_0)L}$

$$x_{HS}(t) = \frac{D}{\left[\frac{(ax(t_0-t)+r_0)^3}{3(at_0-at)}\right]_0^L}$$

$$x_{HS},t) = \frac{3D}{L^3a^2t_0{}^2+3L^2ar_0t_0-2L^3a^2t_0t+L^3a^2t^2-3L^2ar_0t+3Lr_0{}^2}$$

with $b = L^3a^2t_0{}^2+3L^2ar_0t_0+3Lr_0{}^2$, $c = -aL^2(2Lat_0+3r_0)$ and $d = L^3a^2$

$$x_{HS}(t) = \frac{3D}{b+ct+dt^2}$$

GV.Bb

With $a = \frac{r_0}{\left(t_0-t_{clog}\right)^2}$

$$x_{HS}(x,t) = \frac{D}{\int_0^L\left(\frac{a\cdot\left(t-t_{clog}\right)^2-r_0}{L}\cdot x+r_0\right)^2 dx}$$

$$x_{HS}(t) = \left[\frac{3DL^2\left(a\left(t-t_{clog}\right)^2-r_0\right)}{\left(\left(a\left(t-t_{clog}\right)^2-r_0\right)x+Lr_0\right)^3}\right]_L^0$$

X

$$x_{HS}(t) = \frac{3D}{L\left(a^2t^4 - 4a^2t_{clog}t^3 + \left(ar_0 + 6a^2{t_{clog}}^2\right)t^2 + \left(-2at_{clog}r_0 - 4a^2{t_{clog}}^3\right)t + {r_0}^2 + a{t_{clog}}^2r_0 + a^2{t_{clog}}^4\right)}$$

With $b = 4a^2t_{clog}$; $c = ar_0 + 6a^2{t_{clog}}^2$; $d = -2t_{clog}ar_0 - 4a^2{t_{clog}}^3$; $e = {r_0}^2 + ar_0{t_{clog}}^2 + a^2{t_{clog}}^4$

$$x_{HS}(t) = \frac{3D}{L(a^2t^4 - bt^3 + ct^2 + dt + e)}$$

GV.Bc

With $a = -\frac{r_0}{(t_{clog} - t_0)^2}$

$$x_{HS}(x,t) = \frac{D}{\int_0^L \left(\frac{(a\cdot(t-t_0)^2 + r_0) - r_0}{L}\cdot x + (a\cdot(t-t_0)^2 + r_0)\right)^2 dx}$$

$$x_{HS}(t) = \frac{D}{\int_0^L \left((a\cdot(t-t_0)^2 + r_0)\left(\frac{x}{L} + 1\right) - r_0\frac{x}{L}\right)^2 dx}$$

$$x_{HS}(t) = \left[\frac{3D(a{t_0}^2 - 2att_0 + at^2)}{L\left((a(t-t_0)^2 + r_0)\left(\frac{x}{L} + 1\right) - \frac{r_0x}{L}\right)^3}\right]_L^0$$

$$x_{HS}(t) = \frac{3D}{L(7a^2{t_0}^4 - 28a^2{t_0}^3t + (42a^2t^2 + 9ar_0){t_0}^2 + (-28a^2t^3 - 18ar_0t)t_0 + 7a^2t^4 + 9ar_0t^2 + 3{r_0}^2)}$$

With $b = 7a^2{t_0}^4 + 3{r_0}^2 + 9ar_0{t_0}^2$; $c = 28a^2t_0$; $d = 18ar_0t_0$

$$x_{HS}(x,t) = \frac{3D}{L(b - c{t_0}^2t + 1{,}5ct_0t^2 - ct^3 - dt + 7a^2t^4 + 9ar_0t^2)}$$

$$x_{HS}(x,t) = \frac{3D}{L(t(-c{t_0}^2 - d) + t^2(1{,}5ct_0 + 9ar_0) - ct^3 + 7a^2t^4 + b)}$$

With $e = -c{t_0}^2 - d$; $f = 1{,}5ct_0 + 9ar_0$

$$x_{HS}(t) = \frac{3D}{L(et + ft^2 - ct^3 + 7a^2t^4 + b)}$$

The general volume of variant C is the same as variant B.

GV.Bd

With $D = \frac{\dot{m} \cdot L \cdot t_0}{\rho \cdot \pi}$

$$x_{HS}(t) = \frac{3D}{Lr_0{}^2 \left(1 + \frac{\sqrt{-\left(t - \left(t_{clog} + t_0\right)\right)}}{\sqrt{t_{clog}}} - \frac{\left(t - \left(t_{clog} + t_0\right)\right)}{t_{clog}} \right)}$$

$$x_{HS}(t) = \frac{E}{1 + \frac{\sqrt{a - t}}{\sqrt{t_{clog}}} - \frac{a - t}{t_{clog}}}$$

With $E = \frac{3\dot{m} \cdot t_0}{\rho \cdot \pi r_0{}^2}$; $a = t_{clog} + t_0$

GV.Da

$$x_{HS}(x,t) = \frac{D}{\int_0^L \left(\frac{r_0 - \left(\frac{t_0 - t}{t_{clog} - t_0} r_0 + r_0\right)}{L^2} (x - L)^2 + \left(\frac{t_0 - t}{t_{clog} - t_0} r_0 + r_0\right) \right)^2 dx}$$

$x_{HS}(t)$

$$= \frac{D}{\left[\frac{(x-L)^5}{5L^2} (-at_0 + at + 2r_0)^2 + \frac{2}{3L} (-at_0 + at + 2r_0)(at_0 - at + r_0)(x - L)^3 + (at_0 - at + r_0)^2 x \right]_0^L}$$

With $a = \frac{r_0}{t_{clog} - t_0}$, $b = (3L^3 - 10L^2 + 15L)a^2 t_0{}^2 + (-12L^3 + 10L^2 + 30L)ar_0 t_0 + (12L^3 + 20L^2 + 15L)r_0{}^2$, $c = a^2 t_0(-6L^3 + 20L^2 - 30L) + ar_0(12L^3 - 10L^2 - 30L)$ and $d = a^2(3L^3 - 10L^2 + 15L)$

$$x_{HS}(t) = \frac{15D}{(b + tc + t^2 d)}$$

GV.Db

$$x_{HS}(x,t) = \frac{D}{\int_0^L \left(r_0 - \frac{r_0}{(t_0 - t_{clog})^2} \cdot (t - t_{clog})^2 \over L^2 (x-L)^2 + \frac{r_0}{(t_0 - t_{clog})^2} \cdot (t - t_{clog})^2 \right)^2 dx}$$

With $a = \frac{r_0}{(t_0 - t_{clog})^2}$

$$x_{HS}(t) = \frac{D}{\int_0^L \left(\frac{r_0 - a \cdot (t - t_{clog})^2}{L^2} (x-L)^2 + a \cdot (t - t_{clog})^2 \right)^2 dx}$$

$$x_{HS}(t) = \left[D \left(\frac{\left(-at^2 + 2at_{clog}t + r_0 - at_{clog}^2\right)^2 (x-L)^5}{5L^4} + \frac{2a\left(t^2 - 2t_{clog}t + t_{clog}^2\right)\left(-at^2 + 2at_{clog}t + r_0 - at_{clog}^2\right)(x-L)^3}{3L^2} + a^2\left(t^2 - 2t_{clog}t + t_{clog}^2\right)^2 x \right)^{-1} \right]_L^0$$

$$x_{HS}(t) = \frac{15D}{L\left(8a^2t^4 - 32a^2t_{clog}t^3 + \left(4ar_0 + 48a^2t_{clog}^2\right)t^2 + \left(-8ar_0t_{clog} - 32a^2t_{clog}^3\right)t + 3r_0^2 + 4at_{clog}^2r_0 + 8a^2t_{clog}^4\right)}$$

With $b = -32a^2t_{clog};\ c = 4ar_0 + 48a^2t_{clog}^2;\ d = -8ar_0t_{clog} - 32a^2t_{clog}^3;\ e = 3r_0^2 + 4at_{clog}^2r_0 + 8a^2t_{clog}^4$

$$x_{HS}(x,t) = \frac{15D}{L(8a^2t^4 + bt^3 + ct^2 + dt + e)}$$

GV.Dc

$$x_{HS}(x,t) = \frac{D}{\int_0^L \left(\frac{r_0 - \left(-\frac{r_0}{\left(t_{clog} - t_0\right)^2} \cdot (t - t_0)^2 + r_0 \right)}{L^2} (x - L)^2 + \left(-\frac{r_0}{\left(t_{clog} - t_0\right)^2} \cdot (t - t_0)^2 + r_0 \right) \right)^2 dx}$$

With $a = -\frac{r_0}{\left(t_{clog} - t_0\right)^2}$

$$x_{HS}(t) = \frac{D}{\int_0^L \left(\frac{a \cdot (t - t_0)^2}{L^2} (x - L)^2 + (a \cdot (t - t_0)^2 + r_0) \right)^2 dx}$$

$$x_{HS}(t) = \left[D \left(\frac{a^2 (t - t_0)^4 \left(\frac{x^5}{5} - Lx^4 + 2L^2 x^3 + L^4 x \right)}{L^4} + \frac{2a^2 (t - t_0)^4 \left(\frac{x^3}{3} - Lx^2 + L^2 x \right)}{L} + 2r_0 \left(\frac{a(t - t_0)^2 \left(\frac{x^3}{3} - Lx^2 + L^2 x \right)}{L^2} + a(t - t_0)^2 x \right) + a^2 (t - t_0)^4 x + {r_0}^2 x \right) \right]_L^0$$

$$x_{HS}(t) = \frac{15D}{L(28a^2 {t_0}^4 - 112a^2 t {t_0}^3 + (168a^2 t^2 + 40ar_0) {t_0}^2 + (-112a^2 t^3 - 70ar_0 t) t_0 + 28a^2 t^4 + 40ar_0 t^2 + 15{r_0}^2)}$$

With $b = 28a^2 {t_0}^4 + 40ar_0 {t_0}^2 + 15{r_0}^2$; $c = -112a^2 {t_0}^3 - 80ar_0 t_0$; $d = 168a^2 {t_0}^2 + 40ar_0$; $e = -112a^2 t_0$

$$x_{HS}(t) = \frac{15D}{L(b + ct + dt^2 + et^3 + 28a^2 t^4)}$$

GV.Dd

With $D = \frac{\dot{m} \cdot L \cdot t_0}{\rho \cdot \pi}$

$$x_{HS}(t) = \frac{15D}{-8Lr_0{}^2\frac{\left(t-\left(t_{clog}+t_0\right)\right)}{t_{clog}} + 4Lr_0{}^2\frac{\sqrt{-\left(t-\left(t_{clog}+t_0\right)\right)}}{\sqrt{t_{clog}}} + 3Lr_0{}^2}$$

With $a = t_{clog} + t_0$; $E = \frac{15\dot{m}\cdot t_0}{\rho\cdot\pi {r_0}^2}$

$$x_{HS}(t) = \frac{E}{\left(3 + 4\frac{\sqrt{a-t}}{\sqrt{t_{clog}}} - 8\frac{a-t}{t_{clog}}\right)}$$

2.2 Starting parameters for regression fitting (General volume)

For the mathematical fitting using Origin 2021 by OriginLab, the starting parameters were directly calculated from the empirical data. Variables with a theoretical negative value were constrained to negative numbers during fits. The same was done for positive values.

Table 1: Parameters used to fit the models to the data of three repeat reactions.

		Run 1	**Run 2**	**Run 3**
Empirical	t_0**/min**	78	60 (set to 0)	68 (set to 0)
	t_{clog}**/min**	296	333	312
D	$\frac{\dot{m}\cdot L\cdot t_0}{\rho\pi};\ [m^4]$	$5.65\cdot10^{-5}$	$4.35\cdot10^{-5}$	$4.93\cdot10^{-5}$
GV.Aa	$a = \frac{r_0}{t_{clog}-t_0};\ \left[\frac{m}{min}\right]$	$1.38\cdot10^{-5}$	$1.10\cdot10^{-5}$	$1.23\cdot10^{-5}$
GV.Ab	$E = \frac{3\dot{m}\cdot t_0}{L^2\rho\pi}$	$7.72\cdot10^{-6}$	$5.94\cdot10^{-6}$	$6.73\cdot10^{-6}$
	$a = \frac{r_0}{\left(t_0-t_{clog}\right)^2}$	$6.31\cdot10^{-8}$	$4.03\cdot10^{-8}$	$5.04\cdot10^{-8}$
GV.Ac	$E = \frac{3\dot{m}\cdot t_0}{L^2\rho\pi}$	$7.72\cdot10^{-6}$	$5.94\cdot10^{-6}$	$6.73\cdot10^{-6}$
	$a = -\frac{r_0}{\left(t_{clog}-t_0\right)^2}$	$-6.31\cdot10^{-8}$	$-4.03\cdot10^{-8}$	$-5.04\cdot10^{-8}$
GV.Ad	$t_0;\ [min]$	78	60	68
	$t_{clog};\ [min]$	296	333	312
GV.Ba	$a = \frac{r_0}{\left(t_{clog}-t_0\right)L};\ \left[\frac{1}{min}\right]$	$4.91481\cdot10^{-6}$	$3.925\cdot10^{-6}$	$4.391\cdot10^{-6}$

		Run 1	Run 2	Run 3
	$b = L^3a^2{t_0}^2 + 3L^2ar_0t_0 + 3L{r_0}^2$ $[m^3]$	$1.06 \cdot 10^{-5}$	$9.34 \cdot 10^{-5}$	$9.86 \cdot 10^{-5}$
	$c = -aL^2(2Lat_0 + 3r_0); \left[\frac{m^3}{min}\right]$	$-4.30 \cdot 10^{-7}$	$-3.17 \cdot 10^{-7}$	$-3.67 \cdot 10^{-7}$
	$d = L^3a^2; \left[\frac{m^3}{min^2}\right]$	$5.30 \cdot 10^{-10}$	$3.38 \cdot 10^{-10}$	$4.23 \cdot 10^{-10}$
GV.Bb	$a = \frac{r_0}{(t_0 - t_{clog})^2}$	$6.31 \cdot 10^{-8}$	$4.03 \cdot 10^{-8}$	$5.04 \cdot 10^{-8}$
	$b = 4a^2t_{clog}$	$4.72 \cdot 10^{-12}$	$2.16 \cdot 10^{-12}$	$3.17 \cdot 10^{-12}$
	$c = ar_0 + 6a^2{t_{clog}}^2$	$2.28 \cdot 10^{-9}$	$1.20 \cdot 10^{-9}$	$1.63 \cdot 10^{-9}$
	$d = -2t_{clog}ar_0 - 4a^2{t_{clog}}^3$	$-5.25 \cdot 10^{-7}$	$-3.20 \cdot 10^{-7}$	$-4.03 \cdot 10^{-7}$
	$e = {r_0}^2 + ar_0{t_{clog}}^2 + a^2{t_{clog}}^4$	$5.62 \cdot 10^{-5}$	$4.23 \cdot 10^{-5}$	$4.78 \cdot 10^{-5}$
GV.Bc	$a = -\frac{r_0}{(t_{clog} - t_0)^2}$	$-6.31 \cdot 10^{-8}$	$-4.03 \cdot 10^{-8}$	$-5.04 \cdot 10^{-8}$
	$b = 7a^2{t_0}^4 + 3{r_0}^2 + 9ar_0{t_0}^2$	$1.77 \cdot 10^{-5}$	$2.32 \cdot 10^{-5}$	$2.11 \cdot 10^{-5}$
	$c = 28a^2t_0$	$8.70 \cdot 10^{-12}$	$2.72 \cdot 10^{-12}$	$4.83 \cdot 10^{-12}$
	$d = 18ar_0t_0$	$-2.66 \cdot 10^{-7}$	$-1.30 \cdot 10^{-7}$	$-1.85 \cdot 10^{-7}$
GV.Bd	$E = \frac{3\dot{m} \cdot t_0}{\rho \cdot \pi{r_0}^2}$	6.73	5.18	5.87
	$a = t_{clog} + t_0$	374	393	380
GV.Da	$a = \frac{r_0}{t_{clog} - t_0}$	$1.38 \cdot 10^{-5}$	$1.10 \cdot 10^{-5}$	$1.23 \cdot 10^{-5}$
	$b = (3L^3 - 10L^2 + 15L)a^2{t_0}^2 + (-12L^3 + 10L^2 + 30L)ar_0t_0 + (12L^3 + 20L^2 + 15L){r_0}^2$	$4.05 \cdot 10^{-3}$	$4.04 \cdot 10^{-3}$	$4.04 \cdot 10^{-3}$
	$c = a^2t_0(-6L^3 + 20L^2 - 30L) + ar_0(3L^3 - 10L^2 - 30L)$	$-5.75 \cdot 10^{-6}$	$-4.32 \cdot 10^{-6}$	$-4.96 \cdot 10^{-6}$
	$d = a^2(3L^3 - 10L^2 + 15L)$	$5.58 \cdot 10^{-9}$	$3.56 \cdot 10^{-9}$	$4.45 \cdot 10^{-9}$

		Run 1	Run 2	Run 3
GV.Db	$a = \frac{r_0}{(t_0 - t_{clog})^2}$	$6.31 \cdot 10^{-8}$	$4.03 \cdot 10^{-8}$	$5.04 \cdot 10^{-8}$
	$b = -32a^2 t_{clog}$	$-3.77 \cdot 10^{-11}$	$-1.73 \cdot 10^{-11}$	$-2.54 \cdot 10^{-11}$
	$c = 4ar_0 + 48a^2 {t_{clog}}^2$	$1.75 \cdot 10^{-8}$	$9.11 \cdot 10^{-9}$	$1.25 \cdot 10^{-8}$
	$d = -8ar_0 t_{clog} - 32a^2 {t_{clog}}^3$	$-3.76 \cdot 10^{-6}$	$-2.24 \cdot 10^{-6}$	$-2.85 \cdot 10^{-6}$
	$e = 3{r_0}^2 + 4a{t_{clog}}^2 r_0 + 8a^2 {t_{clog}}^4$	$3.38 \cdot 10^{-4}$	$2.40 \cdot 10^{-4}$	$2.78 \cdot 10^{-4}$
GV.Dc	$a = -\frac{r_0}{(t_{clog} - t_0)^2}$	$-6.31 \cdot 10^{-8}$	$-4.03 \cdot 10^{-8}$	$-5.04 \cdot 10^{-8}$
	$b = 28a^2 {t_0}^4 + 40ar_0 {t_0}^2 + 15{r_0}^2$	$9.30 \cdot 10^{-5}$	$1.18 \cdot 10^{-4}$	$1.086 \cdot 10^{-4}$
	$c = -112a^2 {t_0}^3 - 80ar_0 t_0$	$9.70 \cdot 10^{-7}$	$5.40 \cdot 10^{-7}$	$7.33 \cdot 10^{-7}$
	$d = 168a^2 {t_0}^2 + 40ar_0$	$-3.50 \cdot 10^{-9}$	$-3.85 \cdot 10^{-9}$	$-4.07 \cdot 10^{-9}$
	$e = -112a^2 t_0$	$-3.48 \cdot 10^{-11}$	$-1.09 \cdot 10^{-11}$	$-1.93 \cdot 10^{-11}$
GV.Dd	$E = \frac{15\dot{m} \cdot t_0}{\rho \cdot \pi {r_0}^2}$	34	26	29
	$a = t_{clog} + t_0$	374	393	380

The parameters of the successful fits are presented in the following table. From them, t_0 and t_{clog} can be calculated.

2.3 Fit parameters

Table 2: Fit parameters and coefficient of determination for the three reactions' parabolically extrapolated data and the data directly extracted from the contour plots.

		Run 1	Run 2	Run 3
Empirical	t_0**/min**	78	60	68
	t_{clog}**/min**	296	333	312
GV.Aa	a	$3.25 \cdot 10^{-6}$	$6.98 \cdot 10^{-6}$	$4.20 \cdot 10^{-6}$
	D	$7.77 \cdot 10^{-5}$	$7.54 \cdot 10^{-5}$	$9.99 \cdot 10^{-5}$
	t_0	202	241	308

		Run 1	Run 2	Run 3
	R^2	0.99418	0.99887	0.99912
GV.Ab	E	$1.99 \cdot 10^{-4}$	$6.09 \cdot 10^{-5}$	$2.57 \cdot 10^{-4}$
	a	$2.14 \cdot 10^{-9}$	$5.17 \cdot 10^{-9}$	$3.15 \cdot 10^{-9}$
	t_{clog}	2140	1176	1917
	R^2	0.99198	0.99931	0.99815
GV.Ac	E	$1.87 \cdot 10^{-5}$	$1.11 \cdot 10^{-5}$	$1.74 \cdot 10^{-5}$
	a	$-2.67 \cdot 10^{-6}$	$-4.49 \cdot 10^{-6}$	$-2.94 \cdot 10^{-6}$
	t_0	0	2.52	0
	R^2	0.99418	0.99887	0.99912
GV.Ad	t_{clog}	535	374	498
	t_0	84	51	79
	R^2	0.99734	0.99215	0.99952
GV.Ba	E	$2.09 \cdot 10^{-4}$	$1.21 \cdot 10^{-4}$	$1.95 \cdot 10^{-4}$
	b	$9.96 \cdot 10^{-5}$	$1.01 \cdot 10^{-4}$	$9.98 \cdot 10^{-5}$
	c	$-1.60 \cdot 10^{-7}$	$-3.24 \cdot 10^{-7}$	$-1.80 \cdot 10^{-7}$
	d	0	$3.11 \cdot 10^{-10}$	$2.84 \cdot 10^{-11}$
	R^2	0.99722	0.99951	0.9996
GV.Bb	D	$2.24 \cdot 10^{-4}$	$1.83 \cdot 10^{-4}$	$2.25 \cdot 10^{-4}$
	a	$9.68 \cdot 10^{-8}$	$5.15 \cdot 10^{-8}$	$5.79 \cdot 10^{-8}$
	b	$2.82 \cdot 10^{-12}$	0	$8.27 \cdot 10^{-13}$
	c	0	$7.36 \cdot 10^{-11}$	0
	d	$-1.39 \cdot 10^{-7}$	$-4.48 \cdot 10^{-7}$	$-2.07 \cdot 10^{-7}$
	e	$1.13 \cdot 10^{-4}$	$1.60 \cdot 10^{-4}$	1.23E-04$\cdot 10^{-4}$
	R^2	0.99988	0.99985	0.99975
GV.Bc	D	-	-	-
	a	-	-	-
	b	-	-	-
	e	-	-	-
	f	-	-	-

		Run 1	Run 2	Run 3
	R^2	-	-	-
GV.Bd	E	-	-	-
	a	-	-	-
	R^2	-	-	-
GV.Da	D	$2.29 \cdot 10^{-4}$	$1.30 \cdot 10^{-4}$	$1.61 \cdot 10^{-4}$
	b	$1.65 \cdot 10^{-3}$	$1.63 \cdot 10^{-3}$	$1.23 \cdot 10^{-3}$
	c	$-2.62 \cdot 10^{-6}$	$-5.24 \cdot 10^{-6}$	$-2.00 \cdot 10^{-6}$
	d	0	$5.02 \cdot 10^{-9}$	0
	R^2	0.99637	0.99951	0.97962
GV.Db	D	$3.44 \cdot 10^{-4}$	$3.42 \cdot 10^{-4}$	$3.63 \cdot 10^{-4}$
	a	$9.37 \cdot 10^{-8}$	$2.72 \cdot 10^{-8}$	$5.77 \cdot 10^{-8}$
	b	$-2.12 \cdot 10^{-11}$	$-1.16E-27 \cdot 10^{-27}$	$-6.56 \cdot 10^{-12}$
	c	0	0	0
	d	$-1.07 \cdot 10^{-6}$	$-3.60 \cdot 10^{-6}$	$-1.67 \cdot 10^{-6}$
	e	$8.65 \cdot 10^{-4}$	$1.46 \cdot 10^{-3}$	$9.94 \cdot 10^{-4}$
	R^2	0.99988	0.99336	0.99995
GV.Dc	D	$1.38 \cdot 10^{-4}$	$1.48 \cdot 10^{-4}$	$1.81 \cdot 10^{-4}$
	a	$-3.64 \cdot 10^{-8}$	$-4.69 \cdot 10^{-8}$	$-4.19 \cdot 10^{-8}$
	b	$3.37 \cdot 10^{-4}$	$5.66 \cdot 10^{-4}$	$4.67 \cdot 10^{-4}$
	c	0	0	0
	d	$-3.92 \cdot 10^{-9}$	$-8.81 \cdot 10^{-9}$	$-5.61 \cdot 10^{-9}$
	e	0	$-6.69 \cdot 10^{-15}$	$-3.76 \cdot 10^{-27}$
	R^2	0.99502	0.99083	0.99147
GV.Dd	E	-	-	-
	a	-	-	-
	R^2	-	-	-

2.4 Calculated values for t_0 and t_{clog} from the fits

The majority of degrees of correlations for the fits, which were possible, are very high. In the following, t_0 and t_{clog} are shown, as calculated from the parameters above. They were then compared to the empirical values with t_0 set to 0, as the data the fits were carried out on, were

edited in this way. Cells marked greed denote, that the t_0 is close to 0. This is only the case for GV.Aa and GV.Ab. Yellow cells show t_{clog} values with a deviation of less than the factor 2, compared to the empirical corrected value. GV.Db gives the best estimate for t_{clog}, but a poor one for t_0. GV.Aa shows acceptable agreement for both.

If the value for t_0 is not < 25 min, this value is subtracted from the calculated value for t_{clog}, to account for the shift. This was carried out for model HS. Ad.

Table 3: Showing the values for t_0 and t_{clog}, as calculated from the resulting fit parameters.

		Run 1	Run 2	Run 3
Empirical	t_0	78	60	68
	t_0 set to 0	0	0	0
	t_{clog}	296	333	312
	t_{clog} - t_0	218	273	244
GV.Aa	t_0	107	104	138
	t_{clog}	1030	534	851
GV.Ab	t_0	0	0	0
	t_{clog}	2140	1176	1917
GV.Ac	t_0	0	3	0
	t_{clog}	222	138	208
GV.Ad	t_0	-	-	-
	t_{clog}	451	323	419
GV.Ba	t_0	288	167	269
	t_{clog}	-	452	1210
GV.Bb	t_0	309	253	310
	t_{clog}	133	12	83
GV.Bc	t_0	-	-	-
	t_{clog}	-	-	-
GV.Bd	t_0	-	-	-
	t_{clog}	-	-	-
GV.Da	t_0	317	180	222

		Run 1	Run 2	Run 3
	t_{clog}	-	409	-
GV.Db	t_0	474	471	502
	t_{clog}	295	139	273
GV.Dc	t_0	190	204	249
	t_{clog}	477	457	517
GV.Dd	t_0	-	-	-
	t_{clog}	-	-	-

3. Hot Spot Tracking Approach

$$V = \pi \cdot \int_0^L (r(x))^2 dx$$

Tube radius constriction (cylinder) (A)

$$V = \pi \cdot \int_0^L (r_e)^2 dx$$

$$V = \pi \cdot [{r_e}^2 \cdot x]_0^L$$

To find the volume the reaction mixture entering the reactor clears before reaching the point of maximum conversion rate, x_{max} is used instead of L in the integration borders.

$$V_{max} = \pi \cdot [{r_e}^2 \cdot x]_0^{x_{max}}$$

$$V_{max} = \pi \cdot {r_e}^2 \cdot x_{max}$$

$$x_{HS}(t) = \frac{V_{max}}{\pi \cdot {r_e}^2}$$

Linear outlet radius constriction (frustum) (B)

$$V = \pi \cdot \int_0^L \left(\frac{r_e - r_0}{L} \cdot x + r_0\right)^2 dx$$

$$V = \pi \cdot \left[-\frac{L \cdot \left(\frac{(r_e - r_0)}{L} \cdot x + r_0\right)^3}{3 \cdot (r_0 - r_e)} \right]_0^L$$

To find the volume the reaction mixture entering the reactor clears before reaching the point of maximum conversion rate, x_{max} is used instead of L in the integration borders.

$$V_{max} = \pi \cdot \left[-\frac{L \cdot \left(\frac{(r_e - r_0)}{L} \cdot x + r_0 \right)^3}{3 \cdot (r_0 - r_e)} \right]_0^{x_{max}}$$

$$V_{max} = -\pi \cdot \frac{L \cdot \left(\frac{(r_e - r_0)}{L} \cdot x_{max} + r_0 \right)^3}{3 \cdot (r_0 - r_e)} + \frac{L \cdot {r_0}^3}{3 \cdot (r_0 - r_e)}$$

$$x_{HS}(t) = \left(\sqrt[3]{{r_0}^3 - \frac{3 \cdot V_{max} \cdot (r_0 - r_e)}{\pi \cdot L}} - r_0 \right) \cdot \frac{L}{r_e - r_0}$$

Linear inlet radius constriction (reverse frustum) (C)

There are some reactions where fouling has been observed to form more at the inlet, than at the outlet. It has been shown, that fouling chiefly accumulates at the end of a continuous reactor for the presented reaction, however the assumption for the reverse is covered by the following equations.

$$V = \pi \cdot \int_0^L \left(\frac{r_0 - r_i}{L} \cdot x + r_i \right)^2 dx$$

$$V = \pi \cdot \left[\frac{L \cdot \left(\frac{(r_0 - r_i)}{L} \cdot x + r_i \right)^3}{3 \cdot (r_0 - r_i)} \right]_0^L$$

To find the volume the reaction mixture entering the reactor clears before reaching the point of maximum conversion rate, x_{max} is used instead of L in the integration borders.

$$V_{max} = \pi \cdot \left[\frac{L \cdot \left(\frac{(r_0 - r_i)}{L} \cdot x + r_i \right)^3}{3 \cdot (r_0 - r_i)} \right]_0^{x_{max}}$$

$$V_{max} = \frac{\pi L}{3(r_0 - r_i)} \cdot \left(\frac{(r_0 - r_i)}{L} \cdot x_{max} + r_i \right)^3 - \frac{\pi L}{3(r_0 - r_i)} \cdot {r_i}^3$$

$$x_{HS}(t) = \left(\sqrt[3]{\frac{3 \cdot V_{max} \cdot (r_0 - r_i)}{\pi \cdot L} + {r_i}^3} - r_i \right) \cdot \frac{L}{r_0 - r_i}$$

3.1 Time-dependency of the geometrical change given the previous assumptions (Hot Spot Tracking)

Linearly decreasing tube diameter (HS.Aa)

$$x_{HS}(t) = \frac{V_{max}}{\pi \cdot {r_e}^2}$$

$$x_{HS}(t) = \frac{V_{max}}{\pi \cdot \left(\frac{t_0 - t}{t_{clog} - t_0} r_0 + r_0 \right)^2}$$

With $a = \frac{r_0}{t_{clog} - t_0}$ and $D = \frac{V_{max}}{\pi}$

$$x_{HS}(t) = \frac{D}{(a(t_0 - t) + r_0)^2}$$

Cubically decelerating decrease of tube diameter (HS.Ab)

$$x_{HS}(t) = \frac{V_{max}}{\pi \cdot \left(\frac{r_0}{\left(t_0 - t_{clog}\right)^2} \cdot \left(t - t_{clog}\right)^2 \right)^2}$$

For the fit, the formula was simplified by summarizing $\frac{V_{max}}{\pi} \cdot \frac{\left(t_0 - t_{clog}\right)^4}{{r_0}^2}$ as D.

$$x_{HS}(t) = \frac{V_{max}}{\pi} \cdot \frac{\left(t_0 - t_{clog}\right)^4}{{r_0}^2} \cdot \frac{1}{\left(t - t_{clog}\right)^4} = D \cdot \frac{1}{\left(t - t_{clog}\right)^4}$$

Cubically accelerating decrease of tube diameter (HS.Ac)

$$x_{HS}(t) = \frac{V_{max}}{\pi \cdot \left(-\frac{r_0}{\left(t_{clog} - t_0\right)^2} \cdot (t - t_0)^2 + r_0 \right)^2}$$

For the fit, the formula was simplified by summarizing $\frac{V_{max}}{\pi}$ as D, and $-\frac{r_0}{\left(t_{clog} - t_0\right)^2}$ as a.

$$x_{HS}(t) = D \cdot \frac{1}{(a \cdot (t - t_0)^2 + r_0)^2}$$

Square root decrease of tube diameter (HS.Ad)

$$x_{HS}(t) = \frac{V_{max}}{\pi \cdot \left(r_0 \frac{\sqrt{-\left(t - \left(t_{clog} + t_0\right)\right)}}{\sqrt{t_{clog}}} \right)^2}$$

With $D = \frac{V_{max}}{\pi \cdot {r_0}^2}$; $a = t_{clog} + t_0$

$$x_{HS}(t) = \frac{D t_{clog}}{(a - t)}$$

Linearly decrease of frustum outlet radius (HS.Ba)

$$x_{HS}(t) = \left(\sqrt[3]{{r_0}^3 - \frac{3 \cdot V_{max} \cdot \left(r_0 - \left(\frac{t_0 - t}{t_{clog} - t_0} r_0 + r_0 \right) \right)}{\pi \cdot L}} - r_0 \right) \cdot \frac{L}{\left(\frac{t_0 - t}{t_{clog} - t_0} r_0 + r_0 \right) - r_0}$$

With $a = \frac{r_0}{t_{clog} - t_0}$ and $D = \frac{3 \cdot V_{max}}{\pi \cdot L}$

$$x_{HS}(t) = \left(\sqrt[3]{{r_0}^3 + Da(t_0 - t)} - r_0 \right) \frac{L}{a(t_0 - t)}$$

Cubically decelerating decrease of frustum outlet radius (HS.Bb)

$$x_{HS}(t) = \left(\sqrt[3]{{r_0}^3 - \frac{3 \cdot V_{max} \cdot \left(r_0 - \left(\frac{r_0}{\left(t_0 - t_{clog}\right)^2} \cdot \left(t - t_{clog}\right)^2 \right) \right)}{\pi \cdot L}} - r_0 \right) \cdot \frac{L}{\left(\frac{r_0}{\left(t_0 - t_{clog}\right)^2} \cdot \left(t - t_{clog}\right)^2 \right) - r_0}$$

For the data fitting, the formula was simplified. The constant D is comprised of $\frac{3 \cdot V_{max}}{\pi \cdot L}$ and the factor a is equal to $\frac{r_0}{\left(t_0 - t_{clog}\right)^2}$.

$$x_{HS}(t) = \left(\sqrt[3]{{r_0}^3 - D \cdot \left(r_0 - a \cdot \left(t - t_{clog}\right)^2\right)} - r_0\right) \cdot \frac{L}{a \cdot \left(t - t_{clog}\right)^2 - r_0}$$

Cubically decelerating decrease of frustum outlet radius (HS.Bc)

$$x_{HS}(t) = \left(\sqrt[3]{{r_0}^3 - \frac{3 \cdot V_{max} \cdot \left(r_0 - \left(-\frac{r_0}{\left(t_{clog} - t_0\right)^2} \cdot (t - t_0)^2 + r_0\right)\right)}{\pi \cdot L}} - r_0\right) \cdot \frac{L}{\left(-\frac{r_0}{\left(t_{clog} - t_0\right)^2} \cdot (t - t_0)^2 + r_0\right) - r_0}$$

For the data fitting, the formula was simplified. The constant D is comprised of $\frac{3 \cdot V_{max}}{\pi \cdot L} \cdot \frac{r_0}{\left(t_{clog} - t_0\right)^2}$, and the factor a is equal to $-\frac{r_0}{\left(t_{clog} - t_0\right)^2}$.

$$x_{HS}(t) = \left(\sqrt[3]{{r_0}^3 - D \cdot (t - t_0)^2} - r_0\right) \cdot \frac{L}{a(t - t_0)^2}$$

Square root decrease of frustum outlet radius (HS.Bd)

$$x_{HS}(t) = \left(\sqrt[3]{{r_0}^3 - \frac{3 \cdot V_{max} \cdot \left(r_0 - r_0 \frac{\sqrt{-\left(t - \left(t_{clog} + t_0\right)\right)}}{\sqrt{t_{clog}}}\right)}{\pi \cdot L}} - r_0\right) \cdot \frac{L}{r_0 \frac{\sqrt{-\left(t - \left(t_{clog} + t_0\right)\right)}}{\sqrt{t_{clog}}} - r_0}$$

The Bd Term was not further explored, because in GV calculations, B showed bad results.

The C-terms were not further explored, because it is known, that this is not a front-fouling reaction.

3.2 Starting parameters for regression fitting (Hot spot tracking)

To enable the model fits to describe the existing time-space curve the reaction hot spot creates along the reactor path, the model parameters were first estimated using the empirical estimation of the time the fouling starts t_0, the clogging time t_{clog}, and the location of the temperature maximum at t_0, $x_{max,0}$. Assuming a reactor free of fouling, $V_{max,0}$, the volume the reaction needs to reach $x_{max,0}$ is calculated. The measured time-space curves of various repeat reactions show a path that strongly suggests that model C is not applicable. Therefore, only A and B were fitted to the measurement data. Three repeat reactions were evaluated using the models, called Run 1, 2 and 3 in the following. The reaction time was adjusted by subtracting the empirically defined value for t_0. This was done for the data, as well as for the calculation of the starting parameters for the fits.

Table 4: Parameters used to fit the models to the data of three repeat reactions.

		Run 1	**Run 2**	**Run 3**
Empirical	t_0/min	78	60	68
	t_{clog}/min	296	333	312
	$V_{max,0}$/m^3	$5.4 \cdot 10^{-5}$	$4.8 \cdot 10^{-5}$	$5.9 \cdot 10^{-5}$
Aa	D/m^3	$1.71 \cdot 10^{-5}$	$1.52 \cdot 10^{-5}$	$1.89 \cdot 10^{-5}$
	a/$\frac{m}{min}$	$1.38 \cdot 10^{-5}$	$1.10 \cdot 10^{-5}$	$1.23 \cdot 10^{-5}$
Ab	D/m·min^4	$4.29 \cdot 10^{+9}$	$9.39 \cdot 10^{+9}$	$7.44 \cdot 10^{+9}$
Ac	D/m^3	$1.71 \cdot 10^{-5}$	$1.52 \cdot 10^{-5}$	$1.89 \cdot 10^{-5}$
	a/$\frac{m}{min^2}$	$-6.31 \cdot 10^{-8}$	$-4.03 \cdot 10^{-8}$	$-5.04 \cdot 10^{-8}$
Ad	D/m	1.90	1.69	2.10
	a/min	374	393	380
Ba	D/m^2	$1.83 \cdot 10^{-5}$	$1.63 \cdot 10^{-5}$	$2.03 \cdot 10^{-5}$
	a/$\frac{m}{min}$	$1.38 \cdot 10^{-5}$	$1.10 \cdot 10^{-5}$	$1.23 \cdot 10^{-5}$
Bb	D/m^2	$1.83 \cdot 10^{-5}$	$1.63 \cdot 10^{-5}$	$2.03 \cdot 10^{-5}$
	a/$\frac{m}{min^2}$	$6.31 \cdot 10^{-8}$	$4.03 \cdot 10^{-8}$	$5.04 \cdot 10^{-8}$
Bc	D/$\frac{m^3}{min^2}$	$1.16 \cdot 10^{-12}$	$6.56 \cdot 10^{-13}$	$1.02 \cdot 10^{-12}$
	a/$\frac{m}{min^2}$	$-6.31 \cdot 10^{-8}$	$-4.03 \cdot 10^{-8}$	$-5.04 \cdot 10^{-8}$

3.3 Resulting fit parameters

The results of the mathematical fitting to the experimental data is shown in the next table. The parameter of determination R^2 is also listed. Coefficients of determination over a threshold of 0.9 are marked to indicate more valid models.

Table 5: Fit parameters and coefficient of determination for the three reactions' parabolically extrapolated data and the data directly extracted from the contour plots.

		Run 1	**Run 2**	**Run 3**
Aa parabolic extrapolation	D/m^3	3.01883E-5	-	2.41692E-5
	a/$\frac{m}{min}$	3.39117E-6	-	3.46094E-6
	R^2	1	-	1
Aa* contour plot	D/m^3	2.31718E-5	-	2.41692E-5
	a/$\frac{m}{min}$	2.17883E-6	-	3.46094E-6
	R^2	0.85733	-	1
Ab parabolic extrapolation	D/m·min^4	$4.34 \cdot 10^{+13}$	$2.28 \cdot 10^{+12}$	$1.50 \cdot 10^{+14}$
	R^2	0.99202	0.99931	0.86024
Ab* contour plot	D/m·min^4	$1.50 \cdot 10^{+14}$	$2.49 \cdot 10^{+12}$	$1.50 \cdot 10^{+14}$
	R^2	0.86024	0.96177	0.86024
Ac parabolic extrapolation	D/m^3	$2.02 \cdot 10^{-5}$	$1.36 \cdot 10^{-5}$	$1.91 \cdot 10^{-5}$
	a/$\frac{m}{min^2}$	$-1.21 \cdot 10^{-8}$	$-1.50 \cdot 10^{-8}$	$-1.11 \cdot 10^{-8}$
	R^2	0.97205	0.94896	0.96422
Ac* contour plot	D/m^3	$2.09 \cdot 10^{-5}$	$1.36 \cdot 10^{-5}$	$1.96 \cdot 10^{-5}$
	a/$\frac{m}{min^2}$	$-9.23 \cdot 10^{-9}$	$-1.50 \cdot 10^{-8}$	$-1.04 \cdot 10^{-8}$
	R^2	0.72474	0.94896	0.61858
Ad	D/m	2.88	1.88	2.69
	a/min	619	426	577
	R^2	0.99734	0.99215	0.99952
Ad*	D/m	3.37	1.90	3.04
	a/min	805	433	699
	R^2	0.85133	0.93516	0.66226
Ba	D/m^2	-	-	-

		Run 1	Run 2	Run 3
parabolic extrapolation	a/$\frac{m}{min}$	-	-	-
	R^2	-	-	-
Ba* contour plot	D/m^2	-	-	-
	a/$\frac{m}{min}$	-	-	-
	R^2	-	-	-
Bb parabolic extrapolation	D/m^2	$2.51 \cdot 10^{-5}$	$1.38 \cdot 10^{-5}$	$7.98 \cdot 10^{-4}$
	a/$\frac{m}{min^2}$	$3.52 \cdot 10^{-9}$	$1.05 \cdot 10^{-8}$	$7.99 \cdot 10^{-8}$
	R^2	0.99918	0.83343	0.9996
Bb* contour plot	D/m^2	$2.51 \cdot 10^{-5}$	$1.38 \cdot 10^{-5}$	0.338
	a/$\frac{m}{min^2}$	$3.52 \cdot 10^{-9}$	$1.04 \cdot 10^{-8}$	$1.15 \cdot 10^{-6}$
	R^2	0.99918	0.84023	0.66337
Bc parabolic extrapolation	D/$\frac{m^3}{min^2}$	$2.57 \cdot 10^{-13}$	$2.52 \cdot 10^{-13}$	$2.67 \cdot 10^{-13}$
	a/$\frac{m}{min^2}$	$-1.22 \cdot 10^{-8}$	$-1.58 \cdot 10^{-8}$	-1-30$\cdot 10^{-8}$
	R^2	0.9692	0.82403	0.61263
Bc* contour plot	D/$\frac{m^3}{min^2}$	$2.17 \cdot 10^{-13}$	$2.55 \cdot 10^{-13}$	$2.67 \cdot 10^{-13}$
	a/$\frac{m}{min^2}$	$-9.97 \cdot 10^{-9}$	$-1.60 \cdot 10^{-8}$	$-1.30 \cdot 10^{-8}$
	R^2	0.75566	0.81836	0.61263

3.4 Parameters for t_0, t_{clog}, and $V_{max,0}$ calculation from the fits

The parameters of the fitted models were used to calculate the values for t_0, t_{clog}, and $V_{max,0}$. Before, the time scale of each reaction was adjusted to make $t_0 = 0$, because of this, some models do not allow for re-estimation of t_0. This will be signified with a dash, and otherwise the calculated values will be stated. Red values are far away from the empirically determined values for the reactions, and green values are close. All calculated values for t_{clog} are larger than the observed ones. Models, which overestimate this time by a factor of 3 or less are marked green. Calculated volumes that deviate by less than 25 % are also marked green.

If the value for t_0 is not < 25 min, this value is subtracted from the calculated value for t_{clog}, to account for the shift. This was carried out for model HS. Ad.

Table 6: The values for t_0, t_{clog}, and $V_{max,0}$ as calculated from the resulting fit parameters.

	Run 1			**Run 2**			**Run 3**		
	t_0 /min	t_{clog} /min	$V_{max,0}$ /$m^3 \cdot 10^{-5}$	t_0 /min	t_{clog} /min	$V_{max,0}$ /$m^3 \cdot 10^{-5}$	t_0 /min	t_{clog} /min	$V_{max,0}$ /$m^3 \cdot 10^{-5}$
Aa	318	1202	0.96	-	-	-	222	1089	0.77
Aa*	197	1574	0.74	-	-	-	222	1089	0.77
Ab	-	2218	5.07	-	1236	2.76	-	2958	5.53
Ab*	-	2958	5.53	-	1265	2.75	-	2958	5.53
Ac	-	487	6.34	-	448	4.28	-	519	6.00
Ac*	-	570	6.57	-	448	4.28	-	537	6.15
Ad	-	279	8.15	-	161	5.32	-	262	7.61
Ad*	-	243	9.52	-	159	5.37	-	248	8.60
Ba	-	-	-	-	-	-	-	-	-
Ba*	-	-	-	-	-	-	-	-	-
Bb	2049	1126	7.37	1172	1172	4.04	1012	818	234
Bb*	2049	1126	7.37	1179	506	4.05	1016	965	99000
Bc	-	495	6.16	-	436	4.69	-	480	6.02
Bc*	-	549	6.38	-	433	4.67	-	480	6.02

The model Ac not only shows good coefficients of regression, but also produces plausible values for t_{clog} and $V_{max,0}$. The model Ad shows good coefficients of regression and produces plausible values for t_{clog}.

8.3 Supporting Information for *Spatially resolved reaction calorimetry and fouling monitoring in a continuous tubular emulsion polymerization reactor*

Supplemental Material

Spatially resolved reaction calorimetry and fouling monitoring in a continuous tubular emulsion polymerization reactor

Table of Content

1. Experimental data

The experimental data can be found under DOI 10.25592/uhhfdm.17646.

2. Experimental overview

Table 1: Overview over all considered experiments.

Experiment	Non-insulated/insulated	Calibration/Reaction	For reaction: recency of calibration
0_C	Non insulated	Calibration	
1_C	Insulated	Calibration	
1_R	Insulated	Reaction	1 day
2_R	Non insulated	Reaction	2 weeks
3_C	Insulated	Calibration	
3_R	Insulated	Reaction	1 day
4_R	Non insulated	Reaction	1 week

3. Determination of thermal coefficients of transport α

Inner thermal coefficient of transport $\boldsymbol{\alpha_i}$

Tube with internal flow

$$Nu_m = \left[49.37 + \left(1.615 \cdot \left(\frac{Pe \cdot d_i}{h}\right)^{1/3} - 0.7\right)^3\right]^{1/3} \cdot K$$

$$\text{with } K = \frac{Pr_F}{Pr_W} = \frac{Pr}{\frac{\eta_{Air} \cdot c_{p,Air}}{\lambda_{Air}}}$$

$$\text{with } Pe = \frac{\dot{m} \cdot d_i \cdot \rho_{H2O} \cdot c_{P,H2O}}{\lambda_{H2O}}$$

Constants: $d_i = 0.006$ m; $h = 0.45$ m; $\dot{m} = 8\,\frac{g}{min}$; $\rho_{H2O} = 998\,\frac{kg}{m^3}$; $c_{P,H2O} = 4181\,\frac{J}{kg \cdot K}$; $\lambda_{H2O} = 0.6\,\frac{W}{m \cdot K}$; $\eta_{H2O} = 1\ mPa \cdot s$; $\rho_{Air} = 1.2\,\frac{kg}{m^3}$; $c_{P,Air} = 1010\,\frac{J}{kg \cdot K}$; $\lambda_{Air} = 0.0262\,\frac{W}{m \cdot K}$; $\eta_{Air} = 0.0182\ mPa \cdot s$

Therefore: $Nu_m = 4.83$. The value of Nu_m was adjusted to be 4.26 to fit experimental data better.

$$\alpha_i = \frac{Nu \cdot \lambda_{H2O}}{d_i} = 426\,\frac{W}{m^2 \cdot K}$$

Outer thermal coefficient of transport α_o

Horizontal tube with natural convection $Nu_m = \left(0.60 + 0.387 \cdot (Ra \cdot F_4)^{1/6}\right)^2$

with $Ra = Gr \cdot Pr_w = Gr \cdot \frac{\eta_{Air} \cdot c_{p,Air}}{\lambda_{Air}}$

with $F_4 = \left[1 + \left(\frac{0.559}{Pr}\right)^{9/16}\right]^{-16/9}$

with $Gr = \frac{L^3 \cdot g \cdot \Delta T \cdot \gamma_{Air}}{\left(\frac{\eta_{Air}}{\rho_{Air}}\right)^2}$

with $L = \frac{d_o \cdot \pi}{2}$

Constants: $d_o = 0.017$ m; $Pr = Pr_W$; $g = 9.81 \frac{m}{s^2}$; $\Delta T = 20$ °C; $\gamma_{Air} = 0.003 \frac{1}{K}$

Therefore: $Nu_m = 5.90$

$$\alpha_o = \frac{Nu \cdot \lambda_{Air}}{d_o} = 9 \frac{W}{m^2 \cdot K}$$

4. DOFS calibration process

Supplemental figure 1 depicts the thermocouple readings during a calibration cycle. The thermocouple at position 1 is the inlet temperature and the one at position 6 is the outlet temperature.

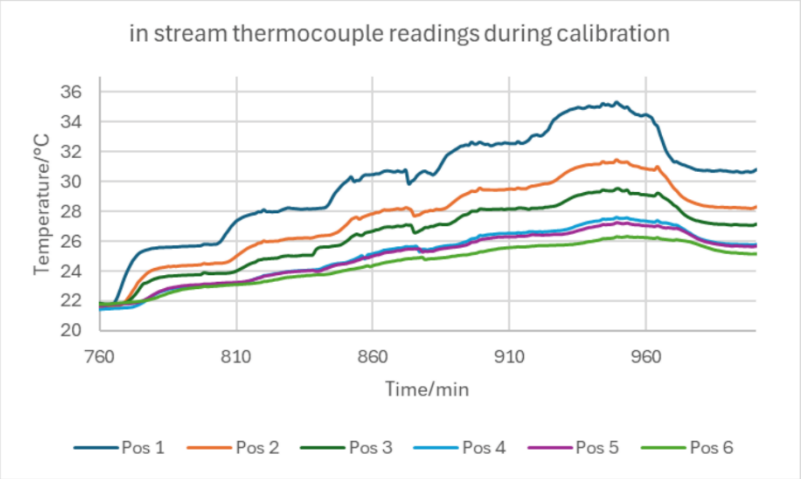

Supplemental figure 1: Thermocouple readings in the reactor stream at the six positions during a calibration cycle.

As stated in the main text, the temperature difference between the instream thermocouple reading and the reading on the reactor wall/the RT is taken, and the loss of heat power is calculated. Because there are six thermocouples in the stream, this is done for all six positions.

From this heat power value, the temperature in the wall at the position of one of the DOFS is calculated (calc. temperature at DOFS A). The following example considers DOFS A, which is in the channel parallel to the stream at $d_{DOFS\,A} = 6.5$ mm. Using the time data from the thermocouple measurements and the DOFS measurements, the signal shift and the calc. temperature data are correlated, and the following graph is generated for position 1:

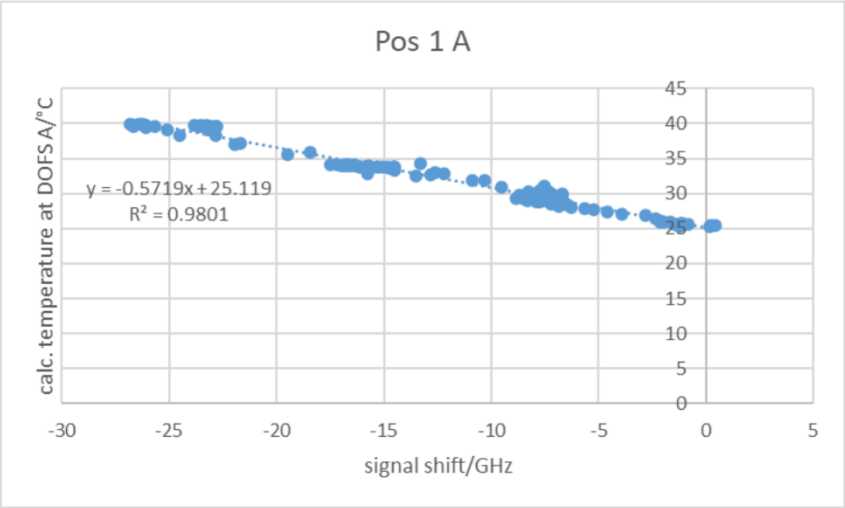

Supplemental figure2: Correlation between signal shift and calc. temperature for DOFS A and resulting fit formula.

The correlation factors $A_1 = -0.5719\ \frac{°C}{GHz}$ and $K_1 = 25.119$ °C result. Table 2 depicts the correlation factors for DOFS A for all six positions together with their R^2 values.

Table 2: Calibration factors for DOFS A at all six positions.

Position	$A_1/\frac{°C}{GHz}$	K_1/°C	R^2
1	-0.5719	25.119	0.9801
2	-0.5406	26.024	0.9721
3	-0.7448	24.978	0.9783
4	-0.5843	25.279	0.9829
5	-0.6914	25.154	0.9715
6	-0.5709	25.836	0.8681

The same is carried out for all DOFS.

It must be noted that long times between calibration and experiments yield bad temperature data. There are many factors that change the sensor output, such as moisture, physical positioning and disturbances. Supplemental figure 3 depicts a spatially resolved temperature reading calculated with two-week-old calibration. In contrast, main text figure 10 depicts a set of experimental data with a fresh calibration.

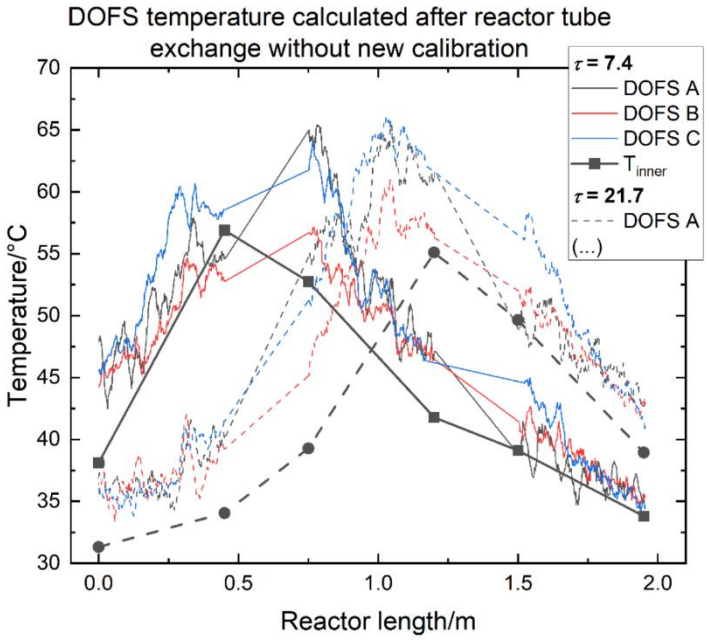

Supplemental figure 3: Spatially resolved temperature reading during reaction at two different points in time, showing thermocouple data and DOFS readings.

Heat loss information can still be gained from these badly calibrated data sets and carrying out the data processing leads to heat sums that are off by constant factors (between 1.2-1.5 for $\dot{Q}_{rad}/\tau$ plot).

5. Calorimetric calibration

During calibration inlet temperatures are held until stationary conditions are reached. When this is the case, it can be assumed that the lost heat through the reactor walls to the environment is equal to the heat lost via the temperature drop along the reactor axis. Therefore, the calculated heat loss is calibrated using the lost heat instream. Supplemental figure 4 shows the lost heat in the stream and the heat loss as directly calculated from the DOFS A and B.

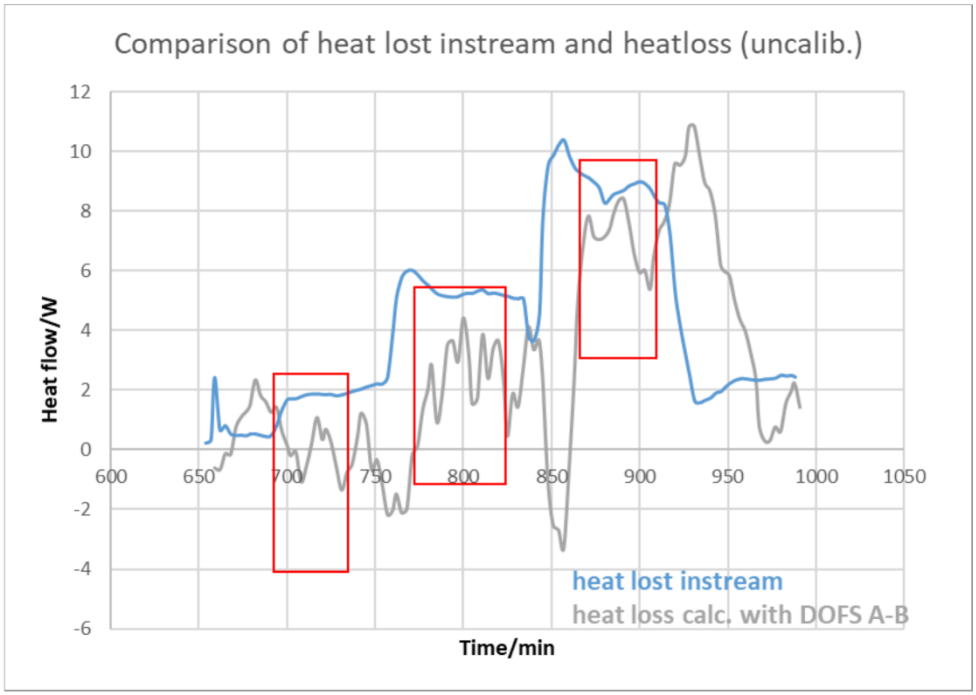

Supplemental Figure 4: Heat lost from instream measurements with thermocouples (blue) and heat loss calculated from the temperature difference between the entire lengths of DOFS A and B (grey).

Due to the thermal latency of the reactor the red windows designate the data used for the calibration. They are the areas of overlap between the measurements. The values in these areas are averaged and then plotted against each other. In the case of the data in supplemental figure 4, a linear dependency with the formula $\dot{Q}_{rad,A-B,calib} = 0.7909 \cdot \dot{Q}_{rad,A-B} + 2.6659$ [W] and

$R^2 = 0.9824$. The calibrated curse is shown in supplemental figure 5. The subsequent supplemental figure 6 shows this calibration applied to the polyreaction data. The agreement between the two conversion calculation methods is good. During this particular reaction the thermal conversion did not drop as quickly (in comparison to the gravimetrical one) as during other experiments. It only begins to drop considerably at 950 min reaction time ($\tau \approx 24$). This is all included in the deviation data in main text figure 12.

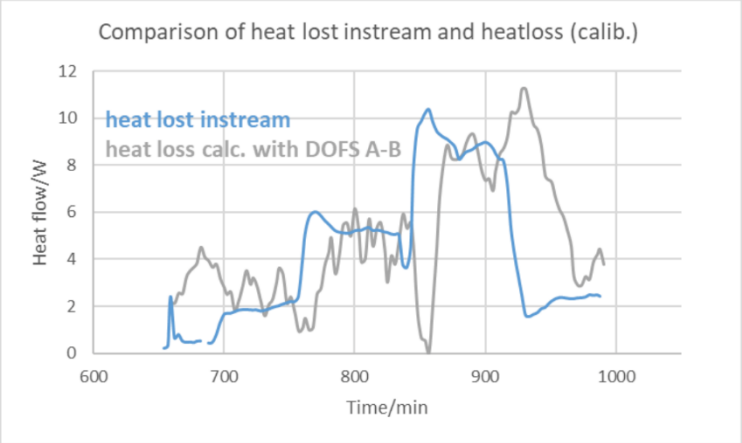

Supplemental Figure 4: Heat lost from instream measurements with thermocouples (blue) and heat loss calculated from the temperature difference between the entire lengths of DOFS A and B (grey), after calibration.

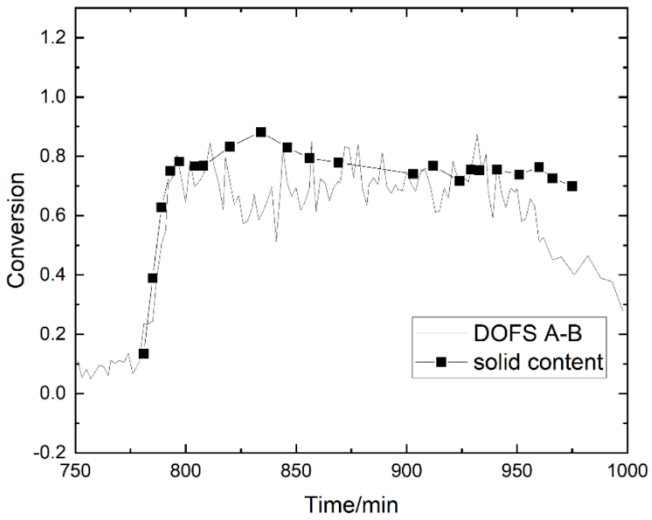

Supplemental Figure 5: The previous calibration applied to reaction data, resulting in thermal conversion information.

8.4 PLA thermal conductivity measurement

Prüfprotokoll: TIMT: 179080081 **Datum:** 14.10.2022

Material: **PLA-3D-1 mm**

Messfläche: 706.86 **A [mm²]** *: Messunsicherheit [%] bezogen auf R_{thxA}

konst. Druck

Spalt [mm]	Kraft [N]	R_{th} [K/W]	λ_{eff} [W/(mK)]	R_{thxA} [mm²K/W]	Druck [bar]	T_{Probe} [°C]	Q_{Mittel} [W]	U* [%]
1.057	71	7.41	0.20	5238.9	1.0	27.7	2.6	9.1
1.054	141	7.42	0.20	5244.6	2.0	27.7	2.6	9.1

Prüfprotokoll: TIMT: 179080081 **Datum:** 14.10.2022

Material: **PLA-3D-2 mm**

Messfläche: 706.86 **A [mm²]** *: Messunsicherheit [%] bezogen auf R_{thxA}

konst. Druck

Spalt [mm]	Kraft [N]	R_{th} [K/W]	λ_{eff} [W/(mK)]	R_{thxA} [mm²K/W]	Druck [bar]	T_{Probe} [°C]	Q_{Mittel} [W]	U* [%]
2.050	71	13.66	0.21	9653.0	1.0	27.5	1.6	13.2
2.045	141	13.69	0.21	9673.7	2.0	27.5	1.6	13.2

Prüfprotokoll: TIMT: 179080081 **Datum:** 14.10.2022

Material: **PLA-3D-3 mm1**

Messfläche: 706.86 **A [mm²]** *: Messunsicherheit [%] bezogen auf R_{thxA}

konst. Druck

Spalt [mm]	Kraft [N]	R_{th} [K/W]	λ_{eff} [W/(mK)]	R_{thxA} [mm²K/W]	Druck [bar]	T_{Probe} [°C]	Q_{Mittel} [W]	U* [%]
2.879	71	18.68	0.22	13202.2	1.0	27.5	1.2	16.6
2.871	141	18.50	0.22	13075.8	2.0	27.5	1.2	16.4

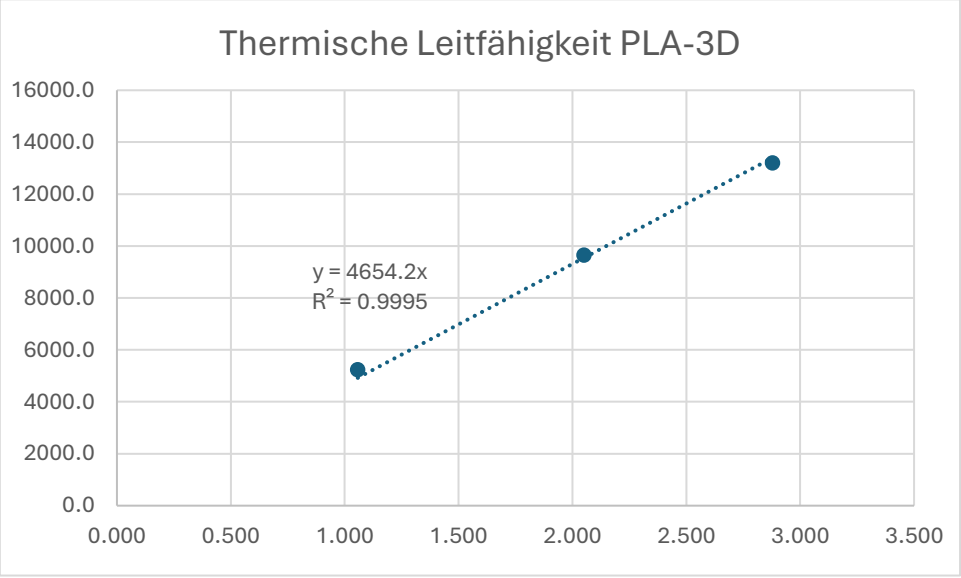

λ [W/(mK)]

0.2148597

8.5 Multi DOFS analysis software *8FiberScan*

8FiberScan User's Manual

The 8FiberScan software was created to enable the automatic scanning of up to eight DOFS using the Fiber Optic Switch 08 (FOS08, Luna Inc.) and the ODiSI-B. The ODB Sensor Config software was purchased from Polytec GmbH (distributor of Luna Inc. in central Europe), as well as the FOS08 and the ODiSI-B with its standard software.

The new software was coded in C++ using the Software Development Kits (SDKs) from the standard software issued with the ODiSI-B and FOS08. Qt Creator 4.10.2 (Community) was used as programming environment.

Please note, that the ODiSI-B was delivered with a tower PC with a PCIe port. Only this PC is able to communicate with the ODiSI-B. The software described in this document has been crafted on that PC and all programs and libraries needed can be found there.

The 8FiberScan software has four main classes, main, mainwindow, sensor and sensorsettings. Main starts the application. Mainwindow contains the functions to start a session, initialize the ODiSI-B, handle manual and automatic sensor scanning, open the sensor settings, save the data and disconnect from the ODiSI-B and end the session. The sensor class contains the functions to identify a sensor, switch the FOS08 ports, scan and average multiple scans. The sensor settings class enables the user to check which sensors have been identified and choose which to use for the measurement.

Functions in the GUI are consciously disabled until certain actions have been taken by the user. Therefore, the use of this program can only be carried out a certain way:

Start a New Session (forces user to choose a directory where a new folder for data from the session will be created, initializes ODiSI-B and identifies all connected sensors).

Sensor Settings (check whether all sensors are identified correctly, if not, check section '*Configurating a new DOFS'*, choose relevant sensors from list)

Tare (scans the relevant sensors multiple times and averages the scans, then saves the tare data)

Manual or Automatic Scan (scans DOFS and saves the data)

Abort Automatic Scan (aborts scan, but finishes the scan in progress first)

All data is immediately saved into the session folder as .txt files with clear designation based on time and date of session and sensor names in use.

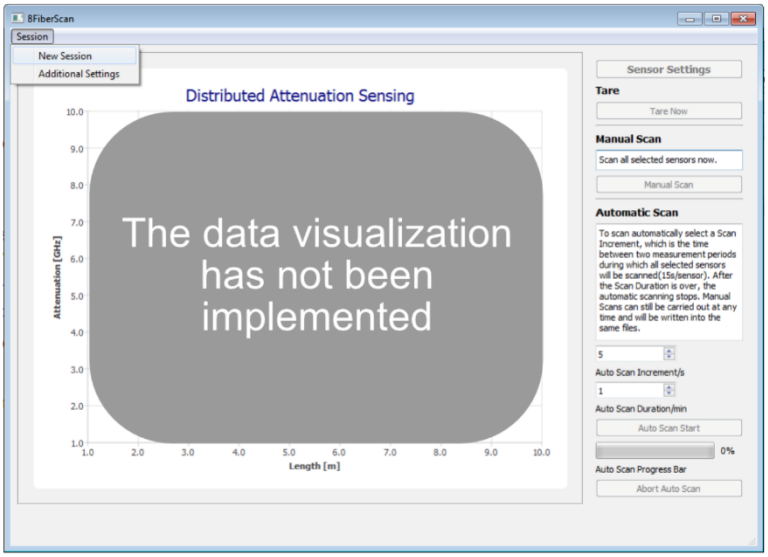

Figure 01: Screenshot from 8FiberScan with a new session being enabled.

Configurating a new DOFS

If your chosen and connected DOFS does not show up after sensor identification (once the sensor settings are available to the user), your DOFS may not be identifiable by the ODB software due to lack of fitting fiber key. The fiber keys are generated using the *ODB Sensor Cfg* software which is also found on the relevant PC. A user's manual is provided for this software. The correct fiber key must be created and saved under a unique name before it can be used.

Configurating the ODiSI-B and FOS08

For the software to communicate with the devices, they need to be connected correctly. A visual description is shown in Figure 02.

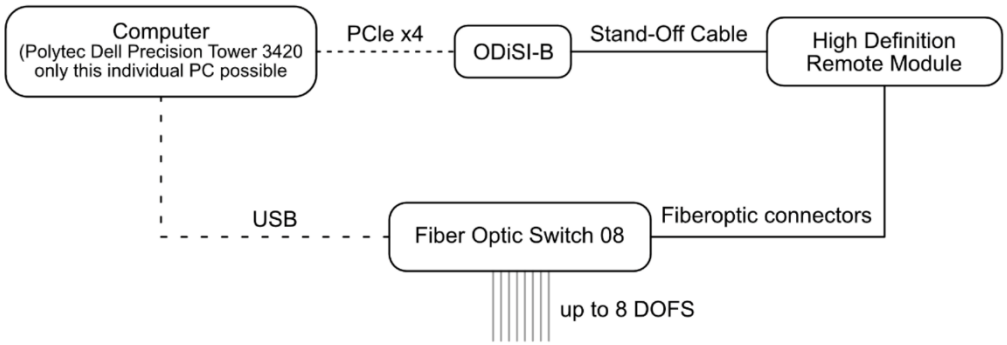

Figure 02: Connection overview between all devices needed for 8FiberScan use.

9. Declaration on oath

I hereby declare on oath, that I have written the present dissertation on my own and have not used other than the acknowledged resources and aids. The submitted written version corresponds to the version on the electronic storage medium. I hereby declare that I have not previously applied or pursued for a doctorate (Ph.D. studies).

Hamburg, Germany, 23.09.2025 

Maria Klippert